# LARGE-VOLUME RHYOLITE GENESIS IN CALDERA COMPLEXES OF THE SNAKE RIVER PLAIN

by

KATHRYN ERIN WATTS

A DISSERTATION

Presented to the Department of Geological Sciences
and the Graduate School of the University of Oregon
in partial fulfillment of the requirements
for the degree of
Doctor of Philosophy

June 2011

DISSERTATION APPROVAL PAGE

Student: Kathryn Erin Watts

Title: Large-volume Rhyolite Genesis in Caldera Complexes of the Snake River Plain

This dissertation has been accepted and approved in partial fulfillment of the requirements for the Doctor of Philosophy degree in the Department of Geological Sciences by:

| | |
|---|---|
| Ilya Bindeman | Chairperson |
| Gregory Retallack | Member |
| Mark Reed | Member |
| W. Andrew Marcus | Outside Member |

and

| | |
|---|---|
| Richard Linton | Vice President for Research and Graduate Studies/Dean of the Graduate School |

Original approval signatures are on file with the University of Oregon Graduate School.

Degree awarded June 2011

DISSERTATION ABSTRACT

Kathryn Erin Watts

Doctor of Philosophy

Department of Geological Sciences

June 2011

Title: Large-volume Rhyolite Genesis in Caldera Complexes of the Snake River Plain

Approved: _____
Dr. Ilya Bindeman

Caldera-forming eruptions are dramatic and destructive natural phenomena, causing severe and sustained consequences to society. This dissertation presents new geochemical and geochronologic data for caldera-forming tuffs and pre- and post-caldera rhyolites of the two youngest caldera complexes in the Snake River Plain (SRP) in the western USA: Heise (6.6-4.5 Ma) and Yellowstone (2.1-0.6 Ma). Caldera complex evolution at Heise and Yellowstone can be described by formation of 3-4 spatially overlapping "nested" calderas, successive collapse of intracaldera fill, and development of a large hydrothermal system.

Comparison between Heise and Yellowstone reveals that late-stage rhyolite eruptions have drastic depletions in $^{18}O$ that require remelting of large volumes (1,000's of $km^3$) of hydrothermally altered rock. Archean xenoliths and Phanerozoic rocks of the crustal basement beneath the SRP province are not depleted in $^{18}O$ and therefore cannot be a source of these rhyolites. Isotopic mixing models indicate that early large-volume rhyolites are produced by melting and hybridization of the crust by mantle-derived basalt, and late-stage rhyolites tap hydrothermally altered portions of intracaldera rocks from previous eruptions.

Caldera-forming eruptions at Heise culminated 4.45 Ma with eruption of the 1,800

km$^3$ Kilgore Tuff, the most voluminous $^{18}$O-depleted rhyolite in the SRP and worldwide. O, Sr, and Nd isotope geochemistry, zircon ages, mineral and whole-rock geochemistry, and liquidus temperatures for Kilgore Tuff samples erupted > 100 km apart are similar and/or overlapping within error, indicating derivation from a remarkably homogeneous low-$\delta^{18}$O magma reservoir ($\delta^{18}$O=3.4‰). Caldera-wide batch assembly and homogenization of variably $^{18}$O-depleted melt pockets with diverse zircon populations can explain the Kilgore Tuff's genesis.

Central Plateau Member (CPM) rhyolites at Yellowstone have the same timing (~2 million years after the initiation of volcanism), magnitude of $\delta^{18}$O depletion (~3‰ depleted relative to normal rhyolites), and cumulative eruptive volume (~4,000-4,500 km$^3$) as the Kilgore Tuff of the Heise volcanic field. Isotopic, age, and geochemical data for CPM rhyolites show that they become progressively more homogeneous and evolved from 260 ka to 75 ka. Whereas the Kilgore Tuff erupted climactically as an explosive caldera-forming tuff, CPM rhyolite eruptions record sequential, predominantly effusive, "snapshots" of magma assembly, homogenization, and differentiation.

This dissertation includes co-authored materials both previously published and submitted for publication.

# CURRICULUM VITAE

NAME OF AUTHOR: Kathryn Erin Watts

GRADUATE AND UNDERGRADUATE SCHOOLS ATTENDED:

University of Oregon, Eugene
Louisiana State University, Baton Rouge

DEGREES AWARDED:

Doctor of Philosophy in Geological Sciences, 2011, University of Oregon
Bachelor of Science in Geology, 2006, Louisiana State University
*Magna Cum Laude*

AREAS OF SPECIAL INTEREST:

Volcanology
Geochemistry
Igneous Petrology

GRANTS, AWARDS, AND HONORS:

Staples Research Fellowship, University of Oregon, 2010

Weiser Scholarship, University of Oregon, 2010

Staples Scholarship, University of Oregon, 2008

Baldwin Research Scholarship, University of Oregon, 2008

Jack Kleinman Memorial Fund Grant for Volcano Research, U.S. Geological Survey, 2007

Outstanding Senior, Louisiana State University Geology Department, 2006

Field Camp Scholarship, Louisiana State University, 2006

PUBLICATIONS:

Watts, K.E., Bindeman, I.N., and Schmitt, A.K., 2011, Large-volume rhyolite genesis in caldera complexes of the Snake River Plain: Insights from the Kilgore Tuff of the Heise volcanic field, Idaho, with comparison to Yellowstone and Bruneau-Jarbidge rhyolites: Journal of Petrology, v. 52, p. 857–890.

Watts, K.E., Leeman, W.P., Bindeman, I.N., and Larson, P.B., 2010, Supereruptions of the Snake River Plain: Two-stage derivation of low-$\delta^{18}O$ rhyolites from normal-$\delta^{18}O$ crust as constrained by Archean xenoliths: Geology, v. 38, p. 503–506.

Bindeman, I.N, Watts, K.E., Schmitt, A.K., Morgan, L.A., and Shanks, P.W., 2007, Voluminous low $\delta^{18}O$ magmas in the Late Miocene Heise volcanic field, Idaho: Implications for the fate of Yellowstone hotspot calderas: Geology, v. 35, p. 1019–1022.

Watts, K.E., 2007, Yellowstone and Heise: Supervolcanoes that lighten up: Geotimes, v. 52, p. 24–29.

ACKNOWLEDGMENTS

Research support for this dissertation was provided by funds from the National Science Foundation to Dr. Ilya Bindeman (EAR-0537872 and EAR/CAREER-844772) and Dr. Axel Schmitt (IF-0732691). I thank the University of Oregon Department of Geological Sciences for numerous research fellowships and scholarships that supported this work and the U.S. Geological Survey for a Jack Kleinman Memorial Fund Grant for Volcano Research that offset field and analytical expenses.

I thank my advisor, Ilya Bindeman, for his guidance and steadfast encouragement. I knew from the very first field season with him in Idaho, when he asked our waitress to make his salmon filet "1.5 times bigger," that he would accept nothing short of my best work, and for that, I am eternally grateful. I thank my dissertation committee members, Greg Retallack, Mark Reed and Andrew Marcus, for their thoughtful guidance during our yearly committee meetings. I thank Axel Schmitt for his unwavering enthusiasm as a collaborator during my numerous visits to the UCLA SIMS facility.

There have been many others who have shaped my academic career and to whom I owe a debt of gratitude. The outstanding Volcanology-Geochemistry-Petrology (VGP) faculty at the University of Oregon has been a tremendous asset in my development as a scientist. They not only provided excellent and challenging curricula, but led through example the importance of collaboration and collegiality. I thank Erwan Martin, Jorge Vazquez, Bill Leeman and Guillaume Girard for many helpful scientific discussions. I would also like to acknowledge two undergraduate student workers, Luke Sitts and Pete Tollan, who assisted me in data collection. Finally, I would like to thank the UO Stable

Isotope Lab manager, Jim Palandri, for keeping the lab population happy, healthy and free of explosions.

In addition to those who deserve credit for my academic achievements are my family and friends, who have supported me and kept me grounded throughout the course of my Ph.D. My mother, father and sister, Lauri, Don and Megan Watts, were always in my corner to provide words of encouragement, love and support when they were needed most. My in-laws, Mary Zalar, Ken Whitten, Dave Fritts and Josh Fritts, have been a true second family to me and I am very grateful for their support. Last, I would like to thank my one-of-a-kind husband, Jeremy Fritts, who taught me that anything worth doing in life is worth doing well, and with a sense of adventure.

*For my mother, Lauri Watts, who taught me that with an education and ambition, life's horizons are limitless*

TABLE OF CONTENTS

Chapter Page

Chapter Page

LIST OF FIGURES

Figure Page



CHAPTER V



APPENDICES

Figure Page

LIST OF TABLES

Table Page

# CHAPTER I

## INTRODUCTION

Explosive rhyolitic eruptions constitute one of the most extreme geologic hazards on Earth. Understanding the processes by which large-volume rhyolitic magmas are generated is thus a prime goal of volcanological studies. However, this has been the subject of controversy for nearly a century. The two main competing models are that they are formed by 1) partial melting of silicic crustal rocks and 2) fractional crystallization of mafic parental magmas with or without crustal assimilation. Advances in analytical technology have allowed workers to unravel complex geochemical clues from rhyolite deposits that require important modifications to these two end member models. Based on the example of large-volume rhyolites in the Snake River Plain (SRP), this dissertation highlights the importance of wholesale recycling (remelting) of volcanic and plutonic rocks in the very shallow crust.

Over the past 16 Ma, a time-progressive chain of large volcanic fields, spanning > 800 km from eastern Oregon to western Wyoming, has been interpreted as the "track of the Yellowstone hot spot" in the SRP volcanic province (Pierce & Morgan, 1992). More than 200 explosive rhyolitic eruptions have been produced in the SRP (Nash *et al*., 2006), many of which are among the largest known volcanic eruptions on Earth, exceeding 1,000 $km^3$ in eruptive volume. A deep (> 400 km depth) mantle plume, currently beneath Yellowstone National Park in northwestern Wyoming (Waite *et al*., 2006), is thought to have provided the heat source for rhyolite genesis in the SRP. However, unique

geochemical signatures (namely $^{18}O$ depletions) of many rhyolites in the SRP province preclude the possibility of direct derivation from crustal or mantle sources. Instead, these signatures indicate significant involvement of meteoric water, and thus, fingerprint the shallow crust.

The youngest volcanic field in the SRP volcanic province, the Yellowstone Plateau volcanic field in western Wyoming (2.1-0.6 Ma), was the first documented case of $^{18}O$-depleted rhyolites in the SRP (Friedman *et al*., 1974; Hildreth *et al*., 1984; Taylor, 1986). Since these landmark studies, several other large volcanic fields in the SRP have also been found to exhibit significant $^{18}O$ depletions, including the Heise volcanic field in eastern Idaho (6.6-4.5 Ma) (Morgan & McIntosh, 2005; Bindeman *et al*., 2007), and the Bruneau-Jarbidge and Twin Falls volcanic fields (12.7-9.5 Ma) in central Idaho (Boroughs *et al*., 2005; Bonnichsen *et al*., 2008; Ellis *et al*., 2010). Therefore, these "unique" signatures may in fact be the norm rather than the exception in the SRP.

Despite the extreme abundance of $^{18}O$-depleted ("low-$\delta^{18}O$") rhyolites in the SRP, totaling more than 10,000 $km^3$ in eruptive volume, a model for their genesis remains elusive. In this dissertation I present new data for the two youngest SRP caldera complexes, Heise and Yellowstone, which I use to construct a unified model of SRP rhyolite genesis. I synthesize new data with published data for SRP rhyolites, and compare my new model with models previously proposed by other workers. Importantly, the model of rhyolite genesis that I advocate for SRP caldera complexes may be applicable to other large caldera centers elsewhere on Earth for which the characteristic $^{18}O$ depletions are either undiscovered or less pronounced, for instance due to less

extreme $^{18}O$ depletions in meteoric waters at low elevations and equatorial latitudes. Below, I provide a brief summary of each of my dissertation chapters.

Chapter II, VOLUMINOUS LOW $\delta^{18}O$ MAGMAS IN THE LATE MIOCENE HEISE VOLCANIC FIELD, IDAHO: IMPLICATIONS FOR THE FATE OF YELLOWSTONE HOTSPOT CALDERAS, was co-authored with my faculty advisor Ilya Bindeman at the University of Oregon, Axel Schmitt of the University of California, Los Angeles, and Lisa Morgan and Pat Shanks of the U.S. Geological Survey. This chapter was published in the journal *Geology* in 2007 (Bindeman *et al*., 2007). In this study we present new oxygen isotope and zircon geochronology data for all major rhyolites of the Heise volcanic field in eastern Idaho and compare $\delta^{18}O$ age trends with the younger Yellowstone Plateau volcanic field in western Wyoming. We find that the occurrence of low-$\delta^{18}O$ magmas at Heise and Yellowstone characterizes a mature stage of individual volcanic cycles in each caldera complex, when shallow, hydrothermally altered intracaldera rocks are remelted in very large volumes.

Chapter III, SUPERERUPTIONS OF THE SNAKE RIVER PLAIN: TWO-STAGE DERIVATION OF LOW-$\delta^{18}O$ RHYOLITES FROM NORMAL-$\delta^{18}O$ CRUST AS CONSTRAINED BY ARCHEAN XENOLITHS, was co-authored with William Leeman of the National Science Foundation, my faculty advisor Ilya Bindeman, and Peter Larson of Washington State University. This chapter was published in the journal *Geology* in 2010 (Watts *et al*., 2010). This paper presents new oxygen isotope data for Archean crustal xenoliths from three localities in the SRP. New oxygen isotope data was synthesized with published oxygen, strontium and neodymium isotope datasets for SRP xenoliths, rhyolites and basalts to construct isotopic mixing models. Results indicate that

normal-$\delta^{18}O$ rhyolites can be generated by partial melting and hybridization of the crust by mantle-derived basalt, and low-$\delta^{18}O$ rhyolites tap hydrothermally altered portions of normal-$\delta^{18}O$ rhyolitic rocks.

Chapter IV, LARGE-VOLUME RHYOLITE GENESIS IN CALDERA COMPLEXES OF THE SNAKE RIVER PLAIN: INSIGHTS FROM THE KILGORE TUFF OF THE HEISE VOLCANIC FIELD, IDAHO WITH COMPARISON TO YELLOWSTONE AND BRUNEAU-JARBIDGE RHYOLITES, was co-authored with my faculty advisor Ilya Bindeman at the University of Oregon and Axel Schmitt of the University of California, Los Angeles. This chapter was published in the *Journal of Petrology* in 2011 (Watts *et al*., 2011). We investigate in detail the last caldera-forming eruption of the Heise volcanic field, the 4.45 Ma Kilgore Tuff. We synthesize multiple datasets, including oxygen isotope data obtained by laser fluorination and ion microprobe, U-Pb zircon ages, mineral chemistry, whole-rock major and trace element geochemistry, strontium and neodymium isotope geochemistry, and thermometry data. Our findings support derivation of the Kilgore Tuff from remelting of hydrothermally altered intracaldera and subvolcanic portions of the first normal-$\delta^{18}O$ Heise tuff, the 6.62 Ma Blacktail Creek Tuff. New Heise data are also compared with published data for Yellowstone and Bruneau-Jarbidge rhyolites.

Chapter V, YOUNG AND VOLUMINOUS RHYOLITES OF THE YELLOWSTONE CALDERA: AN ISOTOPE AND GEOCHRONOLOGY STUDY OF INDIVIDUAL PHENOCRYSTS REVEALS PROGRESSIVE HOMOGENIZATION OF AN EVOLVING MAGMA RESERVOIR, was co-authored with my faculty advisor Ilya Bindeman at the University of Oregon and Axel Schmitt of the University of California,

Los Angeles. This chapter was prepared for submission to *Earth and Planetary Science Letters*. In this study, we present new data for young Central Plateau Member (CPM) rhyolites of the Yellowstone caldera, a predominantly effusive phase of post-caldera volcanism that followed the last caldera-forming eruption at Yellowstone 0.64 Ma. Using oxygen isotopes and U-Th ages for single zircon crystals, we find a trend of increasing homogenization of CPM rhyolites with decreasing age, supporting a model of batch assembly and homogenization of variably $^{18}O$ depleted melts beneath the Yellowstone caldera.

# CHAPTER II

# VOLUMINOUS LOW $\delta^{18}O$ MAGMAS IN THE LATE MIOCENE HEISE VOLCANIC FIELD, IDAHO: IMPLICATIONS FOR THE FATE OF YELLOWSTONE HOTSPOT CALDERAS

This chapter was published in *Geology* in 2007, volume 35, pages 1019-1022 (Bindeman et al., 2007). Coauthors Ilya Bindeman and Axel Schmitt provided funding for the project and assisted in data acquisition. Coauthors Lisa Morgan and Pat Shanks provided guidance during field work. I performed the bulk of the analyses and was the second author.

## VOLUMINOUS RHYOLITES OF THE SNAKE RIVER PLAIN AND THE HEISE VOLCANIC FIELD

Patterns of basaltic and silicic volcanism of the Snake River Plain (SRP; Fig. 1) follow 2 cm/yr plate migration over a Yellowstone mantle plume (Christiansen, 2001; Yuan and Dueker, 2005) that taps progressively older, thicker, more differentiated, and more fertile silicic crust (Morgan et al., 1984; Nash et al., 2006). Partial melting of crust above the plume head caused the formation of large silicic magma bodies that erupted explosively and effusively in a series of 0.5–1 Ma caldera clusters yielding ~40 voluminous (>300 $km^3$) rhyolitic supereruptions since 16 Ma (e.g., Perkins and Nash 2002; Bonnichsen et al., 2007). These eruptive clusters, or nested caldera complexes, have a 2–3 m.y. lifespan that may reflect the duration of piecemeal assembly of

batholithic bodies in the lower and upper crust. The silicic magma bodies are density traps for basaltic magma input from the Yellowstone mantle plume and thus provide a focused heat source for crustal melting.

**Figure 1.** Map of Snake River Plain (SRP) showing Heise and Yellowstone Plateau (YP) caldera complexes. Dark shaded area in Heise volcanic field indicates extent of Kilgore ignimbrite from Morgan and Macintosh (2005). Post-caldera units dated in this study (Table 1) are indicated by bold letters: IC—Indian Creek; JB—Juniper Buttes; LH—Long Hollow; SR—Sheridan Reservoir.

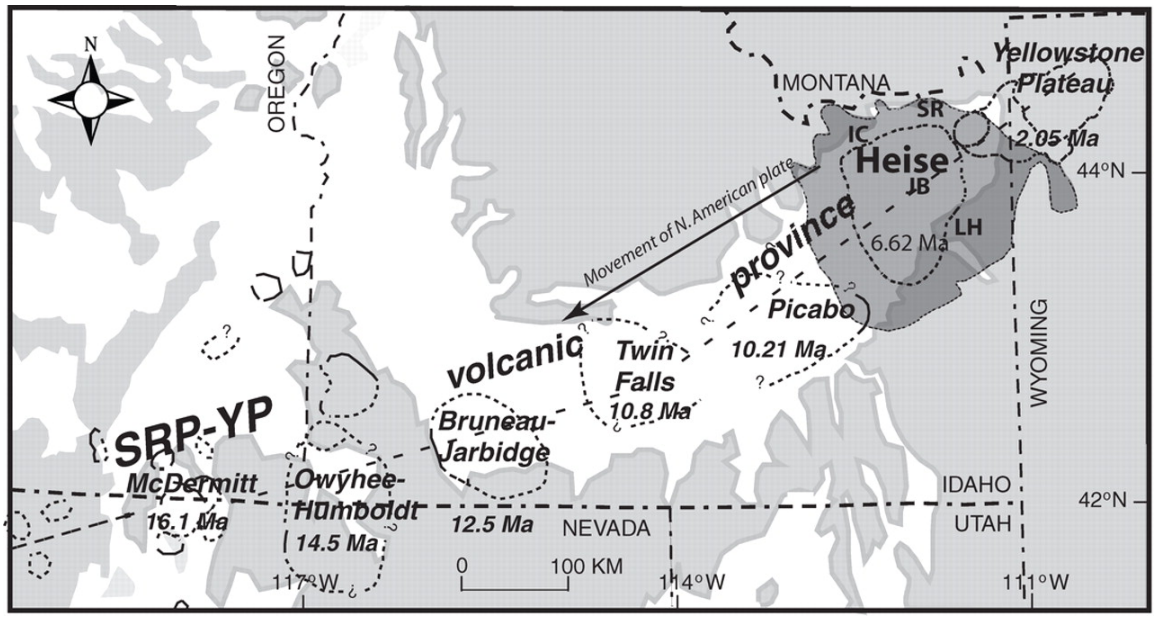


The currently active and best-studied Yellowstone complex includes three nested calderas that formed since its inception ca. 2.1 Ma. Here we focus on the 6.6–4.0 Ma Heise caldera complex that directly precedes Yellowstone and includes four nested calderas (Table 1). The Heise volcanic field is far better preserved than any of the earlier caldera complexes within the Snake River Plain. It contains a distinct resurgent dome, Juniper Buttes, and post-caldera rhyolitic lavas in the center and along the projected ring fracture of the caldera (Fig. 1). Therefore, the Heise field offers the second-best example

of magmatism along the Snake River Plain and, along with Yellowstone, delineates general patterns for understanding the origin of rhyolites. Here we report oxygen isotope analyses of phenocrysts and ion microprobe U-Pb ages of zircons in the Heise volcanic field and discuss important similarities and differences with Yellowstone (Table 1). This work significantly expands the number and volume of severely $^{18}O$ depleted magmas in the Snake River Plain. The appearance of low $\delta^{18}O$ magmas seems to herald the terminal stages in the evolution of individual volcanic cycles.

Successive eruptions of four large-volume ignimbrite units in the 6.6–4.0 Ma Heise volcanic field (Table 1) resulted in the formation of four large and overlapping calderas: the 1200 $km^3$ Blacktail Creek tuff, ~750 $km^3$ Walcott tuff, ~300 $km^3$ Conant Creek tuff, and 1800 $km^3$ Kilgore tuff (ignimbrite) (volume estimates are from Morgan and McIntosh, 2005). The $^{40}Ar/^{39}Ar$ dating of widely distributed Kilgore samples yielded indistinguishable ages consistent with a single eruption event and inferred source vents in the north and in the south of the caldera (Morgan and McIntosh, 2005). Pre-caldera and post-caldera lavas and domes have been previously mapped, but few reliable age data are available. All magmas in Heise are high-silica rhyolites (74–76 wt% $SiO_2$) with similar phenocryst phases of sanidine, plagioclase, quartz, pyroxenes, opaques, zircon, ±biotite, but they exhibit variations in phenocryst abundance from nearly aphyric (Walcott) to more crystal rich (10%–20%; Blacktail Creek tuff).

**Table 1.** U-Pb zircon ages and $\delta^{18}O$ values of phenocrysts in major tuffs and lavas from the Heise volcanic field, Idaho

| Cycle, Unit | Sample | Volume ($km^3$) | Ar-Ar eruption age (m.y.) | U-Pb concordia age (m.y.) (n) | $\delta^{18}O$ (‰) average | | | Melt (‰) | Temperature (°C) | | $^{86}Sr_i/^{86}Sr_i$ |
|---|---|---|---|---|---|---|---|---|---|---|---|
| | | | | | Quartz | Zircon | Sanidine | (Calc.) | Zrc sat | Liq | |
| **I. Blacktail Creek** | 95–2001a | 1200 | 6.62 ± 0.03 | 6.92 ± 0.28 (12) | 6.4 | 4.81 | | 6.0 | 848 | 824 | 0.7115 |
| **II. Walcott** | 06HS-18 | 750 | 6.27 ± 0.04 | | 7.3* | | 5.48 | 5.9 | 786 | 856 | 0.7128 |
| Wolverine Creek | 06HS-16 | <100? | 5.59 ± 0.05 | 5.45 ± 0.14 (15) | | | 6.08† | 6.1 | 799 | 855 | |
| **III. Conant Creek** | 06HS-5 | 300 | 5.51 ± 0.13 | 5.70 ± 0.19 (10) | 6.4* | | 5.43 | 5.8 | 859 | 942 | |
| **IV. Kilgore** | TNP96–43 | 1800 | 4.45 ± 0.05 | 4.59 ± 0.26 (10) | 4.46 | **1.58**,1.69 *1.58* | | 3.3 | 842 | 845 | 0.7104- |
| | 2000–17 | " | 4.45 ± 0.06 | 4.49 ± 0.25 (12) | 4.33 | 1.50 | | 3.3 | 874 | 843 | 0.7109 |
| post-Kilgore, intracaldera lavas | | | | | | | | | | | |
| Long Hollow | 626.1 | <20 | 3.5 ± 0.4* | 4.28 ± 0.18 (13) | 4.68 | 1.92,*1.65* | 3.78 | 4.2 | 816 | 780 | |
| Indian Creek | 06HS-1 | <20 | 4.14 ± 0.09* | 3.96 ± 0.18§ (6) | *1.40* | 1.21,1.12 | 3.02 | 3.4 | 858 | 868 | |
| | | | | 4.11 ± 0.27# (6)<br>4.46 ± 0.17‡ (21) | | | | | | | |
| Juniper Buttes | 06HS-4 | <20 | 3.3–3.7† | 4.29 ± 0.15 (9) | | | 3.80 | 4.2 | 811 | 778 | |
| Sheridan Reservoir | 06HS-19 | <20 | | 2.07 ± 0.19 (14) | 4.55 | 2.51,2.37<br>2.25 | 3.74 | 4.1 | 886 | 857 | |

Ages were corrected for the initial ($^{234}U/^{230}Th$) disequilibria using Sharer (1984). Zircon oxygen isotope analyses are by size fractions: bold = > 150 μm, air abraded; underlined = > 105 μm; normal font = bulk; italics = < 53 μm. Liquidus (Liq) temperatures were determined in MELTS program at 4 wt% water and 1.5 kbar pressure; Zrc sat are calculated zircon saturation temperatures.

*Old K-Ar ages and Sr isotope values were reported in Morgan and McIntosh (2005).

†Fresh glass.

§Rims (0-2 μm).

#Rims (5-7 μm).

‡Cores.

## OXYGEN ISOTOPE RESULTS AND U-PB AGES OF ZIRCON: HEISE VERSUS YELLOWSTONE

Oxygen isotope values of quartz, zircon, and sanidine phenocrysts of the major ignimbrites and post-caldera units differ dramatically despite overall compositional similarities (Fig. 2). Our new analyses demonstrate that the Blacktail Creek, Walcott, and Conant Creek large-volume tuffs have normal $\delta^{18}O$ values, while the youngest and the most voluminous ignimbrite in the sequence, the Kilgore tuff, and post-Kilgore lavas are strongly depleted in $\delta^{18}O$ by 3‰ (Fig. 2).

**Figure 2.** Oxygen isotope phenocryst values vs. $^{40}Ar/^{39}Ar$ eruptive age for volcanic rocks of Heise volcanic field (this work) as compared to Yellowstone (data from Bindeman and Valley, 2001). Major episodes of caldera formation are labeled by the name of the caldera-forming ignimbrite (Table 1). Note progressive depletion of $\delta^{18}O$ values in each caldera cluster, interpreted here to represent remelting of hydrothermally altered rocks progressively buried by caldera collapses. Zircons in low $\delta^{18}O$ Kilgore ignimbrite and post-caldera lavas are in isotopic equilibrium with quartz and feldspar and do not show $\delta^{18}O$ variation as a function of size (Table 1). Abbreviations: HRT—Huckleberry Ridge tuff; MFT—Mesa Falls tuff; LCT—Lava Creek tuff. VSMOW—Vienna standard mean ocean water.

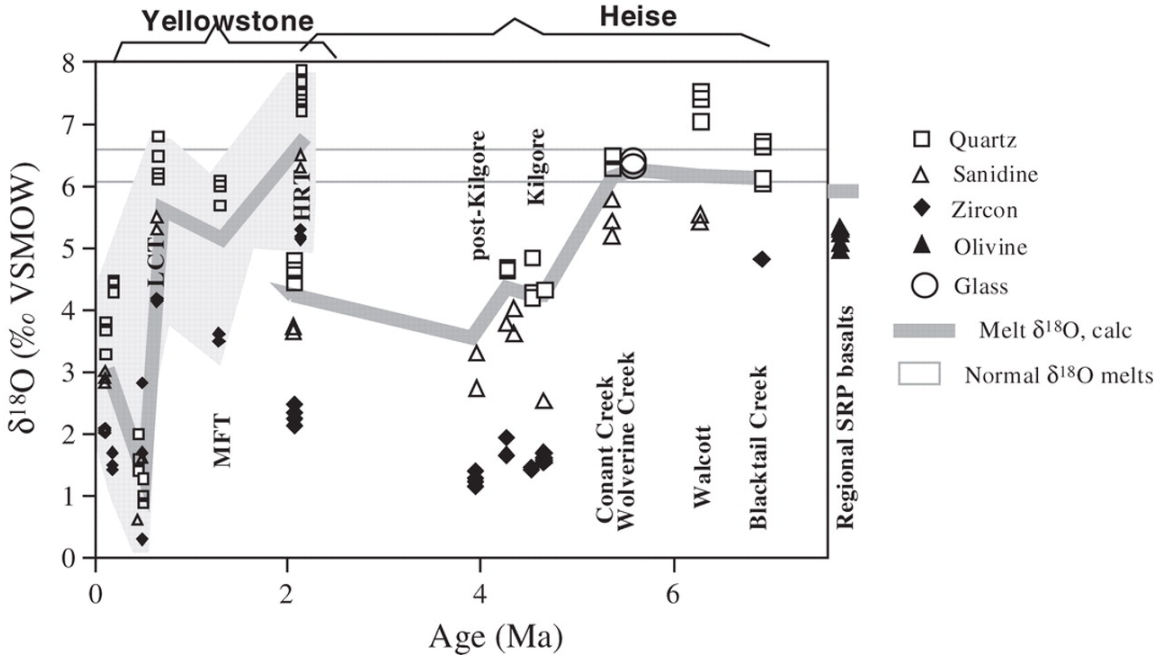

Zircon represents a near-liquidus phase in these crystal-poor high-silica rhyolites and thus provides a somewhat better, near-liquidus, proxy for $\delta^{18}O_{melt}$ than quartz, which crystallized last among all major phenocryst phases and is absent in crystal-poor varieties of tuffs. Using $\Delta^{18}O_{melt\text{-}zircon}$ of 1.8‰ applicable at magmatic temperatures of ~800 °C, we estimate Kilgore and post-Kilgore $\delta^{18}O_{melt}$ to be ~3.3‰ and ~3‰, respectively, lower relative to normal $\delta^{18}O$ rhyolites that result from mantle magma differentiation (Fig. 2). Zircons were sieved into large, intermediate, and small size fractions (>105 μm, <50 μm), and analyzed in bulk as described in Bindeman and Valley (2001). In addition, larger size fractions of zircons were air abraded in a corundum abrader that removed outermost ~20%–35% of zircons and yielded cores. However, no differences between large zircons or zircon cores and small zircons were found at Heise, suggesting that core to rim oxygen isotope zoning is either absent or very subtle (<0.4‰). Moreover, quartz-zircon and sanidine-zircon oxygen isotopic fractionations at Heise (Fig. 2; Table 1) are in equilibrium, and are consistent with temperatures of 700−800 °C using fractionation factors from Valley et al. (2003), and with liquidus and zircon saturation temperatures (Table 1). The lack of oxygen isotopic zoning in zircons distinguishes Heise from Yellowstone and Timber Mountain calderas (Bindeman and Valley, 2001; Bindeman et al., 2006), where isotopically zoned zircons are present in low $\delta^{18}O$ magmas. Post-caldera lavas show somewhat variable $\delta^{18}O_{zircon}$ values but lack a sawtooth pattern in the $\delta^{18}O$ versus eruption age plot for Yellowstone (Fig. 2).

U-Pb zircon ages were determined in nine samples: two samples of Kilgore ignimbrite, four samples of post-Kilgore rhyolites, and one sample each of Blacktail Creek, Conant Creek, and Wolverine Creek tuffs (Table 1). The U-Pb ages in most

samples are normally distributed and therefore are treated as single populations. Disequilibrium-corrected $^{206}Pb/^{238}U$ zircon crystallization ages overlap within uncertainty with $^{40}Ar/^{39}Ar$ sanidine eruption ages. Post-Kilgore rhyolite of Long Hollow erupted at the inferred ring fracture, and rhyolites of Juniper Buttes in the resurgent dome are identical in age. In the earliest post-Kilgore lava, the Indian Creek rhyolite, the outermost ~3–5 μm zircon rims yield U-Pb zircon crystallization ages that agree with the K-Ar eruption age and are ~0.5 m.y. younger than cores that have Kilgore tuff age (ca. 4.5 Ma). This earliest low $\delta^{18}O$ post-Kilgore intracaldera lava may represent residual low $\delta^{18}O$ Kilgore magma that was still remaining in the magma body after caldera collapse. The latest post-Kilgore low $\delta^{18}O$ Heise rhyolite, Sheridan Reservoir, has a U-Pb zircon age of 2.07 Ma that significantly postdates the Kilgore tuff eruption and has ~0.7‰ higher $\delta^{18}O_{zircon}$ values. Furthermore, U-Pb zircon age of Sheridan Reservoir rhyolite overlaps the age of Huckleberry Ridge tuff of Yellowstone. This suggests that dying low $\delta^{18}O$ volcanism at Heise was contemporaneous with the initially high $\delta^{18}O$ volcanism at the newly developing Yellowstone center. Pre-Heise xenocrysts are extremely rare in lavas and tuffs, and were found in only one sample (Juniper Buttes), where two zircons yielded ages of 49 and ca. 55 Ma.

The comparison between Heise and its immediate successor Yellowstone is instructive: both produced high-silica, low $\delta^{18}O$ rhyolites with similar magmatic temperatures (Table 1; Nash et al., 2006). However, there are several features of the Heise rhyolites that are different from smaller-volume but more strongly $\delta^{18}O$ depleted rhyolites erupted at Yellowstone: (1) Heise zircons have crystallization ages that are comparable to the Ar-Ar eruption ages; (2) zircons are in $\delta^{18}O$ isotopic equilibrium with

quartz and sanidine, and zircon size fractions are homogeneous in $\delta^{18}O$, while Yellowstone zircons are zoned by 5‰; (3) post-Kilgore volcanic units retain levels of $\delta^{18}O$ depletion similar to those of Kilgore for more than 2 m.y. of post-caldera activity; and (4) the low $\delta^{18}O$ Kilgore ignimbrite has lower $^{87}Sr/^{86}Sr$ ratios (Table 1) compared to the preceding tuff units, while the low $\delta^{18}O$ post-caldera Yellowstone rhyolites always show higher $^{87}Sr/^{86}Sr$ values, interpreted by Hildreth et al. (1991) as evidence for high $^{87}Sr/^{86}Sr$, low $\delta^{18}O$ brines entering the magma chamber.

Bindeman and Valley (2001) estimated that in Yellowstone low $\delta^{18}O$ small-volume post-caldera rhyolites zircon resided for 5–10 k.y., while larger volume tuffs of the Mesa Falls tuff and Lava Creek tuff lack inherited cores, perhaps due to longer accretion times. We interpret the origin of zircons in the Kilgore tuff and post-caldera units as representing longer magmatic residence in which inherited high $\delta^{18}O$ pre-Kilgore zircons became annealed of $\delta^{18}O$ zoning through diffusion, solution-reprecipitation, and new growth in a voluminous low $\delta^{18}O$ Kilgore magma body.

## LOW $\delta^{18}O$ MAGMATISM: SOURCE-RELATED FLUKE OR PREDETERMINED OUTCOME OF CALDERA CLUSTER EVOLUTION?

Boroughs et al. (2005) interpreted the newly discovered abundant low $\delta^{18}O$ magmas in the older 12–10 Ma central Snake River Plain volcanic systems of Bruneau-Jarbidge and Twin Falls (Fig. 1) as due to melting of low $\delta^{18}O$ Eocene–Cretaceous source rocks of the Idaho batholith, 200 km west of Heise. Melting of an older low $\delta^{18}O$ crustal source cannot apply to Heise or Yellowstone because of the sharp isotopic contrast between early and late tuffs erupted from their respective nested caldera complexes (Fig.

2). Furthermore, our analyses of olivine phenocrysts in seven high $^{3}He/^{4}He$ Snake River Plain basalts erupted through and around the Heise field returned expected $\delta^{18}O$ values of 4.8‰–5.2‰ (Fig. 2), precluding a mantle low $\delta^{18}O$ source. What caused the formation of >1800 $km^3$ of low $\delta^{18}O$ magmas at Heise?

Here we attempt to connect the level of $\delta^{18}O$ depletion with erupted magmatic volumes as a model for genesis of low $\delta^{18}O$ rhyolites in caldera settings. Figure 3 plots the inferred volumes of known low $\delta^{18}O$ magmas in caldera settings throughout the western United State and the level of their $\delta^{18}O$ depletion that show an overall positive correlation of volume with $\delta^{18}O$. The most depleted post-caldera Yellowstone lavas at 0‰ represent pure remelting of the hydrothermally altered carapace around the magma chamber. The first voluminous erupted unit of Yellowstone, the Huckleberry Ridge tuff, is normal $\delta^{18}O$ (6.5‰–7.5‰), while subsequent Yellowstone units Mesa Falls and Lava Creek tuffs are moderately $\delta^{18}O$ depleted and contain some carapace-derived low $\delta^{18}O$ component. Eruptive volumes of low $\delta^{18}O$ central Snake River Plain rhyolites (data from Boroughs et al., 2005) are loosely defined, but it appears that larger units plot on the western U.S. caldera trend while smaller units are displaced toward lower eruptive volumes for a given $\delta^{18}O$ value (Fig. 3). This may either reflect underestimation of the eruptive volumes or suggest the influence of some other low $\delta^{18}O$ source such as the Idaho Batholith. In contrast, the Kilgore tuff is more $\delta^{18}O$ depleted relative to its peers, and plots to the right of the main "diluting" trend. Note that the $\delta^{18}O$ value of meteoric hydrothermal fluids at Heise should be either comparable to that of Yellowstone or somewhat higher due to the lower altitude of the Heise field. We propose that the Kilgore

**Figure 3.** Origin of large-volume low $\delta^{18}O$ magmas in caldera settings. A: $\delta^{18}O$ values of bulk magma plotted against its eruptive volume, where low $\delta^{18}O$, 0‰ hydrothermally altered rock or magma are bulk mixtures between normal $\delta^{18}O$ magma and 7‰ (lower curve) and 9‰ (upper curve) lower crustal magma, respectively. Mixing lines are drawn assuming ellipsoidal geometry of magma chambers from panel B, in which low $\delta^{18}O$ rocks are confined to the intracaldera block. In A, Yellowstone magmas define a trend of mixing between most $\delta^{18}O$ depleted, ~0‰ Canyon flow (CF) rhyolites of small 40 $km^3$ volume and normal $\delta^{18}O$, 8‰ Huckleberry Ridge tuff (HRT)–type magma. The most $\delta^{18}O$ depleted CF rhyolite from Yellowstone represents 100% remelting of the low $\delta^{18}O$ hydrothermally altered rocks, while HRT-type magma that erupted at the inception of volcanism at Yellowstone represents the lower crust–derived normal $\delta^{18}O$ component. Intermediate $\delta^{18}O$ magmas such as Lava Creek tuff (LCT), Mesa Falls tuff (MFT), and post-LCT 0.2 Ma Yellowstone rhyolites are plotted vs. their respective eruptive volumes and plot on the overall Yellowstone mixing (or low $\delta^{18}O$ diluting) trend. The voluminous 1000 $km^3$ low $\delta^{18}O$ Ammonia Tanks tuff (AT) of Timber Mountain Caldera complex, Nevada (Bindeman et al., 2006), also plots on this mixing trend. Thin lines are central Snake River Plain (SRP) low $\delta^{18}O$ units (Boroughs et al., 2005) with poorly defined volumes plot variably. VSMOW—Vienna standard mean ocean water. B: Conceptual model of mixing of low $\delta^{18}O$ carapace melt with normal $\delta^{18}O$ magma from below in caldera settings. The low $\delta^{18}O$ end member is diluted over progressively larger magma volumes when vertical and horizontal sizes of the magma chamber increase. Bulk $\delta^{18}O$ of final magma results from volumetric contributions from the low $\delta^{18}O$ cap and the normal $\delta^{18}O$ magma chamber as indicated by the ellipsoids. Based on these constraints, the more voluminous Kilgore magma body taps a greater proportion (~40%) of low $\delta^{18}O$ carapace compared to Yellowstone. Alternatively, if $\delta^{18}O$ depletion in the carapace is greater compared to Yellowstone, smaller proportions of low $\delta^{18}O$ melts will suffice.

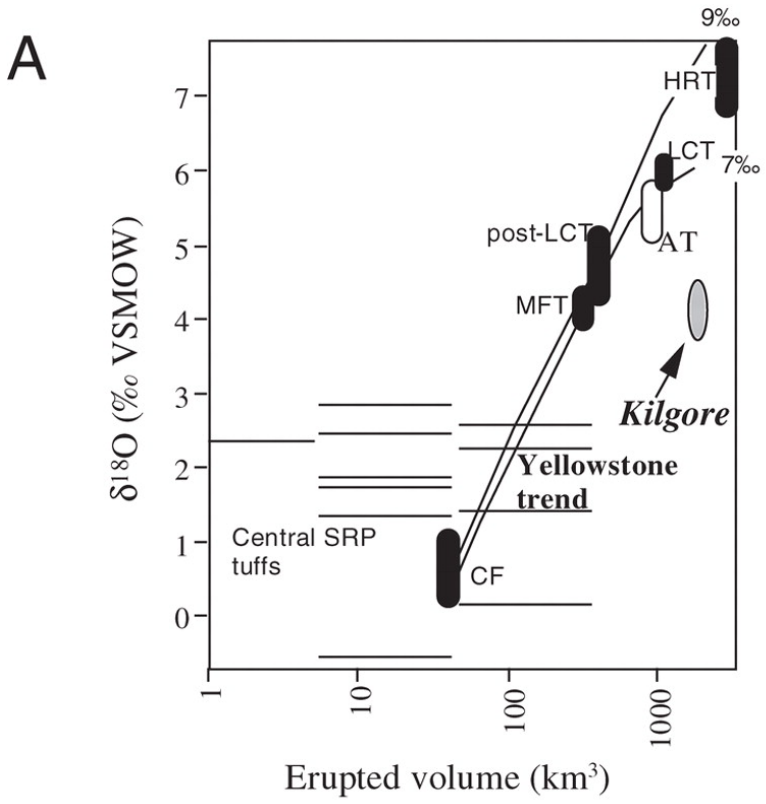
A
9‰
HRT
LCT
7‰
AT
post-LCT
MFT
Kilgore
Yellowstone
trend
Central SRP
tuffs
CF
δ18O (‰ VSMOW)
Erupted volume (km3)
0
1
2
3
4
5
6
7
1
10
100
1000

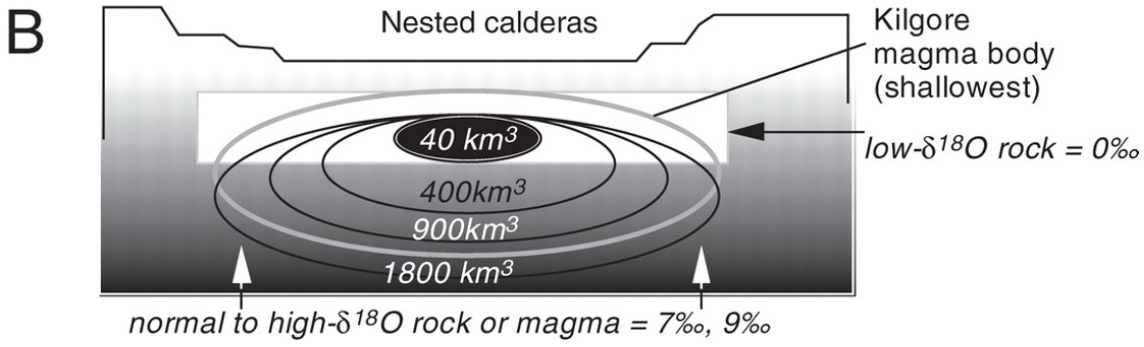
B
Nested calderas
Kilgore
magma body
(shallowest)
low-δ18O rock = 0‰
40 km3
400km3
900km3
1800 km3
normal to high-δ18O rock or magma = 7‰, 9‰

tuff represents the eruption of a comparatively shallow magma body that has digested a significant proportion of a low $\delta^{18}O$ carapace formed by down-dropped caldera fill and shallow intrusives from earlier caldera cycles (Fig. 3). Shallow venting of the Kilgore magma body is evident from a series of low-altitude vents located in the circumference of the caldera that operated in a fire-fountaining mode, as suggested by Morgan (1988). In addition, the large aerial extent of the Kilgore caldera suggests a high aspect ratio of the collapsed caldera and therefore a rather small vertical drawdown (Fig. 1; Morgan, 1988).

## LOW $\delta^{18}O$ MAGMAS: WHY ARE THEY SO ABUNDANT?

The significant level of depletion of Kilgore magma requires tens of percent of hydrothermally altered assimilant to be added to the initial pre-Kilgore, post–Conant Creek mantle-derived magma. By mass balance, the 3‰ depletion would require a process more in line with bulk melting, digestion, or reactive assimilation (e.g., Bindeman and Valley, 2001; Beard et al., 2005) rather than conventional assimilation–fractional crystallization (e.g., Balsley and Gregory, 1998). The amount of basalt required to generate ~1000 $km^3$ of silicic magma from a protolith that cooled below solidus to ~500–600 °C, and was altered by low $\delta^{18}O$ hydrothermal fluids, is estimated to be 250–500 $km^3$[1]. At high (Hawaiian) magma production rates of 0.001 $km^3/km^2/yr$, the assembly of a Kilgore-size magma body would require a minimum of 10–20 k.y., and

[1] This calculation is based on 1.5 kJ/kg K heat capacity of basalt, 600 °C basalt cooling from 1250 °C liquidus to 550 °C ambient temperature, 400 kJ/kg latent heat of its crystallization, yielding a total of 1450 kJ/kg for basalt. It takes ~300–400 kJ/kg to melt a granitic rock by reheating it by 300 °C and increasing the melt fraction by 50%, or only ~200 kJ/kg if the initial rock is already a glassy high-silica rhyolite with few crystals, and so little or no latent heat of fusion is required. At assumed heat transfer efficiency (e.g., Dufek and Bergantz, 2005) of 40%–20% for the preheated near solidus rhyolite, the basalt can melt 2–5 times the volume of rhyolite.

this time may be sufficiently long to dissolve and reprecipitate inherited zircons, explaining the lack of inherited cores.

## FATE OF YELLOWSTONE HOTSPOT CALDERA COMPLEXES: FROM NORMAL TO LOW $\delta^{18}O$ MAGMAS

This study demonstrates that despite the outlined differences between Yellowstone and Heise, a systematic trend emerges: volcanism starts with the eruption of normal $\delta^{18}O$ magmas by partial melting of preexisting crust, results in formation of several partially overlapping calderas, and terminates with the appearance of low $\delta^{18}O$ magmas. The low $\delta^{18}O$ magmas hallmark the final stages of individual volcanic cycles, when volcanic cannibalism last taps down-dropped hydrothermally altered volcanic and subvolcanic rocks associated with earlier successive caldera collapses. After that, the melting potential of the crustal block becomes exhausted and voluminous silicic magma extraction ceases, even if thermal input from the mantle remains similarly high. However, lingering small-volume, low $\delta^{18}O$, post-caldera volcanism such as Sheridan Reservoir rhyolite, driven by fresh basalt input, is possible and is produced by wholesale remelting of the solidified low $\delta^{18}O$ Kilgore batholith, contemporaneous with formation of Huckleberry Ridge batholith nearby. Due to progressive plate migration relative to the mantle plume (Fig. 1), large-volume crustal melting, starting with normal $\delta^{18}O$ magmas, is initiated at a new location of fertile crust. The first cycle of caldera-forming eruptions at Yellowstone produced normal $\delta^{18}O$ magma much like the first-cycle magmas at Heise. We suggest that this crustal evolution scenario demonstrated for Yellowstone and Heise

serves as a model for older caldera complexes along the Snake River Plain and perhaps elsewhere, pending better dating, volume estimation, and oxygen isotope analysis.

**BRIDGE**

In Chapter II, I showed that the Heise volcanic field in eastern Idaho shares key similarities with the younger Yellowstone Plateau volcanic field in western Wyoming. The progression from normal-$\delta^{18}O$ to low-$\delta^{18}O$ magmas at Heise and Yellowstone may be indicative of the fate of Yellowstone hot spot calderas, whereby remelting of the uppermost crustal carapace signifies a terminal stage of rhyolite genesis from the crustal block. In Chapter III, I expand my investigation to a suite of Archean crustal xenoliths in the central and eastern SRP. I use isotopic data to constrain the composition of the crustal basement in the SRP, and test and expand the model proposed in Chapter II by constructing isotopic mixing models.

# CHAPTER III

## SUPERERUPTIONS OF THE SNAKE RIVER PLAIN: TWO-STAGE DERIVATION OF LOW-$\delta^{18}O$ RHYOLITES FROM NORMAL-$\delta^{18}O$ CRUST AS CONSTRAINED BY ARCHEAN XENOLITHS

This chapter was published in *Geology* in 2010, volume 38, pages 503-506 (Watts et al., 2010). Coauthors William Leeman and Peter Larson provided the xenolith samples and assisted in the editorial process. Coauthor Ilya Bindeman provided guidance during analytical work and editorial assistance. I performed the laboratory work and was the primary author.

## INTRODUCTION

The Snake River Plain–Yellowstone Plateau (SRP-YP) volcanic province in the western United States has produced some of the most voluminous rhyolitic eruptions on Earth. Most rhyolites in the SRP-YP province were generated by partial melting and hybridization of continental crust by massive basaltic intrusions into the North American craton (Leeman et al., 2008). More than 10,000 $km^3$ of low-$\delta^{18}O$ rhyolite (1‰–6‰ depleted from normal magmatic values) has erupted from four volcanic fields in the SRP-YP volcanic province (Figs. 1A and 1B). Because oxygen is the most abundant element in rhyolitic melts, understanding the cause of these isotopic depletions is essential for resolving the petrogenesis of SRP-YP rhyolites. This remains a topic of great debate. Some workers advocate melting of a pre-Miocene low-$\delta^{18}O$ crustal source such as

**Figure 1.** A: Map of the Snake River Plain–Yellowstone Plateau (SRP-YP) volcanic province with the locations and ages of major volcanic fields and crustal features. Crustal features include outcrops of Archean (black) and Proterozoic (stippled) basement, and the Jurassic–Eocene Idaho batholith (hatched). The $^{87}Sr/^{86}Sr = 0.706$ line defines a west to east transition from Mesozoic–Paleozoic accreted oceanic terranes ($^{87}Sr/^{86}Sr < 0.706$) to the Precambrian craton of North America ($^{87}Sr/^{86}Sr > 0.706$). Velocity and direction of movement of the North America (NA) plate is shown by the black arrow. Stars mark the crustal xenolith localities of this study: Square Mountain–Magic Reservoir (SM), Craters of the Moon (COM), and Spencer-Kilgore (SK). B: Oxygen isotope composition versus longitude for SRP-bounding crust and SRP rhyolites. Oxygen isotope ranges are shown for Bruneau-Jarbidge (BJ), Twin Falls (TF), Heise (H), and Yellowstone Plateau (YP) rhyolites. The number beneath the label is the volume of low-$\delta^{18}O$ rhyolite erupted in each volcanic field. Note: See Appendix Table A1 for compilation of references for $\delta^{18}O$ values of SRP-bounding crust and SRP rhyolites.

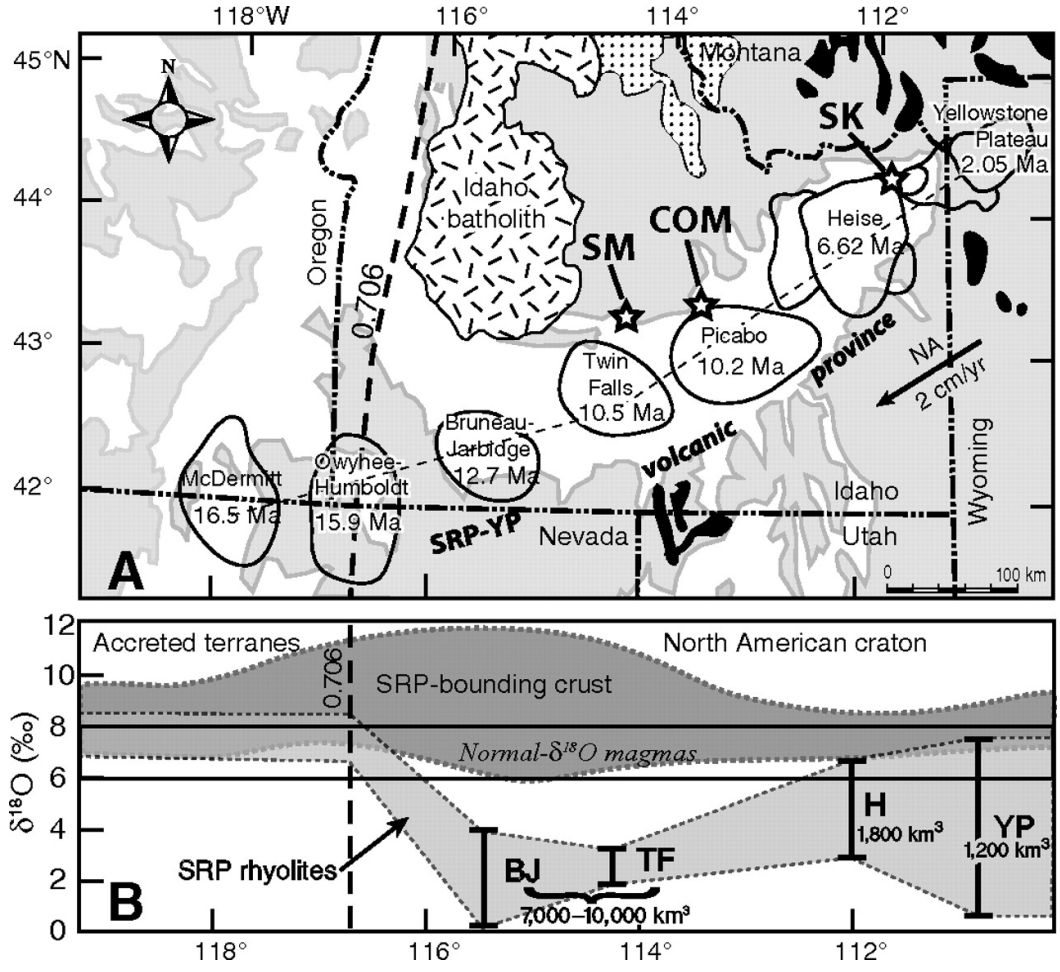

hydrothermally altered portions of the Idaho batholith (Boroughs et al., 2005), whereas others prefer a model of wholesale remelting and batch assembly of hydrothermally altered intracaldera rhyolites from Miocene-Pleistocene eruptions (Bindeman et al., 2007). Archean crustal xenoliths brought to the surface by Pliocene–Holocene lavas provide samples of cratonic North American crust underlying the SRP-YP volcanic province, and thus an opportunity to constrain the oxygen isotope composition of the largest crustal reservoir in the SRP. Here, we provide oxygen isotope data for a suite of such xenoliths from the central and eastern SRP (Fig. 1A; Table 1).

## GEOLOGIC BACKGROUND

The SRP-YP volcanic province extends from eastern Oregon to western Wyoming along a 700 km chain of northeast-trending volcanic fields defined by caldera centers (Fig. 1A). The Bruneau-Jarbidge, Twin Falls, Heise, and Yellowstone Plateau volcanic fields exhibit extreme heterogeneity and depletion in magmatic $\delta^{18}O$, with a total erupted volume of more than 10,000 $km^3$ of low-$\delta^{18}O$ rhyolites, whereas nearly all rhyolites erupted to the west of the inferred Archean crust boundary ($^{87}Sr/^{86}Sr = 0.706$ line) fall within a normal-$\delta^{18}O$ range (Figs. 1A and 1B). Despite their remarkable volume, evidence for suitable crustal sources for low-$\delta^{18}O$ magmas is scarce in the SRP. Available oxygen isotope data for crustal basement rocks that predate the SRP show a normal-$\delta^{18}O$ profile from west to east, ranging from ~6‰ to 10‰ (Fig. 1B; Appendix Table A1). Oxygen isotope data for individual plutons that compose the Idaho batholith show that it is heterogeneous with a few sufficiently low-$\delta^{18}O$ regions to source the low-

$\delta^{18}O$ magmas of the central SRP (Boroughs et al., 2005). However, the majority of the Idaho batholith is normal- to high-$\delta^{18}O$ (~8‰–11‰; Criss and Fleck, 1987).

## XENOLITH SAMPLES

The 20 crustal xenoliths analyzed in this study are a representative subset of more than 260 samples collected by Leeman et al. (1985) at three localities in the SRP: Square Mountain–Magic Reservoir, Craters of the Moon, and Spencer-Kilgore (Fig. 1A). These xenoliths are granulite facies gneisses with varying proportions of quartz, plagioclase, alkali feldspar, orthopyroxene, clinopyroxene, Fe-Ti oxides, and interstitial glass. The freshest samples indicate equilibration at 700–800 °C and ~5 kbar, corresponding to a crustal depth of 15 km (Leeman et al., 1985). U-Pb zircon dating of xenoliths from each locality confirms that they are Archean in age, and documents the presence of the North American craton to a western extent of 114.5°W (Wolf et al., 2005). Among the samples analyzed, 14 xenoliths were previously analyzed for Sr and Nd isotopes, 10 were analyzed for Pb isotopes, and 4 have been dated by U-Pb zircon geochronology (Leeman et al., 1985; Wolf et al., 2005).

## RESULTS

### Oxygen Isotopes

All xenoliths analyzed in this study have normal $\delta^{18}O$ values, ranging from ~6‰ to 9‰ (Table 1). Unlike the extremely heterogeneous Sr, Nd, and Pb isotope values, the O isotope values for the SRP crustal xenoliths define a narrow range and lack low-$\delta^{18}O$ values or supracrustal high-$\delta^{18}O$ values that are characteristic of crust elsewhere (e.g.,

Taylor, 1986). The xenoliths from the Spencer-Kilgore locality have slightly lower $\delta^{18}O$ values (~6‰–7‰) compared to those from the Craters of the Moon and Square Mountain–Magic Reservoir localities (~7‰–9‰), but all xenolith samples fall within the $\delta^{18}O$ range of crustal rocks exposed to the north and south of the SRP province, and thus, the $\delta^{18}O$ composition of the Archean crust sampled by the xenoliths is heterogeneous within a typical crustal range (Fig. 1B; Appendix Tables A1 and A2).

**Table 1.** Isotopic data for SRP xenoliths

| Sample | Longitude | U-Pb zircon age (Ga)* | $\frac{^{87}Sr}{^{86}Sr}$ | $\frac{^{143}Nd}{^{144}Nd}$ | $\frac{^{206}Pb}{^{204}Pb}$ | $\frac{^{207}Pb}{^{204}Pb}$ | $\frac{^{208}Pb}{^{204}Pb}$ | Average $\delta^{18}O$ (‰) |
|---|---|---|---|---|---|---|---|---|
| **SK locality** | 111.7°W | | | | | | | |
| B1 | | | 0.70579 | 0.511467 | 16.73 | 15.45 | 37.25 | 6.42 |
| B2 | | | 0.70235 | 0.510918 | – | – | – | 7.26 |
| B3 | | | 0.70382 | 0.510883 | 14.18 | 14.98 | 34.71 | 7.26 |
| B10 | | | 0.70246 | 0.510809 | 14.80 | 14.81 | 33.73 | 6.77 |
| R4 | | | 0.70274 | 0.511154 | – | – | – | 6.75 |
| 73-68X | | | 0.72550 | 0.510895 | 14.95 | 15.18 | 43.18 | 6.95 |
| SK-3 | | 3.10, 2.90, 2.76 | – | – | – | – | – | 6.26 |
| **COM locality** | 113.5°W | | | | | | | |
| CKI-1 | | | 0.73359 | 0.510499 | 13.56 | 14.72 | 35.01 | 9.35 |
| 70-40 | | | 0.71525 | 0.510454 | 14.11 | 14.82 | 35.73 | 7.76 |
| SI-1 | | | 0.71795 | 0.510590 | 16.09 | 15.64 | 59.07 | 6.98 |
| COM-1 | | | 0.81728 | 0.510228 | – | – | – | 7.43 |
| COM-9A | | 2.60–2.50 | – | – | – | – | – | 9.20 |
| COM-9B | | | – | – | – | – | – | 7.91 |
| COM-14 | | | – | – | – | – | – | 6.43 |
| COM-22 | | 3.20, 2.75 | – | – | – | – | – | 6.85 |
| COM-25 | | | – | – | – | – | – | 6.67 |
| **SM locality** | 114.5°W | | | | | | | |
| SM-2A | | | 0.73138 | 0.511484 | 16.36 | 15.50 | 35.22 | 7.78 |
| SM-2F | | | 0.83011 | 0.510874 | 24.65 | 16.87 | 39.29 | 7.50 |
| SM-2G | | | 0.72092 | 0.509973 | 18.76 | 15.88 | 36.90 | 8.09 |
| DM-103 | | 2.57 | 0.73878 | 0.510853 | – | – | – | 7.93 |

Note: Oxygen isotope values for SRP crustal xenoliths are averages of whole-rock powder duplicates. Quartz and pyroxene phenocrysts were analyzed for samples CK-1, 70-40, and SI-1, and $\delta^{18}O$ quartz-pyroxene are consistent with metamorphic fractionation temperatures of 700-800°C: CKI-1 (qtz = 9.47‰), 70-40 (qtz = 8.40‰, pyx = 6.15‰), SI-1 (qtz = 7.43‰, pyx = 4.51‰). See Appendix Table A2 for individual oxygen isotope analyses.
*U-Pb zircon ages were reported in Wolf et al. (2005).

Correlated Sr and O isotopes define separate but overlapping fields of SRP crustal xenoliths and magmas (Fig. 2A). The Sr isotope ratios of all rhyolites at Yellowstone, Heise, and Bruneau-Jarbidge (normal- and low-$\delta^{18}O$) and all SRP basalts overlap with the average xenolith values, which is an expected result for large-volume magma genesis from crustal sources. However, the Nd isotope ratios of Cenozoic SRP rhyolites and basalts are higher than any analyzed Archean xenoliths and require a significant proportion of low Sm/Nd juvenile mantle (Fig. 2B). Similar trends are apparent in plots of Pb isotopes versus O, with Pb isotope ratios that are intermediate between a crust and mantle source (Appendix Fig. A1).

Considering only normal-$\delta^{18}O$ rhyolites, which are the earliest eruptive units of the Yellowstone and Heise caldera centers, we observe that they can be produced by averaging the xenoliths with normal-$\delta^{18}O$ basalt (Figs. 2A and 2B). However, voluminous low-$\delta^{18}O$ rhyolites from the Yellowstone Plateau, Heise, Bruneau-Jarbidge, and Twin Falls volcanic fields do not have $\delta^{18}O$ counterparts among the xenoliths (Figs. 1B, 2A, and 2B). Their formation requires remelting of hydrothermally altered (low-$\delta^{18}O$) rocks—either shallow parts of the basement or earlier magmatic precursors that were strongly modified by meteoric/hydrothermal fluids. This dramatic shift in $\delta^{18}O$ value does not lead to significant changes in Sr, Nd, or Pb isotopes, compared to the extremely heterogeneous xenolith range.

**Sr-O and Nd-O Mixing Models**

Sr-O and Nd-O mixing models presented in Figures 3A and 3B define a three-component mixing field between the crust, the mantle, and a low-$\delta^{18}O$ source in the

**Figure 2.** O, Sr, and Nd isotopic compositions of Spencer-Kilgore, Craters of the Moon, and Square Mountain–Magic Reservoir crustal xenoliths, Yellowstone, Heise, and Bruneau-Jarbidge rhyolites, and Snake River Plain (SRP) basalts. The symbol key applies to Figures 2 and 3. A: $^{87}Sr/^{86}Sr$ plotted against $\delta^{18}O$. Note that $^{87}Sr/^{86}Sr$ of the crustal xenoliths bracket $^{87}Sr/^{86}Sr_i$ of all SRP rhyolites, and that normal-$\delta^{18}O$ ($\delta^{18}O > 6‰$) Yellowstone and Heise rhyolites have O isotope compositions that are bracketed by the normal-$\delta^{18}O$ xenoliths and SRP basalts, whereas low-$\delta^{18}O$ rhyolites do not. Isotopic data for the Idaho batholith are from Criss and Fleck (1987) and are similar in $^{87}Sr/^{86}Sr_i$ to SRP crustal xenoliths and magmas, but generally higher in $\delta^{18}O$. B: $^{143}Nd/^{144}Nd$ plotted against $\delta^{18}O$. Note that all SRP rhyolites have higher $^{143}Nd/^{144}Nd$ than SRP crustal xenoliths, and require contribution from a higher $^{143}Nd/^{144}Nd$ mantle component—SRP basalts. Note: See Appendix Table A3 for O, Sr, Nd, and Pb isotope data and references, and Fig. A1 for plots of $^{206}Pb/^{204}Pb$, $^{207}Pb/^{204}Pb$, and $^{208}Pb/^{204}Pb$ versus $\delta^{18}O$.

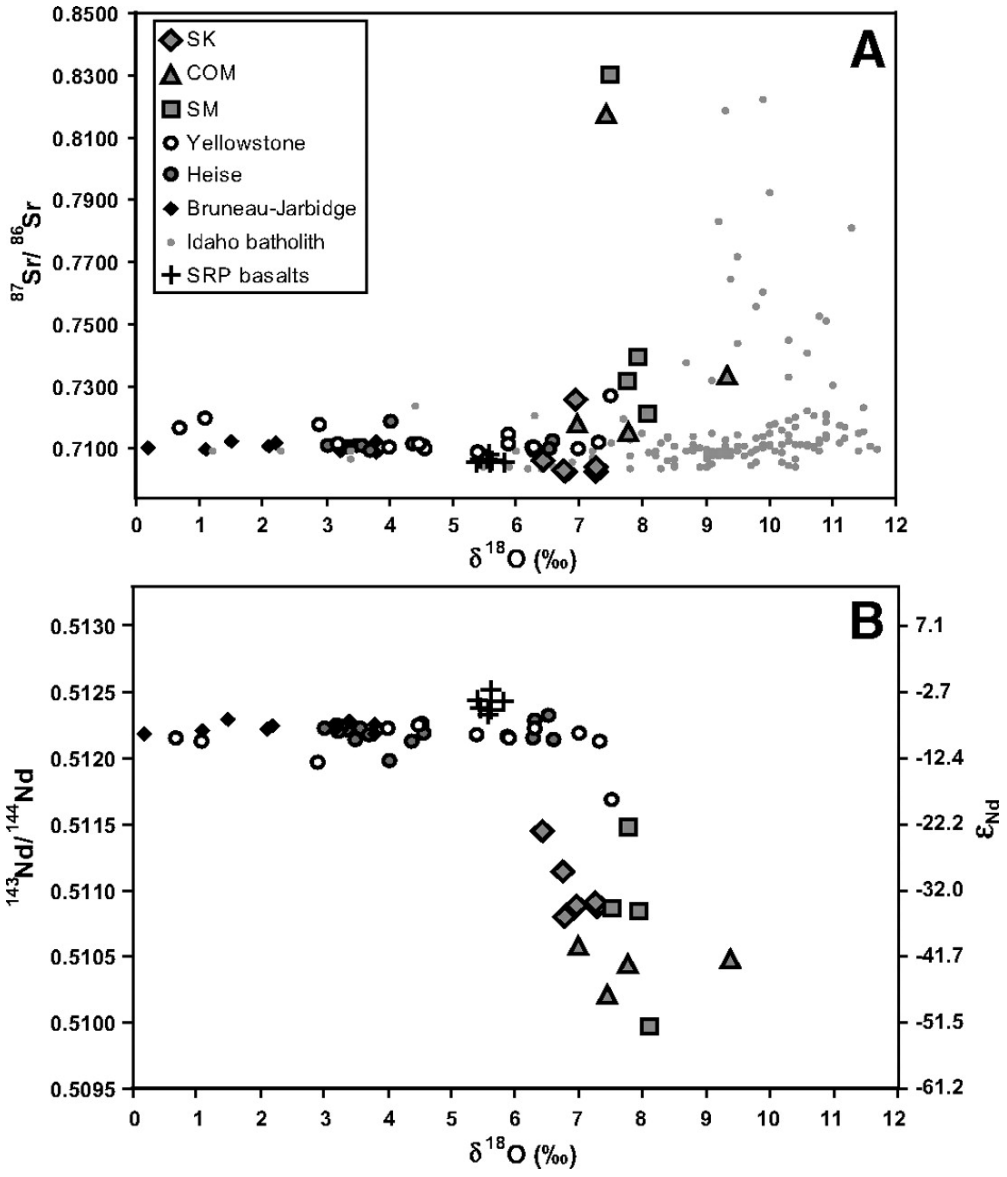

genesis of Yellowstone and Heise rhyolites. The Sr-Nd-O isotopic composition of an isotopically intermediate xenolith sample (DM-103) best approximates the xenolith average and thus was selected as the crust end member. The Sr-Nd-O isotopic composition of the mantle end member is the average of SRP basalts, which represent a combination of plume and lithospheric mantle components (Graham et al., 2009). All normal-$\delta^{18}O$ Yellowstone and Heise rhyolites plot within the Sr-O and Nd-O mixing fields established by the crust and mantle end members and possess variable crust and mantle contributions that are specific to each rhyolite, ranging from ~30% to 50% crust and ~50% to 70% mantle (Figs. 3A and 3B). This result is consistent with previous estimates of crust and mantle proportions in SRP rhyolites (e.g., Bonnichsen et al., 2008; Nash et al., 2006; McCurry and Rodgers, 2009). U-Pb zircon age inheritance establishes genetic ties between normal- and low-$\delta^{18}O$ Yellowstone rhyolites (Bindeman et al., 2008), and we used these known correlations and published O, Sr, and Nd isotope ratios to construct mixing curves between normal- and low-$\delta^{18}O$ rhyolite end members (Figs. 3A and 3B; Appendix Tables A3 and A4). As isotope-isotope mixing models depend on element concentration ratios and define hyperbolas in the mixing space, we used second-order polynomial least-squares regression lines to approximate each mixing curve and then projected these fit lines along the Sr-O and Nd-O axes.

An important result of this modeling is that the fit lines converge at $\delta^{18}O$ values of –1.5‰ to –0.4‰ (Sr-O) and –1.0‰ to 0.7‰ (Nd-O), overlapping at $\delta^{18}O \approx -1$‰ (Figs. 3A and 3B). Because O, Sr, and Nd isotope ratios and concentrations of the rhyolite end members are fixed from published values, and the fit lines were constructed for three independent mixing curves in two separate isotopic systems (Sr-O and Nd-O), this is a

**Figure 3.** Sr-O and Nd-O mixing models. The crust end member (square) was estimated with the crustal xenoliths of this study, from which sample DM-103 is the most representative of the xenolith average: $\delta^{18}O = 7.9‰$, $^{87}Sr/^{86}Sr = 0.7388$, $^{143}Nd/^{144}Nd = 0.5109$. Snake River Plain (SRP) basalts (crosses) were used as the mantle end member: $\delta^{18}O = 5.6‰$, $^{87}Sr/^{86}Sr = 0.7063$, $^{143}Nd/^{144}Nd = 0.5124$. O, Sr, and Nd concentration ratios for binary mantle-crust mixing curves vary from 0.1, 1, and 10, where R = O/Sr (A) and O/Nd (B) are concentration ratios of crust/mantle. Normal-$\delta^{18}O$ Yellowstone and Heise rhyolites plot within the crust-mantle binary mixing field. Second-order polynomial least-squares regression lines ($r^2 \geq 0.96$) were fit to hyperbolic mixing curves between genetically related normal-$\delta^{18}O$ and low-$\delta^{18}O$ Yellowstone rhyolite end members, and these converge at $\delta^{18}O$ values of –1.5‰ to –0.4‰ (A) and –1.0‰ to 0.7‰ (B). The $\delta^{18}O$ fields of convergence (shaded) overlap at $\delta^{18}O \approx -1‰$, which serves as a constrained estimate for the low-$\delta^{18}O$ source of low-$\delta^{18}O$ rhyolites. Heterogeneity in $\delta^{18}O$ and homogeneity in $^{87}Sr/^{86}Sr$ and $^{143}Nd/^{144}Nd$ of low-$\delta^{18}O$ rhyolites can be explained by varying proportions (~20%–80%) of normal-$\delta^{18}O$ rhyolitic components and this low-$\delta^{18}O$ source (see text and Appendix Table A4 for more detail on mixing models).

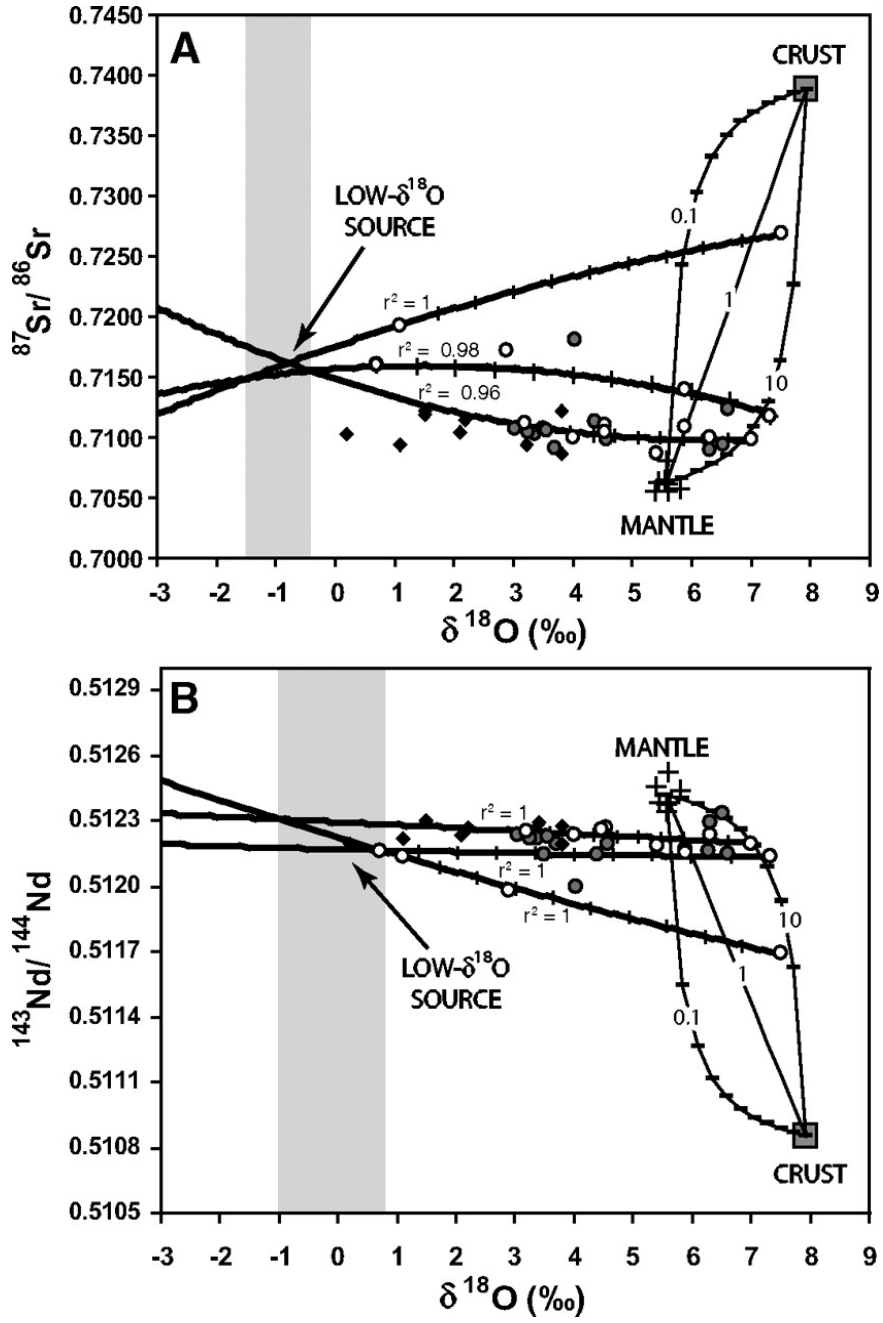


robust result. All low-$\delta^{18}O$ Yellowstone and Heise rhyolites fall along or within these projected mixing curves (Figs. 3A and 3B). The relative proportions of low-$\delta^{18}O$ versus normal-$\delta^{18}O$ components in these rhyolites were estimated with binary mixing curves between the modeled low-$\delta^{18}O$ source compositions and published isotopic compositions of normal-$\delta^{18}O$ rhyolite end members (Appendix Tables A3 and A4). The results indicate

~20%–80% of low-$\delta^{18}O$ ($\delta^{18}O$ = –1.5‰ to –1.0‰) and normal-$\delta^{18}O$ ($\delta^{18}O$ = 7.0‰ to 7.5‰) components. The majority of low-$\delta^{18}O$ rhyolites of the central SRP Bruneau-Jarbidge volcanic field also fall along the main Yellowstone-Heise mixing trend; however, this correlation could be fortuitous because the mixing lines were generated with eastern SRP data, and the Bruneau-Jarbidge volcanic field possesses no normal-$\delta^{18}O$ rhyolites.

The modestly depleted $\delta^{18}O$ value of –1‰ is not nearly as low as some estimates for hydrothermally altered source rocks at Yellowstone (–10‰) or the maximum theoretical depletions based on measured meteoric water values and high water/rock ratios (–15‰) (Hildreth et al., 1984), and this may reflect the difficulty in achieving maximum depletion in $^{18}O$ due to limitations in permeability and/or thermal profiles of crustal source rocks (Taylor, 1986). It is notable that this value is comparable to measured $\delta^{18}O$ values of hydrothermally altered rocks from drill cores in modern volcanic geothermal systems in Iceland (0‰–2‰) and Kamchatka (–1‰) (Bindeman et al., 2004). We adopt the early argument of Taylor (1986) that large percentages of oxygen exchange are impossible to achieve at great depths by naturally percolating groundwaters, even in areas with high thermal gradients, because these waters are rapidly shifted to normal $\delta^{18}O$ values in shallow conditions. The fact that low-$\delta^{18}O$ magmas do not appear in stratovolcanoes or single calderas supports our view that vertical motions associated with multiple caldera collapses (e.g., SRP, Kamchatka) and/or rifting (e.g., Iceland) are key to bringing low-$\delta^{18}O$ source rocks to the temperature conditions appropriate for melting. (With average subsidence depths of 2–5 km per caldera collapse event [Lipman, 1997], two to three overlapping caldera collapses would result in 4–15

km of vertical drawdown. A synvolcanic geothermal gradient of 50–65 °C/km [Leeman et al., 2008] increases ambient temperatures by 200–975 °C, yielding temperature conditions appropriate for rhyolite melting [≥700 °C].)

## CONCLUSIONS

The normal-$\delta^{18}O$ SRP crustal xenoliths analyzed in this study could not have directly sourced the voluminous low-$\delta^{18}O$ magmas of the SRP. We advocate a two-stage magma genesis process in eastern SRP volcanism, whereby the first rhyolites are generated by partial melts of the crust and mantle, creating hybrid magmas with ~30%–50% crust and ~50%–70% mantle contributions, and normal $\delta^{18}O$ values constrained by the oxygen isotope compositions of the crust and mantle reservoirs. Following this first phase of normal-$\delta^{18}O$ magmatism, subsequent magmas tap hydrothermally altered volcanic and plutonic portions of phase one rhyolites, maintaining the original Sr and Nd isotopic signatures, but recording variable $\delta^{18}O$ values. The $\delta^{18}O$ heterogeneity of phase two, low-$\delta^{18}O$ rhyolites reflects varying proportions (~20%–80%) of hydrothermally altered source rocks ($\delta^{18}O \approx -1‰$) and normal-$\delta^{18}O$ rocks and magmas ($\delta^{18}O \approx 7‰$). We suggest that the moderately depleted $\delta^{18}O$ value of –1‰ for this common low-$\delta^{18}O$ source is a geologically constrained, "typical" value for SRP caldera source rocks, in which $\delta^{18}O$ heterogeneities of variably hydrothermally altered intracaldera and subvolcanic rocks are averaged on a caldera-wide scale. We discourage the use of extremely low $\delta^{18}O$ values (i.e., <–5‰) when modeling assimilation/crustal melting. The derived –1‰ value requires that larger proportions of (–1‰) crust be present in magmas, and this warrants consideration of the "room problem," accommodated through a

combination of bulk remelting (Bindeman et al., 2007) caldera collapses and Basin and Range extension (e.g., Bonnichsen et al., 2008). At Yellowstone and Heise, low-$\delta^{18}O$ rhyolites dominate after ~2 million years, three caldera collapses, and 2500 $km^3$ of normal-$\delta^{18}O$ rhyolitic eruptions (Bindeman et al., 2007), which may be a direct indicator of the time required for melting, assembly, and homogenization of large volumes of crust and mantle components in phase one magmatism, and concurrent accumulation, fracturing, and hydrothermal alteration of sufficient volumes of volcanic rock to source the voluminous second phase of low-$\delta^{18}O$ rhyolites. This model of magma genesis may be applicable to other large nested caldera centers in the SRP-YP volcanic province and elsewhere. Importantly, the higher (–1‰) value that we estimate for typical low-$\delta^{18}O$ source components means that many nominally "normal" rhyolites may in fact be subtly depleted. Recognition of time-progressive $^{18}O$ depletion is key to evaluating this model on a global scale.

**BRIDGE**

In Chapter III, I presented isotopic data for Archean crustal xenoliths in the SRP that allowed me to construct isotopic mixing models for SRP rhyolites. My models support a two-stage magma genesis process, in which stage one, normal-$\delta^{18}O$ rhyolites are generated by partial melting and hybridization of the crust by mantle-derived basalt and stage two, low-$\delta^{18}O$ rhyolites tap ~20%-80% of hydrothermally altered portions of stage one rhyolites. In Chapter IV, I build on chapters II and III by presenting a detailed investigation of the last caldera-forming tuff at Heise, the 4.45 Ma Kilgore Tuff. I compare my results for the Kilgore Tuff with large-volume rhyolites produced in the

Yellowstone and Bruneau-Jarbidge volcanic centers to draw conclusions about rhyolite genesis in the broader SRP province.

# CHAPTER IV

# LARGE-VOLUME RHYOLITE GENESIS IN CALDERA COMPLEXES OF THE SNAKE RIVER PLAIN: INSIGHTS FROM THE KILGORE TUFF OF THE HEISE VOLCANIC FIELD, IDAHO WITH COMPARISON TO YELLOWSTONE AND BRUNEAU-JARBIDGE RHYOLITES

This chapter was published in *Journal of Petrology* in 2011, volume 52, pages 857-890 (Watts *et al.,* 2011). Coauthors Ilya Bindeman and Axel Schmitt provided funding for the project, guidance during analytical work, and editorial assistance. I performed the majority of the laboratory work and was the primary author.

## INTRODUCTION

The Snake River Plain–Yellowstone Plateau (SRP–YP) volcanic province in the western USA is one of the largest and most productive silicic igneous provinces on Earth (Fig. 1 inset; Mason *et al*., 2004). Explosive caldera-forming rhyolite eruptions delineate the 16 Myr track of the Yellowstone hotspot in the SRP (Pierce & Morgan, 1992), with spatially overlapping, or nested, caldera complexes in the two youngest centers (Fig. 1 inset; Christiansen, 2001; Morgan & McIntosh, 2005). In each caldera center, volcanism begins with uplift along the axis of the Yellowstone hotspot swell (Smith & Braile, 1994) and ends with subsidence of the crust and burial by younger basalt flows. SRP rhyolites are typically hot and dry (Branney *et al*., 2008), and have radiogenic isotope values that

**Figure 1.** Map showing the location of the Heise volcanic field in the eastern Snake River Plain (SRP). The Yellowstone Plateau volcanic field, located immediately to the NE, is also indicated. Caldera boundaries at Heise (Morgan & McIntosh, 2005) and Yellowstone Plateau (Christiansen, 2001) are indicated by the bold dashed lines. Sampling localities for the Heise units presented in this study are shown by the symbols, with labels that correspond to the Map ID column in Table 1. Kilgore Tuff sampling localities are indicated in bold (KT #1–4). The inferred extent of the the Kilgore Tuff ignimbrite is shaded in dark gray, and Kilgore Tuff vent areas are bounded by fine dashed lines (taken from Morgan & McIntosh, 2005). Inset in the upper left corner is a generalized map of the Snake River Plain–Yellowstone Plateau (SRP–YP) volcanic province showing the locations and ages of the major volcanic fields and crustal features, including outcrops of Archean (black) and Proterozoic (stippled) basement, and the Jurassic–Eocene Idaho batholith (short-line shading). The $^{87}Sr/^{86}Sr = 0{\cdot}706$ line defines a west to east transition from Mesozoic–Paleozoic accreted oceanic terranes ($^{87}Sr/^{86}Sr < 0{\cdot}706$) to the Precambrian craton of North America ($^{87}Sr/^{86}Sr > 0{\cdot}706$).

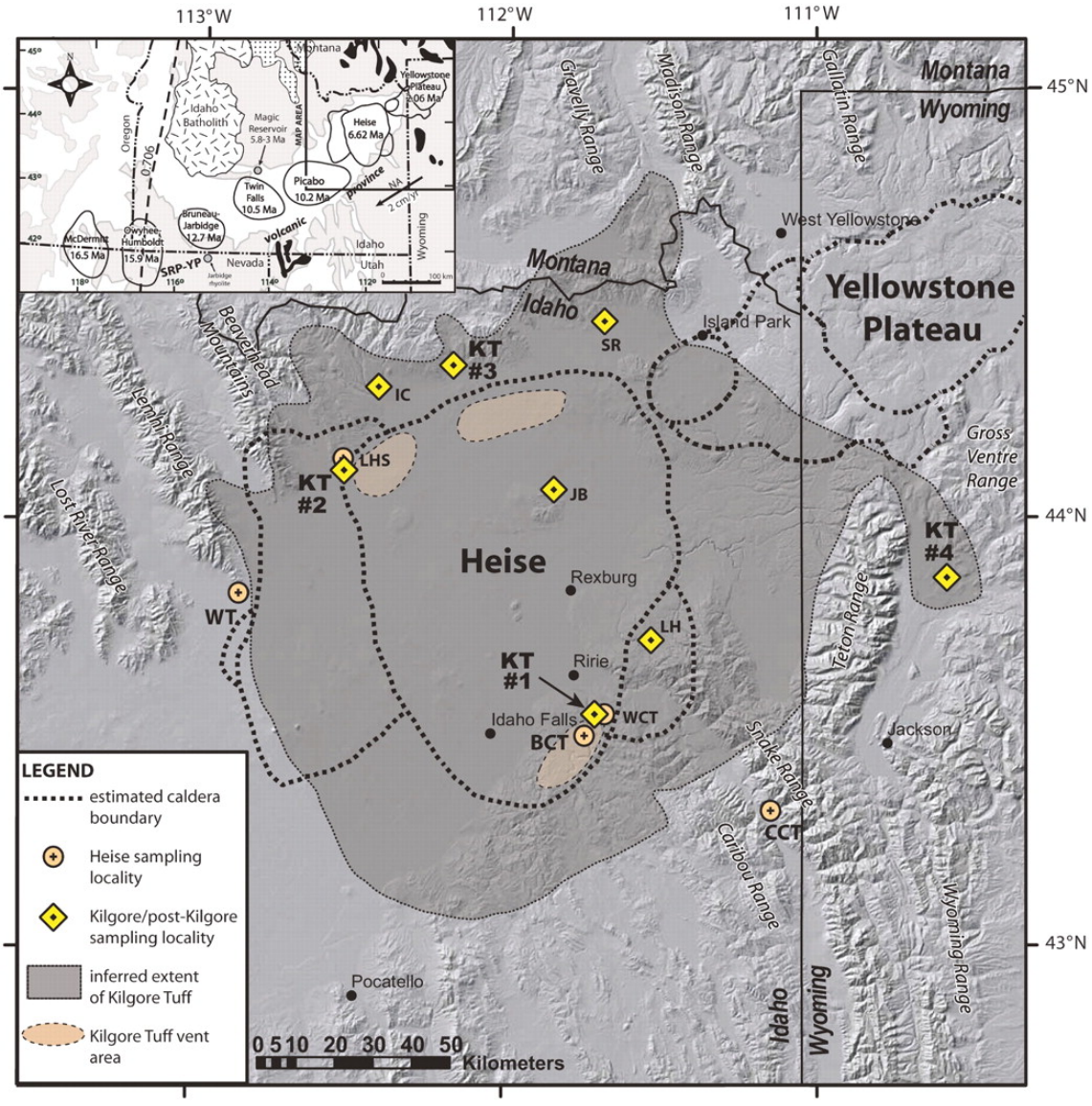

require a significant mantle component (Hildreth *et al*., 1991; Nash *et al*., 2006; McCurry & Rodgers, 2009).

One of the most striking aspects of rhyolitic volcanism in the SRP–YP province is the extreme abundance of low-$\delta^{18}O$ rhyolite; more than 10,000 $km^3$ of low-$\delta^{18}O$ ($\delta^{18}O < 6‰$) rhyolites have erupted in the SRP over the past 16 Myr (Hildreth *et al*., 1984; Bindeman & Valley, 2001; Boroughs *et al*., 2005; Bindeman *et al*., 2007). Such magmas require a significant component of oxygen derived from low-$\delta^{18}O$ meteoric waters, and thus fingerprint the shallow (<10 km) crust (Taylor, 1986). Understanding the process by which voluminous low-$\delta^{18}O$ SRP magmas are formed is critical to evaluation of past and present volcanism in the SRP–YP volcanic province. The low-$\delta^{18}O$ SRP rhyolites may also provide important insights into shallow rhyolite genesis worldwide, particularly in regions where meteoric waters are not as strongly depleted in $^{18}O$ (e.g. equatorial latitudes, low elevations), and consequently do not imprint rhyolites with low-$\delta^{18}O$ signatures that would reveal their shallow crustal origins.

Although some workers advocate melting of a pre-Miocene hydrothermally altered low-$\delta^{18}O$ crustal source, such as the Idaho Batholith (Fig. 1 inset), to explain low-$\delta^{18}O$ rhyolite genesis in the SRP (Boroughs *et al*., 2005), the normal–high $\delta^{18}O$ signatures of the vast majority of the Idaho Batholith (Criss & Fleck, 1987) and xenoliths of SRP basement rocks (Watts *et al*., 2010) argue against direct derivation from a pre-existing low-$\delta^{18}O$ crustal source. Influx of meteoric waters and/or assimilation of hydrothermally altered (low-$\delta^{18}O$) wall-rocks into magmas (Hildreth *et al*., 1984) presents significant mass-balance problems (Taylor, 1986), but wholesale remelting of hydrothermally

altered intracaldera blocks eliminates some of these mass-balance constraints (Bindeman *et al*., 2008).

As the most voluminous low-$\delta^{18}O$ rhyolite in the SRP and worldwide, the Kilgore Tuff is a key unit to evaluate outstanding questions concerning low-$\delta^{18}O$ rhyolite genesis. To investigate the origin of the low-$\delta^{18}O$ Kilgore Tuff, we performed oxygen isotope analyses of phenocrysts from all major caldera-forming tuffs and lavas of the Heise volcanic field. We determined U–Pb zircon ages, which were synthesized with Ar–Ar eruption ages (Morgan & McIntosh, 2005), to determine crystal residence time scales and to assess the connection between zircon age zoning/inheritance and $\delta^{18}O$ depletion in Heise tuffs and lavas, as has been found for Yellowstone rhyolites (Bindeman *et al*., 2001, 2008). We determined major and trace element geochemistry, mineral chemistry, Sr and Nd isotopic geochemistry, and magmatic temperatures to compare the geochemical identities of normal-$\delta^{18}O$ and low-$\delta^{18}O$ Heise rhyolites and to document temporal compositional variations.

We compare all of the new Heise data presented here with published data for two of the best-studied caldera centers in the SRP that, like Heise, have generated large volumes of low-$\delta^{18}O$ rhyolite: the Yellowstone Plateau volcanic field in the eastern SRP and the Bruneau–Jarbidge volcanic field in the central SRP (Fig. 1 inset). We propose a general model of rhyolite genesis in the SRP that satisfies all the available data for the low-$\delta^{18}O$ Kilgore Tuff cycle, and highlight patterns in caldera cluster evolution that predict its appearance in the Heise volcanic field. Furthermore, this work provides multiple lines of evidence that voluminous crystal-poor silicic magmas can be generated rapidly in the shallow crust by batch assembly of isotopically heterogeneous pockets of

melt. This process occurs on time scales that are within error of U-Pb zircon dating methods.

## GEOLOGICAL BACKGROUND

The Heise volcanic field is located in eastern Idaho, immediately SW of the younger Yellowstone Plateau volcanic field in western Wyoming (Fig. 1). Like Yellowstone, Heise is a well-preserved volcanic field, with a large (~100 km × 100 km) nested caldera complex and extensive deposits along the margins of the SRP and lower elevations of the surrounding Basin and Range mountains (Fig. 1; Morgan & McIntosh, 2005). Exposures of the Kilgore Tuff span ~20 000 $km^2$ across parts of Idaho, Montana and Wyoming, and range from <3 m to >120 m thick, with the thickest deposits located near three inferred source vent areas along the northern and southern margin of the Kilgore caldera (Fig. 1; Morgan & McIntosh, 2005). According to anisotropy of magnetic susceptibility (AMS) measurements and grain-size distributions (Morgan, 1988), the three source vents of the Kilgore Tuff are separated by lateral distances of ~50–100 km; two of the vents are located in areas where the Kilgore caldera overlaps the older Heise caldera boundaries (Fig. 1).

The 1800 $km^3$ Kilgore Tuff is the youngest and most voluminous of four major caldera-forming eruptions in the Heise volcanic field (Table 1; Morgan & McIntosh, 2005). The three major caldera-forming eruptions that preceded it include the 1200 $km^3$ Blacktail Creek Tuff, 750 $km^3$ Walcott Tuff, and 300 $km^3$ Conant Creek Tuff (Morgan & McIntosh, 2005). Based on intracaldera and extracaldera areas of 7000 $km^2$ and 13 000 $km^2$, respectively (Fig. 1; Morgan & McIntosh, 2005), and an average

extracaldera deposit thickness of 50 m (Morgan, 1988; Morgan & McIntosh, 2005), minimum intracaldera and extracaldera volumes of 350 $km^3$ and 650 $km^3$, *c*. 1000 $km^3$ total volume, are conservative volume estimates for the Kilgore Tuff. The intracaldera thickness of the Kilgore Tuff is not known, but if comparable with the 1 km thickness observed for other large-volume tuffs (e.g. Bishop Tuff), then a much larger total volume of *c*. 8000 $km^3$ is possible. An approximation of intracaldera volume as twice the extracaldera volume (Bacon, 1983) yields an intracaldera volume of 1300 $km^3$, *c*. 2000 $km^3$ total volume, which is similar to the 1800 $km^3$ volume estimate published by Morgan & McIntosh (2005). As most Heise tuff exposures are densely welded ignimbrite (see Branney *et al*., 2008), the dense rock equivalent (DRE) volumes are in effect equal to the rock volumes.

Like voluminous caldera-forming tuffs at Yellowstone, the Kilgore Tuff and other Heise tuffs erupted through Archean crust, a fact confirmed by the location of the Heise volcanic field ~300 km east of the 0·706 isopleth that defines the west–east transition from Mesozoic accreted terranes ($^{87}Sr/^{86}Sr < 0{\cdot}706$) to the Precambrian craton of North America ($^{87}Sr/^{86}Sr > 0{\cdot}706$), Archean crustal xenolith localities that extend from 111·7°W to 114·5°W along the axis of the SRP (Leeman *et al*., 1985; Watts *et al*., 2010), and exposures of Archean basement rocks that surround the eastern SRP (Fig. 1 inset). The Cretaceous–Eocene Idaho Batholith forms significant surface outcrops in the central SRP (Fig. 1 inset), but its eastern boundary is ~200 km west of the Heise volcanic field, and thus it is not likely to be a crustal source of the Kilgore Tuff or any of the other eastern SRP tuffs (see Boroughs *et al*., 2005).

Smaller volume post-Kilgore rhyolites erupted effusively near the inferred ring fracture zone and as resurgent domes within the Kilgore caldera (Fig. 1; Morgan & McIntosh, 2005). The Indian Creek rhyolite and Long Hollow rhyolite are located ~10 km north and ~5 km east of the Kilgore caldera boundary, respectively (Fig. 1). The Juniper Buttes rhyolite is located in the center of the Kilgore caldera (Fig. 1), and occurs as a glassy dome complex with a well-defined rectilinear fault pattern that is comparable in scale with resurgent domes in large caldera complexes elsewhere (Morgan & McIntosh, 2005). The central location of the Juniper Buttes dome complex relative to the inferred Kilgore Tuff source vents (Fig. 1), and the presence of Kilgore Tuff exposures within the dome complex, support the interpretation that it is a young resurgent dome of the Kilgore caldera (Morgan & McIntosh, 2005).

## METHODS

U–Pb dating of Heise zircons was performed with a CAMECA ims 1270 ion microprobe at The University of California, Los Angeles (UCLA). Approximately 20–30 zircon grains from each sample were hand-picked, mounted in epoxy, polished to ~75% of their original size, and mapped using reflected light and back-scatter electron microscopy. We followed standard protocols for the analysis of youthful zircons (Schmitt *et al*., 2003; Bindeman *et al*., 2006). Ion intensities were measured in 12–15 cycles using a mass-filtered $^{16}O$-primary ion beam of ~15 nA focused to an oval 25–30 μm spot. AS3 (Paces & Miller, 1993) reference zircons were used to calibrate U, Th, and Pb sensitivities. U–Pb ages were adjusted for initial U–Th disequilibrium using techniques

described by Schärer (1984), Reid (2003), and Bindeman *et al*. (2006), typically resulting in an ~80 kyr age increase.

Oxygen isotope analyses were performed at the University of Oregon stable isotope laboratory using $CO_2$-laser fluorination (e.g. Bindeman, 2008). Single and bulk silicate mineral grains, ranging in weight between 0·6 and 2 mg, were reacted in the presence of $BrF_5$ reagent to liberate oxygen gas. The gas generated in the laser chamber was purified through a series of cryogenic traps held at liquid nitrogen temperature, and a mercury diffusion pump was used to remove traces of fluorine gas. Oxygen was converted to $CO_2$ gas in a small platinum–graphite converter, the yield was measured, and then $CO_2$ gas was analyzed on a MAT 253 mass spectrometer. Four to seven Gore Mt. Garnet ($\delta^{18}O = 5{\cdot}75‰$) standards were analyzed together with the unknowns during each analytical session. Variability of the measured $\delta^{18}O$ values of the standards ranged from 0·1 to 0·25‰ less than their empirical value, and unknown samples were adjusted to correct for this small day-to-day variability on the SMOW scale. The average precision on standards and duplicates of single grains and bulk analyses was better than 0·1‰. A small subset of zircons were analyzed for oxygen isotopes with a CAMECA ims 1270 ion microprobe at UCLA. For these analyses, we targeted the same zircon spots (after repolishing) as dated by U–Pb, following the polishing protocols of Kita *et al*. (2009) to ensure maximum flatness of the mount. Instrumental calibrations and analytical methods were the same as those used for the Bindeman *et al*. (2008) ion microprobe study of Yellowstone zircons.

Major element compositions of plagioclase, orthopyroxene and clinopyroxene phenocrysts were measured with a CAMECA SX-100 electron microprobe at the

University of Oregon using a 15 kV accelerating voltage, 30 nA beam current, and a beam diameter of 5 μm. A combination of mineral standards was used. Major and trace element whole-rock X-ray fluorescence (XRF) analyses were obtained at the GeoAnalytical Lab at Washington State University on a ThermoARL Advant'XP+sequential X-ray fluorescence spectrometer. Sr and Nd isotope analyses of crushed whole-rock powders were obtained by isotope dilution-thermal ionization mass spectrometry (ID-TIMS) at Central Washington University.

Magmatic temperatures were calculated using a variety of methods. Ti-in-zircon temperatures were calculated from Ti concentrations in single zircon phenocrysts using established protocols (Watson & Harrison, 2005). Ti concentrations were measured with a CAMECA ims 1270 ion microprobe at UCLA. Zircon saturation temperatures were calculated using whole-rock major element compositions and the methods of Watson & Harrison (1983). Liquidus temperatures were calculated with whole-rock major element compositions and MELTS thermodynamic modeling software (Ghiorso & Sack, 1995). The MELTS runs were performed at 1·5 kbar and 3 wt % $H_2O$, which are typical pressures and water contents for eastern SRP rhyolites (Gansecki, 1998).

## U–PB ZIRCON GEOCHRONOLOGY

New U–Pb zircon ages for the major tuffs and lavas of the Heise volcanic field were combined with U–Pb zircon ages previously reported by us (Bindeman *et al*., 2007) and Ar–Ar eruption ages published by Morgan & McIntosh (2005). In total, U–Pb zircon ages have been determined for 13 Heise samples: four samples of the Kilgore Tuff, four samples of post-Kilgore lavas, and five samples of major tuffs that predate the Kilgore

Tuff (Table 1). Where direct comparison with $^{40}Ar/^{39}Ar$ eruption ages is possible, disequilibria corrected $^{206}Pb/^{238}U$ zircon crystallization ages overlap within 95% confidence of the eruption ages, and in most cases zircon crystallization ages are ~0·1–0·3 Myr older than the eruption ages, as observed for silicic magma centers worldwide (Table 1; Reid, 2003; Simon *et al*., 2009). U–Pb zircon crystallization ages of the three major caldera-forming eruptions that preceded the final low-$\delta^{18}O$ Kilgore Tuff cycle, including the normal-$\delta^{18}O$ Blacktail Creek Tuff (6·92 ± 0·28 Ma), Walcott Tuff (6·37 ± 0·26 Ma) and Conant Creek Tuff (5·70 ± 0·19 Ma), are separated by ~500–700 kyr intervals, a periodicity that is similar to the ~750 kyr periodicity of major caldera-forming eruptions at Yellowstone (Lanphere *et al*., 2002), but is longer than the ~200–400 kyr periodicity of the Bruneau–Jarbidge eruptive center to the west (Fig. 1 inset; Bonnichsen *et al*., 2008).

In this study we define a new unit that postdates the Conant Creek Tuff and predates the Kilgore Tuff, called here the 'Pre-Kilgore Tuff'. This unit is an airfall deposit collected at the base of a Kilgore Tuff stratigraphic sequence (KT #1 in Fig. 1; see 'Kilgore Tuff stratigraphic sequence' section). It has a U–Pb zircon age of 4·87 ± 0·20 Ma, which is ~300 kyr older than the Kilgore Tuff (Table 1). Although the Pre-Kilgore Tuff is stratigraphically separated from the overlying Kilgore Tuff by ~11 m of paleosols (see 'Kilgore Tuff stratigraphic sequence' section), it has a distinctive, low-$\delta^{18}O$ isotopic signature that is identical to that of the Kilgore Tuff (Table 1). Thus, we classify it as an early eruptive phase of the low-$\delta^{18}O$ Kilgore cycle.

**Table 1.** Volumes, Ar–Ar ages, U–Pb ages, O, Sr, and Nd isotopic compositions, and temperatures of Heise samples

| | Unit | Sample | Map ID | Volume ($km^3$) | Ar–Ar eruption age (Ma) | U–Pb concordia age (Ma) (*n*) | $\delta^{18}O$ (‰) average | | | Magma (‰) (Calc.) | Temperature (°C) | | | $^{87}Sr/^{86}Sr_i$ | $^{143}Nd/^{144}Nd$ |
|---|---|---|---|---|---|---|---|---|---|---|---|---|---|---|---|
| | | | | | | | Quartz | Zircon | Sanidine | | Ti-in-zrc | Zrc sat | Liq | | |
| I | Blacktail Creek Tuff | 95-2001a | BCT | 1200 | 6·62 ± 0·03 | 6·92 ± 0·28 (12) | 6·40 | 4·81 | — | 6·6 | 819 | 848 | 869 | 0·71238 | 0·51214 |
| II | Walcott Tuff | 06HS-18 | WT | 750 | 6·27 ± 0·04 | 6·37 ± 0·26 (10) | — | 4·17 | 5·57 | 6·1 | — | 786 | 861 | 0·70991 | 0·51216 |
| | Lidy Hot Springs rhyolite | 08HS-10 | LHS | >10? | 6·20 ± 0·05 | — | — | — | 3·68 | 4·4 | — | 822 | 871 | 0·71137 | 0·51214 |
| | Kelly Canyon rhyolite | 1103·1 | — | >10? | 5·7 ± 0·1* | — | — | — | 5·66 | 6·4 | — | — | — | — | — |
| | Wolverine Creek Tuff | 06HS-16 | WCT | <100? | 5·59 ± 0·05 | 5·45 ± 0·14 (15) | — | — | 5·83 | 6·5 | — | 799 | 868 | 0·70947 | 0·51233 |
| III | Conant Creek Tuff | 06HS-5 | CCT | 300 | 5·51 ± 0·13 | 5·70 ± 0·19 (10) | — | 3·96 | 5·52 | 5·9 | *709* | 859 | 949 | 0·70894 | 0·51229 |
| | Pre-Kilgore Tuff | 06HS-14 | KT #1 | ? | — | 4·87 ± 0·20 (10) | 3·29 | 1·89 | 2·81 | 3·5 | — | 945 | 990 | 0·71071 | 0·51214 |
| IV | Kilgore Tuff | TNP96-43 | KT #4 | 1800 | 4·52 ± 0·07 | 4·49 ± 0·25 (12) | 4·33 | 1·61 | 2·88 | 3·4 | 808 | 874 | 871 | 0·71028 | 0·51222 |
| | Kilgore Tuff | 95-2017b | KT #2 | 1800 | 4·51 ± 0·05 | 4·59 ± 0·26 (10) | 4·29 | 1·50 | 2·74 | 3·3 | 826 | 842 | 872 | 0·71037 | 0·51224 |
| | Kilgore Tuff | 95-2015 | KT #3 | 1800 | 4·44 ± 0·07 | — | — | — | 2·93 | 3·6 | — | 852 | 871 | — | — |
| | Kilgore Tuff | 06HS-10 | KT #1 | 1800 | 4·43 ± 0·08 | 4·58 ± 0·24 (10) | — | — | 2·65 | 3·3 | — | 850 | 870 | 0·71047 | 0·51221 |
| | Kilgore Tuff | 06HS-11 | KT #1 | 1800 | 4·43 ± 0·08 | 4·58 ± 0·18 (10) | — | — | 2·97 | 3·6 | — | 842 | 870 | 0·71065 | 0·51222 |
| | Kilgore Tuff | 95-2010 | KT #1 | 1800 | 4·43 ± 0·08 | — | — | — | 2·71 | 3·3 | — | 849 | 872 | — | — |
| | Juniper Buttes rhyolite | 06HS-4A | JB | >10? | — | 4·29 ± 0·15 (9) | — | — | 3·86 | 3·7 | *730* | 811 | 871 | 0·70985 | 0·51219 |
| | Long Hollow rhyolite | 626·1 | LH | >10? | — | 4·28 ± 0·18 (13) | 4·51 | 1·83 | 3·88 | 3·7 | — | 816 | 871 | 0·70917 | 0·51219 |
| | Indian Creek rhyolite | 06HS-1 | IC | >10? | — | 3·96 ± 0·18† (6)<br>4·11 ± 0·27‡ (6)<br>4·46 ± 0·17§ (21) | — | 1·23 | 3·44 | 3·0 | *782* | 858 | 875 | 0·71073 | 0·51223 |
| | Sheridan Reservoir rhyolite¶ | 06HS-19 | SR | >10? | — | 2·07 ± 0·19 (14) | 4·53 | 2·34 | 3·79 | 4·0 | *784* | 886 | 864 | 0·71815 | 0·51199 |

Roman numerals signify the four major caldera-forming cycles of the Heise volcanic field. Volumes are from Morgan & McIntosh (2005), and estimated for units without published volumes. $^{40}Ar/^{39}Ar$ eruption ages with 2σ are from Morgan & McIntosh (2005) for the same Heise units or samples or sampling localities. $^{206}Pb/^{238}U$ concordia ages with 95% confidence intervals are from this study and Bindeman *et al*. (2007); TNP96-43 and 95-2017b ages are corrected for a typesetting error in Table 1 of Bindeman *et al*. (2007). Magma $\delta^{18}O$ values were calculated from phenocryst analyses, with fractionation factors from Bindeman & Valley (2002) for zircon ($\Delta^{18}O_{melt–zircon}$ = 1·6–1·9‰) and Bindeman *et al*. (2001) for sanidine ($\Delta^{18}O_{melt–sanidine}$ = 0·5–0·7‰) for liquidus temperatures of 800–950°C. (See Appendix Table B3 for compilation of all Heise $\delta^{18}O$ data.) $TiO_2$ activity for Ti-in-zircon temperatures was calculated modifying a procedure in Wark *et al*. (2007) using published ilmenite and ulvöspinel compositions and temperatures for Heise units (Henshaw, 2002); $aTiO_2$ ranged from 0·39 to 0·50. Ti-in-zircon temperatures in italics were calculated using the average $aTiO_2$ for Heise rhyolites (0·5). Zircon saturation temperatures were calculated from whole-rock compositions as done by Watson & Harrison (1983). Liquidus temperatures were calculated with MELTS at 1·5 kbar and 3 wt % $H_2O$. *Old K-Ar age published by Morgan and McIntosh (2005); †Rims(0-2 μm); ‡ Rims (5-7 μm); §Cores; ¶Post-Huckleberry Ridge Tuff unit (see text for details).

U–Pb zircon crystallization ages of four Kilgore Tuff samples from three localities that span >150 km across eastern Idaho and western Wyoming (KT #1, KT #2, KT #4; Fig. 1) cluster tightly in age, averaging 4·56 ± 0·23 Ma [95% confidence interval (CI)] (Table 1). We found no evidence of significantly older zircons in the low-$\delta^{18}O$ Kilgore Tuff, in contrast to what has been found for low-$\delta^{18}O$ Yellowstone rhyolites (see Bindeman *et al*., 2001). The difference in the U–Pb zircon crystallization age and Ar–Ar eruption age of the Kilgore Tuff indicates a crystal residence time of ~110 kyr (e.g. Reid, 2003), which is longer than crystal residence timescales of major caldera-forming tuffs at Yellowstone (~15–70 kyr; Bindeman *et al*., 2001) and shorter than crystal residence timescales of major tuffs at Bruneau–Jarbidge (~300–900 kyr; Cathey & Nash, 2004), but comparable with the ~100–150 kyr crystal residence timescales of many large-volume (>100 $km^3$) tuffs around the world (e.g. Vazquez & Reid, 2004; Charlier *et al*., 2005; Simon & Reid, 2005).

Smaller volume post-Kilgore lavas have younger U–Pb ages between 3·96 and 4·29 Ma (Table 1). These units have low-$\delta^{18}O$ signatures that are distinctive of the Kilgore cycle (~3–4‰) and have similar mineral chemistry and major, trace and isotopic geochemistry to the Kilgore Tuff (See 'Oxygen isotopes', 'Petrography and mineral chemistry', and 'Whole-rock geochemistry' sections; Tables 1–3). Their appearance suggests that low-$\delta^{18}O$ magmatism lingered in the Heise volcanic field for ~0·5 Myr after the Kilgore Tuff eruption, periodically tapping residual Kilgore magma beneath the Kilgore caldera. This notion is supported by significant U–Pb age zoning in zircons of the post-Kilgore Indian Creek rhyolite, which have cores (4·46 ± 0·17 Ma) that correspond in

age to the Kilgore Tuff, and rims that are ~0·5 Myr younger (Table 1; Bindeman *et al*., 2007).

The U–Pb age of the Sheridan Reservoir rhyolite (2·07 ± 0·19 Ma) is ~2 Myr younger than any Heise unit, and overlaps in eruption age with the Huckleberry Ridge Tuff [2·06 Ma (Ar–Ar; Lanphere *et al*., 2002)] and post-Huckleberry Ridge Tuff units [1·86–1·78 Ma (K–Ar; Obradovich, 1992)] of the Yellowstone Plateau volcanic field. Contrary to the previous interpretation that the Sheridan Reservoir rhyolite is a late-stage post-Kilgore unit of the Heise volcanic field (Morgan & McIntosh, 2005; Bindeman *et al*., 2007), new Sr and Nd isotope data (see 'Strontium and neodymium isotopes section') and trace element data (e.g. Ba concentrations; Table 3), combined with the young U–Pb age and low-$\delta^{18}O$ signature of the Sheridan Reservoir rhyolite (Table 1), suggest that it is a post-Huckleberry Ridge Tuff unit that belongs to the Yellowstone Plateau volcanic field. Temporally and spatially, the Sheridan Reservoir rhyolite is related to the 2·06 Ma Huckleberry Ridge Tuff caldera collapse, and if emanating from the ring fracture of the Huckleberry Ridge Tuff caldera, the lateral distance covered by the Sheridan Reservoir rhyolite is ~20 km (Fig. 2). This means that rhyolites comparable in scale with voluminous post-Lava Creek Tuff Central Plateau Member rhyolites may have been produced much earlier in the evolution of the Yellowstone Plateau volcanic field than previously thought (see Christiansen, 2001).

## KILGORE TUFF STRATIGRAPHIC SEQUENCE

We investigated in detail one of the type-localities of the Heise volcanic field (KT #1 in Fig. 1), a thick (>14 m) stratigraphic sequence of Heise volcanic rocks and

**Figure 2.** Detailed location map for the NE part of Fig. 1 showing the locations and ages of the Yellowstone and Heise calderas and the boundaries of post-Huckleberry Ridge Tuff (Yellowstone) rhyolite flows (GC, Green Canyon flow; BM, Bishop Mountain flow; BC, Blue Creek flow; HQ, Headquarters flow). The Sheridan Reservoir rhyolite (SR) is located ~20 km NW of the western margin of the Huckleberry Ridge Tuff caldera and has a U–Pb age (2·07 Ma; Table 1) that is identical to the age of the Huckleberry Ridge Tuff (2·06 Ma; Lanphere *et al*., 2002). New data for the SR rhyolite presented in this study indicate that it is a post-Huckleberry Ridge Tuff unit, rather than a post-Kilgore Tuff unit (see text for further details).

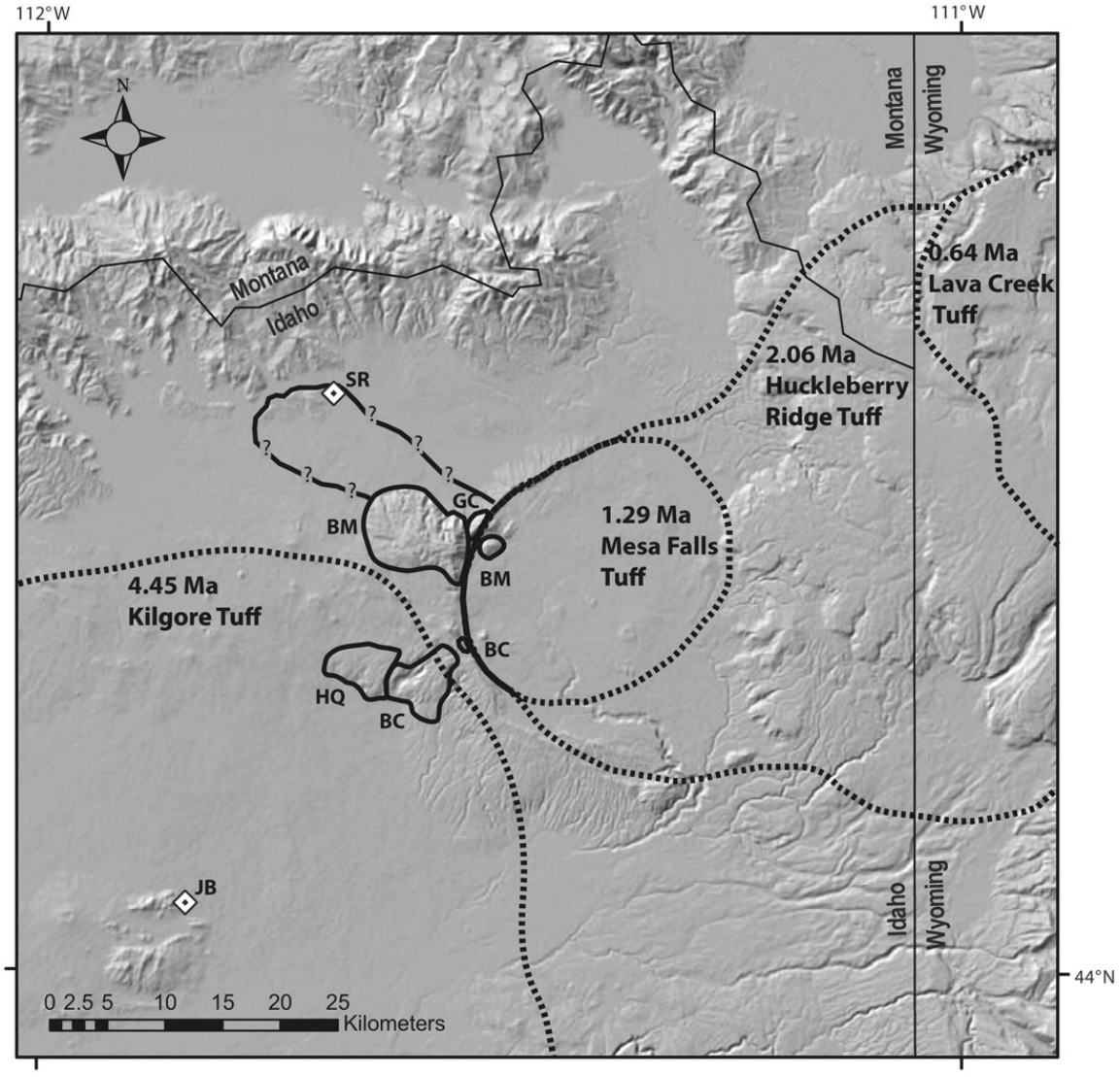

intercalated sediments exposed in a road-cut on Meadow Creek Road in eastern Idaho (Hackett & Morgan, 1988; Morgan & McIntosh, 2005). This stratigraphic section is underlain by the 5·59 Ma Wolverine Creek Tuff of the Heise volcanic field and overlain by the 2·06 Ma Huckleberry Ridge Tuff of the Yellowstone Plateau volcanic field (Fig. 3; Hackett & Morgan, 1988). Thick outflow (8–11 m) and intracaldera (>150 m) facies of the oldest exposed Heise tuff, the Blacktail Creek Tuff, are located along the margins of Ririe Lake, ~5 km west of and stratigraphically below the Meadow Creek road-cut (Hackett & Morgan, 1988).

Although this section has previously been classified as a thick outflow facies ignimbrite of the Kilgore Tuff that was emplaced as several pyroclastic flows in rapid succession (Hackett & Morgan, 1988; Morgan & McIntosh, 2005), our work indicates that only an airfall deposit at the base (08HS-KG-3 and 06HS-14) and a thick (~2 m) vitrophyre at the top (06HS-10, 06HS-11) are primary (Fig. 3). Paleosol structures, coarse lithic layers, and reworked and trough cross-bedded pumice clasts are present throughout the section, providing clear evidence for time breaks between the airfall at the base and the capping vitrophyre (Fig. 3). Whole-rock major and trace element geochemistry of 14 samples from this stratigraphic section shows that most samples (excluding the Kilgore Tuff vitrophyre at the top) are moderately to severely altered relative to primary Heise rhyolite compositions, as indicated by lower $Na_2O$ and $K_2O$, higher FeO, MgO and $TiO_2$, lower Rb, Ce, Nb and higher Sr (Appendix Table B1). In some samples, pumice clasts are cemented by lacustrine calcite. We note that deviations from typical Heise rhyolite compositions are smallest for pumice-rich units of the stratigraphic section, and that

**Figure 3.** Stratigraphy of the Heise pyroclastic sequence at Meadow Creek Road in eastern Idaho (site location KT #1 in Fig. 1). Field photographs and descriptions are shown with a schematic stratigraphic section. U–Pb dated units (this study) at the base (Pre-Kilgore Tuff airfall; 4·87 ± 0·20 Ma) and top (Kilgore Tuff vitrophyre; 4·58 ± 0·18 Ma) bracket the age of the pyroclastic rocks and intercalated sediments that form the Pre-Kilgore Tuff sequence. Coarse lithic layers, paleosols, and trough cross beds indicate intervening time breaks. The Pre-Kilgore Tuff airfall is underlain by the Heise Wolverine Creek Tuff (Ar–Ar age of 5·59 ± 0·05 Ma; Morgan & McIntosh, 2005), and the Kilgore Tuff vitrophyre is overlain by the Yellowstone Huckleberry Ridge Tuff (Ar–Ar age of 2·06 ± 0·01 Ma; Lanphere *et al*., 2002).

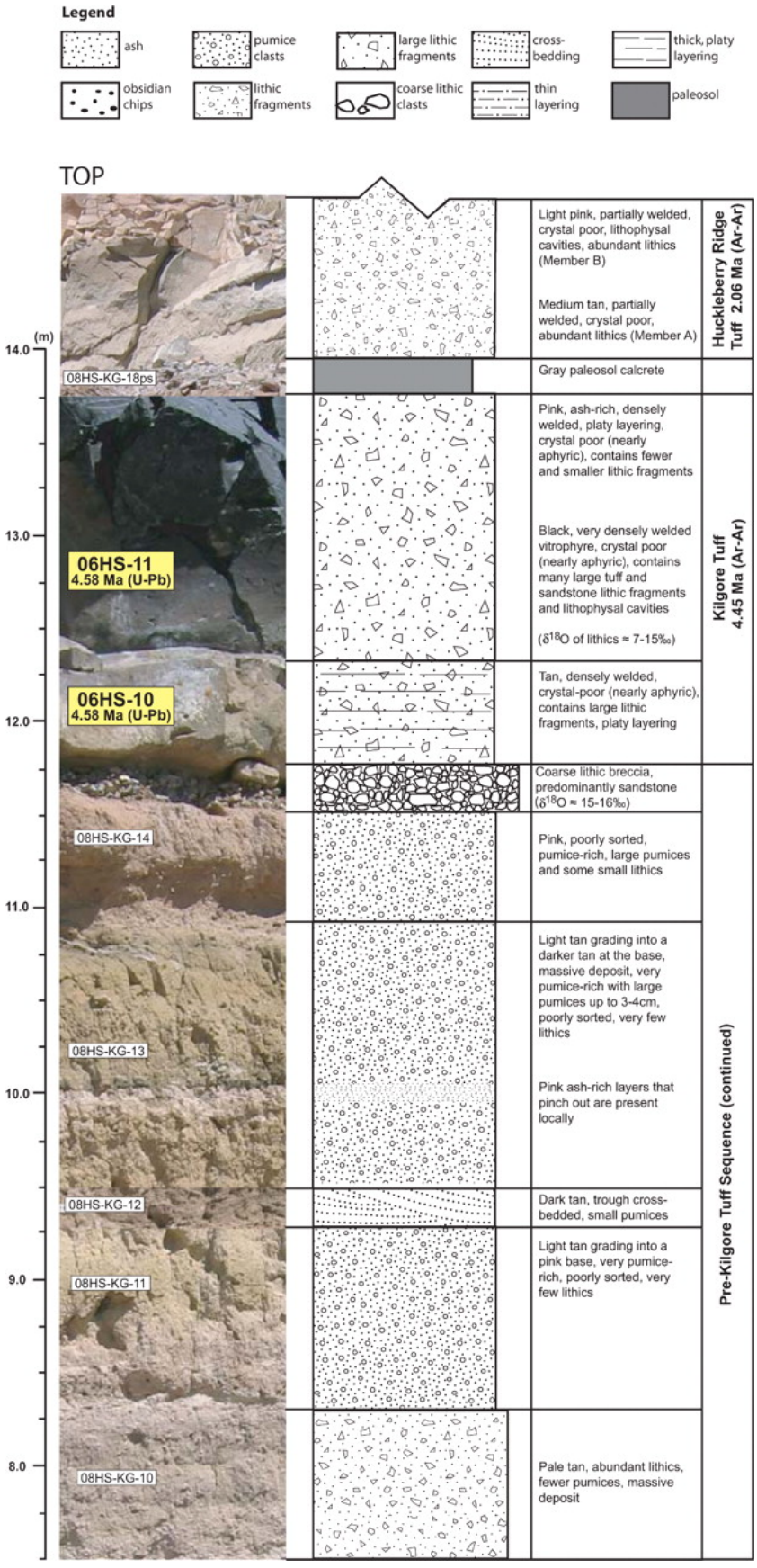
Legend
ash
pumice clasts
large lithic fragments
cross-bedding
thick, platy layering
obsidian chips
lithic fragments
coarse lithic clasts
thin layering
paleosol
TOP
(m)
14.0
13.0
12.0
11.0
10.0
9.0
8.0
08HS-KG-18ps
06HS-11
4.58 Ma (U-Pb)
06HS-10
4.58 Ma (U-Pb)
08HS-KG-14
08HS-KG-13
08HS-KG-12
08HS-KG-11
08HS-KG-10
Light pink, partially welded, crystal poor, lithophysal cavities, abundant lithics (Member B)
Medium tan, partially welded, crystal poor, abundant lithics (Member A)
Huckleberry Ridge Tuff 2.06 Ma (Ar-Ar)
Gray paleosol calcrete
Pink, ash-rich, densely welded, platy layering, crystal poor (nearly aphyric), contains fewer and smaller lithic fragments
Black, very densely welded vitrophyre, crystal poor (nearly aphyric), contains many large tuff and sandstone lithic fragments and lithophysal cavities
(δ18O of lithics ≈ 7-15‰)
Tan, densely welded, crystal-poor (nearly aphyric), contains large lithic fragments, platy layering
Kilgore Tuff 4.45 Ma (Ar-Ar)
Coarse lithic breccia, predominantly sandstone (δ18O ≈ 15-16‰)
Pink, poorly sorted, pumice-rich, large pumices and some small lithics
Light tan grading into a darker tan at the base, massive deposit, very pumice-rich with large pumices up to 3-4cm, poorly sorted, very few lithics
Pink ash-rich layers that pinch out are present locally
Dark tan, trough cross-bedded, small pumices
Light tan grading into a pink base, very pumice-rich, poorly sorted, very few lithics
Pale tan, abundant lithics, fewer pumices, massive deposit
Pre-Kilgore Tuff Sequence (continued)

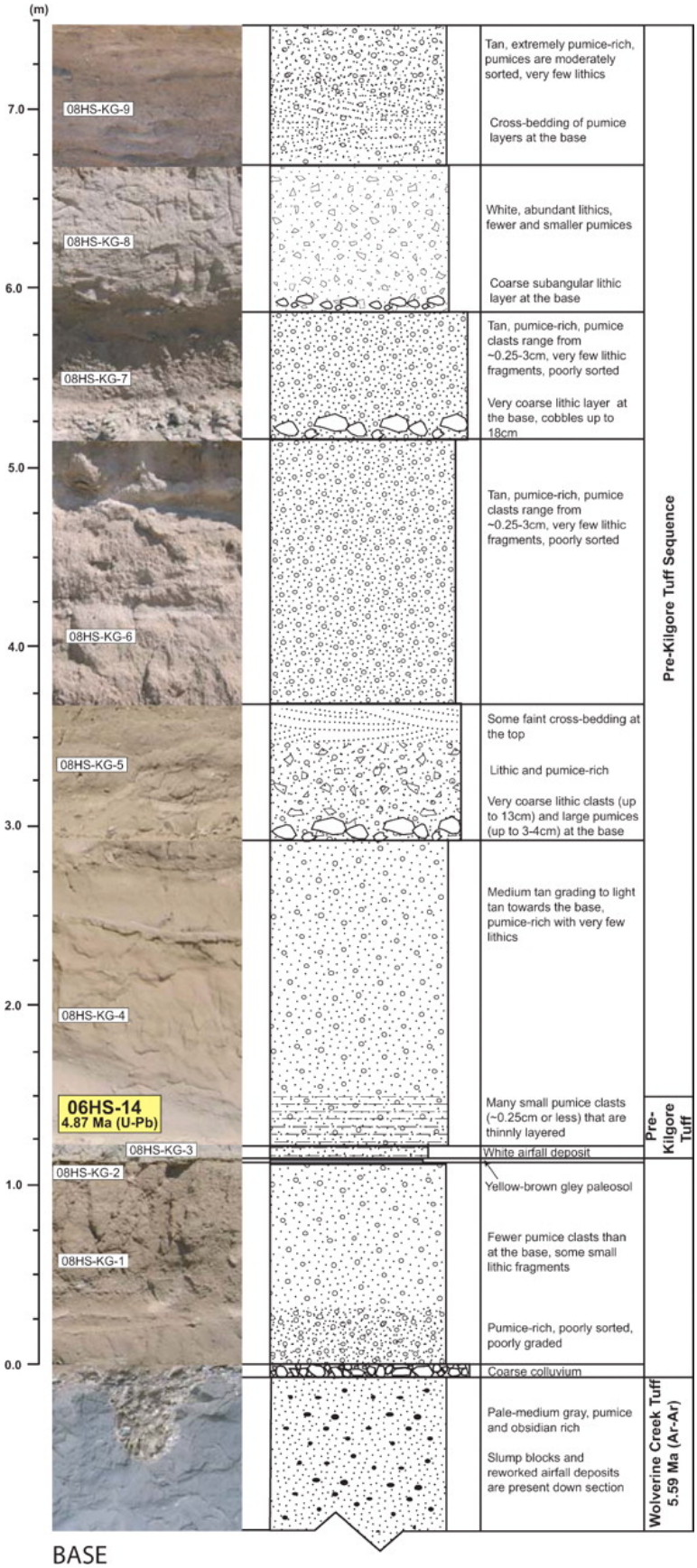
(m)
7.0
6.0
5.0
4.0
3.0
2.0
1.0
0.0
08HS-KG-9
08HS-KG-8
08HS-KG-7
08HS-KG-6
08HS-KG-5
08HS-KG-4
06HS-14
4.87 Ma (U-Pb)
08HS-KG-3
08HS-KG-2
08HS-KG-1
Tan, extremely pumice-rich, pumices are moderately sorted, very few lithics
Cross-bedding of pumice layers at the base
White, abundant lithics, fewer and smaller pumices
Coarse subangular lithic layer at the base
Tan, pumice-rich, pumice clasts range from ~0.25-3cm, very few lithic fragments, poorly sorted
Very coarse lithic layer at the base, cobbles up to 18cm
Tan, pumice-rich, pumice clasts range from ~0.25-3cm, very few lithic fragments, poorly sorted
Some faint cross-bedding at the top
Lithic and pumice-rich
Very coarse lithic clasts (up to 13cm) and large pumices (up to 3-4cm) at the base
Medium tan grading to light tan towards the base, pumice-rich with very few lithics
Many small pumice clasts (~0.25cm or less) that are thinnly layered
White airfall deposit
Yellow-brown gley paleosol
Fewer pumice clasts than at the base, some small lithic fragments
Pumice-rich, poorly sorted, poorly graded
Coarse colluvium
Pale-medium gray, pumice and obsidian rich
Slump blocks and reworked airfall deposits are present down section
Pre-Kilgore Tuff Sequence
Pre-Kilgore Tuff
Wolverine Creek Tuff
5.59 Ma (Ar-Ar)
BASE

nearly all units have trace element concentrations of Ba, Y and Zr that fall within a typical Heise range (Appendix Table B1).

In addition to major and trace element geochemistry, U–Pb zircon ages, oxygen isotope data ($\delta^{18}O$ and $\Delta^{17}O$), and Sr and Nd isotope data were obtained for a subset of samples from this stratigraphic section (Table 1; Fig. 3). U–Pb zircon ages of an airfall at the base, referred to here as the Pre-Kilgore Tuff (4·87 ± 0·20 Ma), and two samples of a Kilgore Tuff vitrophyre at the top of the section (4·58 ± 0·24 Ma, 4·58 ± 0·18 Ma), corroborate inferential evidence of paleosol thicknesses and pedotypes (e.g. Retallack *et al*., 2002; Davis & Ellis, 2010) that the Pre-Kilgore Tuff is tens to hundreds of thousands of years older than the Kilgore Tuff vitrophyre. Although the U–Pb zircon ages of the Pre-Kilgore Tuff and Kilgore Tuff overlap within uncertainty (95% CI), the presence of more than 11 m of intervening sediments requires a significant (at least tens of thousands of years) time break between them. We refer to this sequence of intercalated volcanic rocks and sediments as the Pre-Kilgore Tuff sequence (Fig. 3).

In addition, we determined that a grey paleosol at the base of the section (08HS-KG-2), a trough-cross bedded unit in the middle of the section (08HS-KG-12), and a paleosol calcrete at the top of the section (08HS-KG-18ps) have mass-independent $\Delta^{17}O$ signatures of + 0·6‰, +1·4‰, and +0·7‰, respectively, indicating atmospheric oxidation of volcanic $SO_2$ by ozone during plinian supereruptions (e.g. Martin & Bindeman, 2009). Carbonate nodules in samples 08HS-KG-12 and 08HS-KG-18ps have $\delta^{18}O$ values of 15·27‰ and 16·06‰, and $\delta^{13}C$ values of –6·26‰ and –5·66‰, respectively. Using the calcite-$H_2O$ $\delta^{18}O$ paleothermometer of O'Neil *et al*. (1969) and modern meteoric water $\delta^{18}O$ values for eastern Idaho (i.e. –14‰; Bowen *et al*., 2007), we calculate pedogenic

carbonate formation temperatures (i.e. ambient air temperatures) of 20°C (08HS-KG-12) and 17°C (08HS-KG-18ps). Temperature estimates made with calcite-$H_2O$ paleothermometers are prone to large uncertainties due to the uncertainty of the oxygen isotopic composition of the waters from which the calcites precipitated. For instance, a 1‰ change in the $\delta^{18}O$ composition of the water (e.g. owing to evaporation) would change our carbonate formation temperature estimates by ±5°C. Nonetheless, the carbonate formation temperature that we calculate for the paleosol sample overlying the Kilgore Tuff (08HS-KG-18ps) is 3°C cooler than that of the paleosol sample beneath it (08HS-KG-12), and if not due to a pre-existing (i.e. pre-Kilgore) climatic trend, the Kilgore Tuff supereruption may have caused climate cooling by several degrees (e.g. Rampino & Self, 1992).

## PETROGRAPHY AND MINERAL CHEMISTRY

### Textural and petrographic description of Heise rhyolites

Large-volume tuffs of the Heise volcanic field are crystal poor (1–20 vol. % phenocrysts) with fine-grained groundmass textures that range from loosely welded (pumiceous, undeformed glass shards) to very densely welded (extensive deformation of glass shards, recrystallization of groundmass). Smaller volume lavas are generally more crystal rich than large-volume tuffs, but range from aphyric to porphyritic (Table 2). All Heise rhyolites have a similar mineralogy, yet differ markedly in the percentage of phenocrysts and the presence or absence of quartz (Table 2). Unlike Yellowstone rhyolites, but similar to Bruneau–Jarbidge rhyolites, quartz in Heise rhyolites is typically subordinate to plagioclase and alkali feldspar and smaller in size (<1 mm).

**Table 2.** Petrological summary of Heise samples

| Unit | Sample | Phenocrysts | | Average phenocryst composition | | |
|---|---|---|---|---|---|---|
| | | vol. % | Abundance | Plag | Cpx | Opx |
| Blacktail Creek Tuff | 95-2001a* | 20 | P, Q, A, C, O, F | $Ab_{67}An_{25}Or_{9}$ | $En_{40}Fs_{20}Wo_{41}$ | $En_{46}Fs_{51}Wo_{3}$ |
| Walcott Tuff | 06HS-18* | 1–2 | P, A, Q, C, O, F | $Ab_{69}An_{21}Or_{9}$ | $En_{37}Fs_{22}Wo_{44}$ | $En_{51}Fs_{46}Wo_{3}$ |
| Lidy Hot Springs rhyolite | 08HS-10 | 20 | P, A, Q, C, O, F | — | — | — |
| Wolverine Creek Tuff | 06HS-16* | 1–2 | P, A, C, O, F | $Ab_{71}An_{20}Or_{9}$ | $En_{47}Fs_{14}Wo_{39}$ | $En_{34}Fs_{63}Wo_{3}$ |
| Conant Creek Tuff | 06HS-5 | 5–7 | P, A, C, O, F | — | — | — |
| Pre-Kilgore Tuff | 06HS-14 | 5 | P, A, Q, C, O, F | — | — | — |
| Kilgore Tuff | 95-2017b | 10 | P, A, Q, C, O, F | — | — | — |
| Kilgore Tuff | TNP 96-43 | 1–2 | P, A, Q, C, O, F | — | — | — |
| Kilgore Tuff | 06HS-10 | 1–2 | P, A, Q, C, O, F | $Ab_{66}An_{26}Or_{8}$ | — | $En_{38}Fs_{58}Wo_{4}$ |
| Kilgore Tuff | 06HS-11 | 1–2 | P, A, Q, C, O, F | $Ab_{69}An_{24}Or_{8}$ | $En_{28}Fs_{32}Wo_{40}$ | — |
| Juniper Buttes rhyolite | 06HS-4a | 1–2 | P, A, C, O, F | $Ab_{64}An_{30}Or_{6}$ | $En_{37}Fs_{20}Wo_{43}$ | $En_{56}Fs_{41}Wo_{3}$ |
| Long Hollow rhyolite | 626.1 | 20 | P, Q, A, O, C, F | — | — | — |
| Indian Creek rhyolite | 06HS-1 | 5 | P, A, C, O, F | $Ab_{70}An_{20}Or_{10}$ | $En_{30}Fs_{30}Wo_{40}$ | $En_{37}Fs_{60}Wo_{4}$ |
| Sheridan Reservoir rhyolite | 06HS-19 | 10 | P, Q, A, C, O, F | — | — | — |

P, plagioclase; Q, quartz; A, alkali feldspar; O, orthopyroxene; C, clinopyroxene; F, Fe–Ti oxides. Trace amounts of apatite and zircon are present in all samples.

*Average phenocryst compositions are from analogous samples of the same units published by Henshaw (2002).

Plagioclase occurs as large (1–3 mm) laths with oligoclase compositions that are similar among all studied Heise units (Table 2; Appendix Fig. B1 and Table B2). In the normal-$\delta^{18}O$ Blacktail Creek, Walcott and Conant Creek tuff units, plagioclase crystals are mostly anhedral and possess oscillatory core–rim zoning, but in low-$\delta^{18}O$ units of the Kilgore Tuff and post-Kilgore rhyolites, plagioclase is more variable, ranging from anhedral to subhedral and unzoned to zoned, with the more crystal-rich samples (5–20 vol. %) exhibiting the most heterogeneity (e.g. sieved cores, resorbed rims, anhedral cores with overgrowth rims, multiple twin generations; Fig. 4a and b).

Orthopyroxene phenocrysts are unzoned and their compositions cluster tightly for each Heise unit (Table 2; Appendix Fig. B1 and Table B2). A similar pattern is observed for clinopyroxene compositions, but with more overlap between units (Table 2; Appendix Fig. B1 and Table B2). The lack of zoning in pyroxene phenocrysts is probably explained by rapid diffusive Fe–Mg re-equilibration with the host melt, as is often observed in high-temperature volcanic rocks (e.g. Cathey & Nash, 2004, 2009; Hildreth & Wilson, 2007), whereas slower diffusion in plagioclase phenocrysts preserves more zoning. Reverse zoning, which would be an indication of reheating, is not observed.

We note that distinct pyroxene chemistry is also characteristic of tuff units in other parts of the SRP (e.g. central SRP Cougar Point Tuff units; Cathey & Nash, 2004).

**Low-$\delta^{18}O$ Kilgore Tuff and post-Kilgore rhyolites**

The Kilgore Tuff is moderately to densely welded with ~1–10 vol. % phenocrysts (Table 2). Plagioclase phenocrysts (average composition of $Ab_{67}An_{25}Or_8$; Table 2; Appendix Table B2) do not typically exhibit core–rim zoning, nor form crystal clusters

**Figure 4.** Photomicrographs of Heise rhyolites in cross-polarized light. plag, plagioclase; opx, orthopyroxene; cpx, clinopyroxene; K-spar, alkali feldspar. Electron microprobe analyses of mineral compositions are indicated in mole fractions of anorthite (An) for plagioclase, enstatite (En) for orthopyroxene and clinopyroxene, and orthoclase (Or) for alkali feldspar. (a) Anhedral plag core with euhedral overgrowth rim. (b) Sieved plag core with opx inclusion. (c) Plag and cpx crystal cluster; crystals do not exhibit significant core–rim zoning. (d) Plag, opx and cpx crystal cluster; crystals do not exhibit significant core–rim zoning. (e) Plag, opx and cpx crystal cluster; plag crystal on the right has a K-spar overgrowth rim. (f) Plag, opx and cpx crystal cluster. (g) Twinned cpx crystal. (h) Twinned cpx crystal.

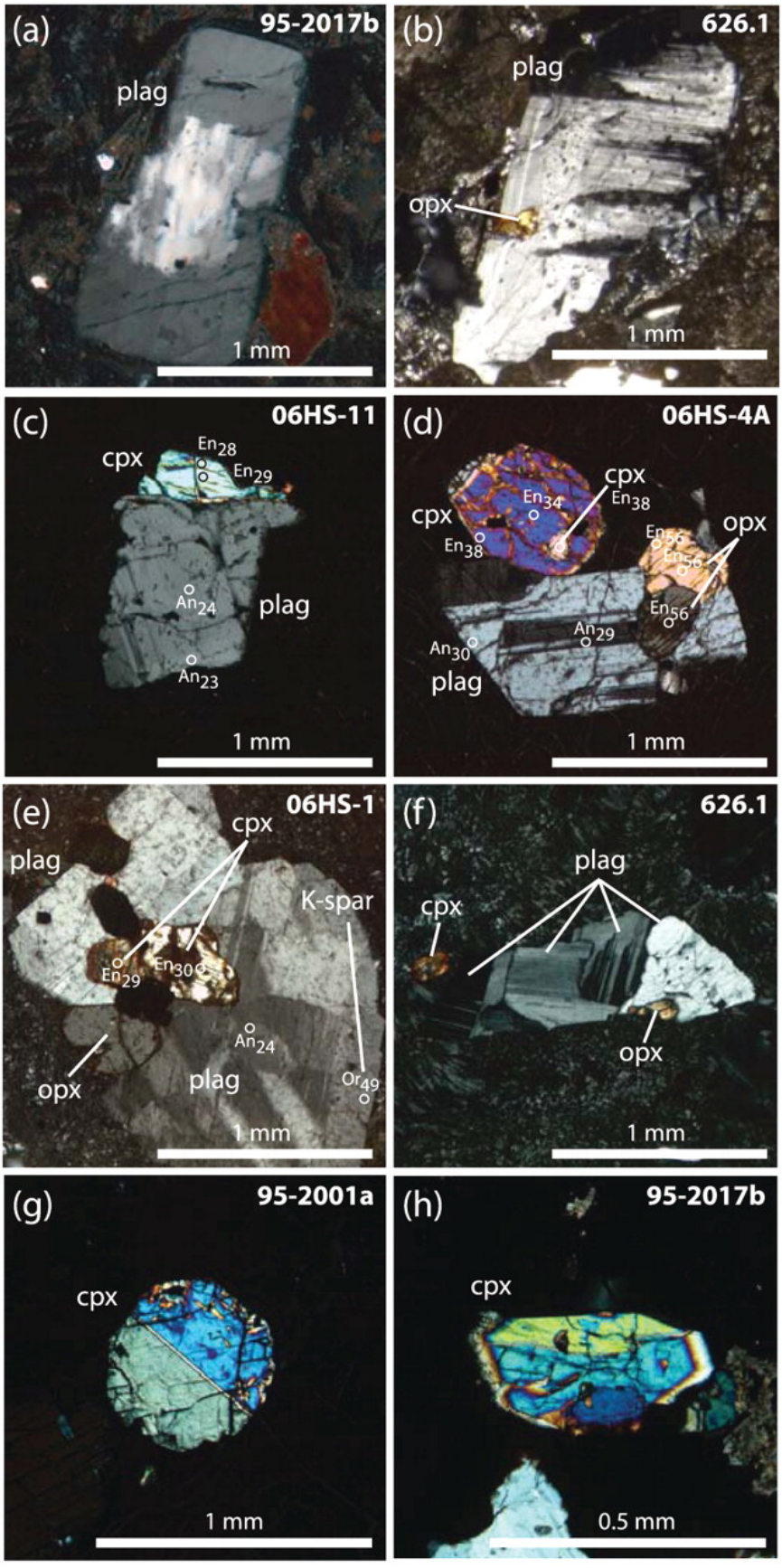
(a)
95-2017b
plag
1 mm
(b)
626.1
plag
opx
1 mm
(c)
06HS-11
cpx
En28
En29
An24
plag
An23
1 mm
(d)
06HS-4A
cpx
En34
cpx
En38
En38
opx
En56
En56
En56
An29
An30
plag
1 mm
(e)
06HS-1
plag
cpx
K-spar
En29
En30
An24
opx
plag
Or49
1 mm
(f)
626.1
plag
cpx
opx
1 mm
(g)
95-2001a
cpx
1 mm
(h)
95-2017b
cpx
0.5 mm

with quartz, but rarely, alkali feldspar overgrowth rims surround plagioclase cores. Very commonly, small (≤1 mm), anhedral–subhedral clinopyroxene and orthopyroxene crystals are attached to larger plagioclase phenocrysts (Fig. 4c). Some clinopyroxene crystals possess sieved cores and homogeneous rims. However, we found no appreciable core–rim zoning in either isolated crystals or glomerocrysts and the average orthopyroxene and clinopyroxene compositions are $En_{38}Fs_{58}Wo_4$ and $En_{28}Fs_{32}Wo_{40}$, respectively (Table 2; Appendix Table B2). Three Kilgore Tuff samples (06HS-10, 06HS-11, 95-2017b) contain anhedral clinopyroxene crystals with simple twins that are petrographically similar to twinned clinopyroxene crystals observed in the Blacktail Creek Tuff (Fig. 4g and h). Magnetite and ilmenite constitute ~1–2 vol. % of the total phenocryst content and are often present in glomerocrystic clusters of plagioclase and pyroxene. The average Fe–Ti oxide temperature obtained from single magnetite–ilmenite pairs in the Kilgore Tuff is 856°C (see 'Magmatic temperatures' section; Henshaw, 2002). Zircon (~50–120 μm) is commonly attached to or included within larger magnetite crystals.

Post-Kilgore lavas range from glassy and nearly aphyric (~1–2 vol. % phenocrysts) to porphyritic (~20 vol. % phenocrysts) (Table 2). Average plagioclase compositions of post-Kilgore lavas are similar to those of the Kilgore Tuff (Table 2; Appendix Fig. B1 and Table B2). A few plagioclase crystals with alkali feldspar overgrowth rims were found in the post-Kilgore Indian Creek rhyolite (e.g. Fig. 4e), but typically plagioclase is isolated and unzoned. As in the Kilgore tuff, orthopyroxene and clinopyroxene commonly occur in crystal clusters with plagioclase (Fig. 4c–f). Average orthopyroxene and clinopyroxene compositions of post-Kilgore rhyolites are nearly

identical to those of the Kilgore tuff, with the exception of the Juniper Buttes rhyolite, which are slightly less evolved (Table 2). Thus, it appears that post-Kilgore lavas generally have similar phenocryst sizes, morphologies and compositions to the Kilgore Tuff.

Overall, the mineralogy of the low-$\delta^{18}O$ Kilgore Tuff and post-Kilgore lavas is similar to that of the normal-$\delta^{18}O$ Heise tuff units that preceded them (Tables 1 and 2). All units lack amphibole and biotite, and the presence or absence of quartz appears to be related to the total crystal content and not the chemical compositions of the rhyolites (Tables 2 and 3). Mineral compositions of normal-$\delta^{18}O$ and low-$\delta^{18}O$ Heise units generally overlap, and although some units define distinct compositional fields (particularly for orthopyroxene; Appendix Fig. B1); these differences do not correspond in any systematic way to $\delta^{18}O$ variations. However, we observe that only the Kilgore Tuff and Blacktail Creek Tuff have clinopyroxene crystals with simple twins (Fig. 4g and h), and only the low-$\delta^{18}O$ Kilgore Tuff and post-Kilgore rhyolites have glomerocrystic clusters of plagioclase, orthopyroxene and clinopyroxene (Fig. 4c–f).

## WHOLE-ROCK GEOCHEMISTRY

### Major elements

The majority of Heise rhyolites are peraluminous to metaluminous high-silica rhyolites with 75–77 wt % $SiO_2$, 12–13 wt % $Al_2O_3$, 0·4–0·9 wt % CaO, 1–2 wt % FeO and 0·1–0·3 wt % MgO (Table 3). These compositions are identical to those of high-silica rhyolites erupted in the neighboring Yellowstone Plateau volcanic field with respect to many major element concentrations and ratios; for example, low CaO and

MgO and high K/Na ratios (Hildreth *et al*., 1984; Christiansen, 2001). They are also similar to those of high-silica rhyolites of the Bruneau–Jarbidge volcanic field in the central SRP, based on common rhyolite classification indexes such as $K_2O/Na_2O$ and molar $Al_2O_3/(CaO + Na_2O + K_2O)$ (Bonnichsen *et al*., 2008). Most Heise tuff units that preceded the low-$\delta^{18}O$ Kilgore tuff and post-Kilgore rhyolites have lower $SiO_2$ and higher FeO and MgO concentrations, indicating that they are less evolved (Table 3). These include the Blacktail Creek Tuff, the Conant Creek Tuff, and the Pre-Kilgore Tuff, which have ~71–74 wt % $SiO_2$, ~2–4 wt % FeO and ~0·3–1 wt % MgO (Table 3). The more evolved, low-$\delta^{18}O$ Kilgore Tuff and post-Kilgore rhyolites have major element compositions that overlap, reflecting the similar mineralogy and mineral chemistry described above for these units.

When whole-rock normative compositions are plotted in the Ab–Or–Qtz system, rhyolites from the Kilgore cycle plot between the 1 kbar and 2 kbar cotectic curves near the ternary minima (Fig. 5). The normative compositions of the Kilgore Tuff and post-Kilgore rhyolites are similar to those of the Blacktail Creek Tuff and Walcott Tuff (Fig. 5). All Heise rhyolites plot within or near the locus of most granite compositions (gray field in Fig. 5), and represent near-eutectic liquids at the low pressure–temperature minimum (i.e. ‘granite minimum’) of the Ab–Or–Qtz system. The average normative compositions of the Yellowstone and Bruneau–Jarbidge rhyolites are similar to those of the Heise rhyolites, but the Yellowstone rhyolites have a larger proportion of normative Qtz and Bruneau–Jarbidge rhyolites have a lower proportion of normative Ab (Fig. 5).

**Table 3.** Major and trace element compositions of Heise samples

| Sample: | 95-2001a | 06HS-18 | 08HS-10 | 06HS-16 | 06HS-5 | 06HS-14 | TNP96-43 | 95-2017b | 95-2015 | 06HS-10 | 06HS-11 | 95-2010 | 06HS-4A | 626.1 | 06HS-1 | 06HS-19 |
|---|---|---|---|---|---|---|---|---|---|---|---|---|---|---|---|---|
| Unit: | Blacktail Creek Tuff | Walcott Tuff | Lidy Hot Springs rhyolite | Wolverine Creek Tuff | Conant Creek Tuff | Pre-Kilgore Tuff | Kilgore Tuff | Kilgore Tuff | Kilgore Tuff | Kilgore Tuff | Kilgore Tuff | Kilgore Tuff | Juniper Buttes rhyolite | Long Hollow rhyolite | Indian Creek rhyolite | Sheridan Reservoir rhyolite[1] |
| Map ID: | BCT | WT | LHS | WCT | CCT | KT #1 | KT #4 | KT #2 | KT #3 | KT #1 | KT #1 | KT #1 | JB | LH | IC | SR |
| Lat. (°N): | 43·51 | 43·81 | 44·13 | 43·53 | 43·32 | 43·53 | 43·86 | 44·13 | 44·35 | 43·53 | 43·53 | 43·53 | 44·06 | 43·71 | 44·29 | 44·46 |
| Long. (°W): | 111·76 | 112·84 | 112·54 | 111·70 | 111·14 | 111·70 | 110·56 | 112·54 | 112·17 | 111·70 | 111·70 | 111·70 | 111·84 | 111·53 | 112·41 | 111·68 |
| *Major element analyses by XRF (wt %)* | | | | | | | | | | | | | | | | |
| $SiO_2$ | 74·40 | 75·49 | 76·67 | 75·81 | 74·26 | 70·78 | 75·75 | 76·01 | 76·42 | 75·95 | 75·90 | 76·13 | 76·32 | 76·31 | 75·27 | 75·85 |
| $TiO_2$ | 0·31 | 0·22 | 0·30 | 0·17 | 0·21 | 0·55 | 0·28 | 0·24 | 0·23 | 0·24 | 0·24 | 0·24 | 0·24 | 0·23 | 0·25 | 0·26 |
| $Al_2O_3$ | 13·14 | 12·03 | 12·31 | 12·60 | 14·17 | 15·86 | 12·48 | 12·30 | 12·29 | 12·49 | 12·17 | 12·23 | 12·58 | 12·39 | 12·82 | 12·17 |
| FeO* | 1·95 | 1·27 | 1·17 | 1·65 | 2·07 | 3·93 | 2·14 | 1·67 | 1·69 | 1·79 | 1·93 | 1·73 | 1·26 | 1·40 | 1·88 | 2·48 |
| MnO | 0·05 | 0·03 | 0·04 | 0·04 | 0·04 | 0·10 | 0·02 | 0·04 | 0·03 | 0·04 | 0·04 | 0·04 | 0·02 | 0·03 | 0·03 | 0·05 |
| MgO | 0·31 | 0·28 | 0·13 | 0·33 | 0·74 | 1·11 | 0·09 | 0·19 | 0·08 | 0·15 | 0·20 | 0·15 | 0·19 | 0·22 | 0·17 | 0·06 |
| CaO | 1·22 | 2·11 | 0·58 | 0·87 | 1·06 | 1·20 | 0·48 | 0·81 | 0·44 | 0·69 | 0·86 | 0·70 | 0·76 | 0·66 | 0·48 | 0·63 |
| $Na_2O$ | 3·30 | 3·45 | 3·40 | 3·28 | 2·08 | 2·54 | 3·53 | 3·06 | 3·60 | 3·07 | 3·27 | 3·20 | 2·71 | 3·36 | 3·51 | 3·70 |
| $K_2O$ | 5·27 | 5·09 | 5·38 | 5·20 | 5·36 | 3·84 | 5·19 | 5·65 | 5·19 | 5·55 | 5·36 | 5·55 | 5·90 | 5·34 | 5·32 | 4·78 |
| $P_2O_5$ | 0·04 | 0·03 | 0·02 | 0·04 | 0·02 | 0·09 | 0·04 | 0·03 | 0·03 | 0·03 | 0·03 | 0·03 | 0·02 | 0·06 | 0·28 | 0·02 |
| *Trace element analyses by XRF (ppm)* | | | | | | | | | | | | | | | | |
| Ba | 1099 | 914 | 840 | 573 | 509 | 974 | 1063 | 832 | 973 | 876 | 878 | 815 | 894 | 774 | 1061 | 2010 |
| Rb | 174 | 171 | 181 | 165 | 147 | 114 | 184 | 176 | 175 | 162 | 162 | 174 | 198 | 189 | 156 | 143 |
| Sr | 84 | 39 | 29 | 40 | 25 | 82 | 34 | 32 | 28 | 26 | 27 | 25 | 40 | 33 | 34 | 61 |
| Zr | 327 | 221 | 239 | 185 | 273 | 538 | 395 | 301 | 325 | 312 | 310 | 324 | 203 | 224 | 332 | 462 |
| Y | 44 | 54 | 52 | 75 | 77 | 78 | 56 | 56 | 52 | 63 | 63 | 57 | 47 | 52 | 65 | 65 |
| Nb | 32 | 41 | 41 | 54 | 56 | 50 | 48 | 47 | 49 | 48 | 48 | 47 | 37 | 42 | 50 | 36 |
| Ga | 18 | 17 | 17 | 22 | 22 | 24 | 20 | 19 | 20 | 20 | 19 | 20 | 17 | 20 | 19 | 20 |
| Zn | 61 | 41 | 45 | 86 | 90 | 116 | 63 | 72 | 57 | 60 | 75 | 61 | 38 | 48 | 62 | 91 |
| Pb | 26 | 23 | 25 | 28 | 26 | 28 | 25 | 24 | 23 | 25 | 29 | 26 | 24 | 27 | 27 | 29 |
| La | 66 | 71 | 67 | 78 | 81 | 75 | 89 | 84 | 85 | 81 | 79 | 83 | 69 | 81 | 87 | 79 |
| Ce | 120 | 136 | 126 | 154 | 159 | 160 | 161 | 157 | 146 | 156 | 161 | 163 | 128 | 142 | 160 | 123 |
| Th | 27 | 26 | 28 | 25 | 26 | 26 | 26 | 26 | 27 | 26 | 26 | 26 | 28 | 29 | 26 | 21 |
| Nd | 45 | 54 | 48 | 61 | 65 | 63 | 68 | 61 | 61 | 58 | 64 | 61 | 44 | 56 | 60 | 66 |
| U | 7 | 7 | 9 | 6 | 5 | 5 | 7 | 7 | 6 | 7 | 6 | 6 | 6 | 8 | 5 | 5 |
| Ni | 4 | 3 | 0 | 5 | 2 | 7 | 4 | 4 | 4 | 3 | 0 | 4 | 4 | 3 | 7 | 4 |
| Cu | 1 | 5 | 0 | 5 | 4 | 10 | 3 | 4 | 2 | 5 | 23 | 2 | 4 | 4 | 7 | 7 |
| Cr | 2 | 2 | 1 | 8 | 5 | 13 | 3 | 2 | 1 | 3 | 6 | 2 | 4 | 4 | 9 | 5 |
| Sc | 5 | 3 | 3 | 2 | 3 | 9 | 4 | 4 | 4 | 4 | 4 | 5 | 3 | 3 | 3 | 4 |
| V | 9 | 24 | 2 | 9 | 2 | 31 | 7 | 6 | 4 | 4 | 5 | 5 | 6 | 6 | 6 | 1 |

[1]Post-Huckleberry Ridge Tuff unit (see text for details); *All Fe given as FeO; Samples are normalized to 100% anhydrous; Map ID corresponds to labels in Fig. 1.

**Figure 5.** Heise whole-rock normative (CIPW) rhyolite compositions plotted in the albite (Ab)–orthoclase (Or)–quartz (Qtz) system. Heise units are shown by the symbols (see legend) and labels (BCT, Blacktail Creek Tuff; WT, Walcott Tuff, LHS, Lidy Hot Springs rhyolite; WCT, Wolverine Creek Tuff; CCT, Conant Creek Tuff; P-KT, Pre-Kilgore Tuff; KT, Kilgore Tuff; JB, Juniper Buttes rhyolite; LH, Long Hollow rhyolite; IC, Indian Creek rhyolite). Ternary cotectic curves and eutectic minima from 20 kbar to 1 kbar are shown (Wyllie *et al*., 1976). The gray shaded field represents the composition of most granites. Heise rhyolite compositions plot near the low-pressure (1–2 kbar) ternary minimum. The average normative compositions of Yellowstone and Bruneau–Jarbidge rhyolites are also shown. The CCT and P-KT units, which plot outside the compositional field of the other Heise units, have relatively low unnormalized major oxide totals but are petrographically fresh and unaltered in hand sample and thin section.

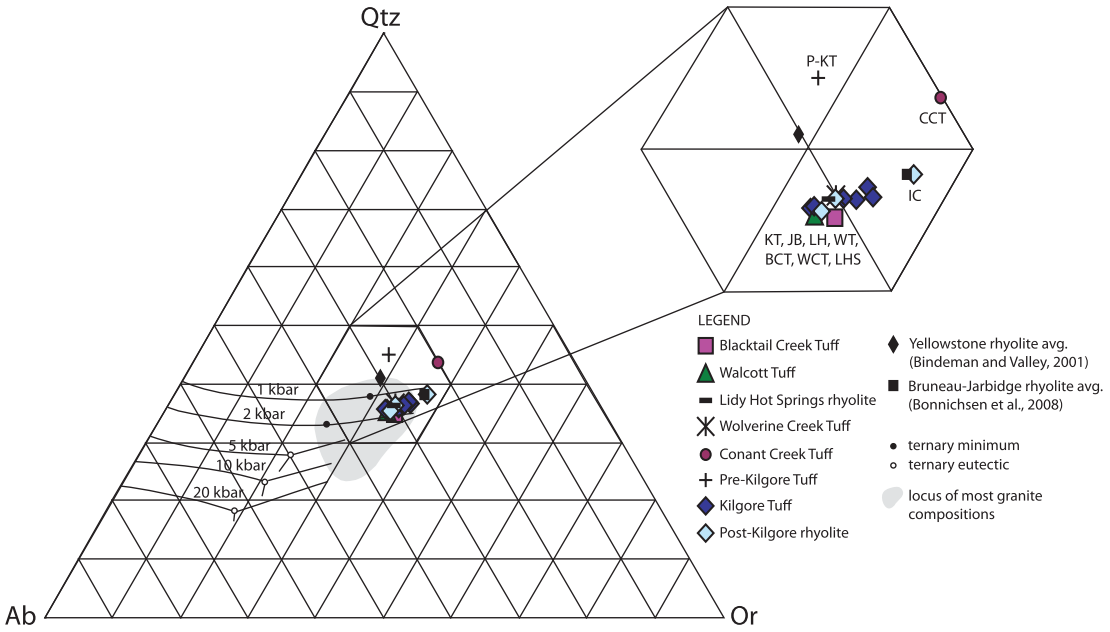


## Trace elements

Concentrations of the large ion lithophile element (LILE) Ba, and the high field strength elements (HFSE) Y, Nb, La, Ce and Nd, reveal temporal trends that define the compositional evolution of the Heise eruptions. In successive eruptions of the Blacktail Creek Tuff, Walcott Tuff, Wolverine Creek Tuff, and Conant Creek Tuff, Ba progressively decreases, whereas Y, Nb, La, Ce and Nd progressively increase (Table 3).

Magmas belonging to the last low-$\delta^{18}O$ Kilgore cycle (4·87–3·96 Ma) have trace element concentrations that are similar to those of the initial Blacktail Creek Tuff eruption.

To investigate the role of fractional crystallization in the temporal variations observed for Heise trace element concentrations, we chose the trace element ratios Rb/Sr and Rb/Ba to assess plagioclase fractionation (removal of Sr and Ba relative to Rb), and Zr/Nb, La/Nb and Ce/Nb to assess clinopyroxene and zircon fractionation (removal of Zr, La and Ce relative to Nb). Rb/Sr and Rb/Ba ratios define an increasing trend for successive Heise eruptions from 6·62 to 5·51 Ma, a sharp decrease with the appearance of the low-$\delta^{18}O$ Pre-Kilgore Tuff at 4·87 Ma, an increase with the low-$\delta^{18}O$ Kilgore Tuff at 4·45 Ma, and a slight decrease with the low-$\delta^{18}O$ post-Kilgore lavas from 4·29 to 3·96 Ma (Fig. 6a and b). Zr/Nb, La/Nb and Ce/Nb ratios reveal a similar temporal pattern (in reverse), with a negative trend for successive Heise eruptions from 6·62 to 5·51 Ma, followed by an increase in the low-$\delta^{18}O$ Pre-Kilgore Tuff at 4·87 Ma, and relatively constant ratios for all low-$\delta^{18}O$ Kilgore Tuff and post-Kilgore units from 4·45 to 3·96 Ma (Fig. 6c–e). Although zoning is present within single Heise tuff units (Morgan, 1988), all available trace element data (Morgan, 1988; Morgan & McIntosh, 2005) indicate that the ranges of concentrations within each tuff are not sufficiently broad to obscure the temporal trends that we observe (e.g. gray shaded fields in Fig. 6c).

Although the Rb/Sr ratios of the Heise rhyolites (~1–7; Fig. 6a) are not nearly as high as those determined for interstitial Yellowstone rhyolite glasses (up to 140; Vazquez & Reid, 2002), or extreme cases found in large-volume rhyolites elsewhere (e.g. up to 2000 for Long Valley rhyolites; Halliday *et al.*, 1989), when combined with other trace element ratios (Fig. 6b–e), they provide a compelling case for small degrees (~10–15%)

**Figure 6.** Temporal variations in trace element ratios of Heise rhyolites. Heise units are indicated by the same symbols and labels as used in Fig. 5. Continuous lines in (a)–(e) show the temporal evolution in trace element ratios for successive Heise eruptions. The gray shaded fields in (c) show the ranges of trace element ratios published by Morgan & McIntosh (2005) for single Heise tuff units. Fractional crystallization of plagioclase (plag), clinopyroxene (cpx) and zircon (zirc) from a common source at ~6·6–5·5 Ma, followed by tapping of a less evolved source at ~4·9 Ma to generate the final Kilgore-cycle magmas, can explain the temporal variations observed (see text and Appendix Table B5 for details).

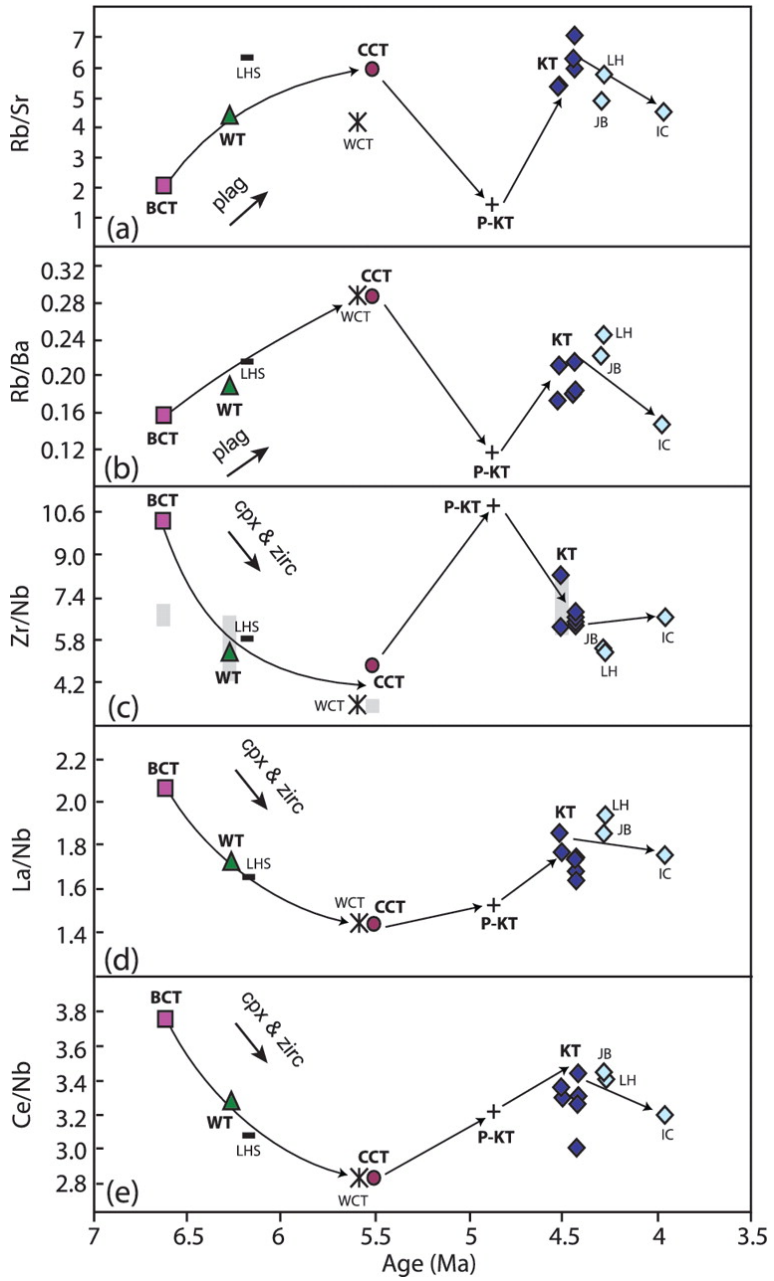

of fractional crystallization of plagioclase (~9–13%), clinopyroxene (~1–2%) and zircon (<1%) from a common rhyolite parent to generate the normal-$\delta^{18}O$ Blacktail Creek Tuff, Walcott Tuff and Conant Creek Tuff (Appendix Table B5). This was followed by tapping of a less evolved, Blacktail Creek Tuff-like magma at 4·87 Ma to generate the final low-$\delta^{18}O$ Kilgore cycle. The more evolved Kilgore and post-Kilgore rhyolite compositions can be generated from the less evolved Pre-Kilgore Tuff magma by ~10% fractional crystallization (Appendix Table B5).

## OXYGEN ISOTOPES

Rhyolites from the Heise volcanic field span a large (~4‰) range in magmatic $\delta^{18}O$. The climactic Kilgore Tuff is the most voluminous low-$\delta^{18}O$ magma yet discovered in the SRP and worldwide. The ~4‰ range in $\delta^{18}O$ exhibited by the Heise rhyolites is similar to those of the Yellowstone and Bruneau–Jarbidge rhyolites, and the timing and magnitude of $\delta^{18}O$ depletion in the three volcanic fields show striking parallels. A summary of our new oxygen isotope data for the Heise volcanic field, with particular emphasis on the final low-$\delta^{18}O$ Kilgore cycle, is provided below. These new data are compared with those for other volcanic centers in the SRP, including the younger Yellowstone and older Bruneau–Jarbidge centers, as well as the contemporaneous Magic Reservoir eruptive center.

### Normal-$\delta^{18}O$ to low-$\delta^{18}O$ evolution in the Heise volcanic field

Volcanism began in the Heise volcanic field at 6·62 Ma with the eruption of the normal-$\delta^{18}O$ Blacktail Creek Tuff (Fig. 7b). This unit, with $\delta^{18}O_{quartz} = 6{\cdot}40$‰ and

$\delta^{18}O_{zircon} = 4{\cdot}81‰$, has a calculated $\delta^{18}O_{magma}$ value of 6·6‰, which is within the range of normal-$\delta^{18}O$ SRP xenoliths and crustal basement rocks ($\delta^{18}O \approx 6{\cdot}5–8{\cdot}5‰$; Watts *et al*., 2010). Post-Blacktail Milo Dry Farm rhyolite is also normal-$\delta^{18}O$, with $\delta^{18}O_{quartz} = 7{\cdot}46‰$ and $\delta^{18}O_{sanidine} = 6{\cdot}75‰$. Normal-$\delta^{18}O$ volcanism continued with the eruption of the Walcott Tuff ($\delta^{18}O = 6{\cdot}1‰$); however, the post-Walcott intracaldera Lidy Hot Springs rhyolite is ~2‰ depleted ($\delta^{18}O_{magma} = 4{\cdot}4‰$) relative to previous normal-$\delta^{18}O$ Heise eruptions (Fig. 7b). Subsequently erupted small-volume Kelly Canyon rhyolite and large-volume Wolverine Creek and Conant Creek tuffs have normal-$\delta^{18}O$ magmatic values of 5·9–6·5‰, although the Conant Creek Tuff is moderately (~0·1‰) depleted relative to the lower boundary of nominally normal-$\delta^{18}O$ rhyolites ($\delta^{18}O = 6‰$) (Fig. 7b).

The final caldera-forming tuff of the Heise volcanic field, the Kilgore Tuff, has extreme (~3‰) depletions from normal-$\delta^{18}O$ magmatic values, with $\delta^{18}O_{quartz} = 4{\cdot}29–4{\cdot}33‰$, $\delta^{18}O_{zircon} = 1{\cdot}50–1{\cdot}61‰$, and $\delta^{18}O_{magma} = 3{\cdot}3–3{\cdot}6‰$ (Fig. 7b). Samples erupted from different vents, >100 km apart, have similar phenocryst oxygen isotope values indicating that magma homogeneity was achieved prior to eruption. The Pre-Kilgore Tuff is nearly identical in $\delta^{18}O$ to the Kilgore Tuff, with $\delta^{18}O_{quartz} = 3{\cdot}29‰$, $\delta^{18}O_{zircon} = 1{\cdot}89‰$, and $\delta^{18}O_{magma} = 3{\cdot}5‰$ (Fig. 7b). We observe that a coarse lithic breccia beneath the Kilgore Tuff (stratigraphically below 06HS-10 in Fig. 3) is high-$\delta^{18}O$, with $\delta^{18}O_{quartz} \approx 15–16‰$. In addition, lithic fragments that constitute ~1–2 vol. % of the Kilgore Tuff (06HS-11 in Fig. 3) are normal–high-$\delta^{18}O$, in nearly equal proportions of propylitically altered normal-$\delta^{18}O$ tuffs ($\delta^{18}O_{whole\ rock} \approx 7–9‰$) and high-$\delta^{18}O$ sandstone ($\delta^{18}O_{quartz} \approx 14–15‰$). Combined, this evidence argues against

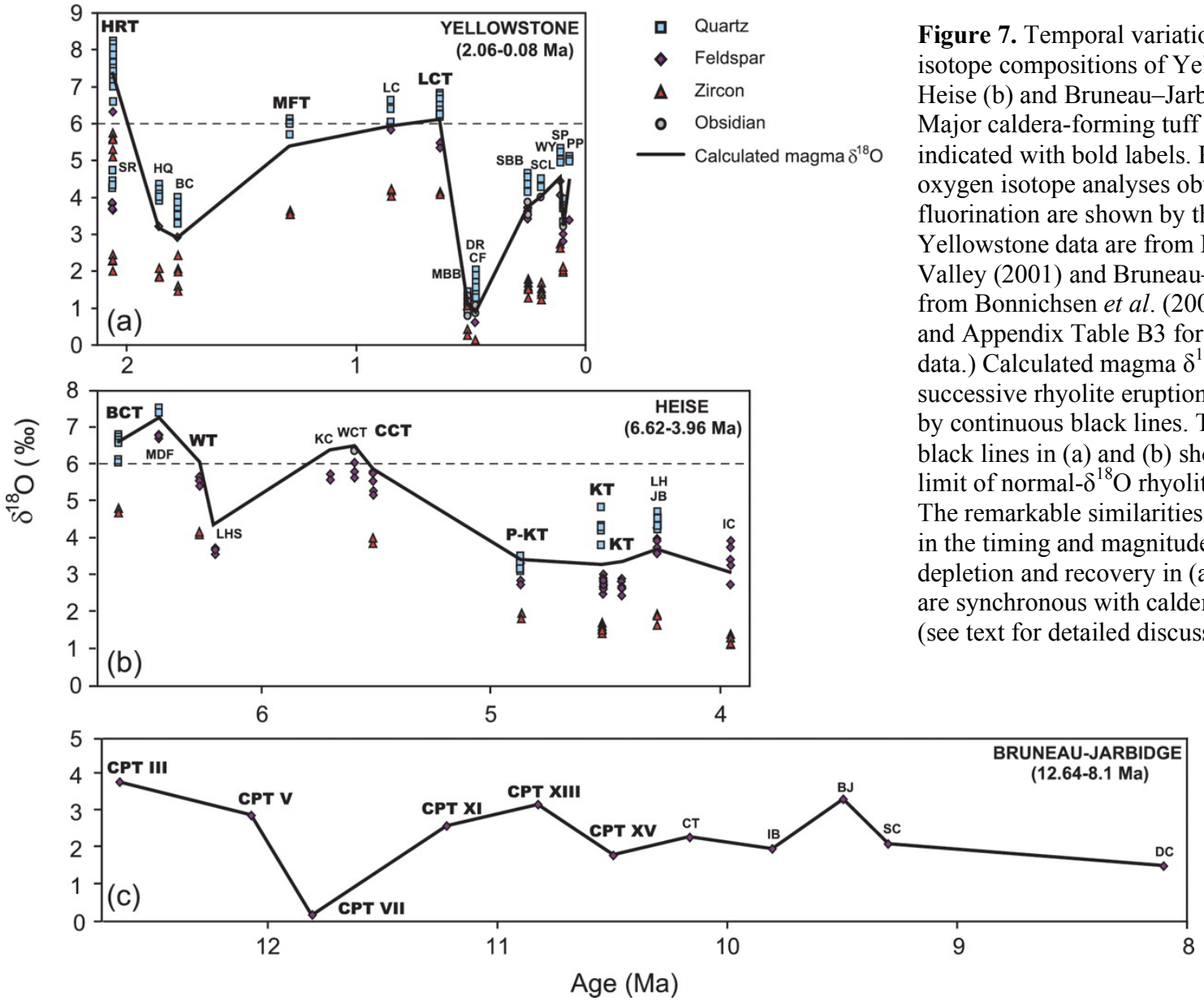


**Figure 7.** Temporal variations in oxygen isotope compositions of Yellowstone (a), Heise (b) and Bruneau–Jarbidge (c) rhyolites. Major caldera-forming tuff units are indicated with bold labels. Phenocryst oxygen isotope analyses obtained by laser fluorination are shown by the symbols. Yellowstone data are from Bindeman & Valley (2001) and Bruneau–Jarbidge data are from Bonnichsen *et al*. (2008). (See Table 1 and Appendix Table B3 for the Heise $\delta^{18}O$ data.) Calculated magma $\delta^{18}O$ values for successive rhyolite eruptions are connected by continuous black lines. The fine dashed black lines in (a) and (b) show the lower limit of normal-$\delta^{18}O$ rhyolites ($\delta^{18}O = 6‰$). The remarkable similarities should be noted in the timing and magnitude of $\delta^{18}O$ depletion and recovery in (a) and (b), which are synchronous with caldera collapse events (see text for detailed discussion).

syneruptive modification of the Kilgore tuff to account for its low-$\delta^{18}O$ signature (see Garcia *et al*., 1998). Smaller volume effusive post-Kilgore Tuff lavas and domes are equally low in $\delta^{18}O$, but encompass a slightly larger $\delta^{18}O$ range than the Kilgore Tuff (Fig. 7b). The Juniper Buttes resurgent dome and Long Hollow rhyolite are ~0·1–0·4‰ elevated from the 3·3–3·6‰ range of the Pre-Kilgore Tuff and Kilgore Tuff. The later Indian Creek rhyolite is ~0·3–0·6‰ lower in $\delta^{18}O$, with $\delta^{18}O_{magma} = 3·0$‰.

***Oxygen isotope compositions of zircon and single phenocrysts***

An interesting result of oxygen isotopic investigation in the Heise volcanic field is that despite $\delta^{18}O$ homogeneity of the Kilgore Tuff on the caldera-wide scale in major phenocrysts, it preserves remarkable $\delta^{18}O$ heterogeneity in accessory zircon. Whereas we find that laser fluorination $\delta^{18}O$ analyses of single phenocrysts of quartz and sanidine and bulk zircon are reproducible within a standard error of less than ~0·1‰ (Table 1), a subset of analyses obtained by ion microprobe for single Kilgore Tuff zircons reveal significant $\delta^{18}O$ heterogeneity (Table 4). These zircon $\delta^{18}O$ values are almost exclusively low, ranging from –1·30‰ to 3·03‰, with the exception of one zircon crystal that has a normal-$\delta^{18}O$ value of 6·07‰ (Fig. 8). The average $\delta^{18}O$ value for zircons analyzed by ion microprobe is nearly identical to the average $\delta^{18}O$ value for bulk zircons analyzed by laser fluorination (Fig. 8). Single zircons from the Pre-Kilgore Tuff are also low-$\delta^{18}O$, and overlap with the Kilgore tuff zircons (Fig. 8), but we note that for the Pre-Kilgore Tuff, the average of single zircon analyses obtained by ion probe is ~1‰ higher than the bulk zircon average obtained by laser fluorination. The fact that the Pre-Kilgore Tuff zircons have U–Pb ages that are ~300 kyr older and slightly higher in $\delta^{18}O$ than the

Kilgore Tuff (Fig. 8), may indicate the progress of (incomplete) zircon annealing via solution–reprecipitation in the early stages of Kilgore Tuff magma formation.

**Table 4.** Oxygen isotopic compositions and U–Pb ages determined by ion microprobe. Single spot analyses of single zircon cores. Errors for oxygen isotopic compositions (1σ ext) are the external errors of KIM-5 zircon standards and are corrected for minor instrumental drift (~0.3‰ over 9 h analysis duration). The average oxygen isotopic compositions in the rightmost column are averages of single analyses for the Pre-Kilgore Tuff (HS-14, $n = 8$) and Kilgore Tuff (HS-10, $n = 9$; HS-11, $n = 9$).

| Sample | U–Pb age (Ma) | 1σ (Ma) | $\delta^{18}O$ (‰) | 1σ ext (‰) | Av. $\delta^{18}O$ (‰) |
|---|---|---|---|---|---|
| HS-14__PKT__g3 | 4·40 | 0·33 | 1·06 | 0·22 | 2·84 |
| HS-14__PKT__g4 | 4·23 | 0·50 | 1·96 | 0·22 | |
| HS-14__PKT__g5 | 4·90 | 0·37 | 0·92 | 0·22 | |
| HS-14__PKT__g6 | 4·78 | 0·59 | 2·45 | 0·22 | |
| HS-14__PKT__g7 | 5·19 | 0·24 | 0·89 | 0·22 | |
| HS-14__PKT__g8 | 4·96 | 0·31 | 5·45 | 0·22 | |
| HS-14__PKT__g9 | 5·07 | 0·30 | 4·96 | 0·22 | |
| HS-14__PKT__g10 | 4·68 | 0·23 | 5·02 | 0·22 | |
| HS-10__Kilg__g1 | 4·25 | 0·35 | −0·40 | 0·22 | 1·30 |
| HS-10__Kilg__g2 | 4·50 | 0·28 | 0·97 | 0·22 | |
| HS-10__Kilg__g3 | 5·08 | 1·16 | 2·65 | 0·22 | |
| HS-10__Kilg__g4 | 4·30 | 0·26 | 3·03 | 0·22 | |
| HS-10__Kilg__g5 | 4·95 | 0·26 | −0·59 | 0·22 | |
| HS-10__Kilg__g6 | 4·50 | 0·33 | 2·76 | 0·22 | |
| HS-10__Kilg__g7 | 4·84 | 0·34 | −0·68 | 0·22 | |
| HS-10__Kilg__g8 | 4·09 | 0·30 | 2·78 | 0·22 | |
| HS-10__Kilg__g9 | 5·06 | 0·27 | 1·22 | 0·22 | |
| HS-11__Kilg__g1 | 4·72 | 0·23 | 1·04 | 0·22 | 1·28 |
| HS-11__Kilg__g2 | 4·73 | 0·30 | 0·46 | 0·22 | |
| HS-11__Kilg__g3 | 4·37 | 0·61 | −0·76 | 0·22 | |
| HS-11__Kilg__g4 | 4·92 | 0·36 | 2·80 | 0·22 | |
| HS-11__Kilg__g5 | 4·35 | 0·28 | −1·30 | 0·22 | |
| HS-11__Kilg__g6 | 4·44 | 0·27 | 0·81 | 0·22 | |
| HS-11__Kilg__g7 | 4·70 | 0·32 | 0·96 | 0·22 | |
| HS-11__Kilg__g9 | 4·57 | 0·29 | 6·07 | 0·22 | |
| HS-11__Kilg__g10 | 4·63 | 0·30 | 1·40 | 0·22 | |

**Figure 8.** Ion microprobe oxygen isotope data for single zircon crystals from the Kilgore Tuff and Pre-Kilgore Tuff. Oxygen isotope compositions are plotted against U–Pb age for single zircon spots. (See Table 4 for the $\delta^{18}O$ and U–Pb data.) The average 1σ error for $\delta^{18}O$ values and U–Pb ages is shown in the bottom right corner. The continuous vertical line is the Ar–Ar eruption age for Kilgore Tuff samples 06HS-10 and 06HS-11 (4·43 Ma; Table 1). The average zircon $\delta^{18}O$ composition of the Kilgore Tuff by ion microprobe (black dashed line), equilibrium magma value for the ion microprobe zircon average (continuous gray line), and laser fluorination zircon average (dashed gray line) are included in the plot.

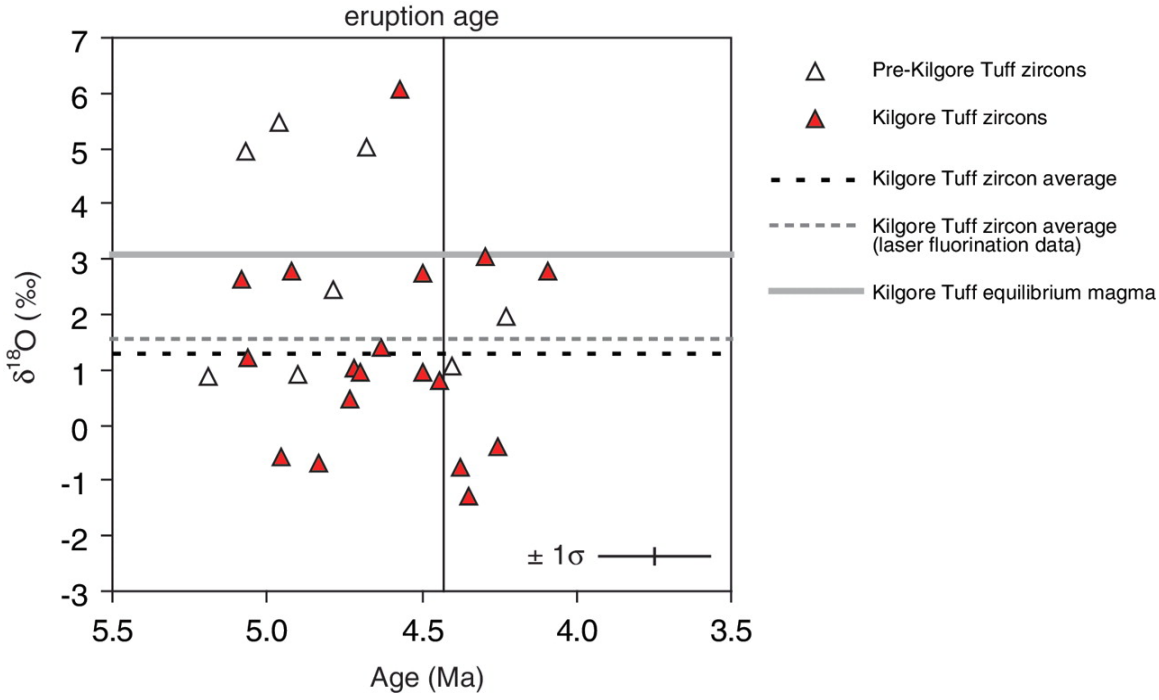


Laser fluorination oxygen isotope data and published mineral pair fractionation factors for quartz–zircon (Trail *et al*., 2009) and quartz–K-feldspar (Zheng, 1993) are consistent with high-temperature oxygen isotopic equilibrium for the Heise rhyolites (Fig. 9a and b). This is in contrast to the strong O-isotope disequilibria that have been documented for many Yellowstone rhyolites (Fig. 9a and b; Bindeman & Valley, 2001; Bindeman *et al*., 2008). However, as indicated by our ion microprobe data for the Kilgore Tuff and Pre-Kilgore Tuff, single zircons preserve significant $\delta^{18}O$ heterogeneity, and require zircon crystallization from multiple, independent magma batches with unique

low-$\delta^{18}O$ values (Fig 8). Because the $\delta^{18}O$ averages of single zircon analyses by ion microprobe match the $\delta^{18}O$ values of bulk zircons obtained by laser fluorination for Kilgore Tuff samples erupted >100 km apart (Table 1; Fig. 7b), and presumably from different parts of the Kilgore magma chamber based on their locations relative to

**Figure 9.** $\delta^{18}O_{quartz}$–$\delta^{18}O_{zircon}$ (a) and $\delta^{18}O_{quartz}$–$\delta^{18}O_{sanidine}$ (b) showing that the Heise rhyolite units (filled squares) are in high-temperature (600–1000°C) oxygen isotopic equilibrium, in contrast to the significant disequilibria observed for Yellowstone rhyolite units (open circles and gray shaded field; Bindeman & Valley, 2001; Bindeman *et al.*, 2008). Published mineral pair fractionation factors for quartz–zircon (Trail *et al.*, 2009) and quartz–K-spar (Zheng, 1993) were used to construct the equilibrium fractionation lines that are shown in (a) and (b) for temperatures of 600°C, 800°C and 1000°C.

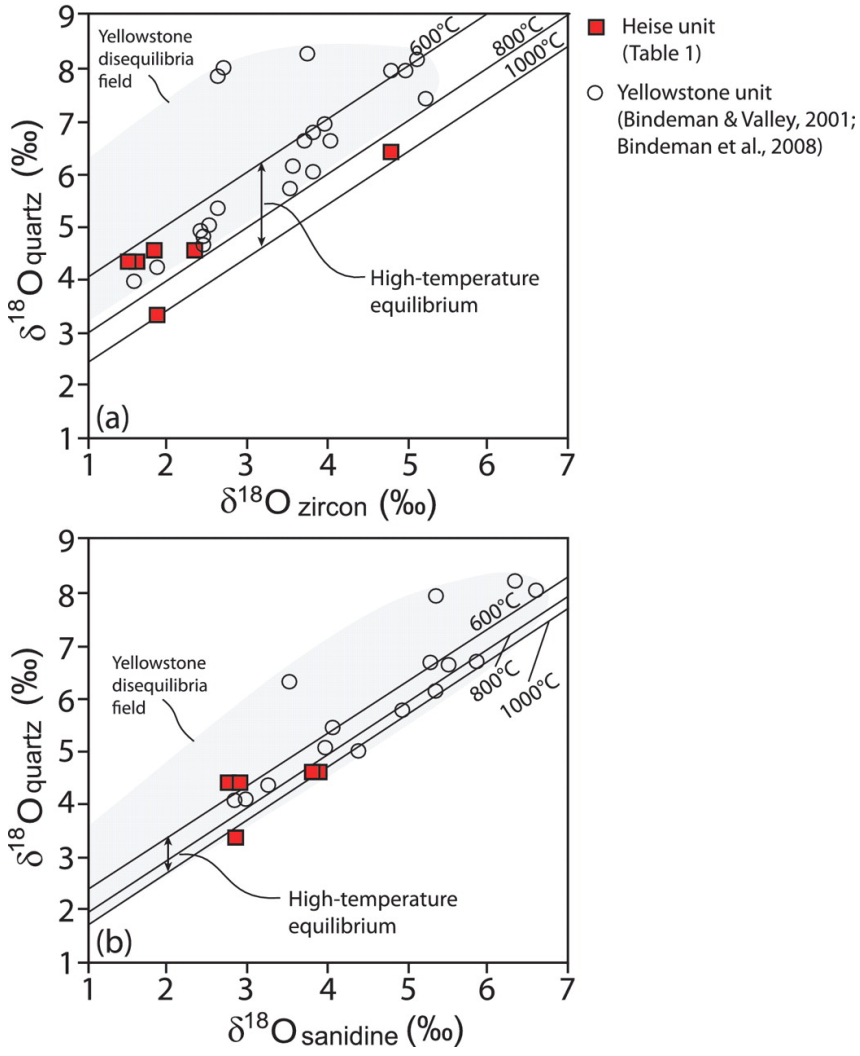

proposed Kilgore Tuff vent sources (Morgan & McIntosh, 2005; Fig. 1), it is evident that a heterogeneous zircon crystal cargo was convectively distributed (averaged) over great lateral distances prior to eruption of the Kilgore Tuff magma.

The zircon $\delta^{18}O$ heterogeneity that we report for the low-$\delta^{18}O$ Kilgore Tuff ($\delta^{18}O$ range of –1·3‰ to 6·1‰) is analogous to the oxygen isotope heterogeneity reported by Cathey *et al*. (2008) for single zircons of the low-$\delta^{18}O$ Bruneau–Jarbidge tuffs ($\delta^{18}O$ range of –3·1‰ to 6·4‰) and that reported by Bindeman *et al*. (2008) for single zircons of low-$\delta^{18}O$ rhyolites from the Yellowstone volcanic field ($\delta^{18}O$ range of –2·2‰ to 7·6‰). This means that all of the voluminous low-$\delta^{18}O$ SRP rhyolites that have been studied thus far contain zircon crystals with diverse $\delta^{18}O$ values. Furthermore, it is evident that assembly of large-volume low-$\delta^{18}O$ magmas with diverse zircon populations can occur rapidly, within error of U–Pb zircon dating (hundreds of thousands of years).

**Comparison with the Yellowstone Plateau volcanic field**

Like Heise, volcanism in the Yellowstone Plateau volcanic field began with the eruption of a normal-$\delta^{18}O$ caldera-forming tuff, the 2·06 Ma Huckleberry Ridge Tuff ($\delta^{18}O_{magma}$ = 7·0–7·5‰) (Fig. 7a). Following the Huckleberry Ridge Tuff eruption, the oxygen isotope trend plunges sharply with the appearance of several low-$\delta^{18}O$ post-Huckleberry Ridge Tuff rhyolites, including the Headquarters flow ($\delta^{18}O_{magma}$ = 3·2‰) and Blue Creek flow ($\delta^{18}O_{magma}$ = 2·9‰) (Fig. 7a). The Sheridan Reservoir rhyolite has an age and $\delta^{18}O$ composition that overlaps these post-Huckleberry Ridge Tuff units ('SR' in Fig. 7a), supporting our interpretation that it is a post-Huckleberry Ridge Tuff rather than a post-Kilgore unit. Low-$\delta^{18}O$ post-Huckleberry Ridge Tuff rhyolites, which erupted

~0·2–0·4 Myr after the first phase of normal-$\delta^{18}O$ eruptions and have depletions of ~3–4‰ from normal-$\delta^{18}O$ values, were comparable in timing and $\delta^{18}O$ depletion with the first low-$\delta^{18}O$ rhyolite in the Heise volcanic field (Lidy Hot Springs rhyolite) (Fig. 7a and b). Like Heise, $\delta^{18}O$ values at Yellowstone recovered after the first appearance of low-$\delta^{18}O$ rhyolites by ~2–3‰ over a period of ~1 Myr, with the eruptions of the Mesa Falls Tuff ($\delta^{18}O_{magma}$ = 5·4‰), the Lewis Canyon rhyolite ($\delta^{18}O_{magma}$ = 5·9‰) and the Lava Creek Tuff ($\delta^{18}O_{magma}$ = 5·9–6·3‰) (Fig. 7a). Post-Lava Creek Tuff rhyolites, including the Upper Basin Member ($\delta^{18}O_{magma}$ = 0·7–1·1‰) and Central Plateau Member ($\delta^{18}O_{magma}$ = 3·2–4·5‰) units, constitute the final pulse of low-$\delta^{18}O$ volcanism in the Yellowstone Plateau volcanic field. This final, low-$\delta^{18}O$ pulse at Yellowstone is analogous to the final, low-$\delta^{18}O$ Kilgore Tuff and post-Kilgore eruptions at Heise in terms of timing (~2 Myr after the initiation of normal-$\delta^{18}O$ volcanism), magnitude of $\delta^{18}O$ depletion (~3‰ depleted relative to normal-$\delta^{18}O$ tuffs), and duration of low-$\delta^{18}O$ eruptions (~0·5–0·9 Myr) (Fig. 7a and b).

**Comparison with the Bruneau–Jarbidge volcanic field**

Unlike Heise and Yellowstone, volcanic eruptions in the Bruneau–Jarbidge volcanic field are exclusively low-$\delta^{18}O$ (Fig. 7c). However, the trend in timing and magnitude of $\delta^{18}O$ depletions in successive Bruneau–Jarbidge eruptions may bear some resemblance to the $\delta^{18}O$ trends observed for Heise and Yellowstone (Fig. 7c). Volcanism in the Bruneau–Jarbidge volcanic field began at 12·64 Ma with the eruption of the Cougar Point Tuff III ($\delta^{18}O_{magma}$ = 3·8‰) (Fig. 7c). Following this eruption, $\delta^{18}O$ values steadily decreased with eruptions of Cougar Point Tuff V ($\delta^{18}O_{magma}$ = 2·9‰) and Cougar

Point Tuff VII ($\delta^{18}O_{magma}$ = 0·2‰). The ~3–4‰ depletion in $\delta^{18}O$ after 1–2 caldera-forming eruptions is consistent with Heise and Yellowstone trends (Fig. 7a–c). Oxygen isotope values recovered by ~2–3‰ over a period of ~1 Myr, with the eruptions of Cougar Point Tuffs XI ($\delta^{18}O_{magma}$ = 2·6‰) and XIII ($\delta^{18}O_{magma}$ = 3·2‰), which is also consistent with Heise and Yellowstone trends (Fig. 7a–c). Cougar Point Tuff XV ($\delta^{18}O_{magma}$ = 1·1‰) and post-Cougar Point Tuff rhyolites ($\delta^{18}O_{magma}$ = 1·5–2·3‰) have $\delta^{18}O$ values that are ~2‰ depleted relative to Cougar Point Tuff XIII, and this too is consistent with the timing and magnitude of $\delta^{18}O$ depletions observed for the final low-$\delta^{18}O$ pulse of volcanism in the Heise and Yellowstone volcanic fields (Fig. 7a–c).

The search for normal-$\delta^{18}O$ rhyolite in the central SRP continues. We report here a new normal-$\delta^{18}O$ analysis for the Jarbidge rhyolite ($\delta^{18}O_{quartz}$ = 8·44‰), which is a 16·8–15·4 Ma large-volume lava unit (Coats *et al*., 1977) that preceded the earliest low-$\delta^{18}O$ rhyolites in the central SRP. Although the origin of this rhyolite is due to either the SRP plume volcanism or contemporaneous northern Nevada extension, the proximity of the Jarbidge rhyolite to the Bruneau–Jarbidge volcanic field (Fig. 1 inset) combined with its age and large volume make it comparable with other rhyolites in the SRP.

**Contemporaneous normal-$\delta^{18}O$ rhyolites of the Magic Reservoir Eruptive Center**

We report new oxygen isotopic and whole-rock chemical data (Table 5) for the 5·8–3 Ma Magic Reservoir eruptive center in central Idaho (Fig. 1 inset). This includes small-volume (<50 $km^3$) ash-flow tuffs and rhyolitic domes that erupted contemporaneously with the Heise volcanic field in eastern Idaho (Fig. 1 inset). Unlike Heise, this center does not exhibit multi-cyclic calderas, permitting an independent

**Table 5.** Locations, ages, oxygen isotopic compositions and whole-rock compositions of Magic Reservoir samples

| Sample: | 07MR-TF | 07MR-DM2 | 07MR-DM3 | 07MR-DM4 | 07MR-DM1b |
|---|---|---|---|---|---|
| Description: | young tuff | Moonstone young dome | Rattlesnake young dome | Dinosaur Ridge young dome | Willow Creek young dome |
| Latitude (°N): | 43·34 | 43·35 | 43·26 | 43·24 | 43·37 |
| Longitude (°W): | 114·40 | 114·46 | 114·35 | 114·34 | 114·57 |
| K–Ar age (Ma): | 5·6–4·8 | 3–4 | 3–4 | 3–4 | 3–4 |
| Av. Qtz $\delta^{18}O$ (‰): | 7·79 | 8·17 | 9·01 | 8·39 | 7·83 |
| Av. Qtz cores $\delta^{18}O$ (‰): | — | 8·04 | 8·78 | 8·59 | 8·56 |
| Magma (‰) (calc.): | 7·4 | 7·8 | 8·6 | 8·0 | 7·4 |
| *Major element analyses by XRF (wt %)* | | | | | |
| $SiO_2$ | 75·17 | 69·71 | 76·10 | — | — |
| $TiO_2$ | 0·26 | 0·69 | 0·06 | — | — |
| $Al_2O_3$ | 12·81 | 13·66 | 13·24 | — | — |
| FeO* | 2·00 | 4·59 | 1·33 | — | — |
| MnO | 0·04 | 0·08 | 0·04 | — | — |
| MgO | 0·15 | 0·43 | 0·00 | — | — |
| CaO | 0·80 | 2·24 | 0·30 | — | — |
| $Na_2O$ | 3·27 | 3·42 | 4·19 | — | — |
| $K_2O$ | 5·49 | 4·96 | 4·73 | — | — |
| $P_2O_5$ | 0·03 | 0·21 | 0·02 | — | — |
| *Trace element analyses by XRF (ppm)* | | | | | |
| Ba | 590 | 1906 | 19 | — | — |
| Rb | 309 | 103 | 455 | — | — |
| Sr | 71 | 217 | 6 | — | — |
| Zr | 299 | 713 | 136 | — | — |
| Y | 80 | 59 | 134 | — | — |
| Nb | 69 | 53 | 122 | — | — |
| Ga | 20 | 19 | 33 | — | — |
| Zn | 54 | 101 | 95 | — | — |
| Pb | 36 | 26 | 63 | — | — |
| La | 102 | 111 | 30 | — | — |
| Ce | 186 | 211 | 81 | — | — |
| Th | 40 | 13 | 57 | — | — |
| Nd | 69 | 79 | 29 | — | — |
| U | 12 | 2 | 20 | — | — |
| Ni | 0 | 0 | 0 | — | — |
| Cu | 5 | 7 | 0 | — | — |
| Cr | 3 | 3 | 1 | — | — |
| Sc | 4 | 7 | 1 | — | — |
| V | 8 | 20 | 6 | — | — |

Average $\delta^{18}O$ values for quartz (Qtz) and quartz cores. Quartz cores were obtained by air abrasion of whole quartz phenocrysts in a corundum mortar. Magma $\delta^{18}O$ values were calculated from quartz phenocryst analyses, with $\Delta^{18}O_{quartz–melt} = 0{\cdot}4‰$, applicable at liquidus temperatures of ~800°C (Bindeman & Valley, 2002). K–Ar ages are from Honjo *et al*. (1986). XRF data are normalized to 100% anhydrous with all Fe as FeO*.

assessment of contemporaneous rhyolitic magmatism of a different style in the SRP. Normal-$\delta^{18}O$ high-silica rhyolites of Magic Reservoir overlap the SRP continental crust in $SiO_2$–$\delta^{18}O$ composition, and in marked contrast to the Heise rhyolites, they span a much narrower $\delta^{18}O$ range within $SiO_2$–$\delta^{18}O$ compositional space (~1‰ vs ~4‰ for Heise) (Fig. 10a). The Sr and Nd isotope compositions of high-silica rhyolites of Magic Reservoir ($^{87}Sr/^{86}Sr = 0{\cdot}7109–0{\cdot}7242$, $^{143}Nd/^{144}Nd = 0{\cdot}51181–0{\cdot}51208$; W. P. Leeman, personal communication) indicate that they contain a significant component of Archean crust. The absence of low-$\delta^{18}O$ rhyolites in the Magic Reservoir eruptive center and the strongly radiogenic Sr and Nd isotope signatures of the Magic Reservoir rhyolites indicate partial melting of normal-$\delta^{18}O$ SRP Archean crust (Fig. 10b). By analogy with Yellowstone, the Magic Reservoir rhyolites define a normal-$\delta^{18}O$ extracaldera trend of magma evolution (Hildreth *et al*., 1991). This supports our view that large, multi-cyclic calderas, which are absent at Magic Reservoir but present at Heise and Yellowstone, are required for the generation of low-$\delta^{18}O$ rhyolites.

**Figure 10.** $\delta^{18}O_{magma}$–$SiO_2$ plots showing the variation of the Heise and Magic Reservoir rhyolite units in relation to the mantle, SRP continental crust, normal-$\delta^{18}O$ differentiation trends [black lines (sources: Matsuhisa, 1979; Sheppard & Harris, 1985; Harris *et al.*, 2000) and gray field labeled 'normal-$\delta^{18}O$ array' (source: Bindeman *et al.*, 2004)] (a), and isotopic mixing of normal-$\delta^{18}O$ and low-$\delta^{18}O$ source components (b). Labels for Heise units are as in Fig. 5. Labels for Magic Reservoir units: MYD, Moonstone young dome; RYD, Rattlesnake young dome; YT, young tuff. Low-$\delta^{18}O$ Heise magmas, which lie below the normal-$\delta^{18}O$ array (a), cannot be produced by isotopic mixing of normal-$\delta^{18}O$ mantle and crust components (b). Their formation requires remelting of hydrothermally altered portions of intracaldera rock from previous Heise eruptions, with an average $\delta^{18}O$ value of ~−1‰ (b). Mixing between mantle and low-$\delta^{18}O$ crust is not confirmed by geological or geochemical evidence, and thus is tentatively indicated with a gray dashed line (b).

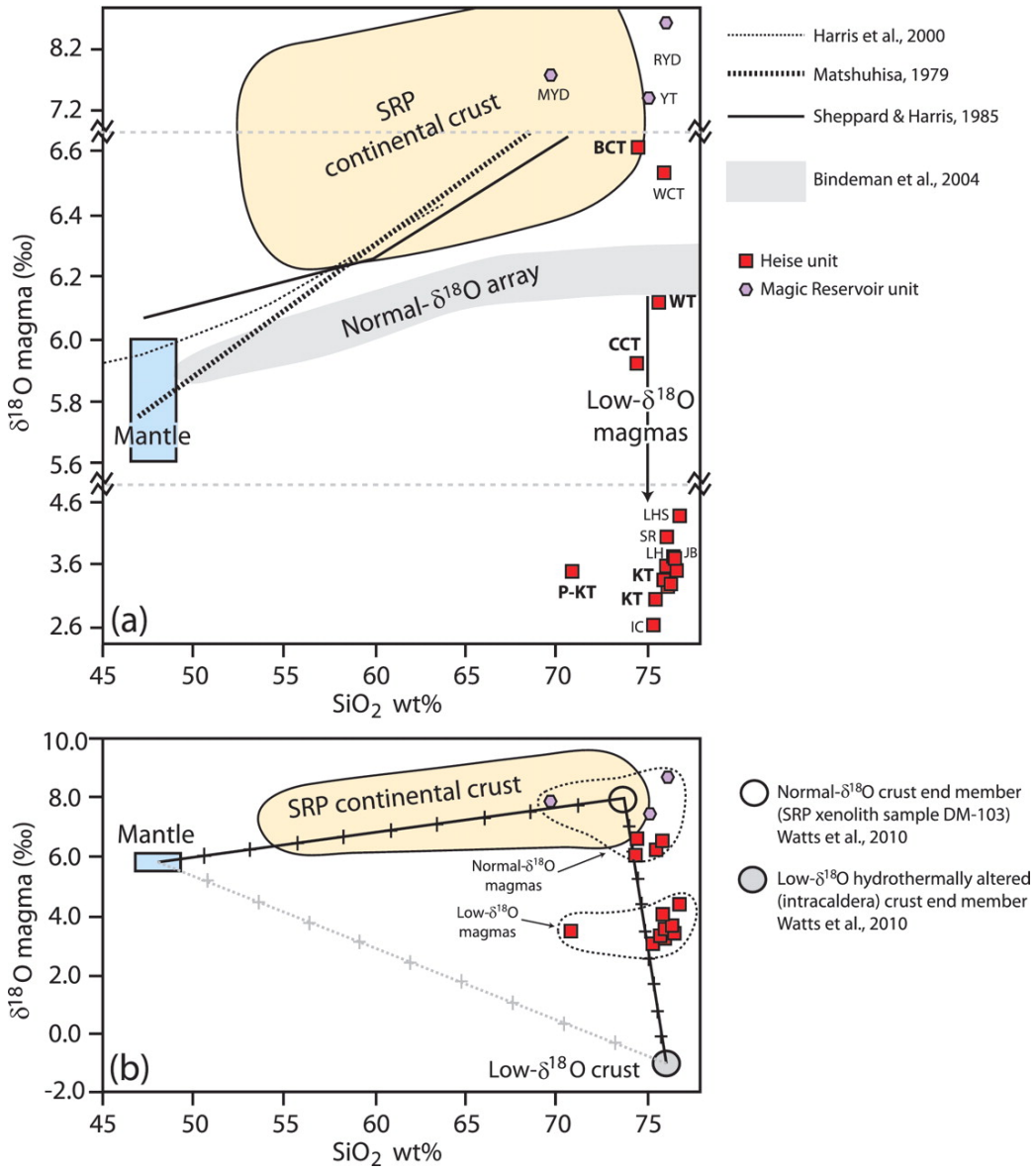

## STRONTIUM AND NEODYMIUM ISOTOPES

New Sr and Nd isotope data for 13 rhyolite samples (tuffs and lavas) of the Heise volcanic field are reported in Table 1. As the Heise rhyolites were derived by melting and hybridization of Archean crust by SRP basalt, they possess highly radiogenic $^{87}Sr/^{86}Sr$ and $^{143}Nd/^{144}Nd$ ratios that span large ranges ($^{87}Sr/^{86}Sr_i = 0{\cdot}70895–0{\cdot}71238$; $^{143}Nd/^{144}Nd = 0{\cdot}51214–0{\cdot}51233$) (Table 1; Fig. 11c and d). Successive normal-$\delta^{18}O$ Heise eruptions have $^{87}Sr/^{86}Sr$ ratios that progressively decrease and $^{143}Nd/^{144}Nd$ ratios that progressively increase (Fig. 11c and d). The trend is reversed with the eruption of the low-$\delta^{18}O$ Pre-Kilgore Tuff, which has $^{87}Sr/^{86}Sr$ and $^{143}Nd/^{144}Nd$ ratios that recover towards Blacktail Creek Tuff values (Fig. 11c and d). The low-$\delta^{18}O$ Kilgore Tuff samples have fairly constant $^{87}Sr/^{86}Sr$ and $^{143}Nd/^{144}Nd$ ratios, whereas the smaller-volume post-Kilgore rhyolites are more variable (Fig. 11c and d).

Whereas decreases in $^{87}Sr/^{86}Sr$ correspond to increases in $^{143}Nd/^{144}Nd$ in earlier Heise eruptions (6·62–4·87 Ma), we observe that for the Kilgore Tuff and post-Kilgore eruptive sequence (4·45–3·96 Ma), decreases in $^{87}Sr/^{86}Sr$ correspond to decreases in $^{143}Nd/^{144}Nd$ (Fig. 11c and d). Unlike the large variations in the Yellowstone tuffs (Fig. 11e and f), the magnitude of change of $^{87}Sr/^{86}Sr$ and $^{143}Nd/^{144}Nd$ ratios in the Kilgore and post-Kilgore eruptive sequence is small, and probably due to minor heterogeneities in the rhyolite reservoirs. Isotopic variations of Sr and Nd in the Heise rhyolites can be explained by binary mixing between Archean crust ($^{87}Sr/^{86}Sr \approx 0{\cdot}7388$, $^{143}Nd/^{144}Nd \approx 0{\cdot}5109$) and SRP basalts ($^{87}Sr/^{86}Sr \approx 0{\cdot}7063$, $^{143}Nd/^{144}Nd \approx 0{\cdot}5124$) in proportions of ~30–50% crust and ~50–70% basalt (McCurry & Rodgers, 2009; Watts *et al.*, 2010). Similar crust–basalt mixing proportions are required for the Yellowstone and

**Figure 11.** Temporal variations of Sr and Nd isotope ratios in Bruneau–Jarbidge (a, b), Heise (c, d), and Yellowstone (e, f) rhyolites. Rhyolite unit labels are the same as in Fig. 7. Sr and Nd isotope data are from Bonnichsen et al. (2008) for Bruneau–Jarbidge rhyolites and Hildreth et al. (1991) and Vazquez & Reid (2002) for Yellowstone rhyolites (see Appendix Table B4). It should be noted that the magnitude of the temporal variations in the Sr and Nd isotope ratios of the Heise rhyolites is intermediate between those for the older Bruneau–Jarbidge volcanic field to the west and the younger Yellowstone Plateau volcanic field to the east (Fig. 1 inset). The Sheridan Reservoir rhyolite (SR; filled square) is included in Yellowstone panels (e) and (f) owing to its disparate age and isotopic composition relative to other Heise units (see text for more detail).

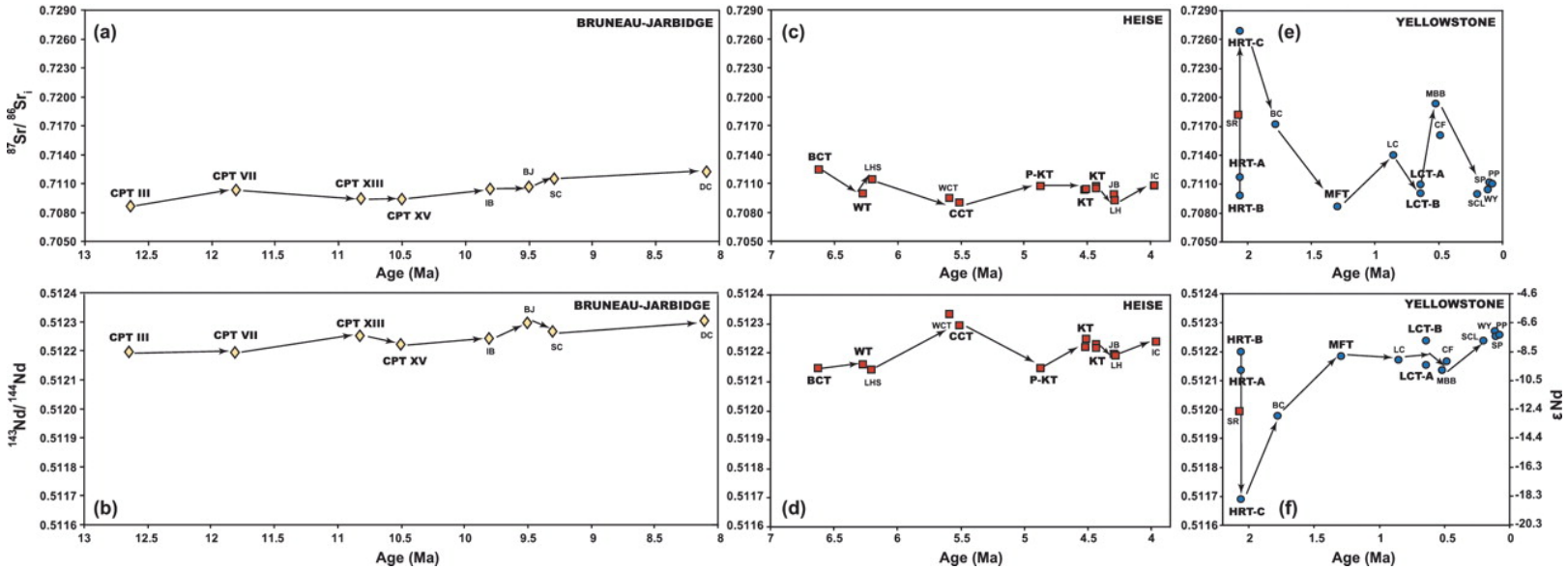

Bruneau–Jarbidge rhyolites, based on the observed isotopic ranges of Sr (0·7080–0·7140) and Nd (0·5121–0·5123) (Fig. 11a–f; Hildreth *et al*., 1991; Bonnichsen *et al*., 2008).

The magnitude of temporal variations in Sr and Nd isotope ratios in the Heise volcanic field is intermediate between those of the older, less heterogeneous Bruneau–Jarbidge volcanic field in the central SRP and the younger, more heterogeneous Yellowstone Plateau volcanic field in the eastern SRP (Fig. 11a–f). This probably reflects the transition into thicker and more strongly radiogenic Archean terrain as volcanism progressed from west to east across the North American craton (Fig. 1 inset). However, preservation bias cannot be ruled out, in which case younger (i.e. more easterly) caldera centers may be better preserved, and thus preserve more heterogeneity, than limited exposures in older parts of the SRP.

There is no correlation between the low $\delta^{18}O$ values and high $^{87}Sr/^{86}Sr$ ratios of the Heise rhyolites, precluding the role of low-$\delta^{18}O$/high $^{87}Sr/^{86}Sr$ hydrothermal brines in low-$\delta^{18}O$ rhyolite genesis in the Heise volcanic field (see Hildreth *et al*, 1991). Compared with the heterogeneity in Sr and Nd isotope ratios in major caldera-forming tuffs at Yellowstone (Huckleberry Ridge Tuff, Lava Creek Tuff), the Sr and Nd isotope ratios of the low-$\delta^{18}O$ Heise Kilgore Tuff are much more homogeneous (Fig. 11c–f). Low-$\delta^{18}O$ post-Kilgore rhyolites of the Heise volcanic field are also more homogeneous in Sr and Nd isotope ratios than low-$\delta^{18}O$ post-Lava Creek Tuff rhyolites of the Yellowstone Plateau volcanic field (Fig. 11c–f).

## MAGMATIC TEMPERATURES

Magmatic temperatures of most Heise rhyolites were within the range of 800–900°C, as determined by several independent methods (Table 1; Fig. 12). MELTS liquidus temperatures are the highest, with temperatures that are ~30° higher than zircon saturation temperatures (whole-rock) and ~80° higher than Ti-in-zircon temperatures for the same units (Fig. 12). In two cases (Conant Creek Tuff, Juniper Buttes), the Ti-in-zircon temperatures are significantly (~100–200°) lower than the calculated MELTS and zircon saturation temperatures (Fig. 12). This discrepancy is noted for many rhyolites

**Figure 12.** Magmatic temperatures of Heise rhyolites as determined by several independent methods (MELTS liquidus temperatures, zircon saturation temperatures, and Ti-in-zircon temperatures). Fe–Ti oxide temperatures from Henshaw (2002) are also included. Labels for Heise units correspond to those used in Fig. 5. Most Heise rhyolites had magmatic temperatures of ~800–900°C. The Pre-Kilgore Tuff (P-KT) had the highest magmatic temperature of ~950–1000°C. Magmatic temperature ranges for Yellowstone rhyolites (gray field) and Bruneau–Jarbidge rhyolites (diagonally shaded field) are shown for comparison.

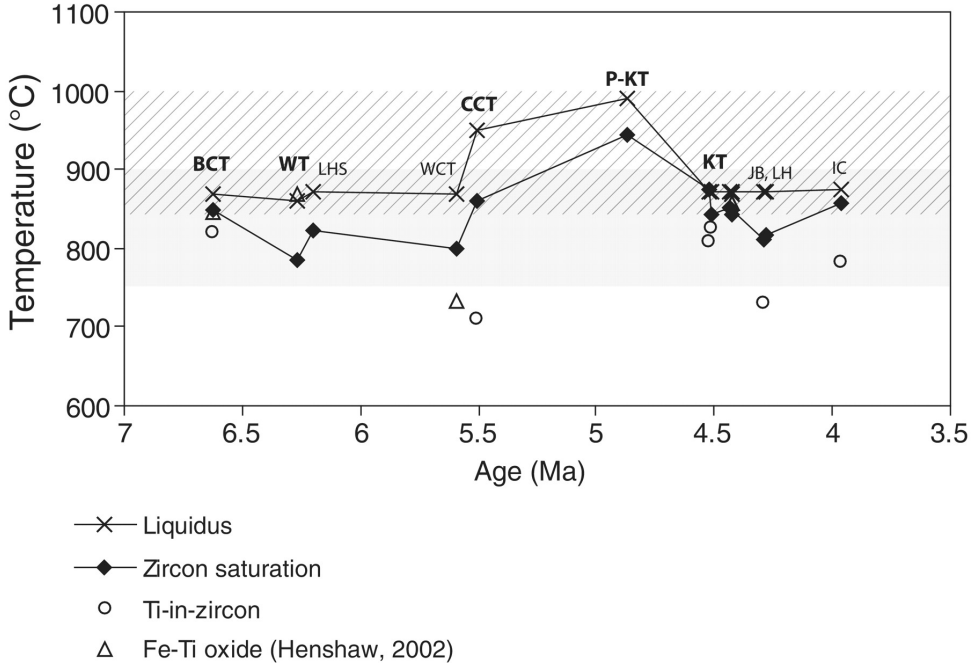

worldwide (Fu *et al*., 2008), and in the case of Heise may be due to uncertain Ti activities, as ilmenite and ulvöspinel compositions are not available for all units (see Wark *et al*., 2007). Our temperature estimates for the Heise rhyolites overlap eruption temperatures determined with the Fe–Ti oxide geothermometer of Ghiorso & Sack (1991) for the Heise Blacktail Creek Tuff, Walcott Tuff, Wolverine Creek Tuff and Kilgore Tuff (734–846°C; Henshaw, 2002; Fig. 12). Liquidus temperatures of Heise rhyolites (~800–900°C) are comparable with, and in some cases higher than, those of younger rhyolites erupted in the neighboring Yellowstone Plateau volcanic field (~750–900°C; Hildreth *et al*., 1984; Bindeman & Valley, 2001; Vazquez *et al*., 2009) and generally lower than the older rhyolites of the Bruneau–Jarbidge volcanic field (~850–1000°C; Cathey & Nash, 2004; Nash *et al*., 2006) (Fig. 12).

## DISCUSSION

The following discussion focuses on the origin of voluminous low-$\delta^{18}O$ rhyolite magmas, based on the example of the 1800 $km^3$ Kilgore Tuff of the Heise volcanic field. We address the following questions: (1) How were the normal-$\delta^{18}O$ Heise tuffs that predate the low-$\delta^{18}O$ Kilgore Tuff generated? (2) What is the origin of the Kilgore Tuff's unique low-$\delta^{18}O$ signature? (3) What model of magma genesis best satisfies all available data for the Kilgore Tuff? (4) How are the low-$\delta^{18}O$ Pre-Kilgore Tuff and post-Kilgore rhyolites related to the Kilgore Tuff? In answering these questions, we highlight key similarities in the pattern of low-$\delta^{18}O$ rhyolite magma genesis at Heise, Yellowstone and Bruneau–Jarbidge, and discuss the suitability of the 4·5 Ma Kilgore Tuff as an analog for the youngest phase of voluminous rhyolitic eruptions at Yellowstone. If our interpretation

for shallow (<10 km crustal depth) and rapid (tens to hundreds of thousands of years) generation of the largest-known low-$\delta^{18}O$ rhyolite in the world is correct, then it provides a compelling case for the occurrence of similar processes worldwide, which may or may not fingerprint eruptive products with the tell-tale low-$\delta^{18}O$ signatures. Our results would seemingly falsify conventional wisdom of slow magma genesis in the deeper crust and call for thermo-mechanical models to answer these questions.

**Normal-$\delta^{18}O$ magma genesis in the Heise volcanic field**

Rhyolitic volcanism in the Heise volcanic field began at 6·62 Ma with the 1200 $km^3$ caldera-forming eruption of the normal-$\delta^{18}O$ Blacktail Creek Tuff, which has a $SiO_2$–$\delta^{18}O$ composition that overlaps that of SRP continental crust (Fig. 10a and b) and a whole-rock normative composition that corresponds to the low-pressure (1–2 kbar) granite minimum in the Ab–Or–Qtz system (Fig. 5). It has the most radiogenic Sr isotope signature of all Heise units (Fig. 11c), indicating that it has the strongest affinity to SRP Archean crust. Its genesis can be explained by ~35% partial melting of SRP Archean crust, based on its near-eutectic granitic composition (Fig. 5) and trace element enrichments and depletions relative to the average upper continental crust composition of Taylor & McLennan (1985) and McLennan *et al*. (2006) (Appendix Table B6). Subsequent normal-$\delta^{18}O$ caldera-forming eruptions of the 750 $km^3$ Walcott Tuff at 6·27 Ma and the 300 $km^3$ Conant Creek Tuff at 5·51 Ma were ~0·5–0·7‰ lower in $\delta^{18}O$ than the Blacktail Creek Tuff, but still within the normal-$\delta^{18}O$ range for high-silica rhyolites (Figs 7b and 10a, b). These rhyolites maintain the same basic mineralogy (± quartz), mineral chemistry, and whole-rock major element geochemistry as the Blacktail

Creek Tuff (Tables 1–3), but define a divergent temporal compositional trend in trace element concentrations of Ba, Y, Nb, La, Ce and Nd (Table 3), Rb/Sr, Rb/Ba, Zr/Nb, La/Nb and Ce/Nb trace element ratios (Fig. 6a–e), and $^{87}Sr/^{86}Sr$ and $^{143}Nd/^{144}Nd$ ratios (Fig. 11c and d).

The data support derivation of the normal-$\delta^{18}O$ Blacktail Creek Tuff, Conant Creek Tuff and Walcott Tuff from a common rhyolitic magma source that was assembled from large-degree (~35%) partial melts of normal-$\delta^{18}O$ SRP crust (Appendix Table B6). Fractional crystallization of ~10–15%, involving plagioclase, clinopyroxene and zircon, of such a magma source can explain the variations in trace element concentrations in these successive caldera-forming eruptions (Appendix Table B5). Because there were 350–760 kyr time gaps between successive eruptions, we do not envision a continuous liquid line of descent from a single magma reservoir, but rather a scenario in which the residual magma was periodically cooled below the solidus and reactivated by fresh injections of basalt, yielding large-volume normal-$\delta^{18}O$ tuffs over the course of ~1 Myr that retain evidence of a common lineage. We do not attempt to determine whether the reservoir remained in a mushy state (Bachmann & Bergantz, 2004) or was produced by periodic underplating by SRP basalt (Leeman *et al*., 2008; McCurry & Rodgers, 2009). However, the high magmatic temperatures of the Heise rhyolites contradict derivation from a near-solidus mush, which would be expected to have temperatures less than 800°C. The progressive decrease in $^{87}Sr/^{86}Sr$ and increase in $^{143}Nd/^{144}Nd$ in normal-$\delta^{18}O$ Heise tuffs may be due to a greater basalt versus crust contribution through time, as periodic injections of basalt accrued in the normal-$\delta^{18}O$ crustal block.

## Low-$\delta^{18}O$ Kilgore Tuff magma genesis

### *Origin of the low-$\delta^{18}O$ signature of the Kilgore Tuff*

The low-$\delta^{18}O$ magmatic values (3·2–3·6‰) of the voluminous Kilgore Tuff require that a significant proportion of its oxygen was derived from low-$\delta^{18}O$ meteoric waters (e.g. Friedman *et al*., 1974; Hildreth *et al*., 1984; Taylor, 1986). Direct exchange with meteoric water diffusing into the melt is an unrealistic scenario given the slow rate of water diffusion into silicic melts and the large amounts of dissolved water (tens of per cent) required to generate O isotope depletions of this magnitude (e.g. Taylor, 1986). Syneruptive exchange between magmas and low-$\delta^{18}O$ crust (e.g. Garcia *et al*., 1998) is also unlikely owing to the $\delta^{18}O$ homogeneity of the Kilgore Tuff and the fact that it contains tuff and sandstone lithic fragments that are normal–high-$\delta^{18}O$ (Fig. 3). The possibility of a low-$\delta^{18}O$ source, such as the Idaho Batholith (e.g. Boroughs *et al*., 2005), is not likely given the fact that all crustal xenoliths and basalts analyzed in the eastern SRP have normal-$\delta^{18}O$ signatures (Hildreth *et al*., 1984; Watts *et al*., 2010). The time-progressive depletion in $\delta^{18}O$ (Fig. 7b) indicates that a process fundamental to the evolution of the Heise volcanic field is key to the genesis of the large-volume low-$\delta^{18}O$ Kilgore Tuff.

### *Correlation between cumulative eruptive volumes and low-$\delta^{18}O$ signatures*

Oxygen is the most abundant element in the Earth's crust and mantle, and thus it is useful to consider the correlation between cumulative eruptive volumes and magmatic $\delta^{18}O$ signatures when assessing rhyolite genesis from crustal and mantle sources. A linear least-squares regression line fit to 16 Heise units for $\delta^{18}O$ versus cumulative eruptive

volume demonstrates a strong negative correlation between the two parameters, with an $R^2 = 0{\cdot}86$ (Fig. 13a). We assume that (1) the erupted rhyolite volumes correspond to similar erupted/intrusive proportions for each tuff, and (2) the magnitude and direction of error in the volume estimates is comparable. Operating under these assumptions, the equation of the line of best fit can be used to predict $\delta^{18}O$ values for a given cumulative eruptive volume. Increments of 1000 $km^3$ decrease the $\delta^{18}O$ value by ~1‰, with cumulative eruptive volumes of 1000 $km^3$, 2000 $km^3$, 3000 $km^3$, and 4000 $km^3$ corresponding to $\delta^{18}O$ values of *c*. 7‰, 6‰, 5‰, and 3–4‰, respectively (Fig. 13a and c).

The data support a systematic progression of shallow crustal recycling in Heise rhyolite genesis, whereby progressively larger proportions of shallow, hydrothermally altered (low-$\delta^{18}O$) crust are tapped in successive rhyolite eruptions. High-temperature oxygen isotope exchange between normal-$\delta^{18}O$ rocks (>6‰) and low-$\delta^{18}O$ Heise meteoric waters (<–10‰) creates hydrothermally altered low-$\delta^{18}O$ rock reservoirs, which upon remelting yield low-$\delta^{18}O$ magmas. Caldera-forming eruptions facilitate this process; pervasive fracturing of the crust during caldera collapse generates conduits for meteoric fluid flow, and thus the development of a hydrothermal system, and vertical downdrop of the caldera floor brings hydrothermally altered intracaldera and subcaldera rocks closer to the underlying heat source for remelting (e.g. Bindeman & Valley, 2001; Bindeman *et al*., 2007). This effect is amplified in a nested caldera environment, as it results in maximum fracturing and vertical drawdown. Low-$\delta^{18}O$ Kilgore cycle magmas ($\delta^{18}O$ of ~3–4‰), which erupted after three overlapping caldera collapses and ~2000 $km^3$ of erupted rhyolite, signify the terminal stage of rhyolite genesis from the crustal block.

**Figure 13.** Magmatic $\delta^{18}O$ vs cumulative eruptive volume. (a) Linear least-squares regression lines for Heise (continuous line; $n = 16$) and Yellowstone (dashed line; $n = 17$) rhyolites show a trend of decreasing $\delta^{18}O$ with cumulative eruptive volume. Magmatic $\delta^{18}O$ values and eruptive volumes for the Heise units are shown in Table 1. Data for Yellowstone units are synthesized from Hildreth *et al*. (1984), Bindeman & Valley (2001), Christiansen (2001), Christiansen *et al.* (2007) and Bindeman *et al*. (2008) (see Appendix Table B4). (b) A linear least-squares regression line for Bruneau–Jarbidge (dashed line) rhyolites shows no trend between $\delta^{18}O$ and cumulative eruptive volume. Magmatic $\delta^{18}O$ values and eruptive volumes for Bruneau–Jarbidge units are synthesized from Bonnichsen *et al*. (2008), Leeman *et al*. (2008), and B. Ellis (unpublished) (see Appendix Table B4). (c) Schematic depiction of the crustal block in the eastern Snake River Plain (after Peng & Humphreys, 1998) showing the Heise–Yellowstone trend of decreasing magmatic $\delta^{18}O$ with cumulative eruptive volume. Magmatic $\delta^{18}O$ values are lowered by ~1‰ for every 1000 $km^3$ of erupted rhyolite.

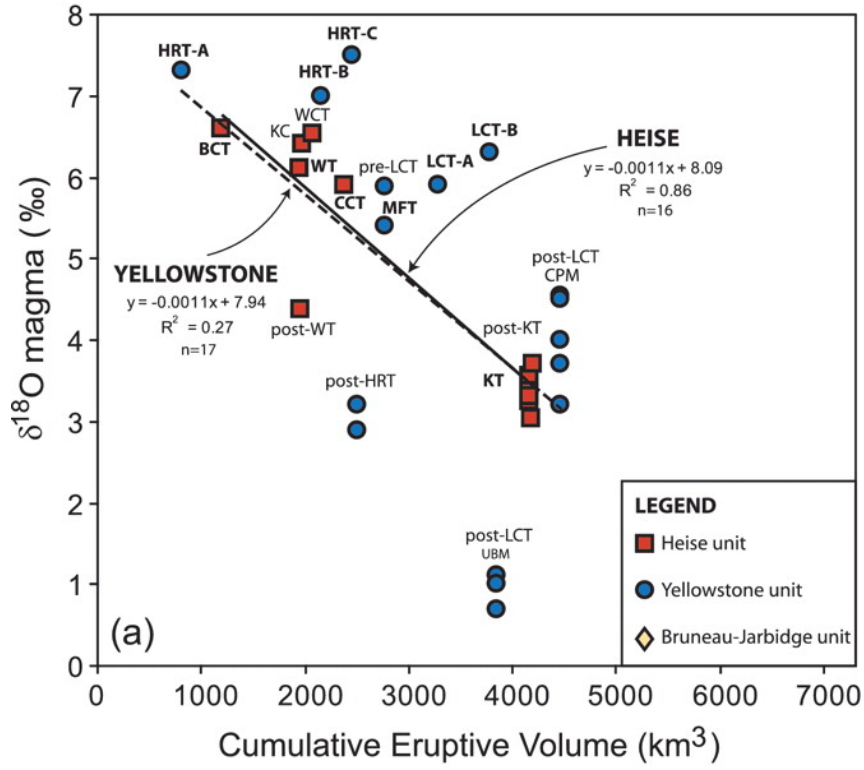
HRT-A
HRT-C
HRT-B
WCT
KC
BCT
WT
pre-LCT
LCT-A
LCT-B
CCT
MFT
HEISE
y = -0.0011x + 8.09
R2 = 0.86
n=16
YELLOWSTONE
y = -0.0011x + 7.94
R2 = 0.27
n=17
post-WT
post-LCT
CPM
post-KT
KT
post-HRT
post-LCT
UBM
LEGEND
Heise unit
Yellowstone unit
Bruneau-Jarbidge unit
(a)
δ18O magma (‰)
Cumulative Eruptive Volume (km3)

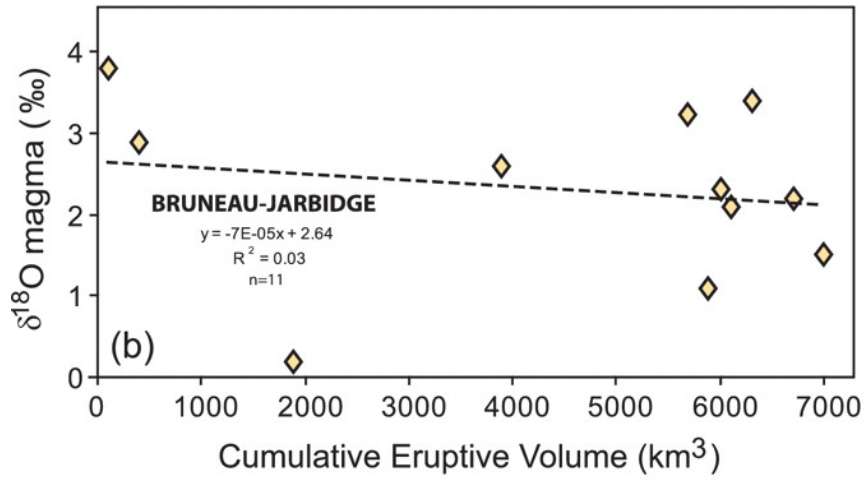
BRUNEAU-JARBIDGE
y = -7E-05x + 2.64
R2 = 0.03
n=11
(b)
δ18O magma (‰)
Cumulative Eruptive Volume (km3)

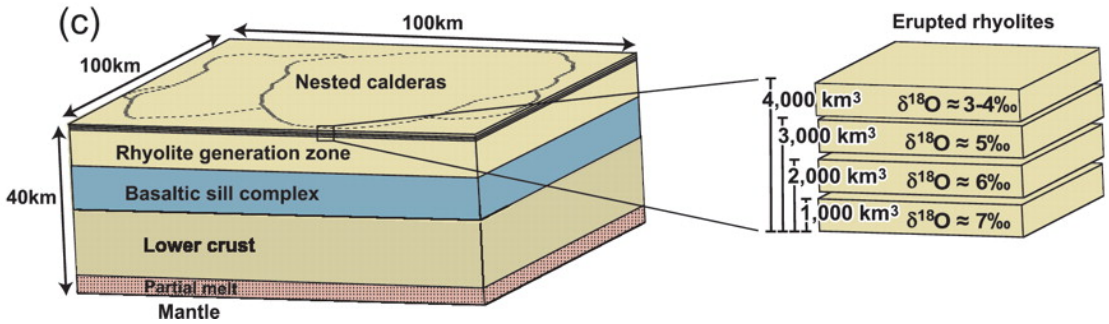
(c)
100km
100km
Nested calderas
Rhyolite generation zone
Basaltic sill complex
Lower crust
Partial melt
Mantle
40km
Erupted rhyolites
4,000 km3 δ18O ≈ 3-4‰
3,000 km3 δ18O ≈ 5‰
2,000 km3 δ18O ≈ 6‰
1,000 km3 δ18O ≈ 7‰

Like that observed for Heise, a trend of decreasing $\delta^{18}O$ with cumulative eruptive volume is evident for the Yellowstone rhyolite units (Fig. 13a). A linear least-squares regression line fit to 17 Yellowstone units yields a nearly identical equation to the one derived for Heise data, though the $R^2$ value is less robust owing to the greater spread in Yellowstone $\delta^{18}O$ data (Fig. 13a). Greater spread in the Yellowstone data is attributed to Pleistocene glaciations that generated significant (negative) torque on the oxygen isotopic values of Yellowstone magmas (Hildreth *et al*., 1984). In contrast, the isotopic compositions of the Miocene–Pliocene Heise magmas were probably not affected by glaciations. Post-Lava Creek Tuff Central Plateau Member units have $\delta^{18}O$ values that overlap those of the Kilgore Tuff and post-Kilgore units ($\delta^{18}O$ of ~ 3–4‰) for essentially the same cumulative eruptive volumes (4470 $km^3$ for Yellowstone versus 4200 $km^3$ for Heise), providing evidence that they represent a terminal stage of rhyolite generation analogous to the final Kilgore cycle of the Heise volcanic field (Fig. 13a and c).

Bruneau–Jarbidge units do not reveal a trend of decreasing $\delta^{18}O$ with cumulative eruptive volume, as observed for the younger and better exposed Heise and Yellowstone units (Fig. 13b). One obvious explanation for the lack of a trend in the Bruneau–Jarbidge units is that eruptive volumes, unit designations, and correlations are poorly defined as a result of erosion and burial by younger units (Bonnichsen *et al*., 2008). Because eruptions in the Bruneau–Jarbidge volcanic field are exclusively low-$\delta^{18}O$ ($\delta^{18}O$ of ~0–4‰), it may be most instructive to compare them with the final stage of low-$\delta^{18}O$ eruptions at Heise (Kilgore Tuff and post-Kilgore units) and Yellowstone (post-Lava Creek Tuff units). For instance, if eruptions were to continue at Heise and Yellowstone beyond 4200 $km^3$ and 4470 $km^3$, it is conceivable that the linear trends would flatten at some critical stage of

$\delta^{18}O$ depletion, owing to the limitations of oxygen isotope exchange in shallow crustal conditions (e.g. Taylor, 1986). It may be that the extremely low-$\delta^{18}O$ values of the majority of Bruneau–Jarbidge rhyolites ($\delta^{18}O$ of ~0–3‰) represent this critical threshold. We do not exclude the possibility that normal-$\delta^{18}O$ eruptions, like the Jarbidge rhyolite (see 'Oxygen isotopes' section), preceded the low-$\delta^{18}O$ Bruneau–Jarbidge eruptions. The presence of normal-$\delta^{18}O$ zircons in low-$\delta^{18}O$ Cougar Point Tuff units (Cathey *et al*., 2008) may be indicative of such a scenario.

### *The Blacktail Creek Tuff: Source of the low-$\delta^{18}O$ Kilgore Tuff*

Based on the new evidence presented in this work, we suggest that the Kilgore Tuff was derived from remelting hydrothermally altered (low-$\delta^{18}O$) volcanic and intrusive portions of the massive Blacktail Creek Tuff, which would have been the deepest, and thus closest to the underlying basaltic heat source, after three prior overlapping caldera-forming eruptions (Fig. 14a–d). This would allow the Kilgore Tuff to maintain the same basic mineralogy (Table 2), mineral chemistry (Table 2), normative composition and phase relations (Fig. 5) as the Blacktail Creek Tuff, but possess a lower $\delta^{18}O$ signature owing to the $^{18}O$ depletion of the Blacktail Creek Tuff protolith. Our observation that the final low-$\delta^{18}O$ Kilgore Tuff cycle magmas define a reversal from the evolutionary trend of earlier tuff eruptions (Blacktail Creek, Walcott, Conant Creek) back towards the Blacktail Creek Tuff composition in trace element concentrations of Ba, Y, Nb, La, Ce and Nd, trace element ratios of Rb/Sr, Rb/Ba, Zr/Nb, La/Nb and Ce/Nb, and $^{87}Sr/^{86}Sr$ and $^{143}Nd/^{144}Nd$ isotope ratios, supports this hypothesis (Figs 6a–e and 11c, d). Further supporting evidence is the presence of twinned clinopyroxene crystals, which are

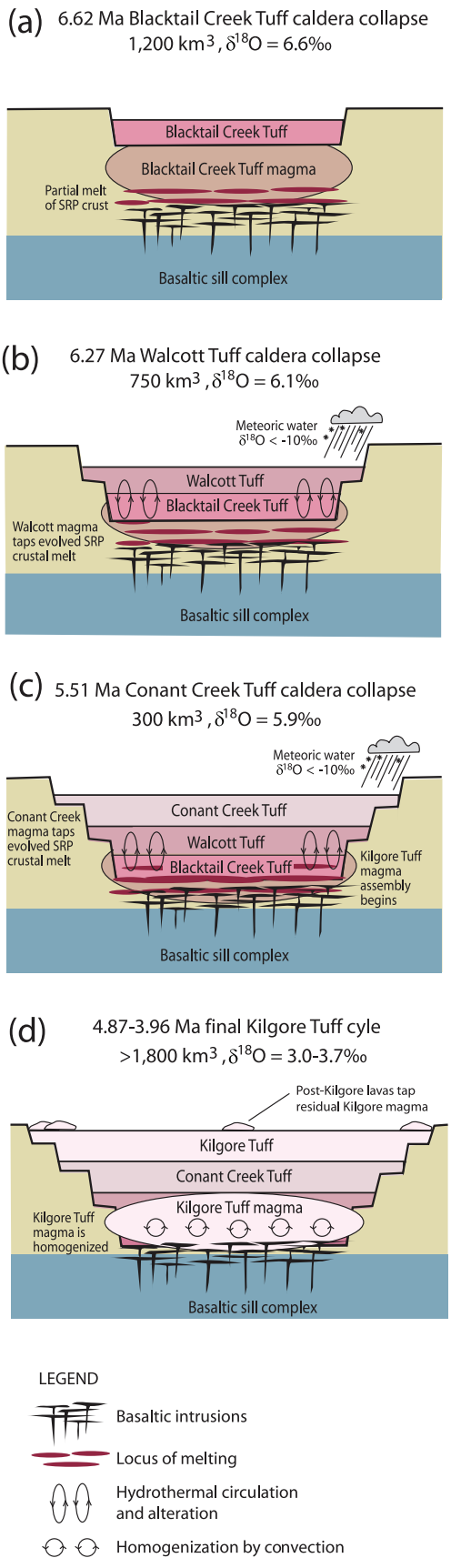


**Figure 14.** Schematic model of rhyolite genesis in the Heise volcanic field. (a) Blacktail Creek Tuff magma assembles from partial melts of normal-$\delta^{18}O$ Snake River Plain (SRP) crust induced by heating from basaltic intrusions in an underlying sill complex [seismically imaged by Peng & Humphreys (1998)]. Blacktail Creek Tuff caldera collapse accommodates the intracaldera fill. (b) Walcott Tuff magma taps evolved, normal-$\delta^{18}O$ SRP crustal melts. Walcott Tuff caldera collapse spatially overlaps the Blacktail Creek Tuff caldera, forming a nested caldera complex that brings intracaldera fill material closer to the underlying heat source. Meteoric waters penetrate shallow caldera fractures, leading to hydrothermal alteration of intracaldera fill by circulating fluids. (c) Conant Creek Tuff magma taps further evolved, normal-$\delta^{18}O$ SRP crustal melts. The slightly low-$\delta^{18}O$ signature of the Conant Creek Tuff magma (~0·1‰ depleted relative to normal-$\delta^{18}O$ rhyolites) can be explained by a minor contribution from hydrothermally altered (low-$\delta^{18}O$) materials. Conant Creek Tuff caldera collapse spatially overlaps the Blacktail Creek and Walcott calderas, resulting in maximum vertical drawdown of the intracaldera rocks. Assembly of the Kilgore Tuff magma begins when hydrothermally altered (low-$\delta^{18}O$) Blacktail Creek Tuff intracaldera rocks intercept the locus of melting above the basaltic sill complex. (d) Kilgore Tuff magma is homogenized as melt pockets coalesce on a large scale to form a voluminous low-$\delta^{18}O$ magma body, ~3‰ depleted relative to the normal-$\delta^{18}O$ rhyolites. Post-Kilgore lavas tap residual low-$\delta^{18}O$ Kilgore Tuff magma, and erupt along the ring fracture zone and as domes in the center of the Kilgore caldera.

observed only in samples of the Blacktail Creek Tuff and Kilgore Tuff (Fig. 4g and h), and the presence of normal-$\delta^{18}O$ tuff lithic fragments within a low-$\delta^{18}O$ Kilgore Tuff vitrophyre (Fig. 3) that match the $\delta^{18}O$ composition of the Blacktail Creek Tuff ($\delta^{18}O \approx 7‰$) (Fig. 7b).

Assuming a 1·5 kJ $kg^{-1}$ $K^{-1}$ heat capacity for basalt (Snyder, 2000), 750°C cooling of basalt from ~1250°C liquidus to 500°C ambient temperature, and a 400 kJ $kg^{-1}$ latent heat of crystallization (Grunder, 1995), the heat contribution to the shallow crust from basalt is estimated to be *c*. 1500 kJ $kg^{-1}$. The heat required to melt glassy, high-silica rhyolite would be *c*. 500 kJ $kg^{-1}$, based on a 1·3 kJ $kg^{-1}$ $K^{-1}$ heat capacity of rhyolite (Snyder, 2000), 350°C heating of rhyolite from 500°C ambient temperature to 850°C liquidus, and negligible latent heat of fusion. With a basalt heat transfer efficiency of 20–40% (Dufek & Bergantz, 2005), a basalt volume of ~1–2 times the volume of rhyolite is required. Thus, at high (e.g. Hawaiian) basalt production rates of 0·01 $km^3$ $a^{-1}$, *c*. 100–300 kyr would be necessary to generate the voluminous 1800 $km^3$ Kilgore Tuff by remelting intracaldera portions of the Blacktail Creek Tuff.

### *Achieving homogeneity in the Kilgore Tuff*

Homogeneity in $\delta^{18}O$ values, $^{87}Sr/^{86}Sr$ and $^{143}Nd/^{144}Nd$ ratios, liquidus temperatures and U–Pb zircon ages of samples erupted >100 km apart indicates that the Kilgore Tuff was derived from an extremely voluminous, homogeneous magma chamber. Rather than remelting of an isotopically homogeneous reservoir of low-$\delta^{18}O$ source rocks, it is much more likely that the Kilgore Tuff was incrementally assembled from isotopically heterogeneous batches of melt, generated from remelting of isotopically

heterogeneous source rocks altered by variable water–rock ratios. Ion probe oxygen isotope analyses of single Kilgore Tuff zircons, which are heterogeneous within a low-$\delta^{18}O$ range of *c*. –1 to 3‰ (Fig. 8), support this interpretation. We envision a large subcaldera magma source region (probably >6000 $km^2$ based on the footprint of the Kilgore caldera), in which the primary isotopic heterogeneities of the original protoliths, and secondary heterogeneities resulting from their subsequent alteration, were averaged on a caldera-wide scale. Batches of heterogeneous melt aggregated to form a single well-mixed convecting magma body with a homogeneous geochemical and isotopic composition (Fig. 14c and d). Only refractory zircon phenocrysts retain evidence of this batch assembly process, whereas the less refractory phenocryst phases and host glass were completely reset. Given the fact that the U–Pb ages of single zircons with variable $\delta^{18}O$ values all overlap within an ~300–400 kyr error (Fig. 8), this batch assembly process occurred relatively rapidly.

***The Pre-Kilgore Tuff and Post-Kilgore rhyolites***

The Pre-Kilgore Tuff is tens to hundreds of thousands of years older than the Kilgore Tuff, as indicated by multiple stratigraphic time breaks within ~11 m of section that separate it from the Kilgore Tuff (Fig. 3) and its U–Pb zircon crystallization age of 4·87 Ma (versus 4·58 Ma for the Kilgore Tuff). However, the Pre-Kilgore Tuff has a magmatic $\delta^{18}O$ signature (3·5‰) that is identical to that of the low-$\delta^{18}O$ Kilgore Tuff cycle, and all analyzed phenocryst phases in the Pre-Kilgore Tuff are within the $\delta^{18}O$ range of Kilgore Tuff phenocrysts (Figs 7b and 8), indicating that it is probably a genetically related precursor of the Kilgore Tuff. Sr isotope ratios provide additional

evidence for this genetic link (Fig. 11c), and although the $^{143}Nd/^{144}Nd$ ratio of the Pre-Kilgore Tuff is lower than that of the Kilgore Tuff (Fig. 11d), variations of the observed magnitude are not uncommon for different members of large tuff units (see Hildreth *et al*., 1991; Fig. 11f). The magmatic temperature of the Pre-Kilgore Tuff (~950–1000°C) was ~100°C higher than the other Heise rhyolites, and may represent a hot, initial phase of Kilgore Tuff genesis in which low-$\delta^{18}O$ melt pockets were beginning to accrete on a large scale.

Post-Kilgore rhyolites have U–Pb zircon crystallization ages that overlap those of the Kilgore Tuff and low-$\delta^{18}O$ oxygen isotope signatures between 3·0 and 3·7‰ that are identical to those of the Kilgore Tuff (Table 1; Fig. 7b), indicating that they were probably derived from residual low-$\delta^{18}O$ Kilgore Tuff magma (Fig. 14d). Additional evidence of their common heritage includes their more evolved major element compositions (Table 3), similar Ab–Or–Qtz normative compositions (Fig. 5), similar concentrations of trace elements (Table 3), nearly identical $^{87}Sr/^{86}Sr$ and $^{143}Nd/^{144}Nd$ ratios (Fig. 11c and d), and common liquidus temperatures of ~850–870°C (Table 1). We also observe that all Kilgore and post-Kilgore samples contain glomerocrystic clusters of plagioclase, orthopyroxene and clinopyroxene (Fig. 4c–f), which are absent in other Heise units. U–Pb zircon dating of the 3·96 Ma Indian Creek rhyolite shows that it has inherited zircon cores that are the same age as the Kilgore Tuff (4·46 Ma), establishing a possible genetic link between them (Table 1). About 10% fractional crystallization of the less evolved Pre-Kilgore Tuff magma reservoir would have been required to generate the more evolved Kilgore Tuff and post-Kilgore rhyolites (Appendix Table B5).

**Systematic pattern of low-$\delta^{18}O$ rhyolite genesis at Heise, Yellowstone and Bruneau–Jarbidge**

Key similarities exist between the Heise, Yellowstone Plateau and Bruneau–Jarbidge volcanic fields, and the Kilgore Tuff serves as an important bridging link between them. When looking at trends in magmatic $\delta^{18}O$ through time, a few striking features are apparent in all three volcanic fields: (1) after the first 1–2 caldera collapse events the oxygen isotope trend plunges sharply by ~3–4‰; (2) over the next ~1 Myr of caldera-forming eruptions the oxygen isotope signatures rebound by ~2–3‰; (3) in the final pulse of volcanism the ~2–3‰ recovery is reversed and the low-$\delta^{18}O$ signature re-emerges (Fig. 7a–c). The Kilgore Tuff of the Heise volcanic field is an explosive low-$\delta^{18}O$ tuff, like the Cougar Point tuffs in the Bruneau–Jarbidge volcanic field, but it was erupted after a series of normal-$\delta^{18}O$ tuffs, like the low-$\delta^{18}O$ rhyolite lavas of the Yellowstone Plateau volcanic field. The magnitude and timing of the $\delta^{18}O$ depletions are comparable in all three volcanic fields, but the oscillations are within a ~0–4‰ range at Bruneau–Jarbidge, a ~3–7‰ range at Heise and a ~0–8‰ range at Yellowstone (Fig. 7a–c).

In addition to a progressive transition in O isotope compositions, a transition in Sr and Nd isotope compositions is also apparent in the three volcanic fields. Heterogeneity in Sr and Nd isotope ratios increases from west to east (Fig. 11a–f), probably as a result of changes in the composition of the crust, from thinner and less radiogenic crust in the central SRP to thicker, more radiogenic and more refractory crust in the eastern SRP (see Leeman *et al*., 1992; Manduca *et al*., 1992; Nash *et al*., 2006). Consequently, the nature (e.g. depth, magnitude, frequency) of large silicic caldera-forming eruptions, and in turn,

the style of low-$\delta^{18}O$ rhyolite genesis, varies in a systematic way. Thinner, less refractory crust provides a significant thermal advantage over thick, refractory crust in the formation of shallow crustal melts by heating induced by mantle-derived basalt (e.g. Manea *et al*., 2009); consequently, the number of caldera-forming eruptions is higher in regions of thinner crust (Nash *et al*., 2006; Bonnichsen *et al*., 2008; Leeman *et al*., 2008). Frequent, overlapping caldera-forming eruptions promote large-scale fracturing of the crust and the development of a pervasive hydrothermal system early in the lifespan of a volcanic field. Thus, at Bruneau–Jarbidge, low-$\delta^{18}O$ rhyolite genesis may have happened essentially instantaneously owing to the high frequency of hot, spatially overlapping caldera-forming eruptions at the onset of volcanism, whereas at Heise and Yellowstone, preconditioning of the much thicker, more refractory crust over a ~2 Myr period was required before low-$\delta^{18}O$ rhyolites dominated.

***The Kilgore Tuff: an analog for Quaternary rhyolite eruptions at Yellowstone***

The low-$\delta^{18}O$ Kilgore Tuff has many similarities to the 0·26–0·08 Ma Central Plateau Member rhyolites of the Yellowstone Plateau volcanic field, and thus may serve as their analog. Like the Kilgore Tuff, Central Plateau Member rhyolites erupted after three prior caldera-forming eruptions (~2 Myr after the initiation of volcanism) and are characterized by low $\delta^{18}O$ values that are ~3‰ depleted relative to normal-$\delta^{18}O$ tuffs (Fig. 7a and b). Both the Kilgore Tuff and Central Plateau Member rhyolites are extremely voluminous, ~1800 $km^3$ and ~620 $km^3$, respectively, but differ in the fact that the Kilgore Tuff is an explosive caldera-forming tuff and the Central Plateau Member rhyolites are mostly effusive post-caldera lavas. Rhyolites of the Heise and Yellowstone

Plateau volcanic fields define a negative correlation between $\delta^{18}O$ values and cumulative eruptive volumes, with the Kilgore Tuff and Central Plateau Member rhyolites corresponding to ~4000–4500 $km^3$ of erupted rhyolite, and heralding the terminal stages of rhyolite generation in each volcanic field (Fig. 13a).

In our preferred model of low-$\delta^{18}O$ rhyolite genesis, the evolution from normal-$\delta^{18}O$ to low-$\delta^{18}O$ rhyolites is an expected consequence of large-volume silicic magmatism in nested caldera complex settings, in which each successive caldera-forming eruption displaces material from the crustal block and accommodates vertical downdrop of shallow, hydrothermally altered ($^{18}O$ depleted) intracaldera rock for remelting (Fig. 14a–d; Bindeman & Valley, 2001; Bindeman *et al*., 2007; Watts *et al*., 2010). Whereas the low-$\delta^{18}O$ Kilgore Tuff was probably produced by batch assembly of pockets of melt from variably hydrothermally altered sources that were homogenized in a single, voluminous magma body, the Central Plateau Member rhyolites represent an intermediate stage of assembly, whereby both small and large pockets of melt erupted effusively prior to coalescing into a single magma chamber beneath the crust.

## CONCLUSIONS

The Kilgore Tuff is the largest-known low-$\delta^{18}O$ rhyolite yet discovered. U–Pb zircon ages, mineral chemistry, whole-rock major and trace element geochemistry, Sr and Nd isotope geochemistry, and magmatic temperatures corroborate oxygen isotopic evidence that the Kilgore Tuff erupted from an exceptionally large and homogeneous magma chamber. Extreme oxygen isotopic diversity of ~7‰ in single zircon crystals signifies batch assembly of variably $^{18}O$ depleted melts prior to homogenization of the

Kilgore Tuff magma on a caldera-wide scale. The data support derivation of the Kilgore Tuff magma by remelting and homogenization of variably hydrothermally altered intracaldera and subvolcanic portions of the Blacktail Creek Tuff, which would have been the deepest part of the subsided caldera fill and thus closest to the underlying heat source after three overlapping caldera collapses. Correlations between magmatic $\delta^{18}O$ signatures, eruption ages, and cumulative eruptive volumes at Heise and Yellowstone can be used to predict the Kilgore Tuff's appearance in the Heise volcanic field, and thus support our view that low-$\delta^{18}O$ rhyolite genesis is an expected outcome of caldera cluster evolution in the SRP. Our work further demonstrates that large volumes (thousands of $km^3$) of hot, crystal-poor rhyolitic magma can be generated by rapid remelting in the shallow crust. The Kilgore Tuff may be a useful analog for the most recent phase of rhyolitic eruptions at Yellowstone, and perhaps other large-volume rhyolites in nested caldera complexes around the world.

**BRIDGE**

In Chapter IV, I presented a detailed study of the Kilgore Tuff of the Heise volcanic field and synthesized Heise datasets with published datasets for Yellowstone and Bruneau-Jarbidge rhyolites. Chapter IV supported the rhyolite genesis models proposed in Chapters II and III, and provided the following new insights: 1) The Kilgore Tuff was derived from remelting of hydrothermally altered portions of the first normal-$\delta^{18}O$ Heise tuff, the Blacktail Creek Tuff; 2) The voluminous Kilgore magma body was assembled from heterogeneous batches of melt and homogenized on a caldera-wide (>100 km) scale within hundreds of thousands of years prior to eruption; 3) The Kilgore

Tuff is analogous to the youngest phase of low-$\delta^{18}O$ rhyolite eruptions at Yellowstone (Central Plateau Member rhyolites) based on timing, cumulative eruptive volume and magnitude of $\delta^{18}O$ depletion. In Chapter V, I extend my research to Central Plateau Member rhyolites with an isotope and geochronology study of individual phenocrysts. I synthesize new data with published isotopic, age and geochemical datasets to elucidate the processes by which Yellowstone's youngest (<0.64 Ma) rhyolites were generated.

# CHAPTER V

# YOUNG AND VOLUMINOUS RHYOLITES OF THE YELLOWSTONE CALDERA: AN ISOTOPE AND GEOCHRONOLOGY STUDY OF INDIVIDUAL PHENOCRYSTS REVEALS PROGRESSIVE HOMOGENIZATION OF AN EVOLVING MAGMA RESERVOIR

This chapter was prepared for submission to *Earth and Planetary Science Letters*. Coauthors Ilya Bindeman and Axel Schmitt provided funding for the project, guidance during analytical work, and editorial assistance. I performed the majority of the laboratory work and was the primary author.

## 1. Introduction

Large calderas are produced by catastrophic eruptions of silicic magma that drain huge (100s-1,000s of $km^3$) subcaldera magma reservoirs. The processes and time scales by which such large volumes of silicic magma are assembled in the shallow crust remains an outstanding petrological problem. The advent of microanalytical techniques that enable dating and isotopic measurements of individual crystals has shed new light on the complexities of magma genesis in caldera settings, and particularly the varied contributions of diverse crustal lithologies (e.g., Bacon and Lowenstern, 2005; Charlier et al., 2007; Simon et al., 2007; Watts et al., 2010). One prime example of a caldera complex that has produced large volumes of silicic magma with diverse age and isotopic signatures is the Yellowstone caldera in western Wyoming (Fig. 1). The high-latitude,

intracontinental position of the Yellowstone caldera makes it possible to resolve surface meteoric water signatures in the oxygen isotopic compositions of erupted rhyolites, and therefore fingerprint the uppermost (hydrothermally-altered) crust.

While it has long been recognized that large volumes (> 600 $km^3$) of rhyolite produced by the Yellowstone caldera have drastic depletions in $^{18}O$ that require significant involvement of meteoric water (Friedman et al., 1974; Hildreth et al., 1984; Taylor, 1986; Hildreth et al., 1991), the processes by which such depletions occurred were unclear until age and oxygen isotopic investigation of Yellowstone rhyolites on the single crystal scale (Bindeman and Valley, 2000, 2001; Bindeman et al., 2001). Earlier interpretations included direct influx of meteoric waters into silicic magmas (Hildreth et al., 1984) or assimilation of wall rocks altered by hydrothermal (meteoric) fluids (Hildreth et al., 1991). As addressed by Bindeman and Valley (2000, 2001), each of these schemes is unrealistic based on heat and mass-balance constraints. Individual zircon crystals from early erupted post-caldera rhyolites of the Yellowstone caldera (Upper Basin Member rhyolites) contain unequivocal age and oxygen isotopic evidence for inheritance from specific volcanic protoliths, supporting a magma genesis model of wholesale remelting of hydrothermally altered intracaldera blocks (Bindeman et al., 2008).

Unique low-$\delta^{18}O$ signatures indicate that Upper Basin Member rhyolites were generated by spatially discrete episodes of remelting, which yielded independent parcels of variably $^{18}O$-depleted melts (Bindeman et al., 2008). This study builds on these and other previous results by presenting new age and oxygen isotope data obtained by ion microprobe for individual zircons of the youngest erupted post-caldera rhyolites of the

**Figure 1.** Map showing the distribution of post-Lava Creek Tuff rhyolites in the Yellowstone caldera. The geologic map of Christiansen (2001) was used to define unit boundaries. The Central Plateau Member units analyzed in this study are indicated by the bold labels. Squares mark our sampling localities. The locations of the Biscuit Basin rhyolite flows, including North Biscuit Basin (NBB), Middle Biscuit Basin (MBB), South Biscuit Basin (SBB) and East Biscuit Basin (EBB) are also shown. NBB and SBB are Central Plateau Member units, whereas MBB and EBB are Upper Basin Member units (see text for more detail). Stars mark the inferred vent sources for individual Central Plateau Member rhyolite eruptions (Christiansen, 2001). The Yellowstone caldera margin (bold line) and resurgent dome margins (dashed lines) are taken from Christiansen (2001) and Christiansen et al. (2007). The inset shows the map location in the western U.S.A.

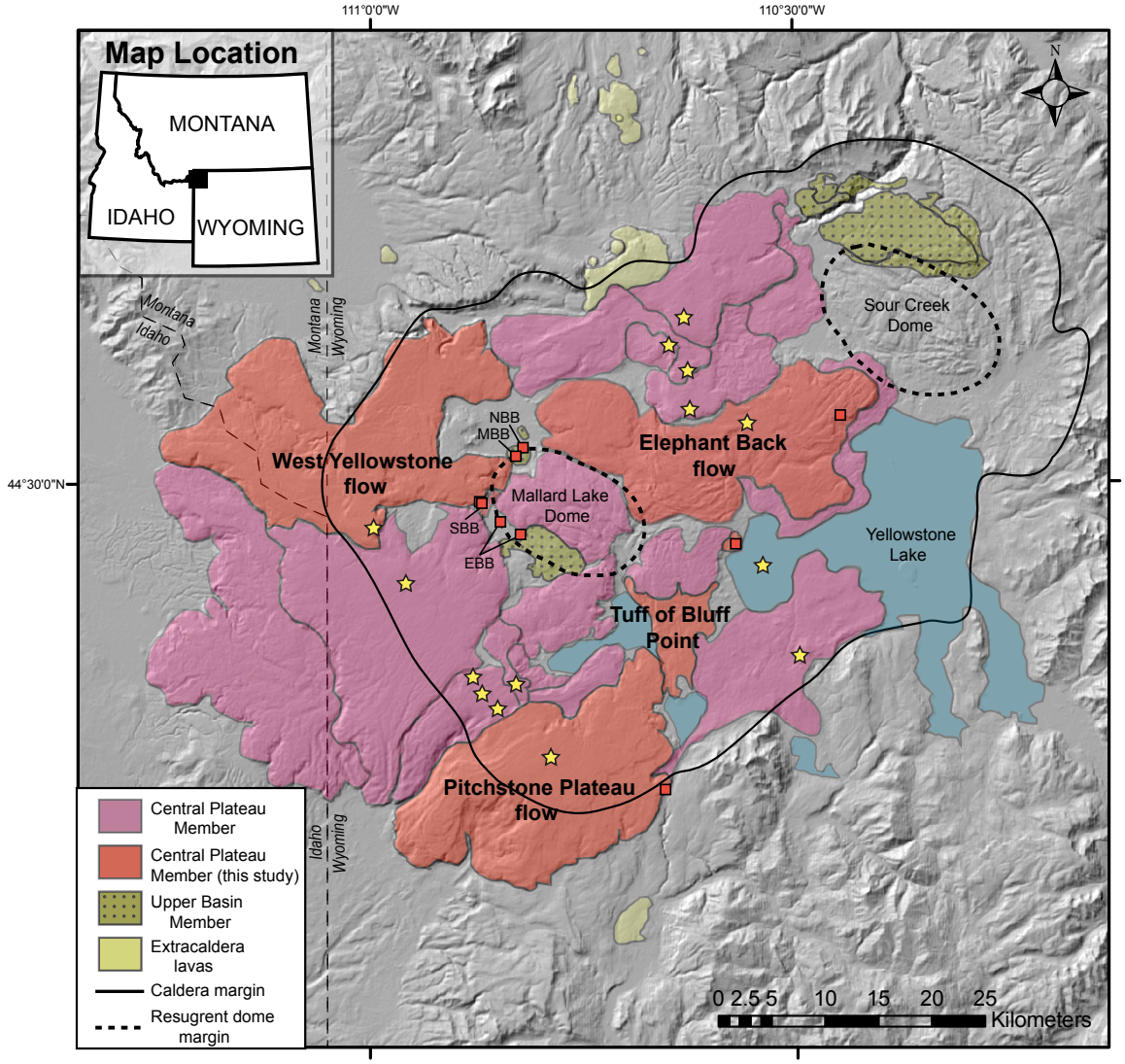

Yellowstone caldera – the Central Plateau Member rhyolites. In addition, we report lead isotope data for individual sanidines of these rhyolites. Our new results clarify differences between Upper Basin Member and Central Plateau Member magma genesis models, and enable us to evaluate end member possibilities for their derivation, for instance from isolated pockets of low-$\delta^{18}O$ melt (Bindeman and Valley, 2000, 2001; Bindeman et al., 2008) or a common, evolving, low-$\delta^{18}O$ magma source (Vazquez and Reid, 2002; Vazquez et al., 2009; Girard and Stix, 2009a).

## 2. Geologic Background

The Yellowstone Plateau volcanic field in western Wyoming-eastern Idaho is the most recent expression of explosive silicic volcanism in the 16 Ma track of the Yellowstone hotspot (Pierce and Morgan, 1992; Nash et al., 2006). Over its ~2 Ma lifespan, the Yellowstone Plateau volcanic field has been the site of three major caldera-forming eruptions: the 2.06 Ma Huckleberry Ridge Tuff (HRT), 1.29 Ma Mesa Falls Tuff (MFT), and 0.64 Ma Lava Creek Tuff (LCT) (Lanphere et al., 2002). Estimated eruptive volumes for these tuffs are 2,450 $km^3$, 280 $km^3$, and 1,000 $km^3$, respectively (Christiansen, 2001). Following formation of the Yellowstone caldera from the LCT eruption, several cycles of predominantly effusive post-caldera volcanism produced a cumulative eruptive volume of more than 600 $km^3$ of rhyolite, partially filling the Yellowstone caldera basin and spilling over the western caldera rim (Fig. 1; Christiansen and Blank, 1972; Christiansen, 2001). These rhyolites represent either residual magma from the third LCT cycle, or perhaps the beginning of a fourth eruptive cycle, owing to

their very large cumulative eruptive volume (Hildreth et al., 1984; Christiansen, 2001; Christiansen et al., 2007).

Post-LCT rhyolites are subdivided into two principal members based on location, age, and composition (Fig. 1). The earliest erupted (~520-470 ka) rhyolites compose the Upper Basin Member (UBM) flows (~50 $km^3$ total volume) located near the Mallard Lake and Sour Creek resurgent domes of the Yellowstone caldera (Fig. 1). UBM flows have more primitive compositions than younger post-LCT rhyolites (Christiansen et al., 2007; Girard and Stix, 2009b), and they have the lowest magmatic $\delta^{18}O$ signatures of all studied Yellowstone rhyolites (Hildreth et al., 1984; Bindeman and Valley, 2001; Bindeman et al., 2008). Oxygen isotope studies of individual UBM units reveal distinct low-$\delta^{18}O$ obsidian values that range from ~0 to 2‰, significant phenocrystic $\delta^{18}O$ heterogeneity spanning an 8‰ range, and zircons with up to 2.1 Ma older cores and inherited (pre-caldera) normal-$\delta^{18}O$ values (Bindeman and Valley, 2001; Bindeman et al., 2008). This evidence is taken to indicate that UBM rhyolite lavas were derived from independent magma batches produced by bulk remelting of hydrothermally altered pre-caldera protoliths (Bindeman et al., 2008).

The youngest (~260-75 ka) and most voluminous post-LCT eruptions compose the Central Plateau Member (CPM) units, which consist of at least 17 lava flows and two pyroclastic tuffs (Christiansen et al., 2007). Individual eruptive volumes of CPM rhyolites are typically on the order of ~10 $km^3$, but several approach ~50-70 $km^3$ (Christiansen et al., 2007). The 50 $km^3$ Tuff of Bluff Point eruption was of sufficient volume and explosivity to generate a smaller caldera within the larger Yellowstone caldera, apparent as a ~10 km wide elliptical depression filled by the western portion of

the Yellowstone Lake (Fig. 1). CPM rhyolites were erupted in discrete batches from vents along two northwest-striking lineaments that bisect the Yellowstone caldera (Fig. 1). However, the rhyolites display no apparent regional differences in composition for different vent localities (Girard and Stix 2009a). Recent studies of Scaup Lake, South Biscuit Basin and North Biscuit Basin flows demonstrate that they have $\delta^{18}O$ ranges similar to CPM rhyolites (Bindeman et al., 2008; this study), and Ar-Ar eruption ages that are ~300 ky younger than other UBM rhyolites (Christiansen et al., 2007; Bindeman et al., 2008; this study), suggesting that they belong to the CPM rather than UBM group. Here, we include them with the 'early' CPM group, and suggest that they are important for understanding the more voluminous 'later' CPM rhyolites.

Like UBM rhyolites, early CPM units exhibit heterogeneity in zircon age and $\delta^{18}O$ values, but have less extreme low-$\delta^{18}O$ obsidian values of ~3 to 4‰ (Bindeman and Valley, 2001; this study). The more voluminous later CPM rhyolites have low-$\delta^{18}O$ melt values of ~3 to 4‰ that match those of the early CPM units, but they possess less phenocrystic $\delta^{18}O$ heterogeneity than early CPM units (Bindeman and Valley, 2001; Bindeman et al., 2008; this study). U-Pb and U-Th zircon ages of later CPM rhyolites closely approximate their respective Ar-Ar eruption ages and individual units reveal no or subtle zircon inheritance from pre-caldera source rocks (Vazquez and Reid, 2002; this study), with the possible exception of the voluminous Solfatara Plateau flow, which exhibits $\delta^{18}O$ zircon disequilibria (Bindeman et al., 2008) and possesses a Pb isotopic composition similar to that of HRT rocks (Vazquez et al., 2009).

## 3. Samples and Methods

In this study, we report new data for four young large-volume CPM rhyolites, including three lava flows (Pitchstone Plateau, West Yellowstone, Elephant Back) and one explosive tuff (Tuff of Bluff Point), two older, small-volume CPM rhyolitic lavas (North Biscuit Basin, South Biscuit Basin), and one newly defined lava that represents the earliest and most primitive UBM unit, the East Biscuit Basin flow (Fig. 1). These units span the full eruptive age range of post-LCT rhyolites and have a broad spatial distribution within the Yellowstone caldera (Fig. 1). With the exception of the East Biscuit Basin flow, which is one of the few low-silica rhyolites at Yellowstone, all samples are high-silica rhyolites with ~5-20 vol% sanidine, quartz, clinopyroxene, orthopyroxene, Fe-Ti oxides and accessory phases (see Appendix C for petrographic descriptions, Fig. C1 for photomicrographs, and Table C1 for whole-rock major and trace element geochemistry). Notably, only North Biscuit Basin, South Biscuit Basin and East Biscuit Basin flows have plagioclase, and East Biscuit Basin lacks sanidine and quartz. Abundant glass reentrants, sieved plagioclase phenocrysts, and anhedral crystal clusters were observed in samples of South Biscuit Basin and East Biscuit Basin lavas, similar to what has been described by Girard and Stix (2009b). Zircon phenocrysts commonly occur as isolated crystals in the groundmass glass or as inclusions within Fe-Ti oxide and pyroxene aggregates. Most zircon crystals are subhedral-euhedral, ~100-200 μm in length, and many exhibit cathodoluminescence (CL) zoning (Fig. 2).

U-Th disequilibrium dating of zircons was performed with a CAMECA ims 1270 ion microprobe at UCLA using a ~30x35 μm spot size, according to the protocols described by Schmitt et al. (2006). Analytical details and operating conditions can be

**Figure 2.** Cathodoluminescence (CL) images of zircons dated for U-Th and U-Pb ages and analyzed for oxygen isotope compositions by ion microprobe. Analyzed spots are bounded by dashed ellipses. U-Th ages and uncertainties are shown in bold text; U-Pb ages are indicated by parentheses. Oxygen isotope compositions of dated zircon spots are shown in italic text. See Table 1 for a compilation of all ion microprobe data. (a) Pitchstone Plateau (PP) zircon, euhedral and unzoned in CL. (b) West Yellowstone (WY) zircon, euhedral with distinct core-rim CL zoning. (c) Elephant Back (EB) zircon, euhedral with subtle core-rim CL zoning. (d) North Biscuit Basin (NBB) zircon, exhibits core-rim zoning in CL, U-Pb age and O isotope composition. (e) and (f) South Biscuit Basin (SBB) zircons, pronounced core-rim zoning in CL, U-Pb and U-Th age, and O isotope composition, cores are CL dark with subtle sector zoning. (g) East Biscuit Basin (EBB) zircon, zoned in CL and U-Pb age. (h) East Biscuit Basin (EBB) zircon, has a U-Pb age that significantly predates the Lava Creek Tuff and post-Lava Creek Tuff eruptions.

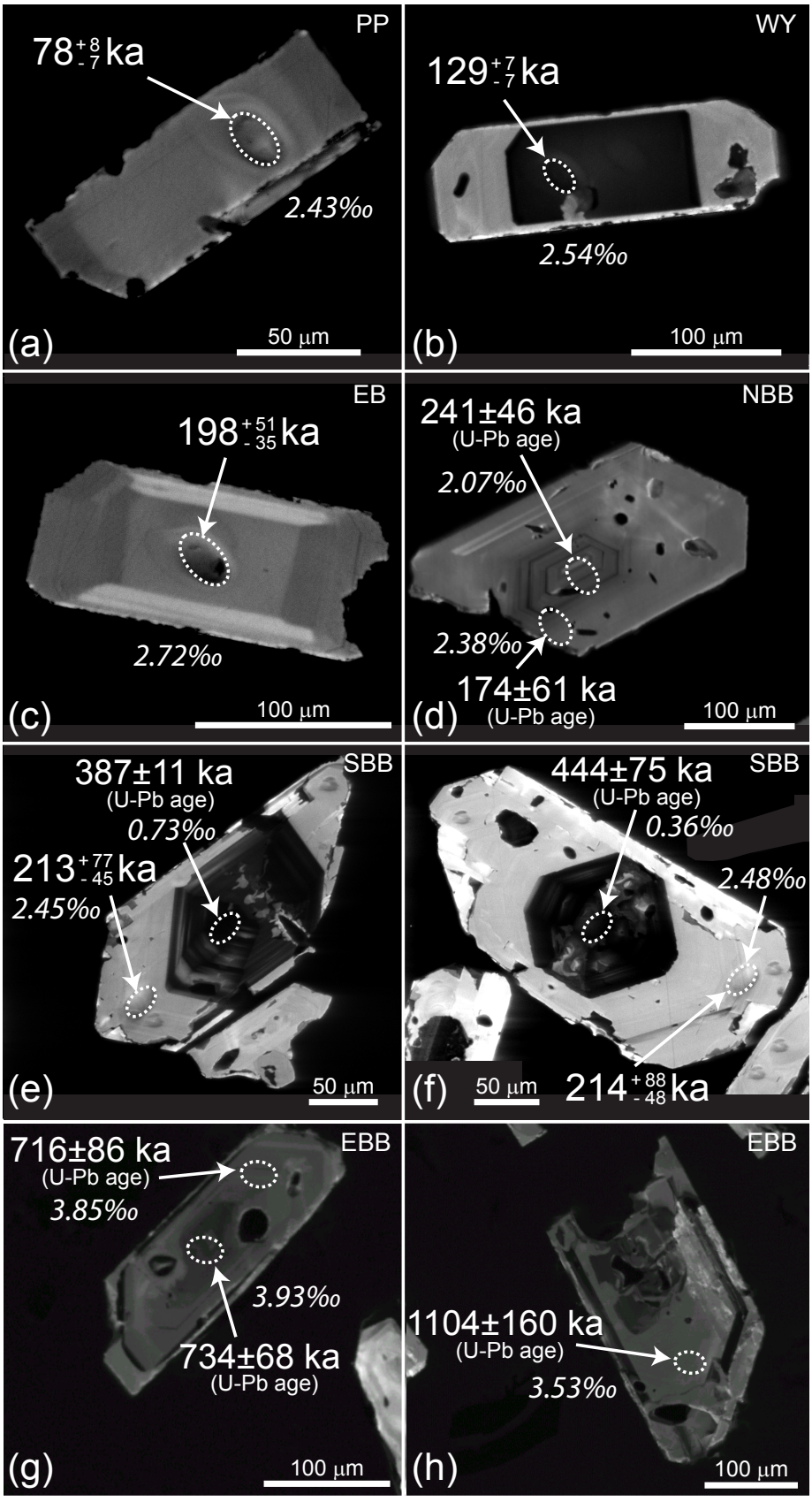
PP
78 +8 -7 ka
2.43‰
(a)
50 μm
WY
129 +7 -7 ka
2.54‰
(b)
100 μm
EB
198 +51 -35 ka
2.72‰
(c)
100 μm
NBB
241±46 ka
(U-Pb age)
2.07‰
2.38‰
174±61 ka
(U-Pb age)
(d)
100 μm
SBB
387±11 ka
(U-Pb age)
0.73‰
213 +77 -45 ka
2.45‰
(e)
50 μm
SBB
444±75 ka
(U-Pb age)
0.36‰
2.48‰
(f)
50 μm
214 +88 -48 ka
EBB
716±86 ka
(U-Pb age)
3.85‰
3.93‰
734±68 ka
(U-Pb age)
(g)
100 μm
EBB
1104±160 ka
(U-Pb age)
3.53‰
(h)
100 μm

found in the Appendix C. A small percentage (<10%) of the analyzed CPM zircon grains were found to be in $^{238}U$-$^{230}Th$ secular equilibrium and were reanalyzed for $^{238}U$-$^{206}Pb$ concordia ages according to the techniques outlined in Schmitt et al. (2003). Two Biscuit Basin samples (East Biscuit Basin and North Biscuit Basin) were dated with U-Pb at Stanford University using a SHRIMP-RG ion microprobe. For these analyses, the analytical techniques and conditions of Williams (1998) were used.

All zircons dated by U-Th and U-Pb were analyzed for $\delta^{18}O$ in subsequent analytical sessions at the UCLA Secondary Ionization Mass Spectrometry (SIMS) facility. Back-scattered electron (BSE) and cathodoluminescence (CL) images of zircon grain mounts enabled us to target the dated ion probe spots. After repolishing (Kita et al., 2009), we determined the $\delta^{18}O$ compositions of the analyzed zircons a few microns below the original dated ion probe pits. Corrections for instrumental mass fractionation (IMF) were made using zircon standard KIM-5 (Valley, 2003), which was mounted in the center of each zircon grain mount. KIM-5 zircons were analyzed repeatedly during each analytical session, with external errors that were typically less than 0.22‰ (1 SD) for each sample block (~15-20 analyzed spots per block). We used the external errors of the KIM-5 zircon standards as the best estimate of the $\delta^{18}O$ uncertainties for our samples.

Pb isotope analyses of sanidine phenocrysts and host groundmass glasses were performed with a Finnigan Neptune MC-ICP-MS laser ablation system at Washington State University using the techniques and operating conditions of Kent (2008), as described in Appendix C. We analyzed four post-LCT units, including an older CPM rhyolite (South Biscuit Basin) and three younger CPM rhyolites (Pitchstone Plateau, Elephant Back, and the Tuff of Bluff Point), all of which were dated for U-Th and U-Pb

ages and analyzed for $\delta^{18}O$ compositions by us. In addition, we determined Pb isotopes for sanidine separates from several members of major caldera-forming tuff eruptions at Yellowstone (HRT [members B and C] and LCT [member A]), which were previously studied for U-Pb ages (Bindeman et al., 2001; Bindeman et al., 2008) and $\delta^{18}O$ compositions (Bindeman and Valley, 2001; Bindeman et al., 2008).

## 4. Results

Results presented below include zircon U-Pb and U-Th crystallization ages and $\delta^{18}O$ compositions, and sanidine Pb isotope compositions. We also include whole-rock thermometry for all studied rhyolites, and synthesize this new data with thermometry results from previous studies. The results in each subsection are organized according to eruption age (oldest to youngest).

### 4.1. Zircon crystallization ages and $\delta^{18}O$ compositions

#### 4.1.1. Earliest Upper Basin Member rhyolite

Zircon dating of the most primitive rhyolite to erupt within the Yellowstone caldera, the East Biscuit Basin flow, reveals that it is also the oldest post-caldera rhyolite, with an error weighted mean U-Pb age (781±76 ka, n=9, mean square of weighted deviates (MSWD)=1.0). This age falls between the Ar-Ar eruption ages of the MFT and LCT (Fig. 3). No sanidine is present in East Biscuit Basin flow, and our attempts to perform $^{40}Ar/^{39}Ar$ dating on plagioclase were unsuccessful, so we are unable to report an Ar-Ar eruption age for this unit. However, eruption of East Biscuit Basin flow within the Yellowstone caldera near the Mallard Lake Resurgent dome (Fig. 1) indicates that it is a

post-LCT rather than pre-LCT flow. The U-Pb zircon age range published by Bindeman et al. (2001) for the Middle Biscuit Basin flow overlaps the broad age range that we find for the East Biscuit Basin flow, and isotopically, the two units are similar (this study; Pritchard and Larson, in prep), suggesting that East Biscuit Basin may be a related UBM unit. Some East Biscuit Basin zircons are zoned in CL and U-Pb age (Fig. 2g) and the oldest zircons are generally present as fragments rather than whole grains (Table 1).

Complementary oxygen isotope data for dated East Biscuit Basin zircon spots reveal that it has zircon $\delta^{18}O$ values that are for the most part higher than LCT zircons, in contrast to other analyzed post-LCT units, which typically have lower zircon $\delta^{18}O$ values (c.f., Bindeman and Valley, 2001; Bindeman et al., 2001; Bindeman et al., 2008). However, East Biscuit Basin does have host glass (obsidian) and plagioclase with low-$\delta^{18}O$ values that are distinctive of post-LCT UBM units, 1.0‰ and 1.4‰, respectively. The average zircon $\delta^{18}O$ value of 4.3±0.3‰ is more than 5‰ higher than the calculated equilibrium zircon value for East Biscuit Basin glass (Fig. 4), and is therefore one of the most extreme cases of oxygen isotopic disequilibrium documented for Yellowstone rhyolites. Unlike other UBM units, there is no clear core-rim $\delta^{18}O$ zoning in East Biscuit Basin zircons, and the $\delta^{18}O$ range of zircon cores and rims is relatively narrow (~2‰) compared to the exceptionally large (~6-8‰) range found for zircons from the Middle Biscuit Basin flow, Dunraven Road flow and Canyon flow (Bindeman et al., 2008).

### 4.1.2. Early Central Plateau Member rhyolites

Zircon age data for the North Biscuit Basin and South Biscuit Basin flows corroborate earlier interpretations that they are distinct units rather than a single Biscuit

Basin rhyolite (Bindeman and Valley, 2001; Bindeman et al., 2008). North Biscuit Basin has an error weighted mean U-Pb age (190±45 ka, n=9, MSWD=0.4) that is unimodal and normally distributed (Fig. 3), consistent with our findings for CPM rhyolites (section 4.1.3.). The $^{40}Ar/^{39}Ar$ sanidine eruption age determined by us for North Biscuit Basin (155±9 ka) is within the ~170-75 ka age range of CPM rhyolite eruptions (Christiansen et al., 2007), indicating that it is an early CPM unit. Core-rim zoning of North Biscuit Basin zircons is apparent in CL and U-Pb age (Fig. 2d), with the oldest core ages closely approximating the Ar-Ar eruption age of the oldest CPM unit, the Scaup Lake flow (257±13 ka) (Christiansen et al., 2007).

South Biscuit Basin flow has a distinctly bimodal zircon age population (Fig. 3). The error weighted mean U-Pb age of the oldest South Biscuit Basin age peak (384±21 ka, n=4, MSWD=0.7) significantly predates the onset of CPM eruptions (~260 ka), however, the youngest South Biscuit Basin age peak (103±16 ka, n=4, MSWD=0.4) is among the youngest documented zircon ages for CPM rhyolites (section 4.1.3.). Older South Biscuit Basin zircons exhibit significant core-rim zoning in CL and age (Fig. 2e-f), and are larger in size than younger South Biscuit Basin zircons (Table 1). Curiously, the $^{40}Ar/^{39}Ar$ sanidine eruption age determined by us for South Biscuit Basin (261±17 ka) is ~160 ky older than the youngest South Biscuit Basin zircon age peak, yet consistent with the $^{40}Ar/^{39}Ar$ sanidine eruption age previously reported by Bindeman et al. (2008) for the same sample (255±11 ka). The U-Th ages of zircon rims surrounding older South Biscuit Basin zircon cores are similar to the Ar-Ar eruption age (Fig. 3). This evidence suggests that South Biscuit Basin contains antecrystic zircon and sanidine crystals, which skew the

**Figure 3.** U-Th and U-Pb ages of individual Yellowstone zircons determined by ion microprobe (see Table 1 for data). Left panels: Error-weighted probability distribution curves for zircon analyses. U-Th zircon ages are shown by the light blue bars; zircons in or close to U-Th secular equilibrium were dated for U-Pb ages, shown by the dark blue bars. Ar-Ar eruption ages are shown by thin vertical lines (Gansecki et al., 1996; Lanphere et al., 2002; Christiansen et al., 2007; this study). K-Ar eruption age for the Elephant Back flow is from Obradovich (1992). For the Pitchstone Plateau flow and West Yellowstone flow, we include the mean U-Th ages (thin dashed lines) and error fields (shaded) published by Vazquez and Reid (2002) for these units. Right panels: Individual zircon analyses (squares; light blue for U-Th ages and dark blue for U-Pb ages) are shown with their error bars (± 1σ). Bold vertical lines show the error-weighted mean U-Th and U-Pb zircon ages. Thin vertical lines show the eruption ages (as indicated and labeled in the left panels).

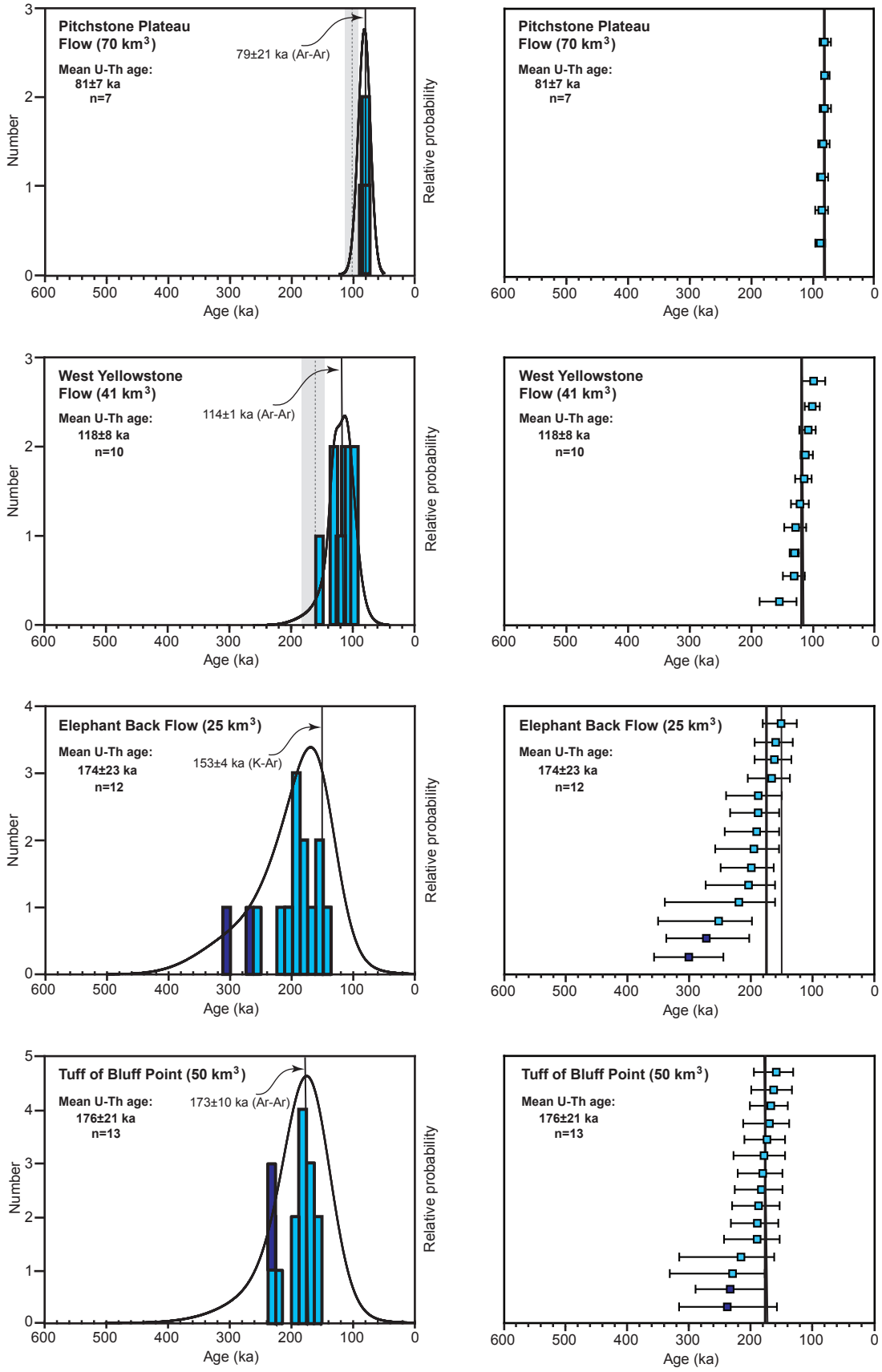
Pitchstone Plateau
Flow (70 km3)
Mean U-Th age:
81±7 ka
n=7
79±21 ka (Ar-Ar)
Number
Relative probability
Age (ka)
West Yellowstone
Flow (41 km3)
Mean U-Th age:
118±8 ka
n=10
114±1 ka (Ar-Ar)
Elephant Back Flow (25 km3)
Mean U-Th age:
174±23 ka
n=12
153±4 ka (K-Ar)
Tuff of Bluff Point (50 km3)
Mean U-Th age:
176±21 ka
n=13
173±10 ka (Ar-Ar)

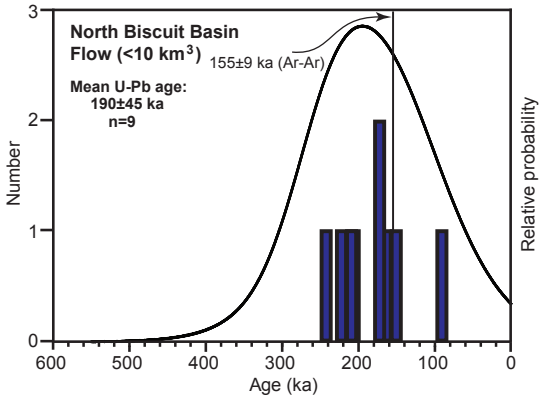
North Biscuit Basin
Flow (<10 km3)
155±9 ka (Ar-Ar)
Mean U-Pb age:
190±45 ka
n=9
Number
Relative probability
Age (ka)

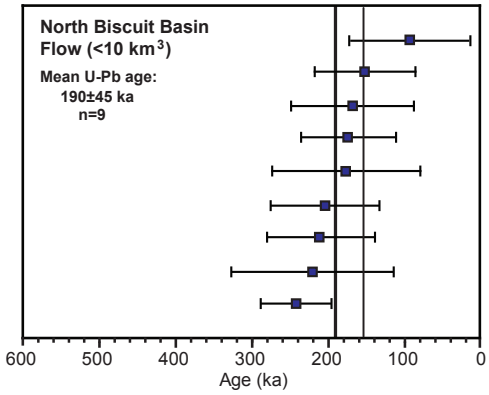
North Biscuit Basin
Flow (<10 km3)
Mean U-Pb age:
190±45 ka
n=9
Age (ka)

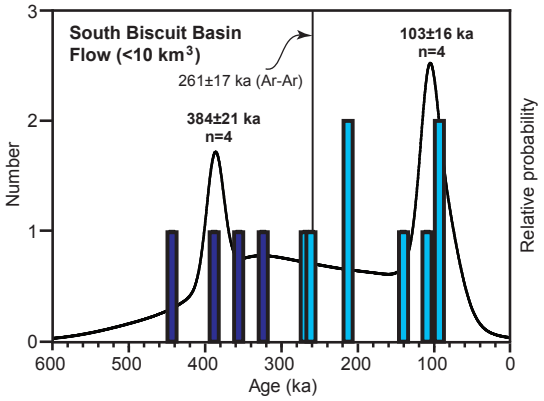
South Biscuit Basin
Flow (<10 km3)
261±17 ka (Ar-Ar)
384±21 ka
n=4
103±16 ka
n=4
Number
Relative probability
Age (ka)

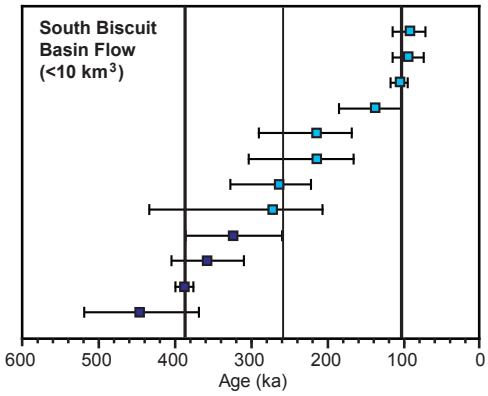
South Biscuit
Basin Flow
(<10 km3)
Age (ka)

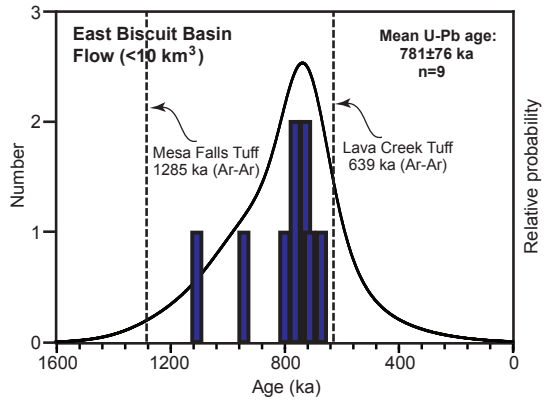
East Biscuit Basin
Flow (<10 km3)
Mean U-Pb age:
781±76 ka
n=9
Mesa Falls Tuff
1285 ka (Ar-Ar)
Lava Creek Tuff
639 ka (Ar-Ar)
Number
Relative probability
Age (ka)

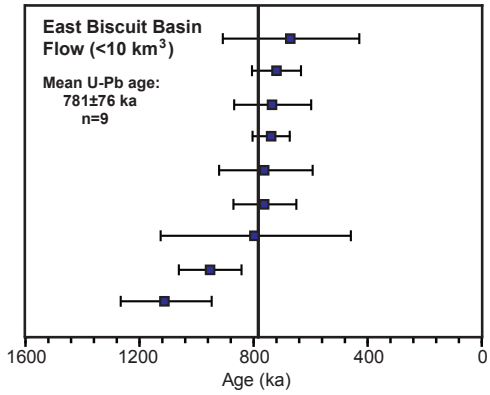
East Biscuit Basin
Flow (<10 km3)
Mean U-Pb age:
781±76 ka
n=9
Age (ka)

**Table 1.** U-Th and U-Pb ages, $\delta^{18}O$ values, and sizes of zircons in studied Yellowstone rhyolites

| Sample | Core/rim | Model U-Th age (ka)* | +1σ | −1σ | U-Pb concordia age (ka) | ±1σ | $\delta^{18}O$ (‰) (same spot) | $\delta^{18}O$ (‰) (adjacent) | ±1σ ext | Length (μm) | Width (μm) |
|---|---|---|---|---|---|---|---|---|---|---|---|
| **Pitchstone Plateau flow (YL02-1)** | | | | | | | | | | | |
| YL02-1_g1 | C | 83 | 9 | -9 | – | – | 3.16 | 3.02 | 0.22 | 133 | 77 |
| YL02-1_g2 | C | 82 | 10 | -9 | – | – | 3.01 | 3.23 | 0.22 | 117 | 51 |
| YL02-1_g3 | C | 78 | 8 | -7 | – | – | 2.43 | – | 0.22 | 144 | 54 |
| YL02-1_g5 | C | 84 | 11 | -10 | – | – | 2.61 | 3.01 | 0.22 | 218 | 60 |
| YL02-1_g6 | C | 87 | 9 | -8 | – | – | 2.44 | 2.61 | 0.22 | 108 | 56 |
| YL02-1_g7 | C | 78 | 10 | -9 | – | – | 2.85 | – | 0.22 | 82 | 49 |
| YL02-1_g8 | C | 79 | 9 | -9 | – | – | 2.14 | 2.90 | 0.22 | 104 | 61 |
| **West Yellowstone flow (YL96-1)** | | | | | | | | | | | |
| YL96-1_g1 | C | 129 | 7 | -7 | – | – | 2.54 | 3.08 | 0.22 | 231 | 73 |
| YL96-1_g2 | C | 126 | 19 | -16 | – | – | 2.92 | 2.85 | 0.22 | 175 | 104 |
| YL96-1_g3 | C | 153 | 34 | -26 | – | – | 2.94 | 2.67 | 0.22 | 243 | 110 |
| YL96-1_g4 | C | 98 | 21 | -17 | – | – | 2.38 | 2.41 | 0.22 | 188 | 103 |
| YL96-1_g5 | C | 120 | 15 | -13 | – | – | 3.08 | – | 0.22 | 154 | 66 |
| YL96-1_g6 | C | 110 | 10 | -9 | – | – | 2.95 | – | 0.22 | 204 | 83 |
| YL96-1_g7 | C | 100 | 13 | -12 | – | – | 2.69 | 3.18 | 0.22 | 203 | 90 |
| YL96-1_g8 | C | 114 | 15 | -13 | – | – | 2.58 | 2.72 | 0.22 | 189 | 75 |
| YL96-1_g9 | C | 129 | 20 | -17 | – | – | 3.11 | 3.04 | 0.22 | 169 | 79 |
| YL96-1_g10 | C | 107 | 14 | -13 | – | – | 2.90 | – | 0.22 | 178 | 72 |
| **Elephant Back flow (06YS-4)** | | | | | | | | | | | |
| YS-4_g1 | C | 345 | ∞ | -124 | 271 | 67 | 3.26 | – | 0.22 | 219 | 104 |
| YS-4_g2 | C | 187 | 54 | -36 | – | – | 3.57 | – | 0.22 | 216 | 84 |
| YS-4_g3 | C | 189 | 54 | -36 | – | – | 2.87 | 2.51 | 0.22 | 197 | 77 |
| YS-4_g4 | C | 198 | 51 | -35 | – | – | 2.72 | 3.21 | 0.22 | 179 | 79 |
| YS-4_g5 | C | 149 | 32 | -24 | – | – | 2.64 | – | 0.22 | 220 | 86 |
| YS-4_g6 | C | 250 | 101 | -52 | 300 | 56 | 2.83 | 2.52 | 0.22 | 245 | 94 |
| YS-4_g8 | C | 194 | 65 | -40 | – | – | 2.48 | – | 0.22 | 207 | 97 |
| YS-4_g9 | C | 165 | 40 | -29 | – | – | 2.40 | 3.21 | 0.22 | 160 | 74 |
| YS-4_g10 | C | 187 | 48 | -33 | – | – | 2.42 | – | 0.22 | 186 | 71 |
| YS-4_g11 | C | 203 | 71 | -43 | – | – | 3.07 | – | 0.22 | 248 | 82 |
| YS-4_g12 | C | 218 | 123 | -56 | – | – | 2.34 | – | 0.22 | 153 | 89 |
| YS-4_g13 | C | 160 | 36 | -27 | – | – | 2.59 | 2.51 | 0.22 | 131 | 60 |
| YS-4_g14 | C | 160 | 34 | -26 | – | – | 2.15 | – | 0.22 | 304 | 114 |
| **Tuff of Bluff Point (06YS-2)** | | | | | | | | | | | |
| YS-2_g1 | C | 368 | ∞ | -132 | 237 | 79 | 2.36 | 2.60 | 0.22 | 371 | 142 |
| YS-2_g2 | C | 189 | 54 | -36 | – | – | 2.74 | 2.86 | 0.22 | 256 | 91 |
| YS-2_g3 | C | 170 | 44 | -31 | – | – | 2.89 | 2.84 | 0.22 | 300 | 112 |
| YS-2_g4 | C | 159 | 37 | -28 | – | – | 2.67 | 2.70 | 0.22 | 338 | 131 |
| YS-2_g5 | C | 179 | 50 | -34 | – | – | 2.84 | 2.49 | 0.22 | 397 | 119 |
| YS-2_g6 | C | 188 | 44 | -31 | – | – | 2.94 | 2.52 | 0.22 | 263 | 107 |
| YS-2_g7 | C | 173 | 39 | -28 | – | – | 2.90 | 2.74 | 0.22 | 182 | 108 |
| YS-2_g8 | C | 186 | 45 | -32 | – | – | 2.65 | 2.29 | 0.22 | 277 | 120 |
| YS-2_g9 | C | 167 | 35 | -26 | – | – | 2.85 | 2.87 | 0.22 | 272 | 90 |
| YS-2_g10 | C | 162 | 37 | -28 | – | – | 2.25 | 2.30 | 0.22 | 245 | 106 |
| YS-2_g11 | C | 229 | 103 | -52 | 232 | 57 | 2.98 | 2.72 | 0.22 | 276 | 111 |
| YS-2_g12 | C | 180 | 42 | -30 | – | – | 2.56 | 2.44 | 0.22 | 247 | 118 |
| YS-2_g13 | C | 215 | 102 | -52 | – | – | 2.60 | 3.09 | 0.22 | 203 | 102 |
| YS-2_g14 | C | 182 | 45 | -32 | – | – | 2.39 | 2.73 | 0.22 | 237 | 140 |
| **North Biscuit Basin flow (08YS-14)** | | | | | | | | | | | |
| KWBBRR-2.1 | C | – | – | – | 92 | 79 | 3.22 | 3.22 | 0.35 | 357 | 214 |
| KWBBR-4.1 | C | – | – | – | 151 | 66 | 2.71 | 6.74 | 0.35 | fragment | fragment |
| KWBBR-3.1 | C | – | – | – | 168 | 80 | 2.61 | 2.71 | 0.35 | fragment | fragment |
| KWBBR-8.1 | R | – | – | – | 175 | 97 | 2.82 | 2.52 | 0.35 | 276 | 149 |
| KWBBRR-9.1 | R | – | – | – | 174 | 61 | 2.38 | – | 0.35 | – | – |
| KWBBR-7.1 | C | – | – | – | 204 | 71 | 2.70 | 2.74 | 0.35 | 229 | 85 |
| KWBBR-2.1 | C | – | – | – | 210 | 72 | 2.90 | – | 0.35 | 328 | 162 |
| KWBBR-5.1 | R | – | – | – | 221 | 106 | 3.29 | 2.30 | 0.35 | fragment | fragment |
| KWBBRC-9.2 | C | – | – | – | 241 | 46 | 2.07 | – | 0.35 | 288 | 114 |
| **South Biscuit Basin flow (YL96-2)** | | | | | | | | | | | |
| YL2_58-3 | R | 213 | 77 | -45 | – | – | 2.45 | – | 0.20 | – | – |
| YL2_3-1 | C | 94 | 22 | -18 | – | – | 3.39 | – | 0.20 | 160 | 95 |
| YL2_52-1 | C | 137 | 50 | -34 | – | – | -0.20 | – | 0.20 | 300 | 105 |
| YL2_4-1 | C | 106 | 11 | -10 | – | – | 2.69 | – | 0.24 | 170 | 105 |
| YL2_5-2 | R | 262 | 65 | -40 | – | – | 2.13 | – | 0.24 | – | – |
| YL2_7-1 | C | 92 | 23 | -19 | – | – | 3.08 | – | 0.20 | 150 | 80 |

## Table 1. (continued).

| | | | | | | | | | | | |
|---|---|---|---|---|---|---|---|---|---|---|---|
| YL2_52-3 | R | 270 | 164 | -63 | – | – | 2.39 | – | 0.20 | – | – |
| YL2_59-2 | R | 214 | 88 | -48 | – | – | 2.48 | – | 0.24 | – | – |
| YL2_6-2 | R | 356 | ∞ | -134 | 322 | 64 | 2.37 | – | 0.24 | – | – |
| YL2_58-1 | C | 321 | 306 | -72 | 387 | 11 | 0.73 | – | 0.20 | 260 | 110 |
| YL2_59-1 | C | 449 | ∞ | -123 | 444 | 75 | 0.36 | – | 0.24 | 300 | 140 |
| YL2_6-1 | C | 326 | ∞ | -103 | 357 | 46 | 1.55 | – | 0.24 | 215 | 70 |
| **East Biscuit Basin flow (08YS-15b)** | | | | | | | | | | | |
| KWEBB-2.1 | C | – | – | – | 667 | 236 | 5.13 | 4.90 | 0.35 | 135 | 144 |
| KWEBB-9.1 | R | – | – | – | 716 | 86 | 3.85 | 4.07 | 0.35 | – | – |
| KWEBB-8.1 | C | – | – | – | 734 | 68 | 3.93 | – | 0.35 | 257 | 89 |
| KWEBB-6.1 | C | – | – | – | 733 | 137 | 4.05 | – | 0.35 | 204 | 86 |
| KWEBB-4.1 | R | – | – | – | 757 | 166 | 3.90 | 4.41 | 0.35 | 220 | 129 |
| KWEBB-7.1 | C | – | – | – | 761 | 110 | 4.84 | 4.99 | 0.35 | fragment | fragment |
| KWEBB-1.1 | C | – | – | – | 793 | 334 | 3.98 | – | 0.35 | fragment | fragment |
| KWEBB-3.1 | C | – | – | – | 949 | 111 | 4.94 | – | 0.35 | fragment | fragment |
| KWEBB-5.1 | C | – | – | – | 1104 | 160 | 3.53 | 3.63 | 0.35 | fragment | fragment |

*Model ages were calculated using zircon-vitrophyre isochrons. Published thermal ionization mass spectrometry (TIMS) data for U and Th isotopes of CPM vitrophyres (Vazquez and Reid, 2002) were used to estimate the initial $^{230}$Th abundances of CPM zircons; average activity ratios of ($^{230}$Th)/($^{232}$Th) = 0.78 ± 0.05 and ($^{238}$U)/($^{232}$Th) = 0.72 ± 0.05 were used for CPM units without published TIMS data. Decay constants: $\lambda_{230}$: $9.158 \times 10^{-6}$ year$^{-1}$; $\lambda_{232}$: $4.9475 \times 10^{-11}$ year$^{-1}$; $\lambda_{238}$: $1.55125 \times 10^{-10}$ year$^{-1}$.

**Figure 4.** Oxygen isotope compositions of individual Yellowstone zircons determined by ion microprobe (see Table 1 for data). Oxygen isotope compositions are plotted against U-Th and U-Pb ages for individual zircon spots. Average zircon $\delta^{18}O$ values for each unit are shown by the solid horizontal lines. For the South Biscuit Basin flow, we include three average zircon $\delta^{18}O$ values (older cores, younger cores, and rims on older cores). Equilibrium zircon $\delta^{18}O$ values, calculated using host glass (obsidian) $\delta^{18}O$ values and $\Delta^{18}O_{melt\text{-}zircon}$= 1.9‰ (applicable for liquidus temperatures of ~800°C; Bindeman and Valley, 2002), are shown by the dashed horizontal lines. The age and oxygen isotope field for Lava Creek Tuff (LCT) zircons (shaded; Bindeman et al., 2008) is included for reference in each panel.

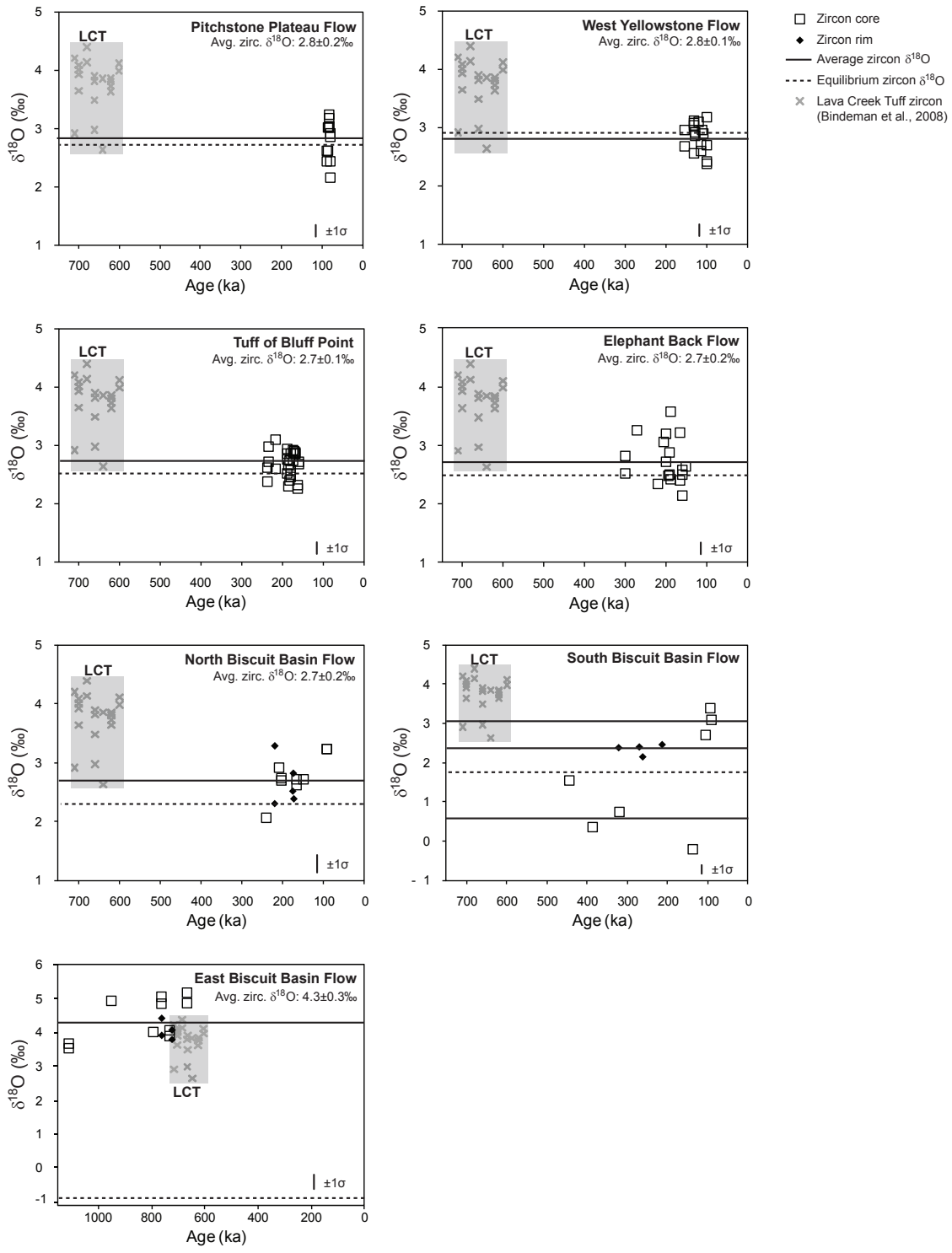
Pitchstone Plateau Flow
Avg. zirc. δ18O: 2.8±0.2‰
West Yellowstone Flow
Avg. zirc. δ18O: 2.8±0.1‰
Tuff of Bluff Point
Avg. zirc. δ18O: 2.7±0.1‰
Elephant Back Flow
Avg. zirc. δ18O: 2.7±0.2‰
North Biscuit Basin Flow
Avg. zirc. δ18O: 2.7±0.2‰
South Biscuit Basin Flow
East Biscuit Basin Flow
Avg. zirc. δ18O: 4.3±0.3‰
LCT
±1σ
δ18O (‰)
Age (ka)
Zircon core
Zircon rim
Average zircon δ18O
Equilibrium zircon δ18O
Lava Creek Tuff zircon
(Bindeman et al., 2008)

apparent ages to older values, similar to the conclusions drawn by Gansecki et al. (1996) for several UBM rhyolites.

Like the zircon age data, oxygen isotope data for dated zircon spots require that the North Biscuit Basin and South Biscuit Basin flows be treated as separate Biscuit Basin units (Fig. 4). North Biscuit Basin has an average zircon $\delta^{18}O$ value of 2.7±0.2‰, which is identical to the average zircon $\delta^{18}O$ values determined for the CPM Tuff of Bluff Point and Elephant Back flow (section 4.1.3.). North Biscuit Basin zircon rims fall within the same $\delta^{18}O$ range as zircon cores and there is no discernable core-rim zoning, however, the calculated equilibrium zircon $\delta^{18}O$ value for North Biscuit Basin is about 0.5‰ lower than the average zircon value, and therefore may indicate subtle oxygen isotopic disequilibrium if not due to analytical uncertainty. South Biscuit Basin exhibits more extreme $\delta^{18}O$ disequilibrium, with zircon populations that up to 2‰ lower and 1‰ higher than the equilibrium value, though the rims of the older zircon cores more closely approximate an equilibrium value (Fig. 4). The calculated equilibrium zircon $\delta^{18}O$ value for South Biscuit Basin is about 1‰ lower than equilibrium values for other CPM units, but clearly more similar in oxygen isotopic composition to CPM than to UBM rhyolites.

### 4.1.3. Central Plateau Member rhyolites

Zircon ages for CPM rhyolite samples are unimodal and normally distributed, indicating single age populations (Fig. 3). This is in contrast to the significant zircon age heterogeneity documented for UBM samples (Bindeman et al., 2001). Error-weighted mean U-Th ages for the Pitchstone Plateau flow (81±7 ka, n=7, MSWD=0.2), West Yellowstone flow (118±8 ka, n=10, MSWD=1.1) and Tuff of Bluff Point (176±21 ka,

n=13, MSWD=0.1) are identical to $^{40}Ar/^{39}Ar$ sanidine eruption ages published by Christiansen et al. (2007) for these units (Fig. 3). Mean U-Th zircon ages previously reported by Vazquez and Reid (2002) for the Pitchstone Plateau and West Yellowstone flows (dashed lines and shaded error fields in Fig. 3) are slightly older than our mean U-Th age estimates, likely because these authors found and included some antecrysts in their age averages. The error-weighted mean U-Th age for the Elephant Back flow (174±23 ka, n=12, MSWD=0.3) is 21 ky older than this unit's published K-Ar sanidine eruption age (Obradovich, 1992), but overlapping it within error (Fig. 3). A few older zircon crystals in the Elephant Back flow and the Tuff of Bluff Point were found to be $^{238}U$-$^{230}Th$ secular equilibrium and redated with U-Pb (dark blue bars in Fig. 3). However, these older zircon grains are also within uncertainty of the U-Th zircon age dating methods. Vazquez and Reid (2002) reported the presence of older zircon grains in several CPM units (Pitchstone Plateau flow, Solfatara Plateau flow, West Yellowstone flow and Dry Creek flow) that match the ~250-300 ka ages of the older grains that we find for the Elephant Back flow and Tuff of Bluff Point.

Oxygen isotope values determined by ion microprobe for dated CPM zircon spots generally overlap within uncertainty (Table 1) and are about 1‰ depleted relative to LCT zircons (Fig. 4). Pitchstone Plateau flow and West Yellowstone flow have identical average zircon $\delta^{18}O$ values of 2.8±0.2‰ and 2.8±0.1‰, respectively, which closely approximate the calculated equilibrium zircon $\delta^{18}O$ values based on laser-fluorination data for host glass (obsidian) and major phenocryst phases of quartz and sanidine (Bindeman and Valley, 2001; Bindeman and Valley, 2002). The Tuff of Bluff Point and Elephant Back flow have slightly lower, but overlapping, average zircon $\delta^{18}O$ values of

2.7±0.1‰ and 2.7±0.2‰, respectively (Fig. 4). Calculated equilibrium zircon $\delta^{18}O$ values for the Tuff of Bluff Point and Elephant Back flow are slightly lower than the average zircon $\delta^{18}O$ values obtained by ion microprobe, but overlap the equilibrium estimates within error (Fig. 4).

### 4.1.4. Comparison to all studied Yellowstone rhyolites

When our new zircon data are combined with all published ion microprobe oxygen isotope data for Yellowstone rhyolites (Fig. 5a; arrows indicate the new units presented in this study), the following features are apparent: (1) East Biscuit Basin flow has zircons with oxygen isotope values that are generally higher than other post-LCT units, but has a low-$\delta^{18}O$ glass value that is distinctive of UBM lavas, (2) North Biscuit Basin zircons fall within the oxygen isotope range defined by CPM lavas, (3) CPM rhyolites have zircons with more homogeneous oxygen isotope compositions than older Yellowstone rhyolites, (4) CPM zircons generally have oxygen isotopic compositions that are in equilibrium with coexisting phenocrysts and groundmass glasses, (5) zircon compositions of individual CPM units overlap within a relatively narrow $\delta^{18}O$ range. Taken together, this new evidence indicates that post-LCT CPM rhyolites can be distinguished from older Yellowstone rhyolites by their relatively homogeneous low-$\delta^{18}O$ zircon oxygen isotope compositions that are in equilibrium with host melts, whereas post-LCT UBM rhyolites are more complex, retaining significant zircon oxygen isotope heterogeneity and disequilibria in low-$\delta^{18}O$ melts. In addition to a trend of increasing homogeneity through time (Fig. 5a), we also observe a positive correlation between

**Figure 5.** (a) Ion microprobe analyses of $\delta^{18}O$ in zircon (squares) plotted against eruption ages for Yellowstone rhyolites. Laser fluorination $\delta^{18}O$ data for quartz (circles), sanidine (open ovals) and glass (filled ovals) are also included. Our new oxygen isotope data for six post-Lava Creek Tuff units (denoted by arrows) are synthesized with data published by Bindeman et al. (2008) for Yellowstone rhyolites. Our new data reveal a trend of increasing homogenization of zircon $\delta^{18}O$ compositions with decreasing eruption age (trend shown with light gray arrows). Unit abbreviations are as follows: Huckleberry Ridge Tuff (HRT) members B and C; Blue Creek flow (BC); Mesa Falls Tuff (MFT); Lava Creek Tuff (LCT); East Biscuit Basin flow (EBB); Middle Biscuit Basin flow (MBB); Canyon flow (CF); Dunraven Road flow (DR); South Biscuit Basin flow (SBB); Scaup Lake flow (SCL); Tuff of Bluff Point (TBP); North Biscuit Basin flow (NBB); Elephant Back flow (EB); West Yellowstone flow (WY); Solfatara Plateau flow (SP); Pitchstone Plateau flow (PP). Eruption ages are from Obradovich (1992); Gansecki et al. (1996); Lanphere et al. (2002), Christiansen et al. (2007), Bindeman et al. (2008), and this study. No eruption age is available for the post-LCT EBB flow; it is plotted immediately after LCT. Eruption ages for NBB and EB are so close that $\delta^{18}O$ symbols for EB were offset to the right to avoid overlap. Modified after Bindeman et al. (2008). (b) Zircon $\delta^{18}O$ ranges plotted against eruptive volumes for post-Lava Creek Tuff rhyolites. Zircon $\delta^{18}O$ ranges are from Bindeman and Valley (2001), Bindeman et al. (2008) and this study. Eruptive volumes are from Christiansen et al. (2007). Our new data reveal a trend of increasing homogenization of zircon $\delta^{18}O$ compositions with increasing eruptive volume (trend shown with light gray arrows). Unit abbreviations are the same as those used in panel (a), with the addition of post-Lava Creek Tuff units Aster Creek flow (AC), Mallard Lake flow (ML) and Summit Lake flow (SL).

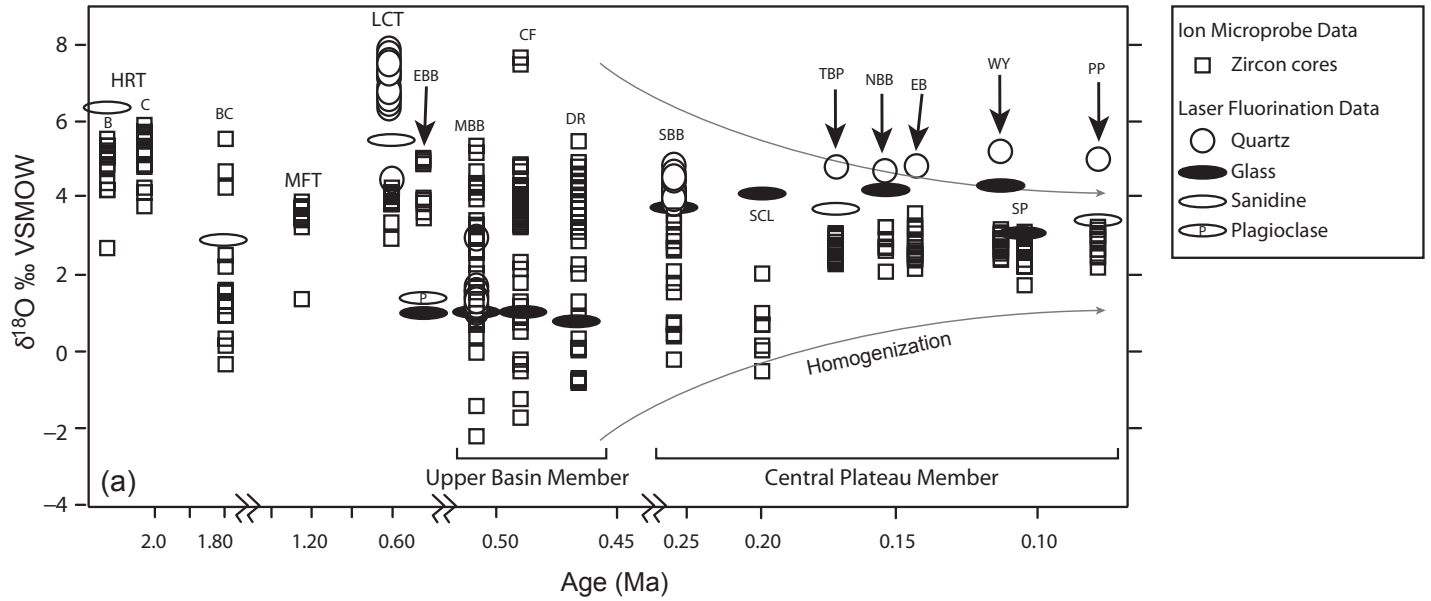
Ion Microprobe Data
Zircon cores
Laser Fluorination Data
Quartz
Glass
Sanidine
Plagioclase
HRT
B
C
BC
MFT
LCT
EBB
MBB
CF
DR
SBB
SCL
TBP
NBB
EB
WY
SP
PP
Homogenization
(a)
Upper Basin Member
Central Plateau Member
δ18O ‰ VSMOW
Age (Ma)
2.0
1.80
1.20
0.60
0.50
0.45
0.25
0.20
0.15
0.10

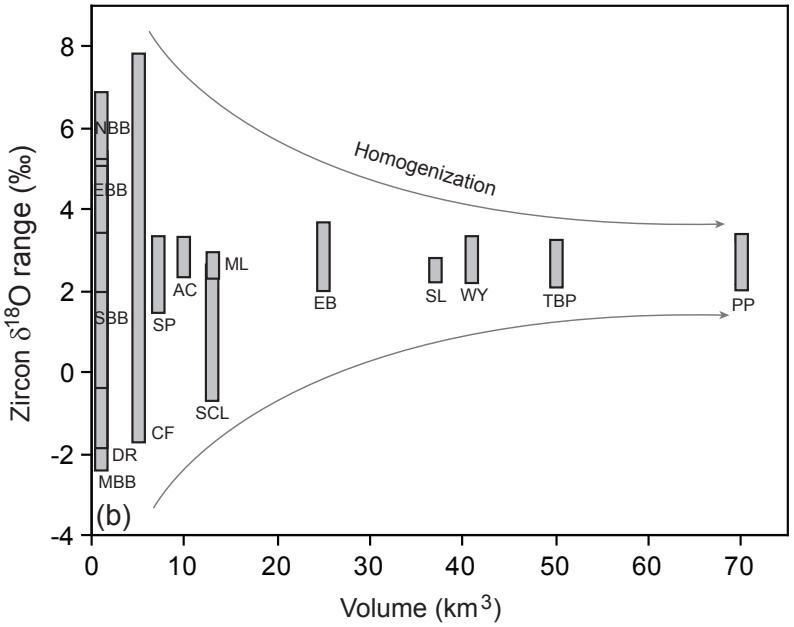
Homogenization
NBB
EBB
SBB
DR
MBB
CF
SP
AC
ML
SCL
EB
SL
WY
TBP
PP
(b)
Zircon δ18O range (‰)
Volume (km3)

zircon homogeneity and eruptive volume, in which more voluminous post-caldera rhyolites tend to have narrower zircon $\delta^{18}O$ ranges (Fig. 5b).

### 4.2. Lead isotope compositions of individual sanidines

#### 4.2.1. Major caldera-forming tuffs

Lead isotope compositions of HRT and LCT sanidines define separate arrays that can be used to differentiate individual units (Fig. 6a). Similar results have been reported for groundmass glasses of HRT and LCT, in which case Pb isotopes can be used to distinguish different compositional fields of tuff members (Doe et al., 1982; Hildreth et al., 1991). Our new Pb isotope data for individual sanidines of HRT members B and C prove that these isotopic differences also exist on the crystal scale, and as found for the groundmass glass, HRT member C has an exceptionally radiogenic Pb isotope signature that is unlike any other Yellowstone unit (Fig. 6a). In contrast, HRT member B has the least radiogenic Pb isotope signature of the units analyzed in this study and it exhibits less phenocrystic heterogeneity than HRT member C or LCT member A (Fig. 6a). This may be due to a lesser degree of crustal contamination in HRT member B relative to other tuff members (Hildreth et al., 1991).

#### 4.2.2. Central Plateau Member rhyolites

The isotopic array defined by CPM sanidines is distinct from those of the caldera-forming tuffs that predate them (Fig. 6a). The fact that the CPM sanidine field does not intersect the LCT field (Fig. 6a) indicates that CPM rhyolites cannot be magmatic remnants of the LCT batholith, as originally proposed by Hildreth et al. (1984). However,

**Figure 6.** (a) Lead isotope compositions of individual Yellowstone sanidines determined by laser ablation (see Table 2 for data). Host glass analyses for Central Plateau Member (CPM) units are shown by the open symbols. Distinct lead isotope compositions are apparent for Huckleberry Ridge Tuff members B and C (HRT-B and HRT-C), Lava Creek Tuff member A (LCT-A), and CPM rhyolites. Note that post-LCT CPM rhyolites do not overlap the LCT compositional array, and therefore cannot be remnants of LCT magma that remained after caldera collapse. (b) Higher resolution version of panel (a), showing lead isotope variation within the CPM rhyolite group. Note that the Pitchstone Plateau flow sanidines and glasses (filled and open circles) form a distinct lead isotope end member in the CPM array and have more homogeneous lead isotope compositions than other CPM units. The average external error (± 1σ) for lead isotope analyses is shown in the bottom right corner.

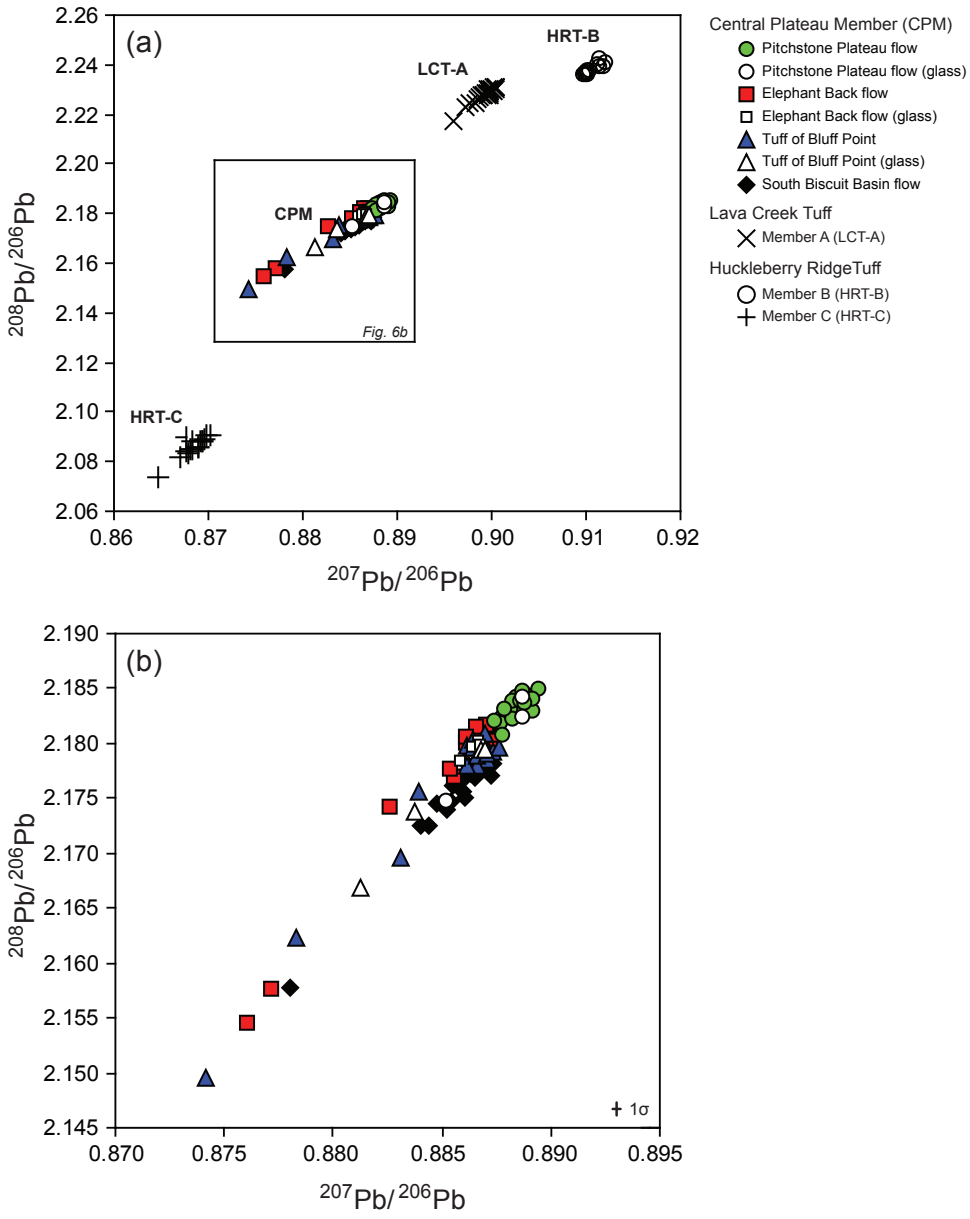
(a)
HRT-B
LCT-A
CPM
Fig. 6b
HRT-C
2.26
2.24
2.22
2.20
2.18
2.16
2.14
2.12
2.10
2.08
2.06
0.86
0.87
0.88
0.89
0.90
0.91
0.92
208Pb/206Pb
207Pb/206Pb
Central Plateau Member (CPM)
Pitchstone Plateau flow
Pitchstone Plateau flow (glass)
Elephant Back flow
Elephant Back flow (glass)
Tuff of Bluff Point
Tuff of Bluff Point (glass)
South Biscuit Basin flow
Lava Creek Tuff
Member A (LCT-A)
Huckleberry RidgeTuff
Member B (HRT-B)
Member C (HRT-C)
(b)
1σ
2.190
2.185
2.180
2.175
2.170
2.165
2.160
2.155
2.150
2.145
0.870
0.875
0.880
0.885
0.890
0.895
208Pb/206Pb
207Pb/206Pb

**Table 2.** Pb isotopes of sanidines in studied Yellowstone rhyolites

| Sample | $^{206}Pb/^{204}Pb$ | ±1σ ext | $^{207}Pb/^{204}Pb$ | ±1σ ext | $^{208}Pb/^{204}Pb$ | ±1σ ext | $^{207}Pb/^{206}Pb$ | ±1σ ext | $^{208}Pb/^{206}Pb$ | ±1σ ext |
|---|---|---|---|---|---|---|---|---|---|---|
| **Pitchstone Plateau flow (YL02-1)** | | | | | | | | | | |
| YL02-1_1.1 | 13.37 | 0.32 | 11.89 | 0.29 | 29.07 | 0.72 | 0.8889 | 0.0006 | 2.1844 | 0.0009 |
| YL02-1_1.2 | 13.02 | 0.32 | 11.58 | 0.29 | 28.33 | 0.72 | 0.8883 | 0.0006 | 2.1837 | 0.0009 |
| YL02-1_1.3 | 13.46 | 0.32 | 11.96 | 0.29 | 29.25 | 0.72 | 0.8887 | 0.0006 | 2.1838 | 0.0009 |
| YL02-1_1.4 | 13.51 | 0.32 | 11.99 | 0.29 | 29.36 | 0.72 | 0.8884 | 0.0006 | 2.1839 | 0.0009 |
| YL02-1_2.1 | 14.27 | 0.32 | 12.67 | 0.29 | 31.02 | 0.72 | 0.8884 | 0.0006 | 2.1830 | 0.0009 |
| YL02-1_2.2 | 14.07 | 0.32 | 12.50 | 0.29 | 30.62 | 0.72 | 0.8884 | 0.0006 | 2.1841 | 0.0009 |
| YL02-1_2.3 | 14.24 | 0.32 | 12.66 | 0.29 | 30.99 | 0.72 | 0.8889 | 0.0006 | 2.1836 | 0.0009 |
| YL02-1_4.1 | 11.88 | 0.32 | 10.52 | 0.29 | 25.76 | 0.72 | 0.8878 | 0.0006 | 2.1823 | 0.0009 |
| YL02-1_4.2 | 12.62 | 0.32 | 11.20 | 0.29 | 27.39 | 0.72 | 0.8882 | 0.0006 | 2.1831 | 0.0009 |
| YL02-1_4.3 | 12.28 | 0.32 | 10.91 | 0.29 | 26.68 | 0.72 | 0.8882 | 0.0006 | 2.1837 | 0.0009 |
| YL02-1_5.1 | 12.13 | 0.32 | 10.77 | 0.29 | 26.30 | 0.72 | 0.8892 | 0.0006 | 2.1830 | 0.0009 |
| YL02-1_5.2 | 8.24 | 0.32 | 7.31 | 0.29 | 17.69 | 0.72 | 0.8887 | 0.0006 | 2.1846 | 0.0009 |
| YL02-1_5.3 | 11.75 | 0.32 | 10.41 | 0.29 | 25.47 | 0.72 | 0.8888 | 0.0006 | 2.1837 | 0.0009 |
| YL02-1_6.1 | 11.37 | 0.32 | 10.09 | 0.29 | 24.60 | 0.72 | 0.8877 | 0.0006 | 2.1818 | 0.0009 |
| YL02-1_6.2 | 11.83 | 0.32 | 10.50 | 0.29 | 25.63 | 0.72 | 0.8883 | 0.0006 | 2.1822 | 0.0009 |
| YL02-1_6.3 | 11.74 | 0.32 | 10.43 | 0.29 | 25.43 | 0.72 | 0.8886 | 0.0006 | 2.1837 | 0.0009 |
| YL02-1_7.1 | 10.97 | 0.32 | 9.72 | 0.29 | 23.78 | 0.72 | 0.8879 | 0.0006 | 2.1832 | 0.0009 |
| YL02-1_7.2 | 11.61 | 0.32 | 10.29 | 0.29 | 25.15 | 0.72 | 0.8874 | 0.0006 | 2.1820 | 0.0009 |
| YL02-1_7.3 | 12.55 | 0.32 | 11.13 | 0.29 | 27.21 | 0.72 | 0.8878 | 0.0006 | 2.1808 | 0.0009 |
| YL02-1_8.1 | 12.48 | 0.32 | 11.07 | 0.29 | 27.09 | 0.72 | 0.8895 | 0.0006 | 2.1849 | 0.0009 |
| YL02-1_8.2 | 12.55 | 0.32 | 11.14 | 0.29 | 27.23 | 0.72 | 0.8892 | 0.0006 | 2.1839 | 0.0009 |
| YL02-1_8.3 | 12.77 | 0.32 | 11.34 | 0.29 | 27.72 | 0.72 | 0.8888 | 0.0006 | 2.1837 | 0.0009 |
| YL02-1_glass-1 | 13.75 | 0.32 | 12.22 | 0.29 | 29.90 | 0.72 | 0.8887 | 0.0006 | 2.1823 | 0.0009 |
| YL02-1_glass-2 | 12.48 | 0.32 | 11.04 | 0.29 | 26.99 | 0.72 | 0.8853 | 0.0006 | 2.1748 | 0.0009 |
| YL02-1_glass-3 | 12.70 | 0.32 | 11.24 | 0.29 | 27.53 | 0.72 | 0.8887 | 0.0006 | 2.1841 | 0.0009 |
| **Elephant Back flow (06YS-4)** | | | | | | | | | | |
| 06YS-4_2.1 | 11.28 | 0.18 | 9.88 | 0.16 | 24.13 | 0.38 | 0.8772 | 0.0004 | 2.1575 | 0.0012 |
| 06YS-4_2.2 | 11.52 | 0.18 | 10.20 | 0.16 | 24.93 | 0.38 | 0.8870 | 0.0004 | 2.1816 | 0.0012 |
| 06YS-4_2.3 | 11.65 | 0.18 | 10.20 | 0.16 | 24.93 | 0.38 | 0.8760 | 0.0004 | 2.1545 | 0.0012 |
| 06YS-4_2.4 | 11.40 | 0.18 | 10.08 | 0.16 | 24.63 | 0.38 | 0.8868 | 0.0004 | 2.1798 | 0.0012 |
| 06YS-4_3.1 | 8.79 | 0.18 | 7.75 | 0.16 | 18.86 | 0.38 | 0.8865 | 0.0004 | 2.1801 | 0.0012 |
| 06YS-4_3.2 | 8.16 | 0.18 | 7.18 | 0.16 | 17.46 | 0.38 | 0.8862 | 0.0004 | 2.1801 | 0.0012 |
| 06YS-4_3.3 | 10.43 | 0.18 | 9.22 | 0.16 | 22.49 | 0.38 | 0.8869 | 0.0004 | 2.1798 | 0.0012 |
| 06YS-4_4.1 | 11.08 | 0.18 | 9.79 | 0.16 | 23.91 | 0.38 | 0.8867 | 0.0004 | 2.1796 | 0.0012 |
| 06YS-4_4.2 | 11.82 | 0.18 | 10.47 | 0.16 | 25.56 | 0.38 | 0.8874 | 0.0004 | 2.1802 | 0.0012 |
| 06YS-4_4.3 | 12.59 | 0.18 | 11.15 | 0.16 | 27.25 | 0.38 | 0.8870 | 0.0004 | 2.1792 | 0.0012 |
| 06YS-4_5.1 | 12.38 | 0.18 | 10.96 | 0.16 | 26.80 | 0.38 | 0.8865 | 0.0004 | 2.1795 | 0.0012 |
| 06YS-4_5.2 | 12.77 | 0.18 | 11.31 | 0.16 | 27.67 | 0.38 | 0.8867 | 0.0004 | 2.1806 | 0.0012 |
| 06YS-4_5.3 | 13.18 | 0.18 | 11.68 | 0.16 | 28.58 | 0.38 | 0.8868 | 0.0004 | 2.1794 | 0.0012 |
| 06YS-4_6.1 | 8.96 | 0.18 | 7.87 | 0.16 | 19.19 | 0.38 | 0.8827 | 0.0004 | 2.1742 | 0.0012 |
| 06YS-4_6.2 | 10.61 | 0.18 | 9.37 | 0.16 | 22.87 | 0.38 | 0.8856 | 0.0004 | 2.1769 | 0.0012 |
| 06YS-4_6.3 | 11.70 | 0.18 | 10.32 | 0.16 | 25.28 | 0.38 | 0.8854 | 0.0004 | 2.1776 | 0.0012 |
| 06YS-4_7.1 | 10.36 | 0.18 | 9.16 | 0.16 | 22.36 | 0.38 | 0.8866 | 0.0004 | 2.1815 | 0.0012 |
| 06YS-4_7.2 | 13.19 | 0.18 | 11.70 | 0.16 | 28.60 | 0.38 | 0.8873 | 0.0004 | 2.1793 | 0.0012 |
| 06YS-4_7.3 | 9.93 | 0.18 | 8.78 | 0.16 | 21.40 | 0.38 | 0.8861 | 0.0004 | 2.1805 | 0.0012 |
| 06YS-4_glass-1 | 11.41 | 0.18 | 10.07 | 0.16 | 24.65 | 0.38 | 0.8859 | 0.0004 | 2.1784 | 0.0012 |
| 06YS-4_glass-2 | 14.42 | 0.18 | 12.79 | 0.16 | 31.33 | 0.38 | 0.8867 | 0.0004 | 2.1801 | 0.0012 |
| 06YS-4_glass-3 | 8.54 | 0.18 | 7.53 | 0.16 | 18.31 | 0.38 | 0.8864 | 0.0004 | 2.1796 | 0.0012 |
| 06YS-4_glass-4 | 11.07 | 0.18 | 9.79 | 0.16 | 23.90 | 0.38 | 0.8868 | 0.0004 | 2.1797 | 0.0012 |
| **Tuff of Bluff Point (06YS-2)** | | | | | | | | | | |
| 06YS-2_1.1 | 12.53 | 0.18 | 11.09 | 0.16 | 27.13 | 0.38 | 0.8863 | 0.0004 | 2.1796 | 0.0012 |
| 06YS-2_1.2 | 12.36 | 0.18 | 10.95 | 0.16 | 26.75 | 0.38 | 0.8871 | 0.0004 | 2.1793 | 0.0012 |
| 06YS-2_1.3 | 12.88 | 0.18 | 11.40 | 0.16 | 27.90 | 0.38 | 0.8862 | 0.0004 | 2.1797 | 0.0012 |
| 06YS-2_1.4 | 12.76 | 0.18 | 11.30 | 0.16 | 27.65 | 0.38 | 0.8869 | 0.0004 | 2.1809 | 0.0012 |
| 06YS-2_3.1 | 7.42 | 0.18 | 6.53 | 0.16 | 15.83 | 0.38 | 0.8865 | 0.0004 | 2.1804 | 0.0012 |
| 06YS-2_3.2 | 7.46 | 0.18 | 6.56 | 0.16 | 15.91 | 0.38 | 0.8867 | 0.0004 | 2.1798 | 0.0012 |
| 06YS-2_3.3 | 8.12 | 0.18 | 7.16 | 0.16 | 17.36 | 0.38 | 0.8870 | 0.0004 | 2.1786 | 0.0012 |
| 06YS-2_3.4 | 8.16 | 0.18 | 7.19 | 0.16 | 17.45 | 0.38 | 0.8871 | 0.0004 | 2.1793 | 0.0012 |
| 06YS-2_4.1 | 8.24 | 0.18 | 7.26 | 0.16 | 17.64 | 0.38 | 0.8864 | 0.0004 | 2.1796 | 0.0012 |
| 06YS-2_4.2 | 8.76 | 0.18 | 7.72 | 0.16 | 18.77 | 0.38 | 0.8866 | 0.0004 | 2.1779 | 0.0012 |
| 06YS-2_4.3 | 8.46 | 0.18 | 7.47 | 0.16 | 18.13 | 0.38 | 0.8874 | 0.0004 | 2.1793 | 0.0012 |
| 06YS-2_5.1 | 11.23 | 0.18 | 9.92 | 0.16 | 24.23 | 0.38 | 0.8861 | 0.0004 | 2.1779 | 0.0012 |
| 06YS-2_5.2 | 11.18 | 0.18 | 9.89 | 0.16 | 24.14 | 0.38 | 0.8866 | 0.0004 | 2.1789 | 0.0012 |
| 06YS-2_5.3 | 11.81 | 0.18 | 10.45 | 0.16 | 25.53 | 0.38 | 0.8871 | 0.0004 | 2.1790 | 0.0012 |
| 06YS-2_6.1 | 6.42 | 0.18 | 5.57 | 0.16 | 13.45 | 0.38 | 0.8742 | 0.0004 | 2.1495 | 0.0012 |
| 06YS-2_6.2 | 7.17 | 0.18 | 6.29 | 0.16 | 15.22 | 0.38 | 0.8831 | 0.0004 | 2.1696 | 0.0012 |
| 06YS-2_6.3 | 11.34 | 0.18 | 10.01 | 0.16 | 24.46 | 0.38 | 0.8839 | 0.0004 | 2.1755 | 0.0012 |
| 06YS-2_6.4 | 8.53 | 0.18 | 7.46 | 0.16 | 18.15 | 0.38 | 0.8783 | 0.0004 | 2.1623 | 0.0012 |
| 06YS-2_9.1 | 10.37 | 0.18 | 9.17 | 0.16 | 22.35 | 0.38 | 0.8876 | 0.0004 | 2.1795 | 0.0012 |
| 06YS-2_glass-1 | 8.44 | 0.18 | 7.44 | 0.16 | 18.07 | 0.38 | 0.8868 | 0.0004 | 2.1795 | 0.0012 |
| 06YS-2_glass-2 | 5.37 | 0.18 | 4.70 | 0.16 | 11.29 | 0.38 | 0.8870 | 0.0004 | 2.1794 | 0.0012 |
| 06YS-2_glass-3 | 4.56 | 0.18 | 3.95 | 0.16 | 9.45 | 0.38 | 0.8813 | 0.0004 | 2.1668 | 0.0012 |
| 06YS-2_glass-4 | 5.41 | 0.18 | 4.70 | 0.16 | 11.34 | 0.38 | 0.8837 | 0.0004 | 2.1737 | 0.0012 |

## Table 2. (continued).

| | | | | | | | | | | |
|---|---|---|---|---|---|---|---|---|---|---|
| **South Biscuit Basin flow (YL96-2)** | | | | | | | | | | |
| YL96-2_1.1 | 11.18 | 0.18 | 9.90 | 0.16 | 24.17 | 0.38 | 0.8872 | 0.0004 | 2.1811 | 0.0012 |
| YL96-2_1.2 | 14.02 | 0.18 | 12.44 | 0.16 | 30.43 | 0.38 | 0.8867 | 0.0004 | 2.1786 | 0.0012 |
| YL96-2_1.3 | 14.16 | 0.18 | 12.55 | 0.16 | 30.69 | 0.38 | 0.8863 | 0.0004 | 2.1779 | 0.0012 |
| YL96-2_1.4 | 14.42 | 0.18 | 12.80 | 0.16 | 31.33 | 0.38 | 0.8869 | 0.0004 | 2.1782 | 0.0012 |
| YL96-2_2.1 | 14.40 | 0.18 | 12.77 | 0.16 | 31.25 | 0.38 | 0.8865 | 0.0004 | 2.1769 | 0.0012 |
| YL96-2_2.2 | 14.87 | 0.18 | 13.17 | 0.16 | 32.25 | 0.38 | 0.8861 | 0.0004 | 2.1770 | 0.0012 |
| YL96-2_2.3 | 14.99 | 0.18 | 13.28 | 0.16 | 32.54 | 0.38 | 0.8858 | 0.0004 | 2.1768 | 0.0012 |
| YL96-2_3.1 | 14.20 | 0.18 | 12.56 | 0.16 | 30.76 | 0.38 | 0.8848 | 0.0004 | 2.1745 | 0.0012 |
| YL96-2_3.2 | 14.52 | 0.18 | 12.86 | 0.16 | 31.48 | 0.38 | 0.8852 | 0.0004 | 2.1739 | 0.0012 |
| YL96-2_3.3 | 15.34 | 0.18 | 13.59 | 0.16 | 33.28 | 0.38 | 0.8854 | 0.0004 | 2.1747 | 0.0012 |
| YL96-2_4.1 | 14.56 | 0.18 | 12.90 | 0.16 | 31.58 | 0.38 | 0.8860 | 0.0004 | 2.1757 | 0.0012 |
| YL96-2_4.2 | 14.90 | 0.18 | 13.22 | 0.16 | 32.36 | 0.38 | 0.8869 | 0.0004 | 2.1778 | 0.0012 |
| YL96-2_4.3 | 15.18 | 0.18 | 13.45 | 0.16 | 32.95 | 0.38 | 0.8863 | 0.0004 | 2.1773 | 0.0012 |
| YL96-2_5.1 | 11.22 | 0.18 | 9.92 | 0.16 | 24.21 | 0.38 | 0.8866 | 0.0004 | 2.1778 | 0.0012 |
| YL96-2_5.2 | 12.25 | 0.18 | 10.85 | 0.16 | 26.49 | 0.38 | 0.8869 | 0.0004 | 2.1778 | 0.0012 |
| YL96-2_5.3 | 11.48 | 0.18 | 10.15 | 0.16 | 24.86 | 0.38 | 0.8860 | 0.0004 | 2.1751 | 0.0012 |
| YL96-2_6.1 | 14.29 | 0.18 | 12.66 | 0.16 | 30.99 | 0.38 | 0.8864 | 0.0004 | 2.1772 | 0.0012 |
| YL96-2_6.2 | 14.68 | 0.18 | 13.03 | 0.16 | 31.87 | 0.38 | 0.8860 | 0.0004 | 2.1770 | 0.0012 |
| YL96-2_6.3 | 14.61 | 0.18 | 12.95 | 0.16 | 31.73 | 0.38 | 0.8863 | 0.0004 | 2.1779 | 0.0012 |
| YL96-2_7.1 | 10.25 | 0.18 | 8.98 | 0.16 | 21.89 | 0.38 | 0.8780 | 0.0004 | 2.1578 | 0.0012 |
| YL96-2_7.2 | 10.40 | 0.18 | 9.18 | 0.16 | 22.38 | 0.38 | 0.8840 | 0.0004 | 2.1724 | 0.0012 |
| YL96-2_7.3 | 10.89 | 0.18 | 9.61 | 0.16 | 23.44 | 0.38 | 0.8844 | 0.0004 | 2.1725 | 0.0012 |
| YL96-2_8.1 | 13.25 | 0.18 | 11.74 | 0.16 | 28.69 | 0.38 | 0.8855 | 0.0004 | 2.1762 | 0.0012 |
| YL96-2_8.2 | 13.78 | 0.18 | 12.22 | 0.16 | 29.88 | 0.38 | 0.8873 | 0.0004 | 2.1771 | 0.0012 |
| YL96-2_8.3 | 14.12 | 0.18 | 12.52 | 0.16 | 30.63 | 0.38 | 0.8874 | 0.0004 | 2.1782 | 0.0012 |
| **Lava Creek Tuff, Member A (LCT-3A)** | | | | | | | | | | |
| LCT-3A_1.1 | 16.20 | 0.32 | 14.57 | 0.29 | 36.01 | 0.72 | 0.8996 | 0.0006 | 2.2298 | 0.0009 |
| LCT-3A_1.2 | 16.13 | 0.32 | 14.50 | 0.29 | 35.84 | 0.72 | 0.8989 | 0.0006 | 2.2279 | 0.0009 |
| LCT-3A_1.3 | 16.66 | 0.32 | 14.99 | 0.29 | 37.02 | 0.72 | 0.8986 | 0.0006 | 2.2261 | 0.0009 |
| LCT-3A_1.4 | 16.50 | 0.32 | 14.85 | 0.29 | 36.67 | 0.72 | 0.8996 | 0.0006 | 2.2273 | 0.0009 |
| LCT-3A_2.1 | 16.52 | 0.32 | 14.87 | 0.29 | 36.79 | 0.72 | 0.8998 | 0.0006 | 2.2298 | 0.0009 |
| LCT-3A_2.2 | 16.68 | 0.32 | 15.02 | 0.29 | 37.12 | 0.72 | 0.9004 | 0.0006 | 2.2312 | 0.0009 |
| LCT-3A_2.3 | 16.70 | 0.32 | 15.03 | 0.29 | 37.20 | 0.72 | 0.8999 | 0.0006 | 2.2299 | 0.0009 |
| LCT-3A_3.1 | 16.59 | 0.32 | 14.91 | 0.29 | 36.87 | 0.72 | 0.8992 | 0.0006 | 2.2277 | 0.0009 |
| LCT-3A_3.2 | 16.75 | 0.32 | 15.07 | 0.29 | 37.26 | 0.72 | 0.8995 | 0.0006 | 2.2289 | 0.0009 |
| LCT-3A_3.3 | 16.80 | 0.32 | 15.14 | 0.29 | 37.39 | 0.72 | 0.8998 | 0.0006 | 2.2293 | 0.0009 |
| LCT-3A_4.1 | 16.68 | 0.32 | 14.97 | 0.29 | 37.01 | 0.72 | 0.8972 | 0.0006 | 2.2229 | 0.0009 |
| LCT-3A_4.2 | 16.80 | 0.32 | 15.12 | 0.29 | 37.32 | 0.72 | 0.8992 | 0.0006 | 2.2279 | 0.0009 |
| LCT-3A_4.3 | 16.86 | 0.32 | 15.19 | 0.29 | 37.50 | 0.72 | 0.8994 | 0.0006 | 2.2283 | 0.0009 |
| LCT-3A_5.1 | 16.69 | 0.32 | 15.01 | 0.29 | 37.12 | 0.72 | 0.8997 | 0.0006 | 2.2292 | 0.0009 |
| LCT-3A_5.2 | 16.77 | 0.32 | 15.11 | 0.29 | 37.34 | 0.72 | 0.9004 | 0.0006 | 2.2304 | 0.0009 |
| LCT-3A_5.3 | 16.84 | 0.32 | 15.17 | 0.29 | 37.48 | 0.72 | 0.9004 | 0.0006 | 2.2306 | 0.0009 |
| LCT-3A_6.1 | 16.75 | 0.32 | 15.08 | 0.29 | 37.27 | 0.72 | 0.8999 | 0.0006 | 2.2279 | 0.0009 |
| LCT-3A_6.2 | 16.74 | 0.32 | 15.08 | 0.29 | 37.24 | 0.72 | 0.9002 | 0.0006 | 2.2290 | 0.0009 |
| LCT-3A_6.3 | 16.88 | 0.32 | 15.18 | 0.29 | 37.56 | 0.72 | 0.8997 | 0.0006 | 2.2281 | 0.0009 |
| LCT-3A_7.1 | 16.60 | 0.32 | 14.90 | 0.29 | 36.74 | 0.72 | 0.8959 | 0.0006 | 2.2175 | 0.0009 |
| LCT-3A_7.2 | 16.75 | 0.32 | 15.06 | 0.29 | 37.24 | 0.72 | 0.8977 | 0.0006 | 2.2244 | 0.0009 |
| LCT-3A_7.3 | 16.74 | 0.32 | 15.03 | 0.29 | 37.14 | 0.72 | 0.8983 | 0.0006 | 2.2249 | 0.0009 |
| LCT-3A_8.1 | 17.06 | 0.32 | 15.34 | 0.29 | 37.93 | 0.72 | 0.8988 | 0.0006 | 2.2270 | 0.0009 |
| LCT-3A_8.2 | 17.05 | 0.32 | 15.38 | 0.29 | 38.03 | 0.72 | 0.9002 | 0.0006 | 2.2312 | 0.0009 |
| LCT-3A_8.3 | 16.85 | 0.32 | 15.18 | 0.29 | 37.53 | 0.72 | 0.8998 | 0.0006 | 2.2293 | 0.0009 |
| **Huckleberry Ridge Tuff, Member B (HRT-1)** | | | | | | | | | | |
| HRT-1_1.1 | 16.14 | 0.32 | 14.65 | 0.29 | 35.90 | 0.72 | 0.9099 | 0.0006 | 2.2361 | 0.0009 |
| HRT-1_1.2 | 16.40 | 0.32 | 14.94 | 0.29 | 36.63 | 0.72 | 0.9101 | 0.0006 | 2.2372 | 0.0009 |
| HRT-1_1.3 | 16.62 | 0.32 | 15.13 | 0.29 | 37.11 | 0.72 | 0.9121 | 0.0006 | 2.2405 | 0.0009 |
| HRT-1_2.1 | 16.12 | 0.32 | 14.64 | 0.29 | 35.94 | 0.72 | 0.9097 | 0.0006 | 2.2359 | 0.0009 |
| HRT-1_2.2 | 16.25 | 0.32 | 14.78 | 0.29 | 36.24 | 0.72 | 0.9100 | 0.0006 | 2.2366 | 0.0009 |
| HRT-1_2.3 | 16.05 | 0.32 | 14.63 | 0.29 | 35.90 | 0.72 | 0.9118 | 0.0006 | 2.2391 | 0.0009 |
| HRT-1_3.1 | 15.95 | 0.32 | 14.52 | 0.29 | 35.59 | 0.72 | 0.9102 | 0.0006 | 2.2356 | 0.0009 |
| HRT-1_3.2 | 16.17 | 0.32 | 14.73 | 0.29 | 36.11 | 0.72 | 0.9115 | 0.0006 | 2.2392 | 0.0009 |
| HRT-1_3.3 | 16.30 | 0.32 | 14.82 | 0.29 | 36.34 | 0.72 | 0.9103 | 0.0006 | 2.2364 | 0.0009 |
| HRT-1_4.1 | 16.21 | 0.32 | 14.75 | 0.29 | 36.17 | 0.72 | 0.9105 | 0.0006 | 2.2376 | 0.0009 |
| HRT-1_4.2 | 16.20 | 0.32 | 14.75 | 0.29 | 36.19 | 0.72 | 0.9113 | 0.0006 | 2.2401 | 0.0009 |
| HRT-1_4.3 | 16.24 | 0.32 | 14.78 | 0.29 | 36.26 | 0.72 | 0.9116 | 0.0006 | 2.2422 | 0.0009 |
| **Huckleberry Ridge Tuff, Member C (HRT-C)** | | | | | | | | | | |
| HRT-C_3.1 | 17.40 | 0.32 | 15.18 | 0.29 | 36.46 | 0.72 | 0.8693 | 0.0006 | 2.088 | 0.0009 |
| HRT-C_3.2 | 17.47 | 0.32 | 15.27 | 0.29 | 36.69 | 0.72 | 0.8702 | 0.0006 | 2.090 | 0.0009 |
| HRT-C_3.3 | 17.08 | 0.32 | 14.90 | 0.29 | 35.78 | 0.72 | 0.8695 | 0.0006 | 2.089 | 0.0009 |
| HRT-C_5.1 | 17.72 | 0.32 | 15.44 | 0.29 | 37.09 | 0.72 | 0.8682 | 0.0006 | 2.085 | 0.0009 |
| HRT-C_5.2 | 17.79 | 0.32 | 15.49 | 0.29 | 37.23 | 0.72 | 0.8690 | 0.0006 | 2.086 | 0.0009 |
| HRT-C_5.3 | 17.71 | 0.32 | 15.44 | 0.29 | 37.10 | 0.72 | 0.8688 | 0.0006 | 2.086 | 0.0009 |
| HRT-C_6.1 | 17.56 | 0.32 | 15.30 | 0.29 | 36.74 | 0.72 | 0.8682 | 0.0006 | 2.085 | 0.0009 |
| HRT-C_6.2 | 17.58 | 0.32 | 15.31 | 0.29 | 36.76 | 0.72 | 0.8676 | 0.0006 | 2.084 | 0.0009 |
| HRT-C_6.3 | 17.70 | 0.32 | 15.42 | 0.29 | 37.03 | 0.72 | 0.8679 | 0.0006 | 2.083 | 0.0009 |
| HRT-C_7.1 | 14.30 | 0.32 | 12.44 | 0.29 | 29.89 | 0.72 | 0.8682 | 0.0006 | 2.088 | 0.0009 |

**Table 2. (continued).**

| | | | | | | | | | | |
|---|---|---|---|---|---|---|---|---|---|---|
| HRT-C_7.2 | 16.96 | 0.32 | 14.79 | 0.29 | 35.55 | 0.72 | 0.8697 | 0.0006 | 2.090 | 0.0009 |
| HRT-C_7.3 | 15.59 | 0.32 | 13.56 | 0.29 | 32.63 | 0.72 | 0.8677 | 0.0006 | 2.090 | 0.0009 |
| HRT-C_8.1 | 16.87 | 0.32 | 15.20 | 0.29 | 37.36 | 0.72 | 0.9017 | 0.0006 | 2.221 | 0.0009 |
| HRT-C_8.2 | 16.95 | 0.32 | 15.29 | 0.29 | 37.59 | 0.72 | 0.9020 | 0.0006 | 2.221 | 0.0009 |
| HRT-C_8.3 | 16.86 | 0.32 | 15.21 | 0.29 | 37.38 | 0.72 | 0.9016 | 0.0006 | 2.220 | 0.0009 |
| HRT-C_9.1 | 17.49 | 0.32 | 15.24 | 0.29 | 36.63 | 0.72 | 0.8691 | 0.0006 | 2.088 | 0.0009 |
| HRT-C_10.1 | 18.22 | 0.32 | 15.81 | 0.29 | 37.94 | 0.72 | 0.8647 | 0.0006 | 2.073 | 0.0009 |
| HRT-C_11.1 | 18.01 | 0.32 | 15.67 | 0.29 | 37.63 | 0.72 | 0.8671 | 0.0006 | 2.082 | 0.0009 |
| HRT-C_12.1 | 17.78 | 0.32 | 15.50 | 0.29 | 37.25 | 0.72 | 0.8694 | 0.0006 | 2.088 | 0.0009 |

Uncertainties of Pb isotope ratios are ± 1σ external errors for a NIST 612 glass standard (Baker et al., 2004). We note that HRT-C grain 8 is an outlier and not included in Fig. 6a.

the CPM field does fall between the HRT and LCT fields (Fig. 6a), consistent with the interpretations of Bindeman et al. (2008) for derivation of post-LCT rhyolites from remelting of HRT, LCT and pre-LCT intracaldera rocks. Similar to the results reported for Pb isotope compositions of CPM groundmass glasses (Doe et al., 1982; Hildreth et al., 1991; Vazquez et al., 2009), the CPM sanidines analyzed in this study have overlapping Pb isotope compositions (Fig. 6a and b). Glass analyses from our in-situ rhyolite mounts fall within the Pb isotope fields defined by the sanidines for each CPM unit (Fig. 6b). We observe that the Elephant Back flow, Tuff of Bluff Point and South Biscuit Basin flow have more heterogeneous sanidine compositions than the Pitchstone Plateau flow, which has sanidines that form a less radiogenic Pb isotopic end member in the CPM array (Fig. 6b).

### 4.3. Thermometry of analyzed rhyolites

We determined zircon saturation temperatures and liquidus temperatures for all analyzed rhyolites and synthesized this new data with temperature data published by Bindeman and Valley (2001) and Vazquez et al. (2009) (Fig. 7). When temperatures are plotted against melt $\delta^{18}O$ values for individual UBM units, we find that they have similar oxygen isotope compositions and temperature ranges (~820-900°C), and that the most

primitive East Biscuit Basin flow also has the highest liquidus temperature (~940°C) (Fig. 7a). Temperatures and melt $\delta^{18}O$ values for CPM rhyolites are more variable than UBM rhyolites, with temperatures that range from ~750-900°C (Fig. 7a). However, this may be due to a greater abundance of thermometry data available for CPM units. We observe a trend of decreasing temperature with increasing melt $\delta^{18}O$ values for CPM rhyolites, but it is important to note that the temperature ranges for individual CPM units are often quite large (e.g., ~100°C for the Solfatara Plateau flow) due to discrepancies between the different geothermometers.

When temperatures of CPM rhyolites are plotted against eruption ages (Fig. 7b), we observe a negative trend through time (i.e., younger rhyolites tend to be cooler). Vazquez et al. (2009) first described this trend using a smaller dataset that is now synthesized with our new data in Fig. 7b. However, as addressed above, the temperature ranges for individual CPM units are quite large, making this trend difficult to confirm. A cumulative eruptive volume curve generated from published eruptive volumes and eruption ages for CPM units (Christiansen et al., 2007) shows an inverse correlation with temperature (Fig. 7b). We observe that a spike in the cumulative eruptive volume curve, following eruption of the very voluminous West Yellowstone flow, marks the point at which temperatures of CPM rhyolites begin to decrease.

**Figure 7.** (a) Temperatures of Upper Basin Member (UBM) and Central Plateau Member (CPM) rhyolites plotted against melt $\delta^{18}O$ values. Symbols show the temperatures derived from different thermometry datasets, synthesized from Bindeman and Valley (2001), Vazquez et al. (2009) and this study (see Appendix Table C1 for temperature data). Melt $\delta^{18}O$ values are taken from Bindeman and Valley (2001), Bindeman et al. (2008) and this study. Temperature-melt $\delta^{18}O$ fields for UBM and CPM rhyolites are shaded. Unit abbreviations are the same as those used in Fig. 5. We tentatively indicate a trend of decreasing temperatures with increasing melt $\delta^{18}O$ values (dashed arrows), however, the temperature ranges for individual units are often quite large (e.g., Solfatara Plateau flow; "SP") making this trend difficult to confirm. (b) Temperature and cumulative eruptive volume of Central Plateau Member (CPM) rhyolites plotted against eruption age. Thermometry symbols are the same as those used in panel (a). Volumes and eruption ages are from Christiansen et al. (2007). The cumulative eruptive volume curve is shown as a black line connected by individual units (black circles). Unit abbreviations are the same as those used in Fig. 5, with the addition of CPM units West Thumb flow (WT), Dry Creek flow (DC), Mary Lake flow (MYL), Buffalo Lake flow (BL), Nez Perce Creek flow (NP), Tuff of Cold Mountain Creek (TCM), Bechler River flow (BC), Hayden Valley flow (HV), and Grants Pass flow (GP). We observe that the temperature curve is negatively correlated with the cumulative eruptive volume curve for CPM rhyolites, perhaps indicating cooling of the CPM magma reservoir as eruptions proceeded in the Yellowstone caldera.

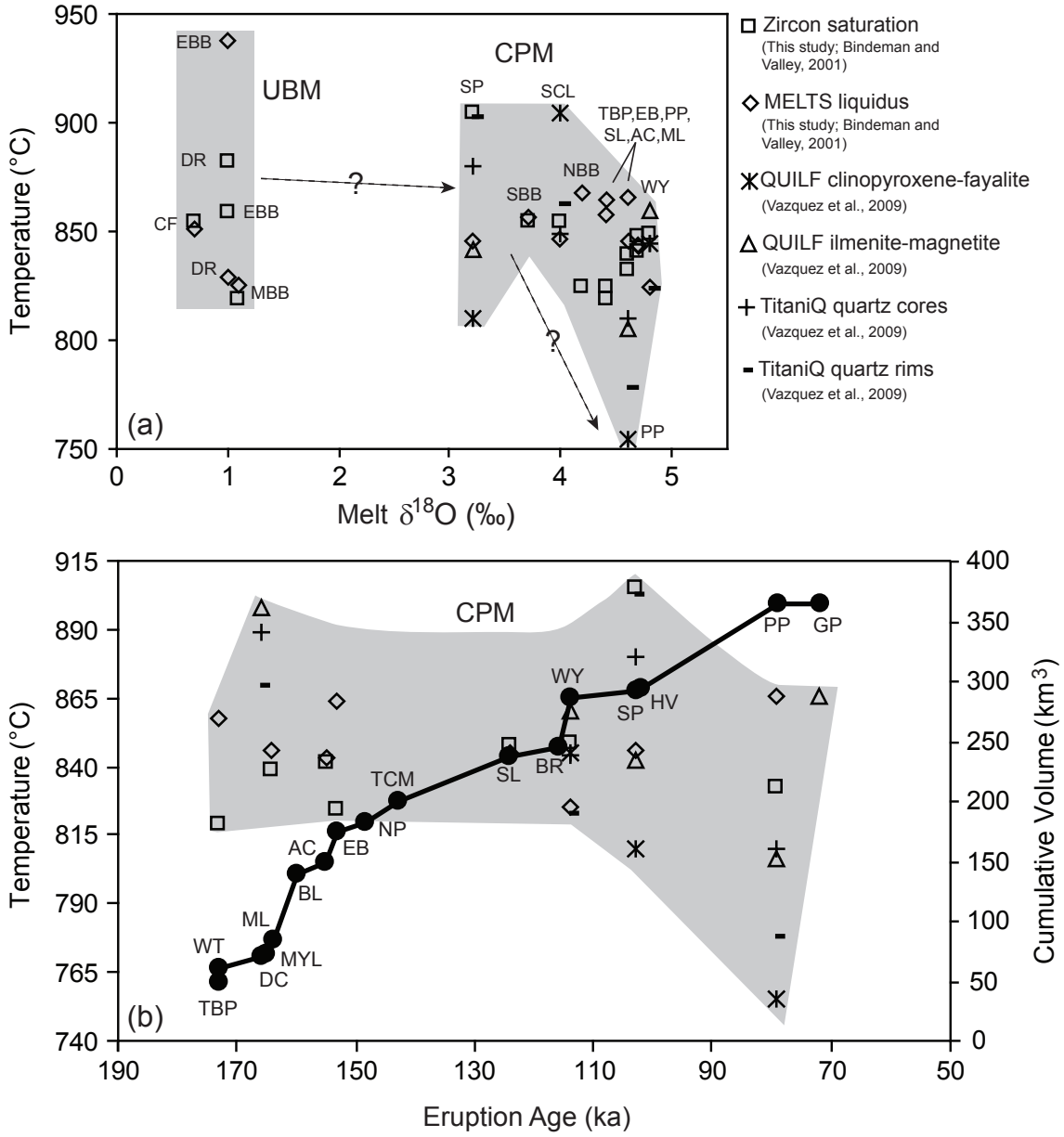
UBM
CPM
EBB
DR
CF
EBB
DR
MBB
SP
SCL
TBP,EB,PP,
SL,AC,ML
NBB
WY
SBB
PP
?
?
(a)
Temperature (°C)
Melt δ18O (‰)
Zircon saturation
(This study; Bindeman and Valley, 2001)
MELTS liquidus
(This study; Bindeman and Valley, 2001)
QUILF clinopyroxene-fayalite
(Vazquez et al., 2009)
QUILF ilmenite-magnetite
(Vazquez et al., 2009)
TitaniQ quartz cores
(Vazquez et al., 2009)
TitaniQ quartz rims
(Vazquez et al., 2009)
CPM
PP
GP
WY
SP
HV
SL
BR
TCM
NP
AC
EB
BL
ML
WT
MYL
DC
TBP
(b)
Temperature (°C)
Cumulative Volume (km3)
Eruption Age (ka)

## 5. Discussion

In the following discussion, we focus on our new age (U-Th and U-Pb) and isotopic (O and Pb) data for post-LCT rhyolites of the Yellowstone caldera. We synthesize our new data with previously published age and geochemical datasets for post-LCT rhyolites to create a unified model of magma genesis. Our discussion is subdivided into three main parts: (1) Model of post-LCT (UBM and CPM) magma genesis; (2) Petrologic, thermal and temporal considerations for CPM magmas; (3) Similarities and differences between CPM rhyolites and the 4.45 Ma Kilgore Tuff of the pre-Yellowstone Heise volcanic field.

### 5.1. Model of post-LCT magma genesis

Our new age and isotopic datasets for CPM rhyolites require several key changes to published post-LCT magma genesis models (Bindeman and Valley, 2000 and 2001; Vazquez and Reid, 2002; Bindeman et al., 2008). The most salient result of this study is that unlike the UBM rhyolites, which were generated from independent parcels of melt with unique oxygen isotopic compositions (Bindeman et al., 2008), many of the voluminous CPM rhyolites have homogeneous oxygen isotopic compositions that permit derivation from a common magma source. There are notable exceptions to this rule, for instance the Scaup Lake flow, South Biscuit Basin flow and Solfatara Plateau flow (Bindeman et al., 2008). However, as we discuss below, the Scaup Lake flow and South Biscuit Basin flow retain important age and isotopic information about the early stages of CPM magma assembly prior to the loss of crystal evidence by convection and homogenization of a large CPM magma reservoir. We discuss our new model for post-

LCT magma genesis chronologically, starting with discussion of the early UBM rhyolite eruptions (~520-470 ka) followed by discussion of the later (~260-75 ka) CPM rhyolite eruptions.

Previous studies of UBM rhyolites (Canyon flow, Dunraven Road flow, Middle Biscuit Basin flow) have shown that they contain a large proportion of zircon xenocrysts with ages and normal-$\delta^{18}O$ values that correspond to HRT, LCT and pre-LCT units (Bindeman et al., 2001; Bindeman et al., 2008). These zircons are not in oxygen isotopic equilibrium with their host low-$\delta^{18}O$ melts, and provide evidence for wholesale remelting of hydrothermally altered ($^{18}O$-depleted in the groundmass) intracaldera rocks of HRT, LCT and pre-LCT protoliths (Bindeman et al., 2008) (Fig. 8). Our new results for the East Biscuit Basin flow indicate that like other UBM units, it contains zircons with a broad age spectrum and normal-$\delta^{18}O$ values that are not in equilibrium with the low-$\delta^{18}O$ host melt, however unlike other UBM units, East Biscuit Basin flow does not contain any zircons with low-$\delta^{18}O$ values or younger (eruption) ages. The East Biscuit Basin flow also has a unique mineralogy and major and trace element geochemistry relative to other UBM units, for instance its lack of sanidine and quartz, lower-silica (~70 wt% $SiO_2$) composition and higher Sr concentration, indicating that it was the first, most primitive rhyolite to erupt with the Yellowstone caldera (Girard and Stix, 2009b). Thermometry results for the East Biscuit Basin flow show that it was also the hottest post-LCT rhyolite (Fig. 7a). Our new zircon data indicate that the East Biscuit Basin flow was generated by rapid remelting of pre-LCT intracaldera protoliths and erupted before a new phase of (low-$\delta^{18}O$) zircon saturation and crystallization could occur.

**Figure 8.** Schematic model of rhyolite genesis at Yellowstone caldera. Eruption of the Lava Creek Tuff ~640 ka caused collapse of the Yellowstone caldera, bringing intracaldera Huckleberry Ridge Tuff (HRT) and Lava Creek Tuff (LCT) rocks in contact with unerupted LCT magma. Hydrothermal circulation cells formed in the intracaldera block, altering rocks with low-$\delta^{18}O$ meteoric fluids. Intracaldera intrusions of unerupted LCT magma caused resurgent doming in the Yellowstone caldera, forming the Mallard Lake and Sour Creek resurgent domes. Melting of intracaldera intrusions and intracaldera rocks formed independent batches of low-$\delta^{18}O$ magma that erupted ~520-470 ka near the Mallard Lake and Sour Creek domes (Upper Basin Member rhyolites). Melting of intracaldera intrusions, intracaldera rocks and Upper Basin Member plutonic remnants formed primitive Central Plateau Member rhyolite batches ~260 ka (South Biscuit Basin (SBB) and Scaup Lake (SCL) flows). The locus of melting expanded in the intracaldera block, and independent rhyolite batches accreted to form a large-volume, low-$\delta^{18}O$ magma reservoir that sourced Central Plateau Member eruptions ~170-75 ka, producing the Tuff of Bluff Point (TBP), Elephant Back flow (EB), North Biscuit Basin flow (NBB), West Yellowstone flow (WY) and Pitchstone Plateau flow (PP). Eruptions became progressively more homogeneous, more evolved and cooler through time. Disparate geochemical data for the Solfatara Plateau flow (SP) indicate that it was derived from an independent magma batch. Modified after Bindeman et al. (2008).

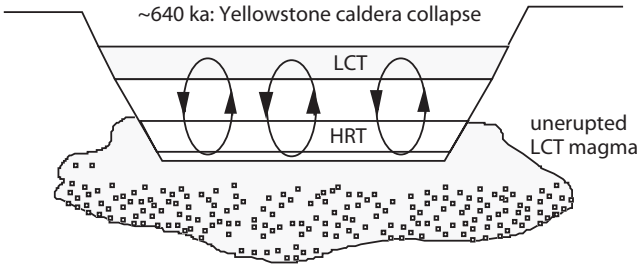
~640 ka: Yellowstone caldera collapse
LCT
HRT
unerupted
LCT magma

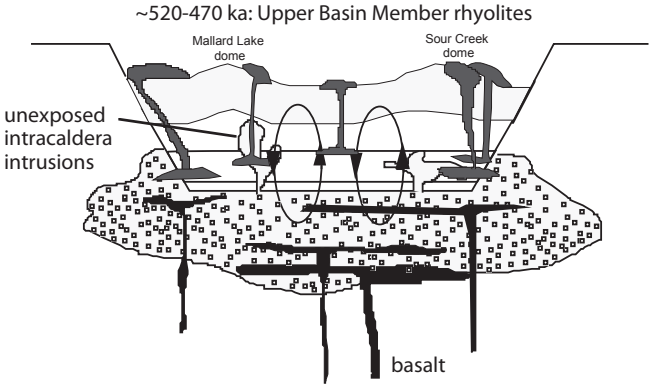
~520-470 ka: Upper Basin Member rhyolites
Mallard Lake
dome
Sour Creek
dome
unexposed
intracaldera
intrusions
basalt

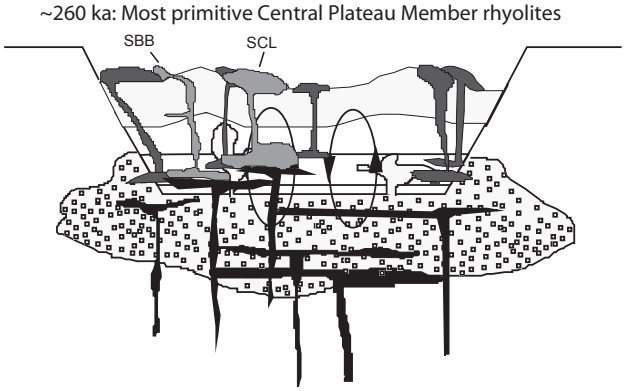
~260 ka: Most primitive Central Plateau Member rhyolites
SBB
SCL

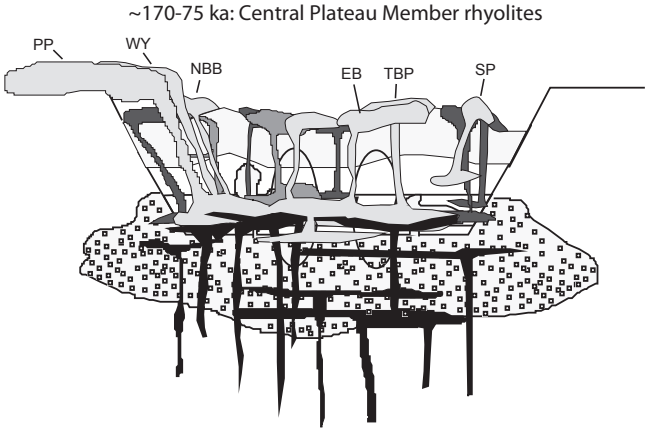
~170-75 ka: Central Plateau Member rhyolites
PP
WY
NBB
EB
TBP
SP

Like UBM rhyolites, the ~260 ka Scaup Lake flow, has a heterogeneous zircon population with $\delta^{18}O$ values that are out of equilibrium with the low-$\delta^{18}O$ host melt (Bindeman et al., 2008). Disequilibrium textures of major phenocryst phases, less-evolved mineral and whole-rock geochemistry, and a lower whole-rock Rb/Sr ratio set this unit apart from other CPM rhyolites (Vazquez and Reid, 2002; Vazquez et al., 2009; Girard and Stix, 2009a). Zircons from the South Biscuit Basin flow have comparably heterogeneous $\delta^{18}O$ values, and both units have zircon cores with the distinctive low-$\delta^{18}O$ signature of UBM rhyolites, suggesting that they represent remelts of intracaldera UBM intrusions (Bindeman et al., 2008). Mineral and whole-rock geochemistry of the Scaup Lake flow and South Biscuit Basin flow are nearly identical and define a unique end member composition of CPM rhyolite eruptions (Girard and Stix, 2009a). Therefore, the Scaup Lake and South Biscuit Basin flows are important bridging links between the UBM and CPM rhyolites, representing the oldest, least-evolved CPM magma batches that retain a genetic connection to the plutonic UBM protoliths that sourced them (Fig. 8).

Younger CPM units (Pitchstone Plateau flow, West Yellowstone flow, Elephant Back flow, Tuff of Bluff Point and North Biscuit Basin flow) are distinctly more homogenous in their zircon $\delta^{18}O$ values and have mineral assemblages that are in oxygen isotopic equilibrium with low-$\delta^{18}O$ groundmass glasses. We propose that these CPM units were derived from batch assembly and homogenization of heterogeneous pockets of low-$\delta^{18}O$ melts, such as the older Scaup Lake and South Biscuit Basin flows, which tapped UBM intrusions (Fig. 8). The fact that CPM rhyolites have zircon populations that fall within a narrow $\delta^{18}O$ range that approximates the homogenized UBM zircon average (Fig. 5a) supports this interpretation. Similar to the observations made by Vazquez et al.

(2009) for age-correlated compositional trends for progressively more-evolved, more-juvenile and cooler CPM rhyolite eruptions through time, we observe that younger CPM rhyolites tend to have less heterogeneous zircon age populations (Fig. 3), slightly higher average zircon $\delta^{18}O$ values (Fig. 4), and less heterogeneous, but more juvenile sanidine lead isotope compositions (Fig. 6). Taken together, this evidence indicates that the CPM rhyolites tapped an evolving magma reservoir in which phenocrystic heterogeneity of discrete magma batches was progressively annealed by convection and homogenization (Fig. 8). Subtle isotopic differences in younger units suggest open-system processes such as assimilation and recharge within the differentiating CPM magma chamber.

**5.2 Petrologic, thermal and temporal considerations for CPM eruptions**

The sequential nature of CPM rhyolite eruptions and detailed constraints on eruption ages and eruptive volumes for CPM units (Christiansen et al., 2007) make it possible to evaluate magma genesis from the onset of eruptions ~260 ka to the last "snapshot" of magma evolution ~75 ka. In this section, we discuss petrologic, thermal and temporal considerations for the model of post-LCT magma genesis presented in section 5.1.

The earliest erupted CPM rhyolites, the ~260 ka Scaup Lake and South Biscuit Basin flows, define the least evolved end member composition of CPM rhyolite eruptions in terms of common fractionation indices such as $Al_2O_3$ (plagioclase and sanidine), $TiO_2$ (Fe-Ti oxides), Rb/Sr (plagioclase and sanidine) and Zr/Nb (zircon) (Appendix Fig. C2). We estimate ~25-30% fractional crystallization (30% plagioclase, 60% sanidine, 10% quartz) to derive the youngest and most evolved Pitchstone Plateau flow from the more

evolved Scaup Lake and South Biscuit Basin flows (see Appendix Table C2 for fractional crystallization calculations). We note that this estimate is significantly less than the original estimate of >40% fractional crystallization by Vazquez and Reid (2002), which was based on a higher Rb/Sr ratio that is revised to a lower ratio in Vazquez et al. (2009). In addition to the geochemical disparities between old and young CPM rhyolites, distinct petrographic differences are also apparent. Disequilibrium mineral textures are commonly observed in thin sections of the Scaup Lake and South Biscuit Basin flows, indicating incomplete annealing of crystals, whereas progressively younger CPM units have more euhedral phenocrysts with fewer disequilibrium mineral textures (Appendix Fig.C1).

If younger CPM rhyolites were indeed assembled from batches of early CPM magmas, like the Scaup Lake and South Biscuit Basin flows, annealing of crystals would have had to have been completed by the time of eruption of the Tuff of Bluff Point, North Biscuit Basin flow and Elephant Back flow (~170-155 ka), which have distinct and homogeneous zircon ages and O isotope compositions relative to the earliest CPM eruptions (Fig. 5a). For a liquidus temperature of 850°C and a Zr undersaturation of 40 ppm, ~30 ky is required for complete dissolution of a spherical zircon phenocryst 100μm in diameter (Watson, 1996). This time requirement is consistent with the ≥90 ky age gap between early (~260 ka) versus late (~170-75 ka) CPM eruptions. Based on the exceptionally large cumulative eruptive volume of CPM rhyolites (>600 $km^3$; Christiansen et al., 2007), batch assembly would have had to proceed at a rate of at least ~3-4 $km^3$/ky. Assuming basalt can melt ~1-2 times the volume of rhyolite, this corresponds to a basaltic input rate of ~1-4 $km^3$/ky. Interestingly, this assembly process

seems to have been thermally buffered until ~110 ka, based on the similarity of thermometry results for CPM rhyolites up until this point (Fig. 7b). After the eruption of the very voluminous West Yellowstone flow (41 $km^3$), CPM magmas appear to become cooler through time (Fig. 7b). If this trend is real (despite the significant spread in the compiled thermometry data), then this may mark the point in time at which batch assembly stopped beneath the Yellowstone caldera. In this scenario, the negative correlation between cumulative eruptive volume and temperature reflects cooling of the assembled CPM magma reservoir as recorded by sequential rhyolite eruptions. The young Pitchstone Plateau flow represents one of the last (and largest) extractions of magma from this assembled source.

### 5.3 Analogy between CPM eruptions and the 4.45 Ma Kilgore Tuff

The 4.45 Ma Kilgore Tuff was the final caldera-forming eruption of the Heise volcanic field in eastern Idaho, a large caldera complex that precedes Yellowstone in the Yellowstone hotspot track (Morgan and McIntosh, 2005). By analogy with Yellowstone, the Kilgore caldera cycle represents a terminal stage of caldera cluster evolution that produced an exceptionally large volume (>1,800 $km^3$) of low-$\delta^{18}O$ rhyolite, comparable in timing, magnitude of $\delta^{18}O$ depletion and cumulative eruptive volume to the CPM phase of rhyolitic eruptions at Yellowstone caldera (Watts et al., 2011). While individual Kilgore Tuff zircons exhibit a wide range in $\delta^{18}O$ values, from -1.3‰ to 6.1‰, laser fluorination analyses of bulk zircon and less refractory phenocrysts phases of quartz and sanidine have homogeneous $\delta^{18}O$ values that correspond to a low-$\delta^{18}O$ magma value of

3.4±0.1‰ for samples erupted >100 km apart, providing a compelling case for batch assembly on a caldera-wide scale prior to the Kilgore Tuff eruption (Watts et al., 2011).

In comparison, most CPM rhyolites are homogeneous in $\delta^{18}O$ even on the single crystal scale, with average zircon values that fall within a narrow low-$\delta^{18}O$ range of 2.7‰ to 2.8‰ (Fig. 4; Fig. 5a). However, the oldest CPM rhyolites, South Biscuit Basin and Scaup Lake flows, exhibit much greater zircon heterogeneity (Fig. 5a). We propose that the homogenization through time effect that we observe for CPM rhyolites (Fig. 5a), whereby they become progressively more homogeneous and retain fewer inherited crystals in younger eruptions, is an expected outcome for caldera cluster evolution: heterogeneities of the intracaldera block are progressively annealed by successive episodes of bulk remelting. While at Yellowstone, these late-stage magmas erupted as sequential "snapshots" over the past 260 ky, the Kilgore Tuff erupted in a single, climactic pulse that tapped an assembled, but not fully annealed, magma chamber.

# CHAPTER VI

# CONCLUSIONS

In this dissertation, I investigated the processes by which large-volume rhyolitic magmas are generated at caldera volcanoes, using the two youngest and best-exposed caldera complexes in the Snake River Plain volcanic province: Heise (6.6-4.5 Ma) and Yellowstone (2.1-0.6 Ma). Below, I summarize the key findings and implications of my research, as presented in each of my dissertation chapters.

In Chapter II, I presented oxygen isotope and geochronology data for rhyolites of the Heise volcanic field in eastern Idaho. This work indicates that the extinct Heise volcano is an important geologic and geochemical analogue of the active Yellowstone volcano in western Wyoming. Both volcanoes produced 3-4 caldera-forming eruptions over the course of ~2 million years, leading to the development of a large nested caldera complex that accommodated thick intracaldera rhyolite deposits. Drastic depletions in $\delta^{18}O$ of voluminous late-stage rhyolite eruptions at Heise and Yellowstone hallmark a mature stage of caldera complex evolution. This chapter advocates a model in which hydrothermally altered ($^{18}O$-depleted) intracaldera rocks from previous eruptions are remelted, or "cannibalized," as successive caldera collapses bring them progressively deeper for remelting. Based on the example of Heise and Yellowstone, this model may also be important for understanding large-volume rhyolite genesis in older, less well-exposed caldera complexes in the Snake River Plain and elsewhere on Earth.

An alternative model of low-$\delta^{18}O$ rhyolite genesis that has been invoked for older caldera complexes in the central Snake River Plain is remelting of a pre-existing low-$\delta^{18}O$ crustal source. In Chapter III, I explored this possibility with a suite of Archean crustal xenoliths from the central and eastern Snake River Plain. Oxygen isotope data for the xenoliths were combined with all available data for Phanerozoic basement rocks, including the Idaho Batholith, showing that the vast majority have normal- to high-$\delta^{18}O$ signatures. Therefore, I find no evidence for a pre-existing low-$\delta^{18}O$ crustal source in the Snake River Plain. Oxygen isotope data were synthesized with strontium and neodymium isotope data for studied xenoliths, and all available oxygen, strontium and neodymium data for Snake River Plain magmas, to construct isotopic mixing models. The data support a two-stage magma genesis process, whereby normal-$\delta^{18}O$ rhyolites are generated by melting and hybridization of Archean crust by mantle-derived basalt, and late-stage, low-$\delta^{18}O$ rhyolites tap hydrothermally altered portions of stage-one rhyolites.

Building on these studies, Chapter IV presented a detailed investigation of the last caldera-forming tuff at Heise, the 4.45 Ma Kilgore Tuff. As the most voluminous (1,800 $km^3$) low-$\delta^{18}O$ rhyolite in the Snake River Plain and worldwide, the Kilgore Tuff is a key unit to evaluate the models of rhyolite genesis advocated in Chapters II and III. Synthesis of oxygen isotope data with zircon geochronology, major and trace element geochemistry, mineral chemistry, strontium and neodymium isotope geochemistry, and thermometry data, reveals that the Kilgore Tuff erupted from a remarkably homogeneous low-$\delta^{18}O$ magma reservoir ($\delta^{18}O$=3.4‰). The data support derivation of the Kilgore Tuff from remelting of hydrothermally altered intracaldera and subvolcanic (plutonic) portions of the first normal-$\delta^{18}O$ Heise tuff, the 6.62 Ma Blacktail Creek Tuff. Single pockets of

melt with variable low-$\delta^{18}O$ values were assembled and homogenized on a caldera-wide scale prior to the climactic Kilgore Tuff eruption, and the best record of this process is provided by the $\delta^{18}O$ diversity in individual Kilgore Tuff zircons ($\delta^{18}O$ of -1.3‰ to 6.1‰). Complementary geochronology data for individual zircons indicates that assembly of the Kilgore magma chamber proceeded rapidly, within error of the zircon dating methods (hundreds of thousands of years).

Chapter IV showed that at Heise and Yellowstone, magmatic $\delta^{18}O$ values can be predicted on the basis of cumulative eruptive volumes, with a decrease in $\delta^{18}O$ by ~1‰ per 1,000 $km^3$ of erupted rhyolite. In addition, a trend of $\delta^{18}O$ depletion through time is apparent, with a~3‰ decrease in $\delta^{18}O$ after ~2 million years of volcanism. In this regard, the Kilgore Tuff is analogous to the most recent phase of rhyolitic eruptions at Yellowstone–the Central Plateau Member rhyolites. In Chapter V, I presented zircon geochronology and oxygen isotope data obtained by ion microprobe for Central Plateau Member rhyolites. Isotopic and age data reveal that Central Plateau Member rhyolites become progressively more homogenous with decreasing eruption age from 260 ka to 75 ka. The progressive increase in zircon homogeneity, coupled with an increase in eruptive volume and differentiation parameters, is evidence of a large, differentiating, isotopically homogeneous magma reservoir beneath the Yellowstone caldera. By analogy with the Kilgore Tuff, Central Plateau Member rhyolites erupted effusively, recording sequential stages of magma assembly and homogenization, whereas the Kilgore Tuff magma chamber erupted catastrophically as a caldera-forming tuff.

In summary, this dissertation provides multiple lines of evidence for large-volume rhyolite genesis from wholesale recycling (remelting) of hydrothermally altered rock in

the very shallow crust. This model forms a new paradigm of rhyolite genesis that may be particularly relevant for volcanoes that produce nested calderas. Pervasive fracturing of the crust during caldera formation generates conduits for meteoric fluid flow, and in turn, the development of a large hydrothermal system, while successive caldera collapses result in maximum vertical drawdown of intracaldera rock for remelting. Batch assembly of heterogeneous pockets of melt and homogenization on a caldera-wide scale happens quickly, within hundreds of thousands of years, and the erupted volumes can be exceptional, >1,800 $km^3$ at Heise and >600 $km^3$ at Yellowstone. The high-latitude, intracontinental position of Snake River Plain caldera complexes make it possible to resolve surface meteoric water signatures that fingerprint these processes. Therefore, in addition to providing new insight into large-volume rhyolite genesis in the Snake River Plain, this dissertation may also shed light on processes occurring in caldera complexes worldwide that may or may not possess rhyolites with the diagnostic $^{18}O$ depletions.

# APPENDIX A

## SUPPLEMENTARY DATA FOR CHAPTER III

**Table A1.** Oxygen isotope values of SRP crustal basement rocks

| Longitude | Location | Age | $\delta^{18}O$ range | Reference |
|---|---|---|---|---|
| 118.78 | Nevada | Cretaceous | 7.5–7.6 | 1 |
| 118.38 | Nevada | Cretaceous | 7.3–9.5 | 1 |
| 118.38 | Nevada | Jurassic | 7.2–8.2 | 1 |
| 118.33 | Nevada | Tertiary | 7.3–8.3 | 1 |
| 118.17 | Nevada | Tertiary | 6.7–7.6 | 1 |
| 117.25 | Nevada | Cretaceous | 9.5–9.7 | 1 |
| 117.22 | Nevada | Cretaceous | 9.2–9.3 | 1 |
| 117.02 | Nevada | Jurassic | 10.2–10.4 | 1 |
| 117.03 | Nevada | Cretaceous | 11.2–11.4 | 1 |
| 116.08 | Idaho | Cretaceous | 7.4–8.4 | 2 |
| 116.02 | Idaho | Cretaceous | 8.3–10.2 | 2 |
| 115.55 | Nevada | Cretaceous | 9.6–10.1 | 1 |
| 115.55 | Nevada | Tertiary | 7.7–9.5 | 1 |
| 115.50 | Nevada | Tertiary | 9.6–9.9 | 1 |
| 115.48 | Nevada | Tertiary | 10.3 | 1 |
| 115.37 | Nevada | Cretaceous | 11.7 | 1 |
| 115.10 | Nevada | Tertiary | 6–8 | 3 |
| 115.07 | Nevada | Tertiary | 7.1–8.1 | 1 |
| 114.57 | Nevada | Jurassic | 8.0–9.6 | 1 |
| 114.48 | Nevada | Precambrian | 6.7–7.9 | 1 |
| 114.38 | Nevada | Tertiary | 8.6 | 1 |
| 114.30 | Nevada | Precambrian | 7.8–8.8 | 1 |
| 114.27 | Nevada | Jurassic | 9.6 | 1 |
| 114.07 | Utah | Tertiary | 7.7–8.7 | 1 |
| 114.01 | Utah | Tertiary | 7.0–8.0 | 1 |
| 113.43 | Utah | Jurassic | 8.9–9.3 | 1 |
| 113.98 | Utah | Tertiary | 8.0 | 1 |
| 113.89 | Utah | Precambrian | 7.8–11.6 | 1 |
| 113.90 | Utah | Precambrian | 8.1–9.7 | 1 |
| 113.86 | Utah | Precambrian | 7.7 | 1 |
| 113.87 | Utah | Precambrian | 7.4 | 1 |
| 111.75 | Utah | Tertiary | 7.3–7.9 | 1 |
| 110.57 | Utah | Tertiary | 7.8 | 1 |
| 110.67 | Utah | Tertiary | 8.3 | 1 |
| 109.80 | Montana | Precambrian | 7.3–9.1 | 4 |

Oxygen isotope values of crustal basement rocks that predate the SRP for Precambrian, Jurassic, Cretaceous and Tertiary intrusive granites. Magmatic values were estimated with measured zircon $\delta^{18}O$ values by adding 1.8 per mil, applicable at magmatic temperatures of ~800°C. References are as follows: (1) King et al., 2004; (2) King et al., 2007; (3) Wickham and Peters, 1990; (4) Valley et al., 2004. Full references are in the Chapter III References Cited section.

**Table A2.** Individual oxygen isotope analyses for SRP xenoliths

| | | $SiO_2$ (wt%) | $\delta^{18}O$ (‰) | average | 1 s.d. | 1 s.e. |
|---|---|---|---|---|---|---|
| **SK locality** | | | | | | |
| B1 | whole rock | 56.07 | 6.42 | 6.42 | 0.00 | 0.00 |
| B1 | whole rock | | 6.42 | | | |
| B2 | whole rock | 63.18 | 7.09 | 7.26 | 0.23 | 0.16 |
| B2 | whole rock | | 7.42 | | | |
| B3 | whole rock | 69.79 | 7.11 | 7.26 | 0.21 | 0.15 |
| B3 | whole rock | | 7.41 | | | |
| B10 | whole rock | 52.23 | 6.84 | 6.77 | 0.09 | 0.07 |
| B10 | whole rock | | 6.70 | | | |
| R4 | whole rock | 54.40 | 6.78 | 6.75 | 0.05 | 0.04 |
| R4 | whole rock | | 6.71 | | | |
| 73-68X | whole rock | 56.77 | 6.79 | 6.95 | 0.22 | 0.15 |
| 73-68X | whole rock | | 7.10 | | | |
| SK-3 | whole rock | 54.90 | 6.35 | 6.26 | 0.12 | 0.09 |
| SK-3 | whole rock | | 6.17 | | | |
| **COM locality** | | | | | | |
| CKI-1 | whole rock | 69.12 | 9.42 | 9.35 | 0.09 | 0.07 |
| CKI-1 | whole rock | | 9.28 | | | |
| CKI-1 | quartz | | 9.38 | 9.47 | 0.12 | 0.09 |
| CKI-1 | quartz | | 9.56 | | | |
| 70-40 | whole rock | 71.36 | 7.91 | 7.76 | 0.21 | 0.15 |
| 70-40 | whole rock | | 7.61 | | | |
| 70-40 | quartz | | 8.40 | | | |
| 70-40 | pyroxene | | 5.97 | 6.15 | 0.25 | 0.18 |
| 70-40 | pyroxene | | 6.33 | | | |
| SI-1 | whole rock | 67.70 | 6.82 | 6.98 | 0.22 | 0.16 |
| SI-1 | whole rock | | 7.14 | | | |
| SI-1 | quartz | | 7.42 | 7.43 | 0.02 | 0.02 |
| SI-1 | quartz | | 7.45 | | | |
| SI-1 | pyroxene | | 4.56 | 4.51 | 0.07 | 0.05 |
| SI-1 | pyroxene | | 4.46 | | | |
| COM-1 | whole rock | 74.56 | 7.49 | 7.43 | 0.08 | 0.06 |
| COM-1 | whole rock | | 7.37 | | | |
| COM-1 | fused whole rock | | 8.10 | 7.91 | 0.27 | 0.19 |
| COM-1 | fused whole rock | | 7.72 | | | |
| COM-9A | whole rock | 73.08 | 9.18 | 9.20 | 0.02 | 0.02 |
| COM-9A | whole rock | | 9.22 | | | |
| COM-9B | whole rock | 54.31 | 8.05 | 7.91 | 0.19 | 0.14 |
| COM-9B | whole rock | | 7.78 | | | |
| COM-14 | whole rock | 72.07 | 6.55 | 6.43 | 0.17 | 0.12 |
| COM-14 | whole rock | | 6.31 | | | |
| COM-22 | whole rock | 68.53 | 6.83 | 6.85 | 0.02 | 0.02 |
| COM-22 | whole rock | | 6.87 | | | |
| COM-25 | whole rock | 72.52 | 6.70 | 6.67 | 0.05 | 0.03 |
| COM-25 | whole rock | | 6.63 | | | |
| **SM locality** | | | | | | |
| SM-2A | whole rock | 65.37 | 7.86 | 7.78 | 0.10 | 0.07 |
| SM-2A | whole rock | | 7.71 | | | |
| SM-2F | whole rock | 69.67 | 7.56 | 7.50 | 0.07 | 0.05 |
| SM-2F | whole rock | | 7.45 | | | |
| SM-2G | whole rock | 68.95 | 8.27 | 8.09 | 0.25 | 0.18 |
| SM-2G | whole rock | | 7.91 | | | |
| DM-103 | whole rock | 73.76 | 7.90 | 7.93 | 0.04 | 0.03 |
| DM-103 | whole rock | | 7.96 | | | |
| DM-103 | fused whole rock | | 7.97 | 7.87 | 0.15 | 0.11 |
| DM-103 | fused whole rock | | 7.76 | | | |

**Table A3.** O, Sr, Nd and Pb compositions of Yellowstone, Heise and Bruneau-Jarbidge rhyolites and SRP and Yellowstone basalts

| | Sample | $\delta^{18}O$ melt (‰) | $^{87}Sr/^{86}Sr_i$ | $^{143}Nd/^{144}Nd$ | $^{206}Pb/^{204}Pb$ | $^{207}Pb/^{204}Pb$ | $^{208}Pb/^{204}Pb$ |
|---|---|---|---|---|---|---|---|
| **Yellowstone rhyolites** | | | | | | | |
| HRT-A | HRT-3A | *7.3* | 0.71171 | 0.51214 | 17.050 | 15.504 | 38.061 |
| HRT-B | HRT-1B | 7.0 | 0.70980 | 0.51220 | 16.998 | 15.497 | 38.083 |
| HRT-C | HRT-C | 7.5 | 0.72685 | 0.51169 | 18.051 | 15.751 | 37.941 |
| Blue Creek Flow | BC-1 | 2.9 | 0.71719 | 0.51198 | — | — | — |
| Mesa Falls Tuff | MFT-2 | 5.4 | 0.70868 | 0.51218 | 17.260 | 15.560 | 38.350 |
| Lewis Canyon rhyolite | YL96-11 | *5.9* | 0.71401 | 0.51217 | 17.291 | 15.573 | 38.447 |
| LCT-A | LCT3a | 5.9 | 0.71093 | 0.51215 | 17.289 | 15.552 | 38.413 |
| LCT-B | LCT-2,B | *6.3* | 0.71000 | 0.51224 | 17.285 | 15.555 | 38.541 |
| Middle Biscuit Basin flow | YL96-20 | 1.1 | 0.71930 | 0.51214 | 17.886 | 15.664 | 38.425 |
| Canyon Flow | YL96-18 | 0.7 | 0.71607 | 0.51217 | 17.806 | 15.633 | 38.348 |
| Scaup Lake Flow | YL96-9 | 4.0 | 0.70993 | 0.51224 | 17.593 | 15.590 | 38.278 |
| Solfatara Plateau flow | YL96-16 | 3.2 | 0.71116 | 0.51225 | 17.356 | 15.546 | 38.106 |
| West Yellowstone flow | YL96-1 | *4.5* | 0.71039 | 0.51227 | 17.548 | 15.579 | 38.261 |
| Pitchstone Plateau flow | | *4.5* | 0.71101 | 0.51226 | 17.525 | 15.575 | 38.243 |
| Refs: | 4 | 4 | 6,7 | 6,7 | 8,9 | 8,9 | 8,9 |
| **Heise rhyolites** | | | | | | | |
| Blacktail Creek | 95-2001a | 6.6 | 0.71238 | 0.51215 | 18.211 | 15.641 | 38.371 |
| Walcott | 06-HS-18 | 6.3 | 0.70991 | 0.51216 | 18.246 | 15.646 | 38.438 |
| Wolverine Creek | 06-HS-16 | 6.5 | 0.70947 | 0.51233 | 18.014 | 15.607 | 38.320 |
| Lidy Hotsprings | 08-HS-10 | 4.4 | 0.71138 | 0.51214 | — | — | — |
| Conant Creek | 06-HS-5 | 6.3 | 0.70895 | 0.51229 | — | — | — |
| Kilgore | TNP 96-43 | 3.4 | 0.71029 | 0.51222 | — | — | — |
| Kilgore | 06-HS-14 | 3.5 | 0.71071 | 0.51215 | — | — | — |
| Kilgore | 95-2017b | 3.3 | 0.71038 | 0.51225 | — | — | — |
| Kilgore | 06-HS-11 | 3.6 | 0.71066 | 0.51223 | — | — | — |
| Kilgore | 06-HS-10 | 3.2 | 0.71048 | 0.51222 | 18.345 | 15.690 | 38.632 |
| Juniper Buttes | 06-HS-4A | 4.6 | 0.70986 | 0.51220 | 17.203 | 15.497 | 38.242 |
| Long Hollow | 626-1 | 3.7 | 0.70917 | 0.51219 | — | — | — |
| Indian Creek | 06-HS-1 | 3.0 | 0.71074 | 0.51224 | — | — | — |
| Sheridan Reservoir | 06-HS-19 | 4.0 | 0.71815 | 0.51199 | — | — | — |
| Refs: | 1,2 | 1,2 | 2 | 2 | 3 | 3 | 3 |
| **Bruneau-Jarbidge rhyolites** | | | | | | | |
| CP III | I-569 | 3.8 | 0.70865 | 0.51219 | — | — | — |
| CP VII | I-841 | 0.2 | 0.71031 | 0.51219 | — | — | — |
| CP XIII | X-37 | 3.2 | 0.70935 | 0.51225 | 18.113 | 15.632 | 38.497 |
| CP XV | I-459 | 1.1 | 0.70938 | 0.51222 | 18.843 | 15.727 | 39.744 |
| Ind. Batt | I-445 | 2.1 | 0.71044 | 0.51224 | 18.716 | 15.712 | 39.734 |
| Brun. Jasp. | I-411 | 3.4 | 0.71062 | 0.51229 | — | — | — |
| Sheep Ck | I-1208 | 2.2 | 0.71150 | 0.51226 | — | — | — |
| Dorsey Ck | I-529 | 1.5 | 0.71220 | 0.51230 | — | — | — |
| Dorsey Ck | I-1001 | 1.5 | 0.71194 | 0.51230 | — | — | — |
| Ticr | L80-78 | 3.8 | 0.71215 | 0.51227 | — | — | — |
| Refs: | 10 | 10,11 | 10 | 10 | 3 | 3 | 3 |
| **Snake River Plain basalts** | | | | | | | |
| Spencer-Kilg | SRP-02 | 5.6 | 0.70617 | 0.51238 | — | — | — |
| Gem Valley | SRP-07 | 5.6 | 0.70650 | 0.51238 | — | — | — |
| near Idaho Falls | SRP-10 | 5.4 | 0.70560 | 0.51246 | — | — | — |
| Quaking Aspen Butte | SRP-13 | 5.4 | 0.70630 | 0.51239 | — | — | — |
| N Robbers Lava Field | SRP-16 | 5.6 | 0.70555 | 0.51252 | — | — | — |
| Antelope Butte | SRP-17 | 5.6 | 0.70803 | 0.51234 | — | — | — |
| Spencer-Kilg | SRP-19 | 5.8 | 0.70570 | 0.51244 | — | — | — |
| Refs: | 12 | 1 | 12 | 12 | | | |

## Table A3. (continued)

| | | | | | | | |
|---|---|---|---|---|---|---|---|
| **Yellowstone basalts** | | | | | | | |
| Osprey basalt | P-104WR | — | 0.70657 | 0.51241 | 16.772 | 15.424 | 37.185 |
| younger basalt of Gerrit | 6YC-140B-WR | — | — | — | 17.240 | 15.490 | 38.230 |
| older basalt of Gerrit | 6YC-142WR | 5.2 | 0.70601 | 0.51246 | 17.310 | 15.520 | 38.240 |
| Madison River basalt | 6YC-139WR | 5.7 | 0.70659 | 0.51234 | 16.840 | 15.470 | 38.280 |
| Madison River basalt | 6YC-139WR | 5.7 | 0.70659 | 0.51234 | 16.789 | 15.400 | 38.115 |
| Falls River basalt | 6YC-145WR | — | — | — | 16.990 | 15.560 | 38.140 |
| Falls River basalt | 6YC-145WR | — | — | — | 16.963 | 15.497 | 37.924 |
| Swan Lake Flat basalt | 6YC-133WR | 5.9 | | | 16.680 | 15.390 | 37.480 |
| Swan Lake Flat basalt | 6YC-133WR | 5.9 | | | 16.696 | 15.386 | 37.502 |
| Swan Lake Flat basalt | 6YC-136WR | — | 0.70578 | 0.512483 | 16.790 | 15.390 | 37.590 |
| basalt of Warm River | 6YC-144WR | 5.4 | 0.70565 | 0.512461 | 17.200 | 15.460 | 38.060 |
| basalt of Warm River | 6YC-144WR | 5.4 | 0.70565 | 0.512461 | 17.232 | 15.505 | 38.132 |
| Junction Butte Basalt | 70-0-59WR | — | — | — | 16.098 | 15.300 | 36.921 |
| Junction Butte Basalt | 70-0-65WR | — | — | — | 16.595 | 15.401 | 37.108 |
| basalt of the Narrows | 70-0-64WR | — | — | — | 16.662 | 15.294 | 36.461 |
| Refs: | 9 | 13 | 6 | 6 | 9 | 9 | 9 |

References: (1) Bindeman et al., 2007; (2) Watts et al., 2011; (3) Leeman, unpublished; (4) Bindeman et al., 2008, values in italics were calculated from data in Bindeman and Valley, 2001; (5) Bindeman and Valley, 2001; (6) Hildreth et al., 1991; (7) Vazquez and Reid, 2002; (8) Vazquez et al., 2009; (9) Doe et al., 1982; (10) Bonnichsen et al., 2008; (11) Ellis, unpublished; (12) Graham et al., 2009; (13) Hildreth et al., 1984; (14) Leeman et al., 1985. Full references are in the Chapter III References Cited section.

**Table A4.** Sr-O and Nd-O binary mixing model data

| | Sample | $\delta^{18}O$ melt (‰) | $^{87}Sr/^{86}Sr_i$ | $^{143}Nd/^{144}Nd$ | O (wt%) | Sr (ppm) | Nd (ppm) |
|---|---|---|---|---|---|---|---|
| **Crust** | | | | | | | |
| crustal xenolith | DM-103 | 7.9 | 0.73878 | 0.510853 | 48.83 | 360 | 25.7 |
| Refs: | 14 | this study | 14 | 14 | 3 | 3 | 3 |
| **Mantle (SRP basalt average)** | | | | | | | |
| R=0.1 | SRP basalts | 5.6 | 0.70626 | 0.51242 | 43.53 | 32 | 2 |
| R=1 | SRP basalts | 5.6 | 0.70626 | 0.51242 | 43.53 | 321 | 23 |
| R=10 | SRP basalts | 5.6 | 0.70626 | 0.51242 | 43.53 | 3209 | 229 |
| Refs: | 12 | 1 | 12 | 12 | 12 | calculated | calculated |
| **Normal-$\delta^{18}O$ rhyolite endmembers** | | | | | | | |
| HRT-A | HRT-3A | 7.3 | 0.71171 | 0.51214 | 49.35 | 21.42 | 97 |
| HRT-B | HRT-1B | 7.0 | 0.70980 | 0.51220 | 48.38 | 49.2 | 77 |
| HRT-C | HRT-C | 7.5 | 0.72685 | 0.51169 | 48.84 | 67.74 | 64 |
| Model HRT melt | — | 7.4 | 0.71928 | 0.51191 | 49.10 | 44.58 | 80.5 |
| Refs: | 4 | 4 | 6 | 6 | 5 | 6 | 3 |
| **Low-$\delta^{18}O$ rhyolite endmembers** | | | | | | | |
| Middle Biscuit Basin flow | YL96-20 | 1.1 | 0.71930 | 0.51214 | 49.37 | 49.2 | 56.6 |
| Canyon Flow | YL96-18 | 0.7 | 0.71607 | 0.51217 | 49.22 | 82.5 | 60.7 |
| Solfatara Plateau flow | YL96-16 | 3.2 | 0.71116 | 0.51225 | 48.78 | 9.0 | 80.23 |
| Refs: | 4 | 4 | 6,7 | 6,7 | 5 | 8,15 | 8,15 |
| **Low-$\delta^{18}O$ source** | — | -1.5 | 0.7150 | 0.5122 | 48.99 | 15 | 60 |
| | — | -1.0 | 0.7160 | 0.5123 | 48.99 | 15 | 60 |
| Refs: | | estimated | estimated | estimated | estimated | estimated | estimated |

Binary mixing models were constructed with the mixing equation and data shown above. Crust and mantle mixing hyperbolas were calculated with $R_{crust}/R_{mantle}$ concentration ratios of 0.1, 1 and 10, where $R=C_O/C_{Sr}$ (Fig. 3A) and $R=C_O/C_{Nd}$ (Fig. 3B). All normal-$\delta^{18}O$ Heise and Yellowstone magmas plot within the crust-mantle mixing field. Mixing lines from normal to low-$\delta^{18}O$ end members were constructed for HRT-A–Canyon flow, HRT-C–Middle Biscuit Basin flow, and HRT-B–Solfatara Plateau flow. Canyon flow and Middle Biscuit Basin flow contain HRT aged zircons, and thus are genetically related to HRT (Bindeman et al., 2008). Trace element and isotope data for phenocrysts and groundmass glasses suggest an HRT lineage for Solfatara Plateau flow (Vazquez et al., 2009). We selected HRT end members with the most similar Sr isotope ratios to the low-$\delta^{18}O$ end members to construct the mixing curves. Second order polynomials were fit to the hyperbolic mixing curves ($R^2 \geq 0.96$) and projected along the Sr-O and Nd-O axes, where they converged at $\delta^{18}O$=-1.5 to -0.4‰ (Sr-O) and $\delta^{18}O$=-1.0 to 0.7‰ (Nd-O) (Fig. 3A and B). Reference key corresponds with that used in Appendix Table A3.

**Figure A1.** Lead isotopes versus $\delta^{18}O$ for SRP crust, mantle and magmas

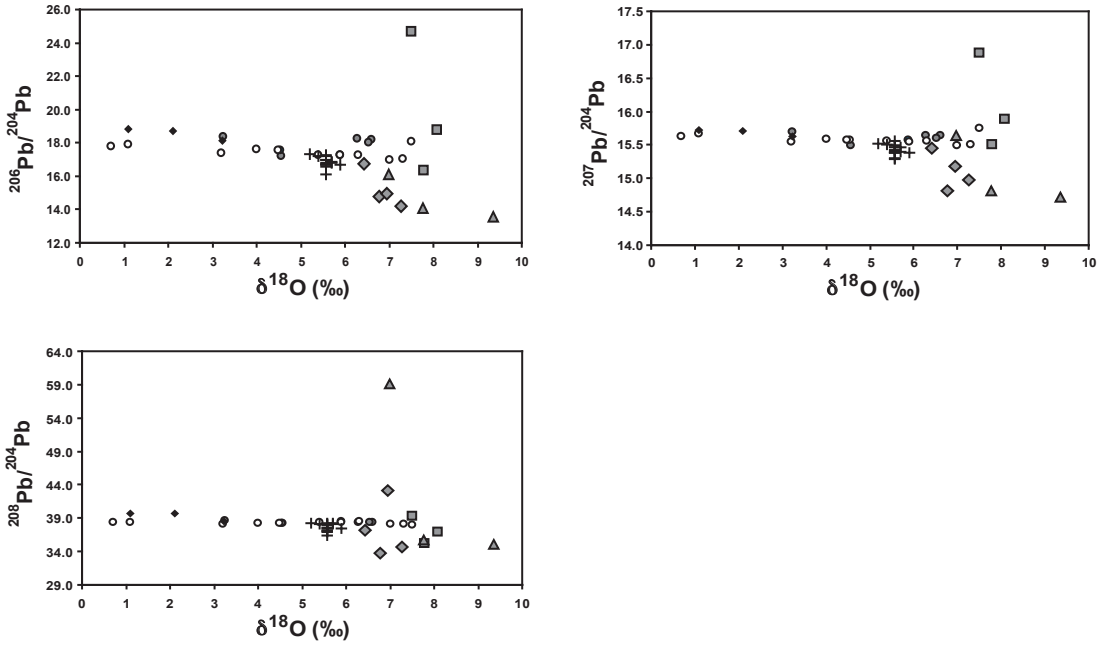


Note: Symbols correspond to the symbol key in Figure 2 of Chapter III.

# APPENDIX B

## SUPPLEMENTARY DATA FOR CHAPTER IV

**Table B1.** Compositions of samples from Meadow Creek Road stratigraphic sequence near Ririe Lake

| Sample | 08HS-KG-1 | 08HS-KG-2 | 08HS-KG-3 | 06HS-14 | 08HS-KG-4 | 08HS-KG-6 | 08HS-KG-7 | 08HS-KG-8 | 08HS-KG-10 | 08HS-KG-11 | 08HS-KG-12 | 08HS-KG-13 | 06HS-10 | 06HS-11 | 08HS-KG-18ps |
|---|---|---|---|---|---|---|---|---|---|---|---|---|---|---|---|
| Description | pumice-rich | gley paleosol | airfall deposit | airfall deposit | pumice-rich | pumice-rich | pumice-rich | lithic-rich | lithic-rich | pumice-rich | cross-bedded | pumice-rich | Kilgore Tuff | Kilgore Tuff | paleosol calcrete |
| Ar-Ar Age (Ma) | – | – | – | – | – | – | – | – | – | – | – | – | 4.43±0.09 | 4.43±0.08 | – |
| U-Pb Age (Ma) | – | – | – | 4.87±0.20 | – | – | – | – | – | – | – | – | 4.58±0.24 | 4.58±0.18 | – |
| $\delta^{18}O$ (‰) | – | – | – | 3.5 | – | – | – | – | – | – | – | – | 3.2 | 3.6 | – |
| $\Delta^{17}O$ (‰) | – | 0.6 | – | – | – | – | – | – | – | – | 1.4 | – | – | – | 0.7 |
| Major element analyses by XRF (unnormalized, all Fe as FeO*) | | | | | | | | | | | | | | | |
| $SiO_2$ | 63.94 | 47.80 | 65.12 | 63.47 | 62.33 | 65.51 | 69.24 | 58.48 | 57.80 | 63.61 | 55.00 | 46.44 | 71.47 | 73.00 | – |
| $TiO_2$ | 0.529 | 2.481 | 0.296 | 0.493 | 0.803 | 0.525 | 0.387 | 0.478 | 0.438 | 0.712 | 0.359 | 0.275 | 0.229 | 0.230 | – |
| $Al_2O_3$ | 14.53 | 13.88 | 14.40 | 14.22 | 14.76 | 12.26 | 11.88 | 10.44 | 10.46 | 13.41 | 8.73 | 7.79 | 11.75 | 11.70 | – |
| FeO* | 3.15 | 10.39 | 2.47 | 3.52 | 4.75 | 3.27 | 2.56 | 2.95 | 2.74 | 4.47 | 2.35 | 1.76 | 1.69 | 1.86 | – |
| MnO | 0.077 | 0.156 | 0.067 | 0.089 | 0.123 | 0.077 | 0.058 | 0.064 | 0.053 | 0.078 | 0.043 | 0.074 | 0.038 | 0.042 | – |
| MgO | 1.08 | 1.70 | 0.55 | 1.00 | 1.01 | 1.02 | 0.68 | 1.13 | 1.05 | 1.51 | 1.21 | 0.69 | 0.14 | 0.19 | – |
| CaO | 1.06 | 1.89 | 0.82 | 1.08 | 1.20 | 2.65 | 1.09 | 8.83 | 8.83 | 1.81 | 12.30 | 18.57 | 0.65 | 0.83 | – |
| $Na_2O$ | 1.96 | 0.87 | 2.00 | 2.28 | 1.98 | 1.52 | 2.04 | 1.16 | 1.30 | 1.58 | 0.94 | 1.30 | 2.89 | 3.15 | – |
| $K_2O$ | 3.37 | 1.01 | 4.23 | 3.44 | 2.98 | 3.11 | 3.80 | 2.25 | 2.58 | 3.05 | 1.92 | 2.52 | 5.22 | 5.15 | – |
| $P_2O_5$ | 0.067 | 0.218 | 0.152 | 0.078 | 0.111 | 0.152 | 0.096 | 0.248 | 0.156 | 0.136 | 0.152 | 0.132 | 0.024 | 0.029 | – |
| total | 89.76 | 80.39 | 90.10 | 89.67 | 90.05 | 90.10 | 91.82 | 86.04 | 85.42 | 90.36 | 83.01 | 79.56 | 94.10 | 96.18 | – |
| Major element analyses by XRF (normalized, all Fe as FeO*) | | | | | | | | | | | | | | | |
| $SiO_2$ | 71.23 | 59.46 | 72.28 | 70.78 | 69.22 | 72.71 | 75.40 | 67.97 | 67.67 | 70.40 | 66.26 | 58.37 | 75.95 | 75.90 | – |
| $TiO_2$ | 0.590 | 3.086 | 0.329 | 0.550 | 0.891 | 0.583 | 0.421 | 0.555 | 0.513 | 0.788 | 0.432 | 0.345 | 0.244 | 0.24 | – |
| $Al_2O_3$ | 16.18 | 17.26 | 15.98 | 15.86 | 16.40 | 13.61 | 12.94 | 12.14 | 12.25 | 14.84 | 10.52 | 9.80 | 12.49 | 12.17 | – |
| FeO* | 3.51 | 12.92 | 2.74 | 3.93 | 5.27 | 3.62 | 2.79 | 3.43 | 3.21 | 4.95 | 2.84 | 2.21 | 1.79 | 1.93 | – |
| MnO | 0.086 | 0.194 | 0.074 | 0.099 | 0.136 | 0.085 | 0.063 | 0.074 | 0.062 | 0.086 | 0.052 | 0.092 | 0.040 | 0.04 | – |
| MgO | 1.21 | 2.12 | 0.61 | 1.11 | 1.13 | 1.13 | 0.74 | 1.31 | 1.23 | 1.67 | 1.46 | 0.87 | 0.15 | 0.20 | – |
| CaO | 1.18 | 2.35 | 0.91 | 1.20 | 1.33 | 2.94 | 1.18 | 10.26 | 10.34 | 2.00 | 14.82 | 23.34 | 0.69 | 0.86 | – |
| $Na_2O$ | 2.18 | 1.08 | 2.22 | 2.54 | 2.20 | 1.69 | 2.22 | 1.35 | 1.52 | 1.74 | 1.14 | 1.64 | 3.07 | 3.27 | – |
| $K_2O$ | 3.76 | 1.26 | 4.70 | 3.84 | 3.31 | 3.46 | 4.13 | 2.62 | 3.02 | 3.38 | 2.31 | 3.17 | 5.55 | 5.36 | – |
| $P_2O_5$ | 0.075 | 0.271 | 0.169 | 0.086 | 0.124 | 0.169 | 0.104 | 0.288 | 0.183 | 0.151 | 0.183 | 0.166 | 0.026 | 0.03 | – |
| total | 100.00 | 100.00 | 100.00 | 100.00 | 100.00 | 100.00 | 100.00 | 100.00 | 100.00 | 100.00 | 100.00 | 100.00 | 100.00 | 100.00 | – |
| Trace element analyses by XRF (ppm) | | | | | | | | | | | | | | | |
| Ba | 789 | 1405 | 556 | 974 | 962 | 647 | 606 | 563 | 506 | 655 | 421 | 522 | 876 | 878 | – |
| Rb | 131 | 57 | 147 | 114 | 114 | 118 | 132 | 88 | 97 | 117 | 75 | 86 | 162 | 162 | – |
| Sr | 115 | 230 | 51 | 82 | 122 | 102 | 64 | 106 | 97 | 133 | 104 | 82 | 26 | 27 | – |
| Zr | 397 | 275 | 352 | 538 | 608 | 263 | 244 | 249 | 231 | 250 | 171 | 152 | 312 | 310 | – |
| Y | 57 | 87 | 88 | 78 | 59 | 49 | 58 | 40 | 42 | 49 | 38 | 44 | 63 | 63 | – |
| Nb | 37 | 28 | 54 | 50 | 43 | 31 | 40 | 23 | 25 | 29 | 19 | 24 | 48 | 48 | – |
| Ga | 21 | 22 | 25 | 24 | 23 | 19 | 20 | 14 | 15 | 18 | 13 | 13 | 20 | 19 | – |
| Zn | 87 | 176 | 87 | 116 | 138 | 100 | 91 | 82 | 82 | 98 | 67 | 57 | 60 | 75 | – |
| Pb | 27 | 12 | 31 | 28 | 26 | 21 | 22 | 17 | 17 | 20 | 13 | 14 | 25 | 29 | – |
| La | 71 | 88 | 96 | 75 | 71 | 52 | 62 | 40 | 43 | 53 | 39 | 40 | 81 | 79 | – |
| Ce | 135 | 81 | 187 | 160 | 135 | 105 | 121 | 81 | 87 | 95 | 65 | 75 | 156 | 161 | – |
| Th | 26 | 9 | 34 | 26 | 22 | 18 | 21 | 14 | 15 | 16 | 11 | 14 | 26 | 26 | – |
| Nd | 55 | 84 | 77 | 63 | 57 | 44 | 49 | 36 | 38 | 42 | 33 | 34 | 58 | 64 | – |
| U | 6 | 6 | 6 | 5 | 6 | 5 | 5 | 4 | 4 | 5 | 6 | 5 | 7 | 6 | – |
| Ni | 7 | 18 | 6 | 7 | 10 | 14 | 9 | 17 | 15 | 23 | 17 | 11 | 3 | 0 | – |
| Cu | 11 | 31 | 7 | 10 | 12 | 14 | 9 | 15 | 13 | 21 | 16 | 10 | 5 | 23 | – |
| Cr | 21 | 53 | 9 | 13 | 25 | 32 | 21 | 35 | 32 | 42 | 28 | 15 | 3 | 6 | – |
| Sc | 9 | 25 | 6 | 9 | 10 | 8 | 5 | 8 | 8 | 10 | 7 | 5 | 4 | 4 | – |
| V | 36 | 91 | 18 | 31 | 55 | 63 | 40 | 62 | 61 | 86 | 56 | 27 | 4 | 5 | – |

**Table B2.** Electron microprobe analyses of Heise phenocrysts

| Sample number | Unit | Mineral | SiO2 | TiO2 | Al2O3 | FeO | MnO | MgO | CaO | Na2O | K2O | P2O5 | total | Xab Xen | Xan Xwo | Xor Xfs |
|---|---|---|---|---|---|---|---|---|---|---|---|---|---|---|---|---|
| 06HS-11_plag-1 | Kilgore Tuff | plag | 61.82 | 0.02 | 23.38 | 0.28 | 0.00 | 0.00 | 5.20 | 8.20 | 1.38 | -0.01 | 100.25 | 0.68 | 0.24 | 0.08 |
| 06HS-11_plag-1 | Kilgore Tuff | plag | 61.58 | 0.01 | 23.12 | 0.28 | 0.02 | 0.00 | 4.85 | 7.62 | 1.34 | -0.01 | 98.81 | 0.68 | 0.24 | 0.08 |
| 06HS-11_plag-1 | Kilgore Tuff | plag | 61.69 | 0.00 | 23.61 | 0.26 | 0.00 | 0.01 | 4.93 | 7.61 | 1.30 | -0.01 | 99.39 | 0.68 | 0.24 | 0.08 |
| 06HS-11_plag-1-rim | Kilgore Tuff | plag | 61.64 | 0.02 | 23.08 | 0.27 | 0.01 | 0.00 | 4.71 | 7.74 | 1.27 | -0.01 | 98.75 | 0.69 | 0.23 | 0.07 |
| 06HS-11_plag-1-rim | Kilgore Tuff | plag | 61.56 | 0.02 | 23.31 | 0.27 | 0.00 | 0.01 | 4.83 | 7.85 | 1.36 | 0.00 | 99.21 | 0.69 | 0.23 | 0.08 |
| 06HS-11_plag-1-rim | Kilgore Tuff | plag | 61.79 | 0.02 | 23.23 | 0.26 | 0.00 | 0.00 | 4.71 | 7.76 | 1.42 | -0.02 | 99.17 | 0.69 | 0.23 | 0.08 |
| 06HS-11_cpx-1 | Kilgore Tuff | cpx | 50.21 | 0.26 | 0.62 | 18.72 | 0.78 | 9.42 | 18.20 | 0.30 | 0.01 | -0.01 | 98.48 | 0.29 | 0.40 | 0.32 |
| 06HS-11_cpx-1 | Kilgore Tuff | cpx | 50.76 | 0.23 | 0.63 | 18.82 | 0.79 | 9.41 | 18.31 | 0.27 | 0.00 | -0.01 | 99.21 | 0.28 | 0.40 | 0.32 |
| 06HS-11_cpx-1 | Kilgore Tuff | cpx | 50.64 | 0.27 | 0.64 | 18.52 | 0.81 | 9.48 | 18.31 | 0.29 | 0.00 | -0.02 | 98.94 | 0.29 | 0.40 | 0.31 |
| 06HS-11_cpx-1-rim | Kilgore Tuff | cpx | 53.07 | 0.23 | 0.69 | 19.35 | 0.84 | 9.07 | 18.01 | 0.37 | 0.04 | -0.01 | 101.66 | 0.28 | 0.39 | 0.33 |
| 06HS-11_cpx-1-rim | Kilgore Tuff | cpx | 51.03 | 0.24 | 0.60 | 19.07 | 0.83 | 9.17 | 18.40 | 0.30 | 0.02 | -0.01 | 99.64 | 0.28 | 0.40 | 0.32 |
| 06HS-10_plag-1 | Kilgore Tuff | plag | 62.07 | 0.01 | 24.14 | 0.26 | 0.00 | 0.00 | 5.39 | 7.55 | 1.37 | 0.00 | 100.77 | 0.66 | 0.26 | 0.08 |
| 06HS-10_plag-1 | Kilgore Tuff | plag | 61.51 | 0.02 | 24.22 | 0.25 | -0.01 | 0.00 | 5.68 | 7.49 | 1.33 | -0.03 | 100.45 | 0.65 | 0.27 | 0.08 |
| 06HS-10_plag-1 | Kilgore Tuff | plag | 62.25 | 0.01 | 24.14 | 0.25 | -0.01 | 0.01 | 5.08 | 7.82 | 1.43 | 0.00 | 100.98 | 0.68 | 0.24 | 0.08 |
| 06HS-10_plag-1-rim | Kilgore Tuff | K-spar | 64.89 | -0.02 | 19.49 | 0.14 | 0.02 | 0.00 | 0.73 | 5.36 | 9.25 | 0.00 | 99.85 | 0.45 | 0.03 | 0.51 |
| 06HS-10_plag-1-rim | Kilgore Tuff | K-spar | 64.63 | -0.02 | 19.21 | 0.16 | 0.01 | 0.00 | 0.72 | 5.12 | 9.33 | 0.00 | 99.16 | 0.44 | 0.03 | 0.53 |
| 06HS-10_plag-1-rim | Kilgore Tuff | K-spar | 64.65 | -0.02 | 19.32 | 0.15 | 0.01 | 0.00 | 0.77 | 5.27 | 9.12 | -0.01 | 99.26 | 0.45 | 0.04 | 0.51 |
| 06HS-10_opx-1 | Kilgore Tuff | opx | 50.50 | 0.16 | 0.27 | 33.36 | 1.35 | 12.77 | 1.58 | 0.05 | 0.01 | -0.02 | 100.04 | 0.39 | 0.03 | 0.57 |
| 06HS-10_opx-1 | Kilgore Tuff | opx | 50.65 | 0.19 | 0.30 | 33.12 | 1.36 | 12.59 | 1.57 | 0.03 | 0.02 | -0.01 | 99.83 | 0.39 | 0.03 | 0.58 |
| 06HS-10_opx-1 | Kilgore Tuff | opx | 50.49 | 0.18 | 0.27 | 33.33 | 1.34 | 12.60 | 1.70 | 0.03 | 0.00 | -0.02 | 99.92 | 0.39 | 0.04 | 0.57 |
| 06HS-10_opx-1-rim | Kilgore Tuff | opx | 50.31 | 0.15 | 0.32 | 33.08 | 1.35 | 13.00 | 1.56 | 0.00 | 0.01 | -0.03 | 99.76 | 0.40 | 0.03 | 0.57 |
| 06HS-10_opx-1-rim | Kilgore Tuff | opx | 50.75 | 0.18 | 0.26 | 32.93 | 1.35 | 12.94 | 1.52 | 0.02 | 0.01 | -0.01 | 99.96 | 0.40 | 0.03 | 0.57 |
| 06HS-10_opx-1-rim | Kilgore Tuff | opx | 50.27 | 0.19 | 0.32 | 33.55 | 1.39 | 12.60 | 1.56 | 0.03 | 0.00 | 0.00 | 99.90 | 0.39 | 0.03 | 0.58 |
| 06HS-10_opx-2 | Kilgore Tuff | opx | 50.41 | 0.20 | 0.29 | 33.48 | 1.40 | 12.18 | 1.53 | 0.00 | 0.01 | -0.01 | 99.52 | 0.38 | 0.03 | 0.59 |
| 06HS-10_opx-2 | Kilgore Tuff | opx | 49.88 | 0.17 | 0.36 | 33.54 | 1.42 | 11.91 | 1.58 | 0.10 | 0.04 | -0.02 | 98.98 | 0.37 | 0.04 | 0.59 |
| 06HS-10_opx-2 | Kilgore Tuff | opx | 50.58 | 0.17 | 0.28 | 33.46 | 1.44 | 12.14 | 1.63 | 0.03 | 0.00 | 0.00 | 99.75 | 0.38 | 0.04 | 0.59 |
| 06HS-10_opx-2-rim | Kilgore Tuff | opx | 50.84 | 0.19 | 0.33 | 34.15 | 1.45 | 11.32 | 1.64 | 0.02 | 0.05 | -0.02 | 99.97 | 0.36 | 0.04 | 0.61 |
| 06HS-10_opx-2-rim | Kilgore Tuff | opx | 50.44 | 0.12 | 0.27 | 34.31 | 1.47 | 11.61 | 1.60 | 0.05 | 0.02 | -0.02 | 99.86 | 0.36 | 0.04 | 0.60 |
| 06HS-10_opx-2-rim | Kilgore Tuff | opx | 50.34 | 0.19 | 0.27 | 33.99 | 1.48 | 11.74 | 1.57 | 0.02 | 0.01 | -0.02 | 99.60 | 0.37 | 0.04 | 0.60 |
| 06HS-4a_plag-1 | Juniper Buttes | plag | 60.92 | 0.01 | 23.89 | 0.31 | 0.00 | 0.01 | 5.97 | 7.10 | 1.16 | -0.01 | 99.37 | 0.64 | 0.30 | 0.07 |
| 06HS-4a_plag-1 | Juniper Buttes | plag | 60.70 | 0.00 | 24.25 | 0.30 | 0.00 | 0.01 | 6.06 | 7.33 | 1.18 | -0.01 | 99.83 | 0.64 | 0.29 | 0.07 |
| 06HS-4a_plag-1 | Juniper Buttes | plag | 60.67 | 0.01 | 24.22 | 0.30 | 0.00 | 0.01 | 6.19 | 7.57 | 1.13 | -0.01 | 100.09 | 0.64 | 0.29 | 0.06 |
| 06HS-4a_plag-1-rim | Juniper Buttes | plag | 60.65 | 0.03 | 24.73 | 0.35 | 0.00 | 0.01 | 6.41 | 7.49 | 1.06 | -0.01 | 100.71 | 0.64 | 0.30 | 0.06 |
| 06HS-4a_plag-1-rim | Juniper Buttes | plag | 60.63 | 0.02 | 24.65 | 0.33 | 0.01 | 0.01 | 6.19 | 7.30 | 1.08 | -0.01 | 100.22 | 0.64 | 0.30 | 0.06 |
| 06HS-4a_plag-1-rim | Juniper Buttes | plag | 60.40 | 0.01 | 24.67 | 0.34 | 0.00 | 0.01 | 6.43 | 7.30 | 1.03 | 0.00 | 100.20 | 0.63 | 0.31 | 0.06 |
| 06HS-4a_cpx-1 | Juniper Buttes | cpx | 51.93 | 0.20 | 0.78 | 14.38 | 0.60 | 11.53 | 20.23 | 0.32 | 0.00 | -0.02 | 99.94 | 0.34 | 0.43 | 0.24 |
| 06HS-4a_cpx-1 | Juniper Buttes | cpx | 52.29 | 0.22 | 0.78 | 14.37 | 0.62 | 11.55 | 20.05 | 0.28 | 0.00 | -0.02 | 100.13 | 0.34 | 0.42 | 0.24 |
| 06HS-4a_cpx-1 | Juniper Buttes | cpx | 52.00 | 0.22 | 0.74 | 14.46 | 0.62 | 11.53 | 20.09 | 0.31 | 0.00 | -0.01 | 99.95 | 0.34 | 0.42 | 0.24 |
| 06HS-4a_cpx-1-rim | Juniper Buttes | cpx | 52.54 | 0.23 | 0.81 | 11.24 | 0.49 | 13.13 | 21.23 | 0.38 | 0.00 | -0.01 | 100.05 | 0.38 | 0.44 | 0.18 |
| 06HS-4a_cpx-1-rim | Juniper Buttes | cpx | 52.68 | 0.23 | 0.84 | 11.43 | 0.51 | 13.41 | 20.40 | 0.31 | 0.00 | -0.02 | 99.79 | 0.39 | 0.43 | 0.19 |
| 06HS-4a_cpx-1-rim | Juniper Buttes | cpx | 53.40 | 0.23 | 0.82 | 11.17 | 0.47 | 13.36 | 21.26 | 0.31 | 0.00 | -0.03 | 100.97 | 0.38 | 0.44 | 0.18 |
| 06HS-4a_cpx-2 | Juniper Buttes | cpx | 53.01 | 0.20 | 0.86 | 11.69 | 0.50 | 13.13 | 20.65 | 0.34 | 0.00 | 0.01 | 100.43 | 0.38 | 0.43 | 0.19 |

**Table B2. continued.**

| | | | | | | | | | | | | | | | | |
|---|---|---|---|---|---|---|---|---|---|---|---|---|---|---|---|---|
| 06HS-4a_opx-3 | Juniper Buttes | opx | 52.57 | 0.15 | 0.40 | 25.34 | 1.00 | 19.17 | 1.17 | 0.04 | 0.00 | -0.01 | 99.79 | 0.56 | 0.02 | 0.42 |
| 06HS-1_plag-1 | Indian Creek | plag | 61.66 | 0.02 | 23.39 | 0.25 | 0.00 | 0.00 | 5.15 | 7.94 | 1.26 | -0.01 | 99.66 | 0.68 | 0.25 | 0.07 |
| 06HS-1_plag-1 | Indian Creek | plag | 61.89 | 0.01 | 22.93 | 0.28 | 0.01 | 0.01 | 4.84 | 8.17 | 1.37 | -0.01 | 99.49 | 0.70 | 0.23 | 0.08 |
| 06HS-1_plag-1-rim | Indian Creek | K-spar | 64.09 | 0.01 | 18.96 | 0.18 | -0.01 | 0.00 | 0.81 | 5.18 | 8.18 | 0.00 | 97.40 | 0.47 | 0.04 | 0.49 |
| 06HS-1_plag-1-rim | Indian Creek | K-spar | 63.60 | -0.01 | 19.05 | 0.16 | -0.04 | 0.01 | 0.68 | 5.02 | 8.23 | -0.01 | 96.69 | 0.46 | 0.03 | 0.50 |
| 06HS-1_plag-1-rim | Indian Creek | K-spar | 64.01 | -0.03 | 19.16 | 0.15 | -0.01 | 0.00 | 0.79 | 5.47 | 7.86 | -0.03 | 97.39 | 0.49 | 0.04 | 0.47 |
| 06HS-1_plag-2 | Indian Creek | plag | 62.58 | 0.03 | 22.64 | 0.32 | 0.01 | 0.00 | 4.53 | 7.91 | 1.60 | -0.01 | 99.62 | 0.69 | 0.22 | 0.09 |
| 06HS-1_plag-2 | Indian Creek | plag | 62.33 | 0.03 | 22.80 | 0.37 | -0.02 | 0.00 | 4.82 | 7.95 | 1.44 | -0.02 | 99.70 | 0.69 | 0.23 | 0.08 |
| 06HS-1_plag-2 | Indian Creek | plag | 62.89 | 0.04 | 22.44 | 0.36 | 0.01 | 0.00 | 4.25 | 7.99 | 1.74 | -0.02 | 99.71 | 0.70 | 0.20 | 0.10 |
| 06HS-1_plag-3 | Indian Creek | plag | 62.39 | 0.03 | 22.49 | 0.26 | -0.01 | 0.00 | 4.26 | 7.99 | 1.59 | -0.01 | 98.98 | 0.70 | 0.21 | 0.09 |
| 06HS-1_plag-3 | Indian Creek | plag | 62.92 | 0.00 | 22.48 | 0.27 | 0.02 | 0.01 | 4.29 | 8.04 | 1.62 | 0.00 | 99.64 | 0.70 | 0.21 | 0.09 |
| 06HS-1_plag-3 | Indian Creek | plag | 62.54 | 0.02 | 22.74 | 0.26 | 0.00 | 0.00 | 4.30 | 8.23 | 1.69 | -0.01 | 99.79 | 0.70 | 0.20 | 0.10 |
| 06HS-1_plag-3-rim | Indian Creek | K-spar | 64.50 | 0.00 | 20.40 | 0.21 | 0.00 | 0.00 | 1.48 | 7.63 | 4.34 | -0.02 | 98.55 | 0.68 | 0.07 | 0.25 |
| 06HS-1_plag-3-rim | Indian Creek | K-spar | 64.48 | 0.00 | 19.97 | 0.21 | 0.02 | 0.00 | 1.21 | 7.35 | 4.64 | -0.01 | 97.89 | 0.66 | 0.06 | 0.28 |
| 06HS-1_plag-3-rim | Indian Creek | K-spar | 64.87 | 0.00 | 20.12 | 0.19 | -0.02 | 0.00 | 1.26 | 7.37 | 4.67 | -0.02 | 98.43 | 0.66 | 0.06 | 0.28 |
| 06HS-1_plag-4 | Indian Creek | plag | 63.86 | -0.01 | 22.13 | 0.21 | 0.01 | 0.00 | 3.66 | 8.01 | 2.34 | -0.01 | 100.20 | 0.69 | 0.17 | 0.13 |
| 06HS-1_plag-4 | Indian Creek | plag | 63.29 | 0.01 | 22.28 | 0.21 | -0.02 | 0.00 | 3.70 | 8.06 | 2.06 | 0.00 | 99.60 | 0.70 | 0.18 | 0.12 |
| 06HS-1_plag-4 | Indian Creek | plag | 63.22 | 0.01 | 21.76 | 0.23 | 0.01 | 0.00 | 3.35 | 8.14 | 2.47 | -0.01 | 99.16 | 0.70 | 0.16 | 0.14 |
| 06HS-1_cpx-1 | Indian Creek | cpx | 50.77 | 0.26 | 0.65 | 18.40 | 0.80 | 9.53 | 18.56 | 0.32 | 0.03 | 0.01 | 99.34 | 0.29 | 0.40 | 0.31 |
| 06HS-1_cpx-1 | Indian Creek | cpx | 50.22 | 0.23 | 0.72 | 18.39 | 0.79 | 9.45 | 18.40 | 0.37 | 0.00 | 0.00 | 98.56 | 0.29 | 0.40 | 0.31 |
| 06HS-1_cpx-1 | Indian Creek | cpx | 50.78 | 0.30 | 0.64 | 18.56 | 0.81 | 9.67 | 18.56 | 0.29 | 0.01 | 0.01 | 99.62 | 0.29 | 0.40 | 0.31 |
| 06HS-1_cpx-2 | Indian Creek | cpx | 51.74 | 0.26 | 0.74 | 17.86 | 0.78 | 10.20 | 18.77 | 0.31 | 0.01 | -0.02 | 100.65 | 0.30 | 0.40 | 0.30 |
| 06HS-1_cpx-2 | Indian Creek | cpx | 51.35 | 0.21 | 0.64 | 18.78 | 0.80 | 9.79 | 18.36 | 0.31 | 0.01 | 0.01 | 100.25 | 0.29 | 0.39 | 0.31 |
| 06HS-1_cpx-2 | Indian Creek | cpx | 51.06 | 0.29 | 0.88 | 16.80 | 0.68 | 10.68 | 18.76 | 0.32 | 0.01 | 0.00 | 99.46 | 0.32 | 0.40 | 0.28 |
| 06HS-1_opx-3 | Indian Creek | opx | 49.70 | 0.18 | 0.32 | 34.32 | 1.42 | 12.05 | 1.71 | 0.03 | 0.00 | 0.00 | 99.73 | 0.37 | 0.04 | 0.59 |
| 06HS-1_opx-3 | Indian Creek | opx | 49.33 | 0.20 | 0.30 | 34.48 | 1.43 | 11.90 | 1.71 | 0.02 | 0.01 | -0.02 | 99.35 | 0.37 | 0.04 | 0.60 |
| 06HS-1_opx-3 | Indian Creek | opx | 49.91 | 0.18 | 0.29 | 34.41 | 1.44 | 11.92 | 1.63 | 0.03 | 0.00 | -0.01 | 99.80 | 0.37 | 0.04 | 0.60 |
| 06HS-1_opx-4 | Indian Creek | opx | 49.71 | 0.18 | 0.31 | 34.46 | 1.40 | 11.76 | 1.56 | 0.00 | 0.00 | -0.02 | 99.36 | 0.37 | 0.03 | 0.60 |
| 06HS-1_opx-4 | Indian Creek | opx | 50.03 | 0.18 | 0.31 | 34.55 | 1.41 | 11.67 | 1.70 | 0.03 | 0.00 | 0.00 | 99.88 | 0.36 | 0.04 | 0.60 |
| 06HS-1_opx-4 | Indian Creek | opx | 50.16 | 0.18 | 0.30 | 34.09 | 1.41 | 11.79 | 1.63 | 0.00 | 0.00 | -0.02 | 99.57 | 0.37 | 0.04 | 0.60 |
| 06HS-1_opx-5 | Indian Creek | opx | 49.85 | 0.15 | 0.28 | 34.44 | 1.47 | 12.14 | 1.56 | 0.05 | 0.00 | -0.02 | 99.93 | 0.37 | 0.03 | 0.59 |
| 06HS-1_opx-5 | Indian Creek | opx | 49.81 | 0.20 | 0.29 | 34.36 | 1.49 | 12.10 | 1.52 | 0.02 | 0.00 | -0.03 | 99.77 | 0.37 | 0.03 | 0.59 |
| 06HS-1_opx-5 | Indian Creek | opx | 50.16 | 0.15 | 0.29 | 34.25 | 1.46 | 12.07 | 1.53 | 0.01 | 0.00 | -0.01 | 99.92 | 0.37 | 0.03 | 0.59 |
| 06HS-1_opx-5-rim | Indian Creek | opx | 49.44 | 0.20 | 0.26 | 34.61 | 1.46 | 11.67 | 1.52 | 0.02 | 0.00 | -0.03 | 99.14 | 0.36 | 0.03 | 0.60 |
| 06HS-1_opx-5-rim | Indian Creek | opx | 49.26 | 0.19 | 0.25 | 35.33 | 1.49 | 11.72 | 1.64 | 0.03 | 0.00 | -0.01 | 99.91 | 0.36 | 0.04 | 0.61 |
| 06HS-1_opx-5-rim | Indian Creek | opx | 49.54 | 0.18 | 0.29 | 34.93 | 1.50 | 11.52 | 1.54 | 0.01 | 0.01 | -0.01 | 99.51 | 0.36 | 0.03 | 0.61 |
| 06HS-1_opx-6 | Indian Creek | opx | 49.35 | 0.14 | 0.30 | 34.87 | 1.42 | 11.66 | 1.64 | -0.01 | 0.00 | -0.02 | 99.36 | 0.36 | 0.04 | 0.60 |
| 06HS-1_opx-6 | Indian Creek | opx | 49.71 | 0.17 | 0.27 | 34.86 | 1.53 | 11.72 | 1.55 | 0.03 | 0.00 | -0.01 | 99.81 | 0.36 | 0.03 | 0.60 |
| 06HS-1_opx-6 | Indian Creek | opx | 50.03 | 0.18 | 0.27 | 34.31 | 1.45 | 12.02 | 1.58 | 0.02 | 0.01 | -0.02 | 99.86 | 0.37 | 0.04 | 0.59 |

**Table B3.** Heise oxygen isotope data

| | Sample | Ar-Ar Age* | $\delta^{18}O$ (‰) | Mineral | Description | Calc. Melt $\delta^{18}O$ (‰) |
|---|---|---|---|---|---|---|
| **Blacktail Creek Tuff (BCT)** | 95-2001a | 6.62 | 6.66 | quartz | 5 crystals | 6.6 |
| | 95-2001a | 6.62 | 6.74 | quartz | 6 crystals | |
| | 95-2001a | 6.62 | 6.06 | quartz | 25 crystals | |
| | 95-2001a | 6.62 | 6.15 | quartz | 10 crystals | |
| | 95-2001a | 6.62 | 4.81 | zircon | bulk | |
| | 95-2001a | 6.62 | 4.80 | zircon | bulk | |
| | 06HS-6 | 6.62 | 6.86 | quartz | 3 crystals | |
| | 06HS-6 | 6.62 | 6.60 | quartz | many crystals | |
| **Milo Dry Farm rhyolite (MDF)** | 08HS-9 | 6.45 (?) | 7.41 | quartz | 1 crystal | 7.3 |
| | 08HS-9 | 6.45 (?) | 7.51 | quartz | 1 crystal | |
| | 08HS-9 | 6.45 (?) | 6.69 | sanidine | 1 crystal | |
| | 08HS-9 | 6.45 (?) | 6.78 | sanidine | 2 crystals | |
| | 08HS-9 | 6.45 (?) | 6.77 | sanidine | 5 crystals | |
| **Walcott Tuff (WT)** | 06-HS-18 | 6.27 | 5.41 | sanidine | – | 6.1 |
| | 06-HS-18 | 6.27 | 5.55 | sanidine | – | |
| | 06-HS-18 | 6.27 | 5.67 | sanidine | 2 crystals | |
| | 06-HS-18 | 6.27 | 5.67 | sanidine | many crystals | |
| | 06-HS-18 | 6.27 | 4.14 | zircon | bulk | |
| | 06-HS-18 | 6.27 | 4.19 | zircon | bulk | |
| **Lidy Hotsprings rhyolite (LHS)** | 08-HS-10 | 6.20 | 3.71 | sanidine | many crystals | 4.4 |
| | 08-HS-10 | 6.20 | 3.57 | sanidine | many crystals | |
| | 08-HS-10 | 6.20 | 3.74 | sanidine | many crystals | |
| **Kelly Canyon rhyolite (KC)** | 1103.1 | *5.7* | 5.74 | sanidine | many crystals | 6.4 |
| | 1103.1 | *5.7* | 5.59 | sanidine | many crystals | |
| **Wolverine Creek Tuff (WCT)** | 06-HS-16 | 5.59 | 5.64 | sanidine | 2 crystals | 6.5 |
| | 06-HS-16 | 5.59 | 6.06 | sanidine | 3 crystals | |
| | 06-HS-16 | 5.59 | 5.80 | sanidine | 4 crystals | |
| | 06-HS-16 | 5.59 | 6.35 | obsidian | – | |
| | 06-HS-16 | 5.59 | 6.36 | obsidian | – | |
| **Conant Creek Tuff (CCT)** | 06-HS-5 | 5.51 | 5.54 | sanidine | 1 crystal | 5.9 |
| | 06-HS-5 | 5.51 | 5.77 | sanidine | 3 crystals | |
| | 06-HS-5 | 5.51 | 5.19 | sanidine | – | |
| | 06-HS-5 | 5.51 | 5.80 | sanidine | – | |
| | 06-HS-5 | 5.51 | 5.31 | sanidine | 2 crystals | |
| | 06-HS-5 | 5.51 | 3.89 | zircon | bulk | |
| | 06-HS-5 | 5.51 | 4.03 | zircon | bulk | |
| **Pre-Kilgore Tuff (P-KT)** | 06-HS-14 | **4.87** | 3.18 | quartz | 5 crystals | 3.5 |
| | 06-HS-14 | **4.87** | 3.12 | quartz | many crystals | |
| | 06-HS-14 | **4.87** | 3.53 | quartz | 3 crystals | |
| | 06-HS-14 | **4.87** | 3.32 | quartz | 5 crystals | |
| | 06-HS-14 | **4.87** | 1.81 | zircon | 10-50µm | |
| | 06-HS-14 | **4.87** | 1.98 | zircon | 10-50µm | |
| | 06-HS-14 | **4.87** | 2.86 | sanidine | 1 crystal | |
| | 06-HS-14 | **4.87** | 2.76 | sanidine | 2 crystals | |
| **Kilgore Tuff (KT)** | TNP 96-43 | 4.52 | 4.33 | quartz | 30 crystals | 3.4 |
| | TNP 96-43 | 4.52 | 1.58 | zircon | >150µm, abraded | |
| | TNP 96-43 | 4.52 | 1.69 | zircon | 50-100µm | |
| | TNP 96-43 | 4.52 | 1.63 | zircon | <53µm | |
| | TNP 96-43 | 4.52 | 1.54 | zircon | <53µm | |
| | TNP 96-43 | 4.52 | 3.05 | sanidine | many crystals | |
| | TNP 96-43 | 4.52 | 2.74 | sanidine | many crystals | |
| | TNP 96-43 | 4.52 | 2.84 | sanidine | many crystals | |

**Table B3. (continued).**

| | | | | | | |
|---|---|---|---|---|---|---|
| **Kilgore Tuff (KT)** | 95-2017b | 4.51 | 4.31 | quartz | – | 3.3 |
| | 95-2017b | 4.51 | 4.85 | quartz | – | |
| | 95-2017b | 4.51 | 3.79 | quartz | 10 crystals | |
| | 95-2017b | 4.51 | 4.21 | quartz | 25 crystals | |
| | 95-2017b | 4.51 | 1.60 | zircon | bulk | |
| | 95-2017b | 4.51 | 1.40 | zircon | bulk | |
| | 95-2017b | 4.51 | 2.84 | sanidine | many crystals | |
| | 95-2017b | 4.51 | 2.71 | sanidine | 3 crystals | |
| | 95-2017b | 4.51 | 2.65 | sanidine | 4 crystals | |
| **Kilgore Tuff (KT)** | 95-2015 | 4.44 | 2.84 | sanidine | – | 3.6 |
| | 95-2015 | 4.44 | 3.06 | sanidine | – | |
| **Kilgore Tuff (KT)** | 06-HS-11 | 4.43 | 2.91 | sanidine | many crystals | 3.6 |
| | 06-HS-11 | 4.43 | 3.03 | sanidine | many crystals | |
| **Kilgore Tuff (KT)** | 06-HS-10 | 4.43 | 2.69 | sanidine | many crystals | 3.3 |
| | 06-HS-10 | 4.43 | 2.76 | sanidine | 3 crystals | |
| | 06-HS-10 | 4.43 | 2.66 | sanidine | many crystals | |
| | 06-HS-10 | 4.43 | 2.50 | sanidine | 3 crystals | |
| **Kilgore Tuff (KT)** | 95-2010 | 4.43 | 2.71 | sanidine | – | 3.3 |
| | 95-2010 | 4.43 | 2.74 | sanidine | – | |
| **Indian Creek rhyolite (IC)** | 06-HS-1 | **3.96** | 1.29 | zircon | >105µm | 3.0 |
| | 06-HS-1 | **3.96** | 1.12 | zircon | >105µm | |
| | 06-HS-1 | **3.96** | 1.40 | zircon | >53µm | |
| | 06-HS-1 | **3.96** | 1.12 | zircon | 53-105µm | |
| | 06-HS-1 | **3.96** | 3.28 | sanidine | – | |
| | 06-HS-1 | **3.96** | 2.75 | sanidine | – | |
| | 06-HS-1 | **3.96** | 3.95 | sanidine | 2 crystals | |
| | 06-HS-1 | **3.96** | 3.76 | sanidine | 3 crystals | |
| | 06-HS-1 | **3.96** | 3.44 | sanidine | 3 crystals | |
| **Juniper Buttes rhyolite (JB)** | 06-HS-4A | **4.29** | 4.03 | sanidine | – | 3.7 |
| | 06-HS-4A | **4.29** | 3.61 | sanidine | – | |
| | 06-HS-4A | **4.29** | 3.95 | sanidine | 2 crystals | |
| **Long Hollow rhyolite (LH)** | 626.1 | **4.28** | 4.64 | quartz | 10 crystals | 3.7 |
| | 626.1 | **4.28** | 4.71 | quartz | 30 crystals | |
| | 626.1 | **4.28** | 4.73 | quartz | many crystals | |
| | 626.1 | **4.28** | 4.20 | quartz | many crystals | |
| | 626.1 | **4.28** | 4.26 | quartz | many crystals | |
| | 626.1 | **4.28** | 4.50 | quartz | many crystals | |
| | 626.1 | **4.28** | 1.92 | zircon | bulk | |
| | 626.1 | **4.28** | 1.92 | zircon | >105µm | |
| | 626.1 | **4.28** | 1.65 | zircon | <78µm | |
| | 626.1 | **4.28** | 3.98 | sanidine | 1 crystal | |
| | 626.1 | **4.28** | 3.78 | sanidine | – | |
| **Sheridan Reservoir rhyolite (SR** | 06-HS-19 | **2.07** | 4.47 | quartz | 2 crystals | 4.0 |
| | 06-HS-19 | **2.07** | 4.80 | quartz | 1 crystal | |
| | 06-HS-19 | **2.07** | 4.34 | quartz | 1 crystal | |
| | 06-HS-19 | **2.07** | 4.50 | quartz | – | |
| | 06-HS-19 | **2.07** | 2.41 | zircon | <53µm | |
| | 06-HS-19 | **2.07** | 2.07 | zircon | <53µm | |
| | 06-HS-19 | **2.07** | 2.37 | zircon | 53-105µm | |
| | 06-HS-19 | **2.07** | 2.51 | zircon | >105µm | |
| | 06-HS-19 | **2.07** | 3.90 | sanidine | – | |
| | 06-HS-19 | **2.07** | 3.75 | sanidine | – | |
| | 06-HS-19 | **2.07** | 3.72 | sanidine | – | |

**Table B3. (continued).**

*Ar-Ar ages published in Morgan & McIntosh (2005); age in italics (Kelley Canyon rhyolite) is an old K-Ar age published in Morgan & McIntosh (2005), ages in bold are U-Pb ages from Bindeman et al. (2007) and this study.

Note: Milo Dry Farm rhyolite has not been dated; it is a post-Blacktail Creek Tuff rhyolite that lies stratigraphically between the Blacktail Creek Tuff and the Walcott Tuff (Morgan & McIntosh, 2005). We used an intermediate age (6.45 Ma) in order to include it in Fig. 7b.

**Table B4.** Yellowstone, Heise and Bruneau-Jarbidge Ar-Ar ages, cumulative eruptive volumes, and O, Sr and Nd isotope data

| | Sample | Ar-Ar Age | Age Ref. | Volume ($km^3$) | Cum. Vol. | $\delta^{18}O$ melt (‰) | $^{87}Sr/^{86}Sr_i$ | $^{143}Nd/^{144}Nd$ | Eps. Nd |
|---|---|---|---|---|---|---|---|---|---|
| **Yellowstone rhyolites** | | | | | | | | | |
| HRT-A | HRT-3A | 2.06 | 1 | 820 | 820 | 7.3 | *0.71171* | *0.512135* | *-9.81* |
| HRT-B | HRT-1B | 2.06 | 1 | 1340 | 2160 | 7.0 | *0.70980* | *0.512198* | *-8.58* |
| HRT-C | HRT-C | 2.06 | 1 | 290 | 2450 | 7.5 | *0.72685* | *0.511689* | *-18.51* |
| post-HRT | | | | 50 | 2500 | | | | |
| Headquarters Flow | HQ-1 | 1.86 | 2 | | 2500 | 3.2 | — | — | — |
| Blue Creek Flow | BC-1 | 1.78 | 2 | | 2500 | 2.9 | *0.71719* | *0.511978* | *-12.87* |
| Mesa Falls Tuff | MFT-2 | 1.29 | 1 | 280 | 2780 | 5.4 | *0.70868* | *0.512184* | *-8.86* |
| Lewis Canyon rhyolite | YL96-11 | 0.853 | 2 | | 2780 | 5.9 | *0.71401* | *0.51217* | *-9.13* |
| LCT-A | LCT3a | 0.639 | 1 | 510 | 3290 | 5.9 | *0.71093* | *0.512154* | *-9.44* |
| LCT-B | LCT-2,B | 0.639 | 1 | 490 | 3780 | 6.3 | *0.71000* | *0.512237* | *-7.82* |
| post-LCT UBM | | | | 70 | 3850 | | | | |
| Middle Biscuit Basin flow | YL96-20 | 0.519 | 3 | | 3850 | 1.1 | *0.71930* | *0.512136* | *-9.79* |
| Dunraven Road Flow | YL96-4 | 0.486 | 3 | | 3850 | 1.0 | — | — | — |
| Canyon Flow | YL96-18 | 0.484 | 3 | | 3850 | 0.7 | *0.71607* | *0.512165* | *-9.23* |
| post-LCT CPM | | | | 620 | 4470 | | | | |
| South Biscuit Basin Flow | YL96-2 | 0.255 | 4 | | 4470 | 3.7 | — | — | — |
| Scaup Lake Flow | YL96-9 | 0.198 | 3 | | 4470 | 4.0 | *0.70993* | *0.512236* | *-7.84* |
| West Yellowstone flow | YL96-1 | 0.114 | 5 | | 4470 | 4.5 | *0.71039* | *0.512271* | *-7.16* |
| Solfatara Plateau flow | YL96-16 | 0.1028 | 5 | | 4470 | 3.2 | *0.71116* | *0.512252* | *-7.53* |
| Pitchstone Plateau flow | 7YC-179 | 0.0791 | 5 | | 4470 | 4.5* | *0.71101* | *0.512267* | *-7.24* |
| References: | 4, 6, 7 | | | 8, 9 | | 4, 6 | 10, 11 | 10, 11 | |
| | | | | | | | | | |
| **Heise rhyolites** | | | | | | | | | |
| Blacktail Creek Tuff | 95-2001a | 6.62 | 12 | 1200 | 1200 | 6.6 | 0.712381 | 0.512146 | -9.60 |
| Walcott Tuff | 06-HS-18 | 6.27 | 12 | 750 | 1950 | 6.1 | 0.709912 | 0.51216 | -9.32 |
| Lidy Hotsprings rhyolite | 08-HS-10 | 6.2 | 12 | 10? | 1960 | 4.4 | 0.71138 | 0.512141 | -9.69 |
| Kelly Canyon rhyolite | 1103.1 | 5.7 | 12 | 10? | 1970 | 6.4 | — | — | — |
| Wolverine Creek Tuff | 06-HS-16 | 5.59 | 12 | 100? | 2070 | 6.5 | 0.709473 | 0.512333 | -5.95 |
| Conant Creek Tuff | 06-HS-5 | 5.51 | 12 | 300 | 2370 | 5.9 | 0.708949 | 0.512293 | -6.73 |
| Kilgore Tuff | 06-HS-14 | **4.87** | this study | 1800 | 4170 | 3.5 | 0.710712 | 0.512145 | -9.62 |
| Kilgore Tuff | TNP 96-43 | 4.52 | 12 | | 4170 | 3.4 | 0.71029 | 0.51222 | -8.15 |
| Kilgore Tuff | 95-2017b | 4.51 | 12 | | 4170 | 3.3 | 0.710378 | 0.512246 | -7.65 |
| Kilgore Tuff | 95-2015 | 4.44 | 12 | | 4170 | 3.6 | — | — | — |
| Kilgore Tuff | 06-HS-11 | 4.43 | 12 | | 4170 | 3.6 | 0.710655 | 0.512229 | -7.98 |

**Table B4. (continued).**

| | | | | | | | | | |
|---|---|---|---|---|---|---|---|---|---|
| Kilgore Tuff | 06-HS-10 | 4.43 | 12 | | 4170 | 3.3 | 0.710476 | 0.512215 | -8.25 |
| Kilgore Tuff | 95-2010 | 4.43 | 12 | | 4170 | 3.3 | — | — | — |
| Indian Creek rhyolite | 06-HS-1 | **3.96** | this study | 10? | 4180 | 3.0 | 0.710736 | 0.512238 | -7.80 |
| Juniper Buttes rhyolite | 06-HS-4A | **4.29** | this study | 10? | 4190 | 3.7 | 0.709858 | 0.512196 | -8.62 |
| Long Hollow rhyolite | 626.1 | **4.28** | this study | 10? | 4200 | 3.7 | 0.709174 | 0.51219 | -8.74 |
| References: | this study | | | 12 | | this study | this study | this study | |
| | | | | | | | | | |
| **Bruneau-Jarbidge rhyolites** | | | | | | | | | |
| CP III | I-569 | 12.64 | 13 | 100 | 100 | 3.8 | 0.70865 | 0.512193 | -8.68 |
| CP V | I-556 | 12.07 | 16 | 300 | 400 | 2.9 | — | — | — |
| CP VII | I-841 | 11.81 | 13 | 1200 | 1900 | 0.2 | 0.71031 | 0.512192 | -8.70 |
| CP XI | I-463 | 11.22 | 13 | 1800 | 3900 | 2.6 | — | 0.512259 | -7.39 |
| CP XIII | X-37 | 10.82 | 13 | 1800 | 5700 | 3.2 | 0.70935 | 0.512248 | -7.61 |
| CP XV | I-459 | 10.5 | 13 | 200 | 5900 | 1.1 | 0.70938 | 0.512219 | -8.17 |
| Cedar Tree | I-1119 | 10.16 | 13 | 100 | 6000 | 2.3 | — | — | — |
| Ind. Batt | I-445 | 9.8 | 13 | 100 | 6100 | 2.1 | 0.71044 | 0.512238 | -7.80 |
| Brun. Jasp. | I-411 | 9.5 | 13 | 200 | 6300 | 3.4 | 0.71062 | 0.512293 | -6.73 |
| Sheep Ck | I-1208 | 9.3 | 13 | 400 | 6700 | 2.2 | 0.7115 | 0.512264 | -7.30 |
| Dorsey Ck | I-529 | 8.1 | 13 | 300 | 7000 | 1.5 | 0.7122 | 0.512304 | -6.52 |
| References: | 13 | | | 14 | | 13, 15, 16 | 13 | 13 | |

*Calculated from quartz data published in Hildreth et al. (1984).

Notes: Ages in bold are U-Pb ages from this study. Volumes with question marks are estimated; no published volumes are available. Sr and Nd values in italics are for different samples of the same units.

References: (1) Lanphere et al., 2002; (2) Obradovich, 1992; (3) Gansecki et al., 1998; (4) Bindeman et al., 2008; (5) Calvert, 2005, as in Christiansen et al., 2007; (6) Bindeman and Valley, 2001; (7) Hildreth et al., 1984; (8) Christiansen et al., 2001; (9) Christiansen et al., 2007; (10) Hildreth et al., 1991; (11) Vazquez and Reid, 2002; (12) Morgan and McIntosh, 2005; (13) Bonnichsen et al., 2008; (14) Leeman et al., 2008; (15) Ellis, unpublished; (16) Savov et al., 2009. Full references are in the Chapter IV References Cited section.

**Table B5.** Fractional crystallization calculations

| | Partition coefficients | | | $\bar{D}$ | | BCT–WT | WT–CCT | P-KT–KT | P-KT–KT |
|---|---|---|---|---|---|---|---|---|---|
| | Plag | Cpx | Zircon | | $C_o$:* | 95-2001a | 06HS-18 | 06HS-14 | 06HS-14 |
| | | | | | $C_l$:* | 06HS-18 | 06HS-5 | 06HS-10 | 06HS-11 |
| | | | | | | $F'$ | $F'$ | $F'$ | $F'$ |
| Sr | 6·8 | 0·98 | — | 6·20 | Sr | 0·86 | 0·91 | 0·80 | 0·81 |
| Ba | 6·95 | 0·1 | — | 6·25 | Ba | 0·97 | 0·89 | 0·98 | 0·98 |
| La | 0·07 | 0·52 | 7·2 | 0·13 | La | 0·91 | 0·87 | 0·92 | 0·94 |
| Ce | 0·032 | 1·54 | 10 | 0·21 | Ce | 0·85 | 0·82 | 1·03 | 0·99 |
| Modal % | 0·8975 | 0·10 | 0·0025 | | Av. $F'$ | 0·90 | 0·87 | 0·93 | 0·93 |
| | | | | | 1 – $F'$ | 0·10 | 0·13 | 0·07 | 0·07 |

*See Table 3 for trace element concentrations for samples 95-2001a, 06HS-18, 06HS-5, 06HS-14, 06HS-10 and 06HS-11.

In order to estimate the amount of fractional crystallization required to generate the trace element ratio variations observed for successive eruptions of the Blacktail Creek Tuff (BCT), Walcott Tuff (WT) and Conant Creek Tuff (CCT) from a common magma reservoir (see Fig. 6a-e), we used published partition coefficients for Sr, Ba, La and Ce for a high-silica rhyolite composition (earthref.org) and the following equation:

$$F' = \frac{C_l}{C_o}^{\left(\frac{1}{\bar{D}-1}\right)}$$

where $F'$ is the fraction of original liquid remaining, $C_o$ is the trace element concentration in the original liquid, $C_l$ is the trace element concentration in the liquid after crystallization, and $\bar{D}$ is the bulk partition coefficient for a modal mineralogy of 0.8975 plagioclase (plag), 0.10 clinopyroxene (cpx), and 0.0025 zircon, which is consistent with our petrographic observations. Using the same approach, we also estimate the amount of fractional crystallization required to generate the Kilgore Tuff (KT) from the Pre-Kilgore Tuff (P-KT). Our results indicate ~10-15% fractional crystallization (*1-F'*) steps from the Blacktail Creek Tuff ($C_o$) to the Walcott Tuff ($C_l$) and the Walcott Tuff ($C_o$) to the Conant Creek Tuff ($C_l$) (see Table B5 above). We chose Kilgore Tuff samples 06HS-10 and 06HS-11 to estimate the amount of fractional crystallization of the Pre-Kilgore Tuff (06HS-14), as these samples are from the same stratigraphic section as the Pre-Kilgore Tuff (see Fig. 3). The results indicate ~10% fractional crystallization of the Pre-Kilgore Tuff to generate the Kilgore Tuff (see Table B5 above).

**Table B6.** Crustal melting calculations

| | Partition coefficients | | | | $\bar{D}$ | $C_o$ | $C_l$ | $F$ |
|---|---|---|---|---|---|---|---|---|
| | Plag | Cpx | Mt | Ilm | | Upper crust* | 95-2001a | |
| Rb | 0·06 | 0·03 | 0·01 | — | 0·05 | 112 | 174 | 0·62 |
| Ba | 0·19 | 0·1 | 0·1 | — | 0·18 | 550 | 1099 | 0·39 |
| Th | 0·11 | 0·1 | 0·01 | 0·427 | 0·11 | 10·7 | 33 | 0·24 |
| U | 0·13 | 0·12 | 0·74 | 0·063 | 0·15 | 2·8 | 7 | 0·33 |
| Nb | 0·07 | 0·02 | — | 6·58 | 0·13 | 12·0 | 31·8 | 0·29 |
| La | 0·07 | 0·52 | 0·8 | 1·31 | 0·16 | 30 | 66 | 0·36 |
| Ce | 0·22 | 0·84 | 0·71 | 1·19 | 0·31 | 64 | 120 | 0·33 |
| Pb | 0·5 | 0·2 | 0·32 | 0·34 | 0·46 | 17 | 26 | 0·35 |
| Sr | 6·8 | 0·98 | 0·017 | 0·74 | 5·89 | 350 | 84 | 0·35 |
| Nd | 0·19 | 1·4 | 0·93 | 0·96 | 0·35 | 26 | 45 | 0·35 |
| Zr | 0·36 | 0·29 | 0·24 | 0·49 | 0·35 | 190 | 327 | 0·36 |
| Y | 0·21 | 0·86 | 0·12 | 0·024 | 0·27 | 22 | 44 | 0·31 |
| Sc | 0·01 | 33 | 1·5 | 5·9 | 3·43 | 13·6 | 5 | 0·37 |
| Modal % | 0·85 | 0·10 | 0·04 | 0·01 | | | Av.F | 0·36 |
| | | | | | | | SD | 0·09 |
| | | | | | | | SE | 0·02 |

SD, standard deviation; SE, standard error.
*Upper continental crust composition from Taylor & McLennan (1985) and McLennan et al. (2006).

In order to estimate the amount of melting required to generate the trace element composition of the earliest Heise Tuff, the Blacktail Creek Tuff (95-2001a), from the upper continental crust composition of Taylor & McLennan (1985) and McLennan et al. (2006), we used published partition coefficients for a suite of trace elements for granite compositions (earthref.org) and the modal batch melting equation:

$$F = \frac{C_o / \left(C_l - \overline{D}\right)}{1 - \overline{D}}$$

where $F$ is the melt fraction, $C_o$ is the trace element concentration in the original solid (upper continental crust), $C_l$ is the trace element concentration in the melt (95-2001a), and $\overline{D}$ is the bulk partition coefficient for a modal mineralogy of 0.85 plagioclase (plag), 0.10 clinopyroxene (cpx), 0.4 magnetite (mt), and 0.1 ilmenite (ilm), which is consistent with the modal mineralogy for upper crustal xenoliths in the Snake River Plain (Leeman et al., 1985). The results indicate an average melt fraction of ~36%±4% (2 std. error), and thus ~30-40% melting of the upper continental crust (see Tables B6 above).

**Figure B1.** Compositional variations of Heise phenocrysts. Large symbols are results from this study, small symbols are results from Henshaw (2002). (a) $Na_2O$ vs. CaO in plagioclase showing a wide compositional range and overlap between most Heise units. (b) FeO vs. MgO in clinopyroxene showing overlapping compositional fields for Heise units, though some separation is apparent (e.g., Kilgore Tuff). (c) FeO vs. MgO in orthopyroxene showing distinct compositional fields for individual Heise units.

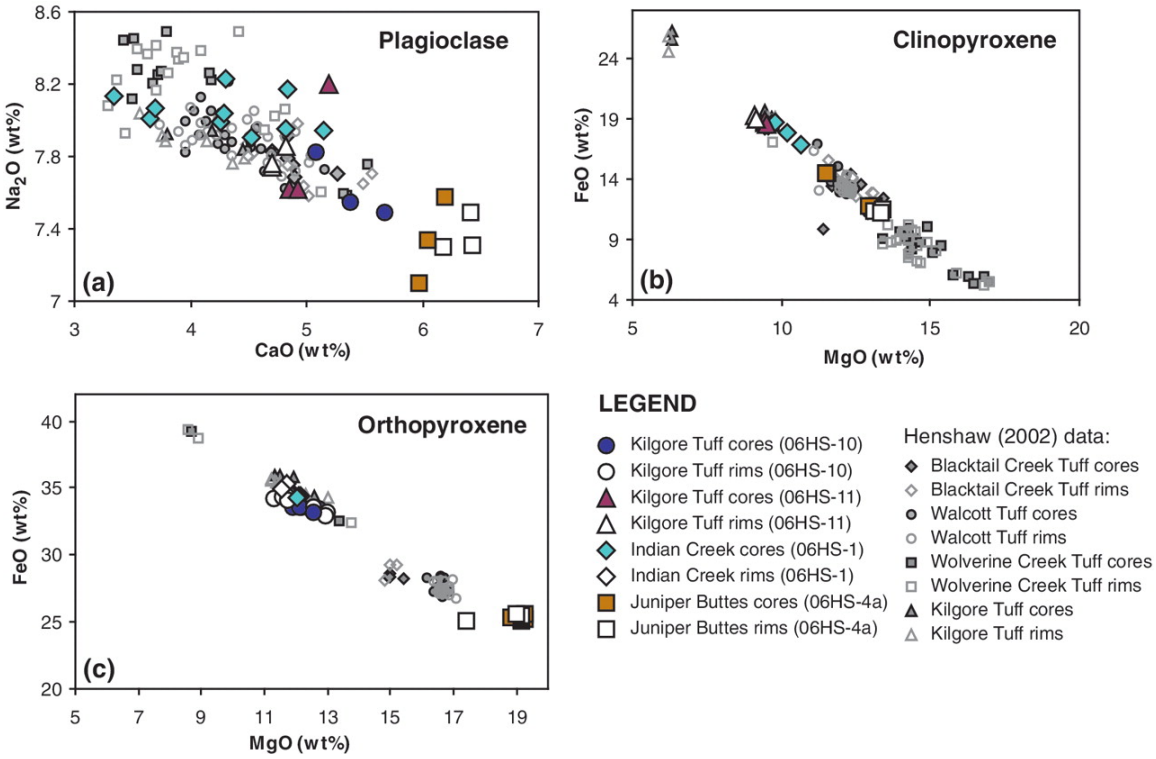

# APPENDIX C

## SUPPLEMENTARY DATA FOR CHAPTER V

**Petrographic Descriptions for Thin Sections of Yellowstone Samples**

Sample: YL02-1
Unit: Pitchstone Plateau flow
Description: ~10 vol% phenocrysts (quartz, sanidine, clinopyroxene, orthopyroxene, Fe-Ti oxides and accessory phases). Crystal clusters of anhedral quartz, zircon is commonly attached to crystal clusters of Fe-Ti oxides and quartz, small glass reentrants observed in a minor proportion of quartz crystals. A few large (~3-4 mm) quartz crystals are observed to have resorbed, glass-rich cores (see Appendix Fig. C1a).

Sample: YL96-1
Unit: West Yellowstone flow
Description: ~5 vol% phenocrysts (quartz, sanidine, clinopyroxene, orthopyroxene, Fe-Ti oxides and accessory phases). Zircon occurs as small isolated crystals in the groundmass. Some zircons are attached to clinopyroxene crystals. Quartz crystals range from euhedral to subrounded, some with anhedral cores (see Appendix Fig. C1b). Glass shard deformation around phenocrysts is observed locally.

Sample: 06YS-4
Unit: Elephant Back flow
Description: ~10 vol% phenocrysts (quartz, sanidine, clinopyroxene, orthopyroxene, Fe-Ti oxides and accessory phases). Many quartz and sanidine crystals have glass reentrants (see Appendix Fig. C1c). Spherulites are abundant.

Sample: 06YS-2
Unit: Tuff of Bluff Point
Description: ~10 vol% phenocrysts (quartz, sanidine, clinopyroxene, orthopyroxene, Fe-Ti oxides and accessory phases). Quartz crystals are subrounded with glass reentrants. Large zircon crystals (~300-400μm) in the groundmass. Sample contains lithic fragments.

Sample: 08YS-14
Unit: North Biscuit Basin flow
Description: ~5 vol% phenocrysts (quartz, sanidine, clinopyroxene, orthopyroxene, Fe-Ti oxides and accessory phases). A couple of anhedral plagioclase crystals were observed, but the majority of feldspar is sanidine. Quartz is subrounded, some possess glass reentrants and large glass inclusions (see Appendix Fig. C1d). Zircon occurs as small isolated crystals in the groundmass and some are attached to Fe-Ti oxides. Groundmass is spherulitic.

**Petrographic Descriptions for Thin Sections of Yellowstone Samples (continued)**

Sample: YL96-2
Unit: South Biscuit Basin flow
Description: ~10 vol% phenocrysts (plagioclase, quartz, clinopyroxene, orthopyroxene, Fe-Ti oxides and accessory phases). Plagioclase crystals are sieved and anhedral, some occur in clusters. Quartz is anhedral with glass reentrants. Some large zircon crystals (~400μm) in the groundmass. Zircon is commonly attached to Fe-Ti oxides and clinopyroxene, sometimes in clusters of anhedral, sieved plagioclase crystals (see Appendix Fig. C1e-f).

Sample: 08YS-15b
Unit: East Biscuit Basin flow
Description: ~20 vol% phenocrysts (plagioclase, quartz, clinopyroxene, orthopyroxene, Fe-Ti oxides and accessory phases). Many plagioclase crystals are pervasively sieved. Clinopyroxene, orthopyroxene and Fe-Ti oxides occur in anhedral crystal clusters. Intense deformation of glass shards around phenocrysts and crystal clusters.

**Table C1.** Whole-rock major and trace element compositions of Yellowstone samples

| Sample | YL02-1 | YL96-1 | 06YS-4 | 06YS-2 | 08YS-14 | YL96-2 | YL96-9 | 08YS-15B |
|---|---|---|---|---|---|---|---|---|
| Unit | Pitchstone Plateau | West Yellowstone | Elephant Back | Tuff of Bluff Point | North Biscuit Basin | South Biscuit Basin | Scaup Lake | East Biscuit Basin |
| Latitude (°N) | | 44.49 | 44.56 | 44.45 | 44.53 | 44.49 | 44.45 | 44.47 |
| Longitude (°W) | | 110.87 | 110.45 | 110.56 | 110.82 | 110.87 | 110.81 | 110.85 |
| Zrc. Sat. T (°C) | 832 | 849 | 824 | 819 | 824 | 854 | 855 | 859 |
| Liquidus T (°C) | 866 | 825 | 864 | 858 | 868 | 857 | 847 | 938 |
| Major element analyses by XRF | | | | | | | | |
| $SiO_2$ | 76.41 | 79.00 | 74.69 | 76.68 | 75.92 | 75.30 | 74.80 | 67.97 |
| $TiO_2$ | 0.13 | 0.14 | 0.17 | 0.16 | 0.17 | 0.25 | 0.25 | 0.57 |
| $Al_2O_3$ | 11.85 | 10.70 | 11.81 | 11.67 | 12.01 | 12.60 | 12.30 | 13.78 |
| FeO* | 1.55 | 1.69 | 1.45 | 1.33 | 1.37 | 1.85 | 1.88 | 4.14 |
| MnO | 0.03 | 0.04 | 0.03 | 0.03 | 0.05 | 0.04 | 0.11 | 0.10 |
| MgO | 0.00 | 0.01 | 0.04 | 0.04 | 0.06 | 0.15 | 0.11 | 0.57 |
| CaO | 0.40 | 0.47 | 0.46 | 0.36 | 0.38 | 0.87 | 0.78 | 2.27 |
| $Na_2O$ | 3.53 | 3.08 | 3.20 | 3.24 | 3.32 | 3.27 | 3.13 | 3.81 |
| $K_2O$ | 5.04 | 4.42 | 5.06 | 5.07 | 5.24 | 4.75 | 4.72 | 3.91 |
| $P_2O_5$ | 0.01 | 0.03 | 0.01 | 0.02 | 0.02 | 0.05 | 0.05 | 0.13 |
| Sum | 98.95 | 99.58 | 96.93 | 98.60 | 98.52 | 99.13 | 99.10 | 97.26 |
| Trace element analyses by XRF (ppm) | | | | | | | | |
| Ba | 65 | 164 | 317 | 353 | 227 | 1100 | 1060 | 1007 |
| Rb | 195 | 162 | 178 | 178 | 192 | 159 | 158 | 136 |
| Sr | 3 | 10 | 15 | 16 | 12 | 67 | 61 | 165 |
| Zr | 262 | 296 | 233 | 218 | 234 | 315 | 312 | 413 |
| Y | 36 | 64 | 65 | 52 | 57 | 56 | 39 | 58 |
| Nb | 62 | 50 | 48 | 46 | 49 | 51 | 51 | 40 |
| Ga | 23 | – | 19 | 18 | 21 | – | – | 22 |
| Cu | 1 | – | 3 | 3 | 2 | – | – | 5 |
| Zn | 82 | – | 83 | 57 | 67 | – | – | 101 |
| Pb | 26 | – | 42 | 27 | 28 | – | – | 24 |
| La | 58 | – | 92 | 84 | 84 | – | – | 69 |
| Ce | 157 | – | 171 | 157 | 163 | – | – | 129 |
| Th | 26 | – | 29 | 27 | 28 | – | – | 20 |
| Nd | 41 | – | 64 | 59 | 60 | – | – | 55 |
| U | 6 | – | 6 | 5 | 6 | – | – | 5 |

All Fe as FeO*.

Data for samples YL96-1, YL96-2 and YL96-9 are from Bindeman and Valley (2001).

Zircon saturation temperatures were calculated from whole-rock compositions as in Watson and Harrison (1983). Liquidus temperatures were calculated with MELTS software (Ghiorso and Sack, 1995) at 1.5 kbar and 3 wt% $H_2O$.

**Table C2.** Fractional crystallization calculations

**Table C2a.**

| | Partition Coefficients | | | |
|---|---|---|---|---|
| | Plag | San | Qtz | $\overline{D}$ |
| Rb | 0.24 | 0.42 | 0 | 0.32 |
| Sr | 11.8 | 12.1 | 0 | 10.80 |
| Modal % | 0.3 | 0.6 | 0.1 | |

**Table C2b.**

| | SCL–PP | SBB–PP |
|---|---|---|
| $C_o$* | YL96-9 | YL96-2 |
| $C_l$* | YL02-1 | YL02-1 |
| | F' | F' |
| Rb | 0.74 | 0.74 |
| Sr | 0.72 | 0.73 |
| Avg. F' | 0.73 | 0.73 |
| 1-Avg. F' | 0.27 | 0.27 |

*See Table C1 for trace element concentrations for samples YL02-1, YL96-2 and YL96-9.

In order to estimate the amount of fractional crystallization required to generate the Rb/Sr ratio observed for the youngest and most evolved CPM rhyolite, the Pitchstone Plateau flow (PP), from the oldest and least evolved CPM rhyolite compositions, the Scaup Lake flow (SCL) and South Biscuit Basin flow (SBB), we used published partition coefficients for Sr and Rb for a high-silica rhyolite composition (earthref.org; see Table C2a) and the following equation:

$$F' = \frac{C_l}{C_o}^{\left(\frac{1}{\overline{D}-1}\right)}$$

where $F'$ is the fraction of original liquid remaining, $C_o$ is the trace element concentration in the original liquid, $C_l$ is the trace element concentration in the liquid after crystallization, and $\overline{D}$ is the bulk partition coefficient for a modal mineralogy of 0.30 plagioclase (plag), 0.60 sanidine (san), and 0.10 quartz (qtz), which is consistent with our petrographic observations. Our results indicate ~25-30% fractional crystallization ($1-F'$) to generate the Pitchstone Plateau composition ($C_l$) from the Scaup Lake and SBB compositions ($C_o$) (see Table C2b).

**Figure C1.** Photomicrographs of Central Plateau Member rhyolites in cross-polarized light. Note that progressively younger units have more euhedral phenocrysts with fewer disequilibrium mineral textures. (a) Pitchstone Plateau flow (PP), large euhedral quartz crystal on the right has a resorbed, glass-rich core that is connected to the groundmass by a glass reentrant. (b) West Yellowstone flow (WY), large euhedral quartz crystal with an anhedral core. (c) Elephant Back flow (EB), twinned sanidine crystal on the left with fractures and sieving, sieved quartz crystal on the right with glass reentrants. (d) North Biscuit Basin flow (NBB), subhedral quartz crystal with sieved core and glass reentrant. (e) South Biscuit Basin flow (SBB), anhedral quartz cluster, quartz crystals have abundant glass reentrants. (f) South Biscuit Basin flow (SBB), anhedral cluster of quartz and plagioclase, many crystals are fractured, plagioclase cores are pervasively sieved with large glass reentrants.

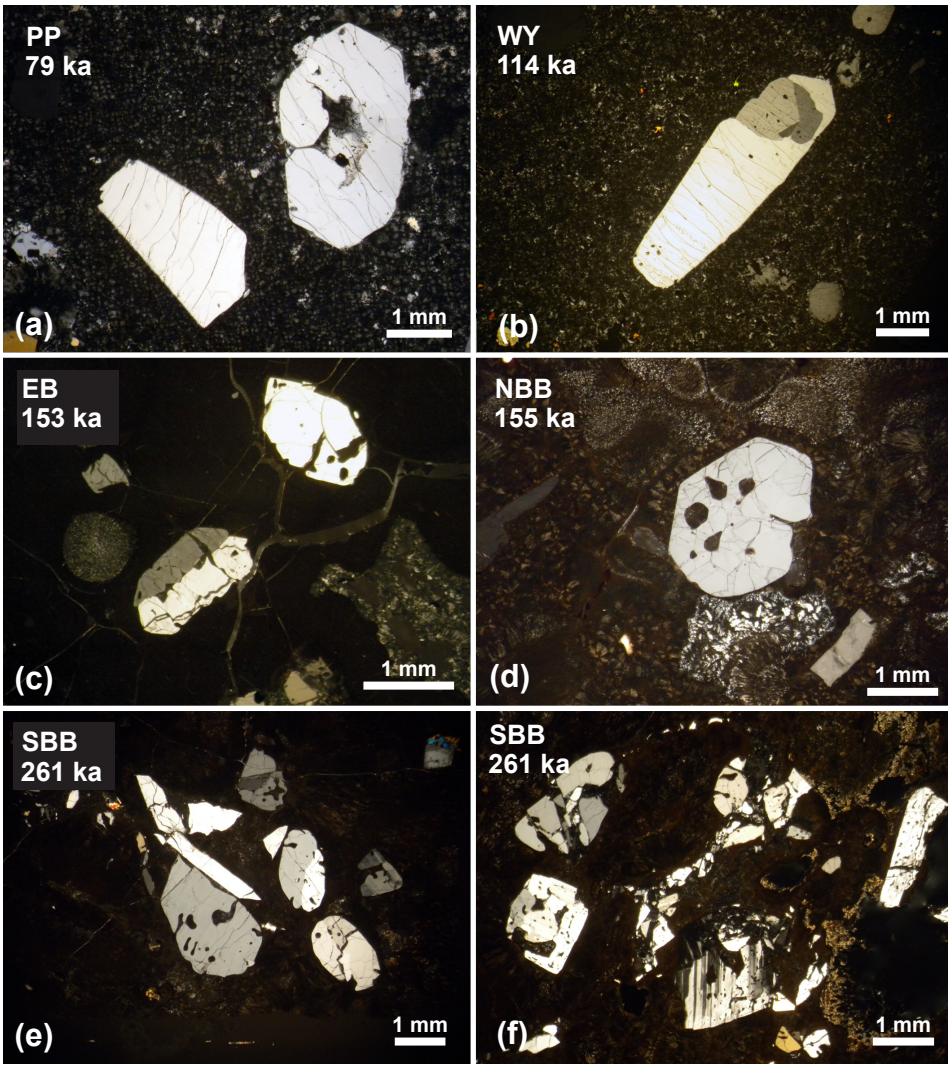

**Figure C2.** Geochemical differentiation parameters plotted against eruption age for Central Plateau Member rhyolites. Geochemical data is synthesized from Bindeman and Valley (2001), Girard and Stix (2009a), Vazquez et al. (2009) and this study (see Appendix Table C1 for major and trace element geochemistry). Eruption ages are from Christiansen et al. (2007). Note that the rhyolites become progressively more evolved with decreasing eruption age. The oldest rhyolites, South Biscuit Basin (SBB) and Scaup Lake (SCL) flows, and the youngest rhyolite, Pitchstone Plateau flow (PP), are labeled in each panel for reference. We estimate ~25-30% fractional crystallization of plagioclase and sanidine to generate the Rb/Sr ratio of the PP flow from the less-evolved SBB and SCL compositions (See fractional crystallization calculations in Appendix Table C2).

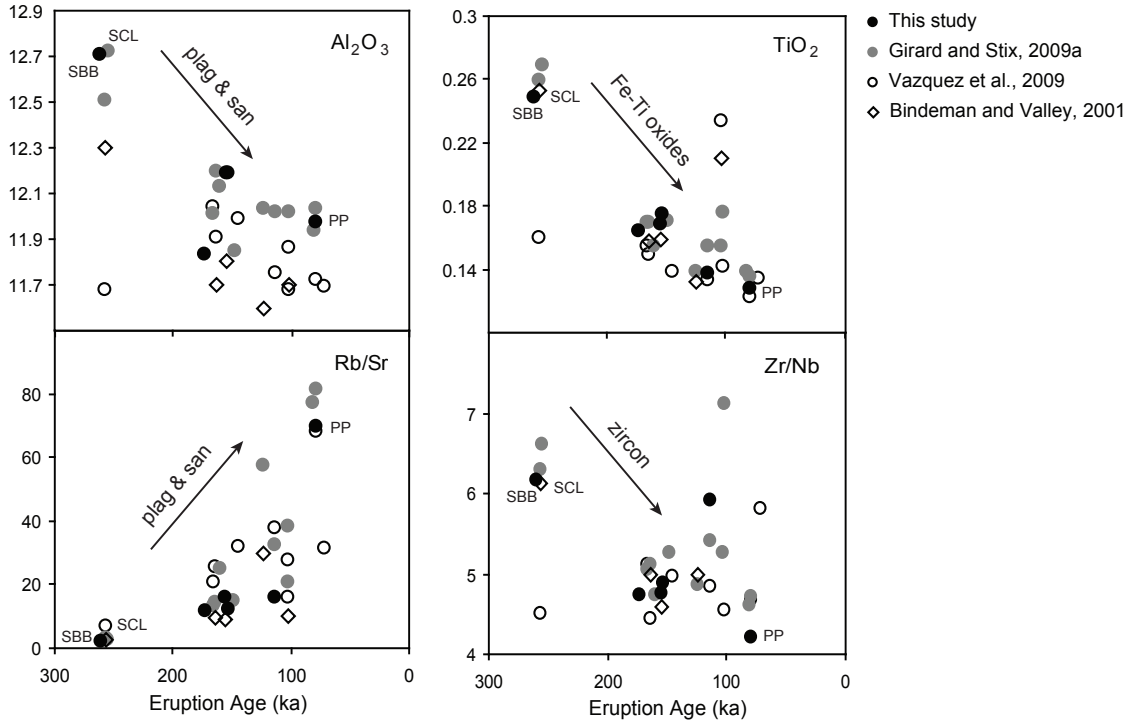

## REFERENCES CITED

### CHAPTER I


Bindeman, I. N., Watts, K. E., Schmitt, A. K., Morgan, L. A. & Shanks, P. W. C. (2007). Voluminous low $\delta^{18}O$ magmas in the late Miocene Heise volcanic field, Idaho: implications for the fate of Yellowstone hotspot calderas. Geology 35, 1019–1022.

Bonnichsen, B., Leeman, W. P., Honjo, N., McIntosh, W. C. & Godchaux, M. M. (2008). Miocene silicic volcanism in southwestern Idaho: geochronology, geochemistry, and evolution of the central Snake River Plain. Bulletin of Volcanology 70, 315–342.

Boroughs, S. B., Wolff, J., Bonnichsen, B., Godchaux, M. & Larson, P. (2005). Large volume, low-$\delta^{18}O$ rhyolites of the central Snake River Plain, Idaho, USA. Geology 33, 821–824.

Ellis, B., Barry, T., Branney, M.J., Wolff, J.A., Bindeman, I.N., Wilson, R. & Bonnichsen, B. (2010). Petrologic constraints on the development of a large-volume, high temperature, silicic magma system: The Twin Falls eruptive centre, central Snake River Plain. Lithos 120, 475–489.

Friedman, I., Lipman, P. W., Obradovich, J. D., Gleason, J. D. & Christiansen, R. L. (1974). Meteoric water in magmas. Science 184, 1069–1072.

Hildreth, W., Christiansen, R. L. & O'Neil, J. R. (1984). Catastrophic isotopic modification of rhyolitic magma at times of caldera subsidence, Yellowstone Plateau Volcanic Field. Journal of Geophysical Research 89, 8339–8369.

Morgan, L. A. & McIntosh, W. C. (2005). Timing and development of the Heise volcanic field, Snake River Plain, Idaho, western USA. Geological Society of America Bulletin 117, 288–306.

Nash, B. P., Perkins, M. E., Christensen, J. N., Lee, D. C. & Halliday, A. N. (2006). The Yellowstone hotspot in space and time: Nd and Hf isotopes in silicic magmas. Earth and Planetary Science Letters 247, 143–156.

Pierce, K. L. & Morgan, L. A. (1992). The track of the Yellowstone hot- spot: volcanism, faulting, and uplift. In: Link, P. K., Kuntz, M. A. & Platt, L. B. (eds) Regional Geology of Eastern Idaho and Western Wyoming. Geological Society of America, Memoirs 179, 1–53.

Taylor, H. P., Jr (1986). Igneous rocks: II. Isotopic case studies of circumpacific magmatism. In: Valley, J. W., Taylor, H. P., Jr & O'Neil, J. R. (eds) Stable Isotopes in High Temperature Geological Processes. Mineralogical Society of America, Reviews in Mineralogy 16, 273–316.

Waite, G.P., Smith, R.B. & Allen, R.M. (2006) $V_P$ and $V_S$ structure of the Yellowstone hot spot from teleseismic tomography: Evidence for an upper mantle plume. Journal of Geophysical Research 111, B04303, 21 pp.

Watts K.E., Leeman W.P. & Bindeman I.N. (2010) Supereruptions of the Snake River Plain: Two Stage derivation of low-$\delta^{18}O$ rhyolites from normal-$\delta^{18}O$ crust as constrained by Archean xenoliths. Geology 38, 503–506.

Watts K.E., Bindeman I.N. & Schmitt A.K. (2011) Large-volume rhyolite genesis in caldera complexes of the Snake River Plain: Insights from the Kilgore Tuff of the Heise volcanic field, Idaho with comparison to Yellowstone and Bruneau-Jarbidge rhyolites. Journal of Petrology 52, 857–890.

**CHAPTER II**

Balsley, S., and Gregory, R.T., 1998, Low-$\delta^{18}O$ magmas, why they are so rare?: Earth and Planetary Science Letters, v. 162, p. 123–136, doi: 10.1016/S0012-821X(98)00161-7.

Beard, J.S., Ragland, P.C., and Crawford, M.L., 2005, Reactive bulk assimilation: A model for crust-mantle mixing in silicic magmas: Geology, v. 33, p. 681–684, doi: 10.1130/G21470.1.

Bindeman, I.N., and Valley, J.W., 2001, Low-$\delta^{18}O$ rhyolites from Yellowstone: Magmatic evolution based on analyses of zircon and individual phenocrysts: Journal of Petrology, v. 42, p. 1491–1517, doi: 10.1093/petrology/42.8.1491.

Bindeman, I.N., Schmitt, A.K., and Valley, J.W., 2006, U-Pb zircon geochronology of silicic tuffs from the Timber Mountain/Oasis Valley caldera complex, Nevada: Rapid generation of large volume magmas by shallow-level remelting: Contributions to Mineralogy and Petrology, v. 152, p. 649–665, doi: 10.1007/s00410-006-0124-1.

Bindeman, I.N., Watts, K.E., Schmitt, A.K., Morgan, L.A., and Shanks, P.W.C., 2007, Voluminous low $\delta^{18}O$ magmas in the late Miocene Heise volcanic field, Idaho: Implications for the fate of Yellowstone hotspot calderas: Geology, v. 35, p. 1019–1022, doi: 10.1130/G24141A.1.

Bonnichsen, B., Leeman, W.P., Honjo, N., McIntosh, W.C., and Godchaux, M.M., 2007, Miocene silicic volcanism in southwestern Idaho: Geochronology, geochemistry, and evolution of the central Snake River Plain: Bulletin of Volcanology, doi: 10.1007/s00445-007-0141-6.

Boroughs, S., Wolff, J., Bonnichsen, B., Godchaux, M., and Larson, P., 2005, Large-volume, low-$\delta^{18}O$ rhyolites of the central Snake River Plain, Idaho, USA: Geology, v. 33, p. 821–824, doi: 10.1130/G21723.1.

Christiansen, R.L., 2001, The Quaternary and Pliocene Yellowstone Plateau Volcanic Field of Wyoming, Idaho, and Montana: U.S. Geological Survey Professional Paper 729-Gp. 145 p.

Dufek, J., and Bergantz, G.W., 2005, Lower crustal magma genesis and preservation: A stochastic framework for the evaluation of basalt–crust interaction: Journal of Petrology, v. 46, p. 2167–2195, doi: 10.1093/petrology/egi049.

Hildreth, W., Halliday, A.N., and Christiansen, R.L., 1991, Isotopic and chemical evidence concerning the genesis and contamination of basaltic and rhyolitic magmas beneath the Yellowstone Plateau Volcanic Field: Journal of Petrology, v. 32, p. 63–138.

Morgan, L.A., 1988, Explosive silicic volcanism in the Eastern Snake Rive Plain [Ph.D. thesis]: Manoa, University of Hawaii–Manoap. 191 p.

Morgan, L.A., and McIntosh, W.C., 2005, Timing and development of the Heise volcanic shield, Snake River Plain, Idaho, western USA: Geological Society of America Bulletin, v. 117, p. 288–306, doi: 10.1130/B25519.1.

Morgan, L.A., Doherty, D.J., and Leeman, W.P., 1984, Ignimbrites of the eastern Snake River Plain, Idaho: Evidence for major caldera-forming eruptions: Journal of Geophysical Research, v. 89, p. 8665–8678.

Nash, B.P., Perkins, M.E., Christensen, J.N., Lee, D.C., and Halliday, A.N., 2006, The Yellowstone hotspot in space and time: Nd and Hf isotopes in silicic magmas: Earth and Planetary Science Letters, v. 247, p. 143–156, doi: 10.1016/j.epsl.2006.04.030.

Perkins, M.E., and Nash, B.P., 2002, Explosive silicic volcanism of the Yellow-stone hotspot: The ash fall tuff record: Geological Society of America Bulletin, v. 114, p. 367–381, doi: 10.1130/0016-7606(2002)114<0367: ESVOTY>2.0.CO;2.

Scharer, U., 1984, The effect of initial 230Th disequilibrium on young U-Pb ages: The Makalu case, Himalaya: Earth and Planetary Science Letters, v. 67, p. 27–39.

Valley, J.W., Bindeman, I.N., and Peck, W.H., 2003, Empirical calibration of oxygen isotope fractionation in zircon: Geochimica et Cosmochimica Acta, v. 67, p. 3257–3266, doi: 10.1016/S0016-7037(03)00090-5.

Yuan, H.Y., and Dueker, K., 2005, Teleseismic P-wave tomogram of the Yellow-stone plume: Geophysical Research Letters, v. 32, article L07304, doi: 10.1029/2004GL022056.

**CHAPTER III**

Bindeman, I.N., and Valley, J.W., 2001, Low-$\delta^{18}O$ rhyolites from Yellowstone: Magmatic evolution based on analyses of zircon and individual phenocrysts: Journal of Petrology, v. 42, p. 1491–1517, doi: 10.1093/petrology/42.8.1491.

Bindeman, I.N., Ponomareva, V.V., Bailey, J.C., and Valley, J.W., 2004, Volcanic arc of Kamchatka: A province with high-$\delta^{18}O$ magma sources and large-scale $^{18}O/^{16}O$ depletion of the upper crust: Geochimica et Cosmochimica Acta, v. 68, p. 841–865, doi: 10.1016/j.gca.2003.07.009.

Bindeman, I.N., Watts, K.E., Schmitt, A.K., Morgan, L.A., and Shanks, P.W.C., 2007, Voluminous low $\delta^{18}O$ magmas in the late Miocene Heise volcanic field, Idaho: Implications for the fate of Yellowstone hotspot calderas: Geology, v. 35, p. 1019–1022, doi: 10.1130/G24141A.1.

Bindeman, I.N., Fu, B., Kita, N.T., and Valley, J.W., 2008, Origin and evolution of silicic magmatism at Yellowstone based on ion microprobe analysis of isotopically zoned zircons: Journal of Petrology, v. 49, p. 163–193, doi: 10.1093/petrology/egm075.

Bonnichsen, B., Leeman, W.P., Honjo, N., McIntosh, W.C., and Godchaux, M.M., 2008, Miocene silicic volcanism in southwestern Idaho: Geochronology, geochemistry, and evolution of the central Snake River Plain: Bulletin of Volcanology, v. 70, p. 315–342, doi: 10.1007/s00445-007-0141-6.

Boroughs, S., Wolff, J., Bonnichsen, B., Godchaux, M., and Larson, P., 2005, Large-volume, low-$\delta^{18}O$ rhyolites of the central Snake River Plain, Idaho, USA: Geology, v. 33, p. 821–824, doi: 10.1130/G21723.1.

Criss, R.E., and Fleck, R.J., 1987, Petrogenesis, geochronology, and hydrothermal systems in the northern Idaho batholith and adjacent areas based on $^{18}O/^{16}O$, D/H, $^{87}Sr/^{86}Sr$, K-Ar, and $^{40}Ar/^{39}Ar$ studies: U.S. Geological Survey Professional Paper 1436, p. 95–137.

Doe, B.R., Leeman, W.P., Christansen, R.L., and Hedge, C.E., 1982, Lead and strontium isotopes and related trace elements as genetic tracers in the upper Cenozoic rhyolite-basalt association of the Yellowstone Plateau volcanic field: Journal of Geophysical Research, v. 87, p. 4785–4806.

Graham, D.W., Reid, M.R., Jordan, B.T., Grunder, A.L., Leeman, W.P., and Lupton, J.E., 2009, Mantle source provinces beneath the northwestern USA delimited by helium isotopes in young basalts: Journal of Volcanology and Geothermal Research, v. 188, p. 128–140, doi: 10.1016/j.jvolgeores.2008.12.004.

Hildreth, W., Christiansen, R.L., and O'Neil, J.R., 1984, Catastrophic isotopic modification of rhyolitic magma at times of caldera subsidence, Yellowstone Plateau volcanic field: Journal of Geophysical Research, v. 89, p. 8339–8369, doi: 10.1029/JB089iB10p08339.

Hildreth, W., Halliday, A.N., and Christiansen, R.L., 1991, Isotopic and chemical evidence concerning the genesis and contamination of basaltic and rhyolitic magma beneath the Yellowstone Plateau volcanic field: Journal of Petrology, v. 32, p. 63–138.

King, E.M., Valley, J.W., Stockli, D.F., and Wright, J.E., 2004, Oxygen isotope trends of granitic magmatism in the Great Basin: Location of the Precambrian craton boundary as reflected in zircons: Geological Society of America Bulletin, v. 116, p. 451–462, doi: 10.1130/B25324.1.

King, E.M., Beard, B.L., and Valley, J.W., 2007, Strontium and oxygen isotopic evidence for strike/slip movement of accreted terranes in the Idaho Batholith: Lithos, v. 96, p. 387–401, doi:10.1016/j.lithos.2006.11.001.

Leeman, W.P., Menzies, M.A., Matty, D.J., and Embree, G.F., 1985, Strontium, neodymium and lead isotopic compositions of deep crustal xenoliths from the Snake River Plain: Evidence for Archean basement: Earth and Planetary Science Letters, v. 75, p. 354–368, doi: 10.1016/0012-821X(85)90179-7.

Leeman, W.P., Annen, C., and Dufek, J., 2008, Snake River Plain–Yellowstone silicic volcanism: Implications for magma genesis and magma fluxes: The Geological Society of London Special Publication 304, p. 235–259, doi: 10.1144/SP304.12.

Lipman, P.W., 1997, Subsidence of ash-flow calderas: Relation to caldera size and magma chamber geometry: Bulletin of Volcanology, v. 59, p. 198–218, doi: 10.1007/s004450050186.

McCurry, M., and Rodgers, D.W., 2009, Mass transfer along the Yellowstone hotspot track I: Petrologic constraints on the volume of mantle-derived magma: Journal of Volcanology and Geothermal Research, v. 188, p. 86–98, doi: 10.1016/j.jvolgeores.2009.04.001.

Nash, B.P., Perkins, M.E., Christensen, J.N., Lee, D.C., and Halliday, A.N., 2006, The Yellowstone hotspot in space and time: Nd and Hf isotopes in silicic magmas: Earth and Planetary Science Letters, v. 247, p. 143–156, doi: 10.1016/j.epsl.2006.04.030.

Taylor, H.P. Jr., 1986, Igneous rocks, II: Isotopic case studies of circumpacific magmatism, in Valley, J.W., et al., eds., Stable isotopes in high temperature geological processes: Reviews in Mineralogy and Geochemistry, v. 16, p. 217–317.

Valley, J.W., Lackey, J. S., Cavosie, A. J., Clechenko, C. C., Spicuzza, M. J, Basei, M.A.S., Bindeman, I. N., Ferreira, V. P., Sial, A.N., King, E. M., Peck, W. H., Sinha, A. K., and Wei, C. S., 2004, 4.4 billion years of crustal maturation: oxygen isotope ratios of magmatic zircon: Contributions to Mineral and Petrology, v. 150, p. 561–580.

Vazquez, J.A., and Reid, M.R., 2002. Time scales of magma storage and differentiation of voluminous high-silica rhyolites and Yellowstone caldera, Wyoming: Contributions to Mineralogy and Petrology, v. 144, p. 274–285.

Vazquez, J.A., Kyriazis, S.F., Reid, M.R., Sehler, R.C., and Ramos, F.C., 2009, Thermochemical evolution of young rhyolites at Yellowstone: Evidence for a cooling but periodically replenished postcaldera magma reservoir: Journal of Volcanology and Geothermal Research, v.188, p. 186–196, doi:10.1016/j.j volgeores.2008.11.030.

Watts, K.E., Leeman, W.P., and Bindeman, I.N., 2010, Supereruptions of the Snake River Plain: Two Stage derivation of low-$\delta^{18}O$ rhyolites from normal-$\delta^{18}O$ crust as constrained by Archean xenoliths: Geology, v. 38, p. 503–506, doi: 10.1130/G30735.1.

Watts, K.E., Bindeman, I.N., and Schmitt, A.K., 2011, Large-volume rhyolite genesis in caldera complexes of the Snake River Plain: Insights from the Kilgore Tuff of the Heise volcanic field, Idaho with comparison to Yellowstone and Bruneau-Jarbidge rhyolites: Journal of Petrology, v. 52, p. 857–890, doi: 10.1093/petrology/egr005

Wolf, D.E., Leeman, W.P., and Vervoort, J.D., 2005, U-Pb zircon geochronology of crustal xenoliths confirms presence of Archean basement beneath the central and eastern Snake River Plain: Geological Society of America Abstracts with Programs, v. 37, no. 7, p. 60.

Wickham, S.M, and Peters, M.T., 1990, An oxygen isotope discontinuity in high-grade rocks of the East Humboldt Range, Nevada: Nature, v. 345, p.150–153, doi:10.1038/345150a0.

**CHAPTER IV**


Bachmann, O. & Bergantz, G. W. (2004). On the origin of crystal-poor rhyolites: extracted from batholithic crystal mushes. Journal of Petrology 45, 1565–1582.

Bacon, C. R. (1983). Eruptive history of mount Mazama and Crater Lake caldera Cascade Range, USA. Journal of Volcanology and Geothermal Research 18, 57–115.

Bindeman, I. N. (2008). Oxygen isotopes in mantle and crustal magmas as revealed by single crystal analysis. In: Putirka, K. D.& Tepley, F. J., III (eds) Minerals, Inclusions and Volcanic Processes. Mineralogical Society of America and Geochemical Society, Reviews in Mineralogy and Geochemistry 69, 445–478.

Bindeman, I. N. & Valley, J. W. (2001). Low-$\delta^{18}O$ rhyolites from Yellowstone: magmatic evolution based on analyses of zircons and individual phenocrysts. Journal of Petrology 42, 1491–1517.

Bindeman, I. N. & Valley, J. W. (2002). Oxygen isotope study of the Long Valley magma system, California: isotope thermometry and convection in large silicic magma bodies. Contributions to Mineralogy and Petrology 144, 185–205.

Bindeman, I. N., Valley, J. W., Wooden, J. L. & Persing, H. M. (2001). Post-caldera volcanism: in situ measurement of U–Pb age and oxygen isotope ratio in Pleistocene zircons from Yellowstone caldera. Earth and Planetary Science Letters 189, 197–206.

Bindeman, I. N., Ponomareva, V. V., Bailey, J. C. & Valley, J. W. (2004). Kamchatka Peninsula: a province with high-$\delta^{18}O$ magma sources and large scale $^{18}O/^{16}O$ depletion of the upper crust. Geochimica et Cosmochimica Acta 68, 841–865.

Bindeman, I. N., Schmitt, A. K. & Valley, J. W. (2006). U–Pb zircon geochronology of silicic tuffs from the Timber Mt/Oasis Valley caldera complex, Nevada: rapid generation of large-volume magmas by shallow-level remelting. Contributions to Mineralogy and Petrology 152, 649–665.

Bindeman, I. N., Watts, K. E., Schmitt, A. K., Morgan, L. A. & Shanks, P. W. C. (2007). Voluminous low $\delta^{18}O$ magmas in the late Miocene Heise volcanic field, Idaho: implications for the fate of Yellowstone hotspot calderas. Geology 35, 1019–1022.

Bindeman, I. N., Fu, B., Kita, N. T. & Valley, J. W. (2008). Origin and evolution of Yellowstone silicic magmatism based on ion micro- probe analysis of isotopically zoned zircons. Journal of Petrology 49, 163–193.

Bonnichsen, B., Leeman, W. P., Honjo, N., McIntosh, W. C. & Godchaux, M. M. (2008). Miocene silicic volcanism in southwestern Idaho: geochronology, geochemistry, and evolution of the central Snake River Plain. Bulletin of Volcanology 70, 315–342.

Boroughs, S. B., Wolff, J., Bonnichsen, B., Godchaux, M. & Larson, P. (2005). Large volume, low-$\delta^{18}O$ rhyolites of the central Snake River Plain, Idaho, USA. Geology 33, 821–824.

Bowen, G. J., Ehleringer, J. R., Chesson, L. A., Stange, E. & Cerling, T. E. (2007). Stable isotope ratios of tap water in the contiguous United States. Water Resources Research 43, W03419.

Branney, M. J., Bonnichsen, B., Andrews, G. D. M., Ellis, B., Barry, T. L. & McCurry, M. (2008). 'Snake River (SR)-type' volcanism at the Yellowstone hotspot track: distinctive products from unusual, high-temperature silicic super-eruptions. Bulletin of Volcanology 70, 293–314.

Cathey, H. E. & Nash, B. P. (2004). The Cougar Point Tuff: implications for thermochemical zonation and longevity of high-temperature, large-volume silicic magmas of the Miocene Yellowstone hotspot. Journal of Petrology 45, 27–58.

Cathey, H. E. & Nash, B. P. (2009). Pyroxene thermometry of rhyolite lavas of the Bruneau–Jarbidge eruptive center, Central Snake River Plain. Journal of Volcanology and Geothermal Research 188, 173–185.

Cathey, H. E., Nash, B. P., Allen, C. M., Campbell, I. H., Valley, J. W. & Kita, N. (2008). U–Pb zircon geochronology and Ti-in-zircon thermometry of large-volume low- $\delta^{18}O$ magmas of the Miocene Yellowstone hotspot (Goldschmidt conference abstract). Geochimica et Cosmochimica Acta 72, A143.

Charlier, B. L. A., Wilson, C. J. N., Lowenstern, J. B., Blake, S., Van Calsteren, P. W. & Davidson, J. P. (2005). Magma generation at a large hyperactive silicic volcano (Taupo, New Zealand) revealed by U–Th and U–Pb systematics in zircons. Journal of Petrology 46,3–32.

Christiansen, R. L. (2001). The Quaternary and Pliocene Yellowstone Plateau Volcanic Field of Wyoming, Idaho, and Montana. US Geological Survey, Professional Papers 729-G, , 145 p.

Christiansen, R. L., Lowenstern, J. B., Smith, R. B., Heasler, H., Morgan, L. A., Nathansen, M., Mastin, L.G., Muffler, L. J. P & Robinson, J. E. (2007). Preliminary assessment of volcanic and hydrothermal hazards in Yellowstone National Park and vicinity. US Geological Survey Open-File Report 1071, 94 p.

Coats, R. R., Green, R. C., Cress, L. D. & Marks, L.Y. (1977). Mineral resources of the Jarbidge Wilderness and adjacent areas, Elko County, Nevada. US Geological Survey Bulletin 1439, 79 p.

Criss, R. E. & Fleck, R. J. (1987). Petrogenesis, geochronology, and hydrothermal systems in the northern Idaho batholith and adjacent areas based on $^{18}O/^{16}O$, D/H, $^{87}Sr/^{86}Sr$, K–Ar, and $^{40}Ar/^{39}Ar$ studies. US Geological Survey Professional Paper 1436, 95–137.

Davis, O. K. & Ellis, B. (2010). Early occurrence of sagebrush steppe, Miocene (12 Ma) on the Snake River Plain. Review of Palaeobotany and Palynology 160, 172–180.

Dufek, J. & Bergantz, G. W. (2005). Lower crustal magma genesis and preservation: A stochastic framework for the evaluation of basalt-crust interaction. Journal of Petrology 46, 2167–2195.

Friedman, I., Lipman, P. W., Obradovich, J. D., Gleason, J. D. & Christiansen, R. L. (1974). Meteoric water in magmas. Science 184, 1069–1072.

Fu, B., Page, F. Z., Cavosie, A. J., Fournelle, J., Kita, N. T., Lackey, J. S., Wilde, S. A. & Valley, J. W. (2008). Ti-in-zircon thermometry: applications and limitations. Contributions to Mineralogy and Petrology 156, 197–215.

Gansecki, C. A. (1998). $^{40}Ar/^{39}Ar$ geochronology and pre-eruptive geochemistry of the Yellowstone Plateau volcanic field rhyolites, PhD thesis, Stanford University, Stanford, CA, 213 pp.

Garcia, M. O., Ito, E., Eiler, J. M. & Pietruszka, A. J. (1998). Crustal contamination of Kilauea Volcano magmas revealed by oxygen isotope analyses of glass and olivine from Pu'u O'o eruption lavas. Journal of Petrology 39, 803–817.

Ghiorso, M. S. & Sack, R. O. (1991). Fe–Ti oxide geothermometry: thermodynamic formulation and the estimation of intensive variables in silicic magmas. Contributions to Mineralogy and Petrology 108, 485–510.

Ghiorso, M. S. & Sack, R. O. (1995). Chemical mass-transfer in magmatic processes IV: A revised and internally-consistent thermodynamic model for the interpolation and extrapolation of liquid–solid equilibria in magmatic systems at elevated temperatures and pressures. Contributions to Mineralogy and Petrology 119, 197–212.

Grunder, A. L. (1995). Material and thermal roles of basalt in crustal magmatism: Case study from eastern Nevada. Geology 23, 952–956.

Hackett, W. R. & Morgan, L. A. (1988). Explosive basaltic and rhyolitic volcanism of the eastern Snake River Plain, Idaho. In: Link, P. K. & Hackett, W. R. (eds) Guidebook to the geology of central and southern Idaho. Idaho Geological Survey Bulletin 27, 283–301.

Halliday, A. N., Mahood, G. A., Holden, P., Metz, J. M., Dempster, T. J. & Davidson, J. P. (1989). Evidence for long residence times of rhyolitic magma in the Long Valley magmatic system: the isotopic record in precaldera lavas of Glass Mountain. Earth and Planetary Science Letters 94, 274–290.

Harris, C., Smith, H. S. & le Roex, A. P. (2000). Oxygen isotope composition of phenocrysts from Tristan da Cunha and Gough Island lavas: Variation with fractional crystallization and evidence for assimilation. Contributions to Mineralogy and Petrology 138, 164–175.

Henshaw, N. D. (2002). Temperature of silicic magmas from the Yellowstone hotspot, MS thesis, University of Utah, Salt Lake City, UT, 181 pp.

Hildreth, W. & Wilson, C. J. N. (2007). Compositional zoning of the Bishop Tuff. Journal of Petrology 48, 951–999.

Hildreth, W., Christiansen, R. L. & O'Neil, J. R. (1984). Catastrophic isotopic modification of rhyolitic magma at times of caldera subsidence, Yellowstone Plateau Volcanic Field. Journal of Geophysical Research 89, 8339–8369.

Hildreth, W., Halliday, A. N. & Christiansen, R. L. (1991). Isotopic and chemical evidence concerning the genesis and contamination of basaltic and rhyolitic magmas beneath the Yellowstone Plateau Volcanic Field. Journal of Petrology 32, 63–138.

Honjo, N., McElwee, K. R., Duncan, R. A. & Leeman, W. P. (1986). K–Ar ages of volcanic rocks from the Magic Reservoir eruptive center, Snake River Plain, Idaho. Isochron West 46, 15–19.

Kita, N. T., Ushikubo, T., Fu, B. & Valley, J. W. (2009). High precision SIMS oxygen isotope analysis and the effect of sample topography. Chemical Geology 264, 43–57.

Lanphere, M. A., Champion, D. E., Christiansen, R. L., Izett, G. A. & Obradovich, J. D. (2002). Revised ages for tuffs of the Yellowstone Plateau volcanic field: Assignment of the Huckleberry Ridge Tuff to a new geomagnetic polarity event. Geological Society of America Bulletin 114, 559–568.

Leeman, W. P., Menzies, M. A., Matty, D. J. & Embree, G. F. (1985). Strontium, neodymium and lead isotopic compositions of deep crustal xenoliths from the Snake River Plain: Evidence for Archean basement. Earth and Planetary Science Letters 75, 354–368.

Leeman, W. P., Oldow, J. S. & Hart, W. K. (1992). Lithosphere-scale thrusting in the western US Cordillera as constrained by Sr and Nd isotopic transitions in Neogene volcanic rocks. Geology 20, 63–66.

Leeman, W. P., Annen, C. & Dufek, J. (2008). Snake River Plain–Yellowstone silicic volcanism: Implications for magma genesis and magma fluxes. In: Annen, C. & Zellmer, G. F. (eds) Dynamics of Crustal Magma Transfer, Storage and Differentiation. Geological Society, London, Special Publications 304, 235–259.

Manduca, C. A., Silver, L. T. & Taylor, H. P. (1992). $^{87}Sr/^{86}Sr$ and $^{18}O/^{16}O$ isotopic systematics and geochemistry of granitoid plutons across a steeply dipping boundary between contrasting lithospheric blocks in western Idaho. Contributions to Mineralogy and Petrology 109, 355–372.

Manea, V. C., Manea, M., Leeman, W. P. & Schutt, D. L. (2009). The influence of plume head–lithosphere interaction on magmatism associated with the Yellowstone hotspot track. Journal of Volcanology and Geothermal Research 188, 68–85.

Martin, E. & Bindeman, I. (2009). Mass-independent isotopic signatures of volcanic sulfate from three supereruption ash deposits in Lake Tecopa, California. Earth and Planetary Science Letters 282, 102–114.

Mason, B. G., Pyle, D. M. & Oppenheimer, C. (2004). The size and frequency of the largest explosive eruptions on Earth. Bulletin of Volcanology 66, 735–768.

Matsuhisa, Y. (1979). Oxygen isotopic compositions of volcanic rocks from the east Japan island arc and their bearing on petrogenesis. Journal of Volcanology and Geothermal Research 5, 271–296.

McCurry, M. & Rodgers, D. W. (2009). Mass transfer along the Yellowstone hotspot track I: Petrologic constraints on the volume of mantle-derived magma. Journal of Volcanology and Geothermal Research 188, 86–98.

McLennan, S. M., Taylor, S. R. & Hemming, S. R. (2006). Composition, differentiation, and evolution of continental crust: constraints from sedimentary rocks and heat flow. In: Brown, M & Rushmer, T. (eds) Evolution and Differentiation of the Continental Crust. Cambridge: Cambridge University Press, pp. 92–134.

Morgan, L. A. (1988). Explosive silicic volcanism in the eastern Snake River Plain, PhD thesis, University of Hawaii–Manoa, Honolulu, HI, 191 p.

Morgan, L. A. & McIntosh, W. C. (2005). Timing and development of the Heise volcanic field, Snake River Plain, Idaho, western USA. Geological Society of America Bulletin 117, 288–306.

Nash, B. P., Perkins, M. E., Christensen, J. N., Lee, D. C. & Halliday, A. N. (2006). The Yellowstone hotspot in space and time: Nd and Hf isotopes in silicic magmas. Earth and Planetary Science Letters 247, 143–156.

Obradovich, J. D. (1992). Geochronology of the Late Cenozoic volcanism of Yellowstone National Park and adjoining areas, Wyoming and Idaho. US Geological Survey, Open-File Report 92–408, 1–45.

O'Neil, J. R., Clayton, R. N. & Mayeda, T. K. (1969). Oxygen isotope fractionation in divalent metal carbonates. Journal of Chemical Physics 51, 5547–5558.

Paces, J. B. & Miller, J. D., Jr (1993). Precise U–Pb ages of Duluth Complex and related mafic intrusions, northeastern Minnesota: Geochronological insights to physical, petrogenetic, paleomagnetic, and tectonomagmatic processes associated with the 1·1 Ga Midcontinent Rift System. Journal of Geophysical Research 98, 13997–14013.

Peng, X. & Humphreys, E. D. (1998). Crustal velocity structure across the eastern Snake River Plain and the Yellowstone swell. Journal of Geophysical Research 103, 7171–7186.

Pierce, K. L. & Morgan, L. A. (1992). The track of the Yellowstone hot- spot: volcanism, faulting, and uplift. In: Link, P. K., Kuntz, M. A. & Platt, L. B. (eds) Regional Geology of Eastern Idaho and Western Wyoming. Geological Society of America, Memoirs 179, 1–53.

Rampino, M. R. & Self, S. (1992). Volcanic winter and accelerated glaciation following the Toba super-eruption. Nature 359, 50–52.

Reid, M. R. (2003). Timescales of magma transfer and storage in the crust. In: Rudnick, R. L. (ed.) The Crust. Treatise on Geochemistry, Vol. 3. Amsterdam: Elsevier, pp. 167–193.

Retallack, G. J., Tanaka, S. & Tate, T. (2002). Late Miocene advent of tall grassland paleosols in Oregon. Palaeogeography, Palaeoclimatology, Palaeoecology 183, 329–354.

Savov, I.P., Leeman, W.P., Lee, C.-T.A. & Shirey, S.B. (2009). Boron isotopic variations in NW USA rhyolites: Yellowstone, Snake River Plain, Eastern Oregon. Journal of Volcanology and Geothermal Research 188, 162–172.

Scharer, U. (1984). The effect of initial $^{230}$Th disequilibrium on young U–Pb ages: the Makalu case Himalaya. Earth and Planetary Science Letters 67, 191–204.

Schmitt, A. K., Grove, M., Harrison, T. M., Lovera, O., Hulen, J. B. & Walters, M. (2003). The Geysers–Cobb mountain magma system, California (Part 1): U–Pb zircon ages of volcanic rocks, conditions of zircon crystallization and magma residence times. Geochimica et Cosmochimica Acta 67, 3423–3442.

Sheppard, S.M. F. & Harris, C. (1985). Hydrogen and oxygen isotope geochemistry of Ascension Island lavas and granites: Variation with crystal crystallization and interaction with sea water. Contributions to Mineralogy and Petrology 91, 74–81.

Simon, J. I. & Reid, M. R. (2005). The pace of rhyolite differentiation and storage in an 'archetypical' silicic magma system, Long Valley, California. Earth and Planetary Science Letters 235, 123–140.

Simon, J. I., Vazquez, J. A., Renne, P. R., Schmitt, A. K., Bacon, C. R. & Reid, M. R. (2009). Accessory mineral U–Th–Pb ages and 40Ar/39Ar eruption chronology, and their bearing on rhyolitic magma evolution in the Pleistocene Coso volcanic field, California. Contributions to Mineralogy and Petrology 158, 421–446.

Smith, R. B. & Braile, L. W. (1994). The Yellowstone hotspot. Journal of Volcanology and Geothermal Research 61, 121–187.

Snyder, D. (2000). Thermal effects of the intrusion of basaltic magma into a more silicic magma chamber and implications for eruption triggering. Earth and Planetary Science Letters 175, 257–273.

Taylor, H. P., Jr (1986). Igneous rocks: II. Isotopic case studies of circumpacific magmatism. In: Valley, J. W., Taylor, H. P., Jr & O'Neil, J. R. (eds) Stable Isotopes in High Temperature Geological Processes. Mineralogical Society of America, Reviews in Mineralogy 16, 273–316.

Taylor, S. R. & McLennan, S. M. (1985). The Continental Crust: its Composition and Evolution. Oxford: Blackwell.

Trail, D., Bindeman, I. N., Watson, E. B. & Schmitt, A. K. (2009). Experimental calibration of oxygen isotope fractionation between quartz and zircon. Geochimica et Cosmochimica Acta 73, 7110–7126.

Vazquez, J. A. & Reid, M. R. (2002). Time scales of magma storage and differentiation of voluminous high-silica rhyolites at Yellowstone caldera, Wyoming. Contributions to Mineralogy and Petrology 144, 274–285.

Vazquez, J. A. & Reid, M. R. (2004). Probing the accumulation history of the voluminous Toba magma. Science 305, 991–994.

Vazquez, J. A., Kyriazis, S. F., Reid, M. R., Sehler, R. C. & Ramos, F. C. (2009). Thermochemical evolution of young rhyolites at Yellowstone: Evidence for a cooling but periodically replenished postcaldera magma reservoir. Journal of Volcanology and Geothermal Research 188, 186–196.

Wark, D. A., Hildreth, W., Spear, F. S., Cherniak, D. J. & Watson, E. B. (2007). Pre-eruption recharge of the Bishop magma system. Geology 35, 235–238.

Watson, E. B. & Harrison, T. M. (1983). Zircon saturation revisited: temperature and compositional effects in a variety of crustal magma types. Earth and Planetary Science Letters 64, 295–304.

Watson, E. B. & Harrison, T. M. (2005). Zircon thermometer reveals minimum melting conditions on earliest Earth. Science 308, 841–844.

Watts, K. E., Leeman, W. P., Bindeman, I. N. & Larson, P. B. (2010). Supereruptions of the Snake River Plain: Two-stage derivation of low-$\delta^{18}O$ rhyolites from normal-$\delta^{18}O$ crust as constrained by Archean xenoliths. Geology 38, 503–506.

Watts K.E., Bindeman I.N. & Schmitt A.K. (2011). Large-volume rhyolite genesis in caldera complexes of the Snake River Plain: Insights from the Kilgore Tuff of the Heise volcanic field, Idaho with comparison to Yellowstone and Bruneau-Jarbidge rhyolites. Journal of Petrology 52, 857–890.

Wyllie, P. J., Huang, W. L., Stern, C. R. & Maaloe, S. (1976). Granitic magmas: possible and impossible sources, water contents, and crystallization sequences. Canadian Journal of Earth Science 13, 1007–1019.

Zheng, Y.-F. (1993). Calculation of oxygen isotope fractionation in anhydrous silicate minerals. Geochimica et Cosmochimica Acta 57, 1079–1091.

**CHAPTER V**

Bacon, C.R., Lowenstern, J.B., 2005. Late Pleistocene granodiorite source for recycled zircon and phenocrysts in rhyodacite lava at Crater Lake, Oregon. Earth Planet. Sci. Lett. 233, 277–293.

Baker J., Peate D., Waight T., Meyzen C. 2004. Pb isotopic analysis of standards and samples using a $^{207}Pb$–$^{204}Pb$ double spike and thallium to correct for mass bias with double-focusing MC-ICP-MS. Chem. Geol. 211, 275–303.

Bindeman, I. N.,Valley, J.W.,Wooden, J. L., Persing, H. M., 2001. Post-caldera volcanism: in situ measurement of U-Pb age and oxygen isotope ratio in Pleistocene zircons from Yellowstone caldera. Earth Planet. Sci. Lett. 189, 197–206.

Bindeman, I. N., Valley, J. W., 2000. The formation of low-$\delta^{18}O$ rhyolites after caldera collapse at Yellowstone, Wyoming, USA. Geology 28, 719–722.

Bindeman, I. N., Valley, J. W., 2001. Low-$\delta^{18}O$ rhyolites from Yellowstone: Magmatic evolution based on analyses of zircons and individual phenocrysts. J. Petrol. 42, 1491–1517.

Bindeman, I. N., Valley, J. W., 2002. Oxygen isotope study of the Long Valley magma system, California: isotope thermometry and convection in large silicic magma bodies. Contrib. Mineral. Petrol. 144, 185–205.

Bindeman, I.N., Fu, B., Kita, N.T., Valley, J.W., 2008. Origin and evolution of Yellowstone silicic magmatism based on ion microprobe analysis of isotopically-zoned zircons. J. Petrol. 49, 163–193.

Charlier, B. L. A., Bachmann, O., Davidson, J. P., Dungan, M. A., Morgan, D., 2007. The upper crustal evolution of a large silicic magma body: evidence from crystal-scale Rb/Sr isotopic heterogeneities in the Fish Canyon magmatic system, Colorado. J. Petrol. 48, 1875–1894.

Christiansen, R.L., Blank, H.R., Jr., 1972. Volcanic stratigraphy of the Quaternary rhyolite plateau in Yellowstone National Park. USGS Prof. Paper 729-B, 23 pp.

Christiansen, R. L., 2001. The Quaternary and Pliocene Yellowstone Plateau Volcanic Field of Wyoming, Idaho, and Montana. USGS Prof. Papers 729-G, 145 pp.

Christiansen, R.L., Lowenstern, J.B., Smith, R.B., Heasler, H., Morgan, L.A., Nathansen, M., Mastin, L.G., Muffler, L.J.P., Robinson, J.E., 2007. Preliminary assessment of volcanic and hydrothermal hazards in Yellowstone National Park and vicinity. USGS Open-File Report 1071 2007, 94 pp.

Doe, B. R., Leeman,W. P., Christiansen, R. L., Hedge, C. E., 1982. Lead and strontium isotopes and related trace elements as genetic tracers in the Upper Cenozoic rhyolite-basalt association of the Yellowstone Plateau volcanic field. J. Geophys. Res. 87, 4785–4806.

Friedman, I., Lipman, P. W., Obradovich, J. D., Gleason, J. D., Christiansen, R. L., 1974. Meteoric water in magmas. Science 184, 1069–1072.

Gansecki, C. A., Mahood, G. A., McWilliams, M. O., 1996. $^{40}Ar/^{39}Ar$ geochronology of rhyolites erupted following collapse of the Yellowstone caldera, Yellowstone Plateau volcanic field: implications for crustal contamination. Earth Planet. Sci. Lett. 142, 91–107.

Ghiorso, M. S., Sack, R. O., 1995. Chemical mass-transfer in magmatic processes IV: A revised and internally-consistent thermodynamic model for the interpolation and extrapolation of liquid-solid equilibria in magmatic systems at elevated temperatures and pressures. Contrib. Mineral. Petrol. 119, 197-212.

Girard, G., Stix, J., 2009a. Rapid extraction of discrete magma batches from a large differentiating magma chamber: the Central Plateau Member rhyolites, Yellowstone Caldera, Wyoming. Contrib. Mineral. Petrol., 160, 441–465.

Girard, G., Stix, J., 2009b. Magma recharge and crystal mush rejuvenation associated with early post-collapse Upper Basin Member rhyolites, Yellowstone caldera, Wyoming. J. Petrol. 50, 2095–2125.

Hildreth,W., Christiansen, R. L., O'Neil, J. R., 1984. Catastrophic isotopic modification of rhyolitic magma at times of caldera subsidence, Yellowstone Plateau Volcanic Field. J. Geophys. Res. 89, 8339–8369.

Hildreth, W., Halliday, A. N., Christiansen, R. L., 1991. Isotopic and chemical evidence concerning the genesis and contamination of basaltic and rhyolitic magmas beneath the Yellowstone Plateau Volcanic Field. J. Petrol. 32, 63–138.

Kent, A.J.R., 2008. In-situ analysis of Pb isotope ratios using laser ablation MC-ICP-MS: Controls on precision and accuracy and comparison between Faraday cup and ion counting systems. J. Analy. Atom. Spect. 23, 968–975.

Kita, N.T., Ushikubo, T., Fu, B., Valley, J.W., 2009. High precision SIMS oxygen isotope analysis and the effect of sample topography. Chem. Geol. 264, 43–57.

Lanphere, M. A., Champion, D. E., Christiansen, R. L., Izett, G. A., Obradovich, J. D., 2002. Revised ages for tuffs of theYellowstone Plateau volcanic field: Assignment of the Huckleberry Ridge Tuff to a new geomagnetic polarity event. Geol. Soc. Amer. Bull. 114, 559–568.

Morgan, L. A., McIntosh,W. C., 2005.Timing and development of the Heise volcanic field, Snake River Plain, Idaho, western USA. Geol. Soc. Am. Bull. 117, 288-306.

Nash, B.P., Perkins, M.E., Christensen, J.N., Lee, D.C., Halliday, A.N., 2006. The Yellowstone hotspot in space and time: Nd and Hf isotopes in silicic magmas. Earth Planet. Sci. Lett. 247, 143–156.

Obradovich, J. D., 1992. Geochronology of the Late Cenozoic volcanism of Yellowstone National Park and adjoining areas, Wyoming and Idaho. USGS Open-File Report 92-408, 1–45.

Paces, J.B., Miller, J.D., Jr., 1993. Precise U-Pb ages of Duluth Complex and related mafic intrusions, northeastern Minnesota: Geochronological insights to physical, petrogenetic, paleomagnetic, and tectonomagmatic processes associated with the 1.1 Ga Midcontinent Rift System. J. Geophys. Res. 98, 13997–14013.

Pierce, K.L., Morgan, L.A., 1992. The track of the Yellowstone hotspot: volcanism, faulting, and uplift. In: Link, P.K., Kuntz, M.A., Platt, L.B. (eds) Regional Geology of Eastern Idaho and Western Wyoming. Geol. Soc. Amer. Mem. 179, 1–53.

Schmitt, A.K., Grove, M., Harrison, T.M., Lovera, O., Hulen, J.B., Walters, M., 2003. The Geysers-Cobb mountain magma system California (Part 1): U–Pb zircon ages of volcanic rocks conditions of zircon crystallization and magma residence times. Geochim. Cosmochim. Acta. 67, 3423–3442.

Schmitt, A. K., Stockli, D. F., Hausback, B. P., 2006. Eruption and magma crystallization ages of Las Tres Vírgenes (Baja California) constrained by combined $^{230}Th/^{238}U$ and (U–Th)/He dating of zircon. J. Volcanol. Geotherm. Res. 158, 281–295.

Simon, J.I., Reid, M.R., Young, E.D., 2007. Lead isotopes by LA-MC-ICPMS: Tracking the emergence of mantle signatures in an evolving silicic magma system. Geochim. Cosmochim. Acta. 71, 2014–2035.

Taylor, H. P., Jr., 1986. Igneous rocks: II. Isotopic case studies of circumpacific magmatism. In: Valley, J. W., Taylor, H. P., Jr & O'Neil, J. R. (eds) Stable Isotopes in High Temperature Geological Processes. Mineral. Soc. of Amer., Rev. Mineral. 16, 273–316.

Valley, J.W., 2003. Oxygen isotopes in zircon. In: Hanchar, J.M., Hoskin, P.W.O. (eds) Zircon. Mineral. Soc. Amer., Rev. Mineral. And Geochem. 53, 343–385.

Vazquez, J. A., Reid, M. R., 2002. Time scales of magma storage and differentiation of voluminous high-silica rhyolites at Yellowstone caldera, Wyoming. Contrib. Mineral. Petrol. 144, 274–285.

Vazquez, J.A., Kyriazis, S.F., Reid, M.R., Sehler, R.C., Ramos, F.C., 2009. Thermochemical evolution of young rhyolites at Yellowstone: Evidence for a cooling but periodically replenished postcaldera magma reservoir. J. Volcanol. Geotherm. Res. 188, 186–196.

Watson, E. B., 1996. Dissolution, growth and survival of zircons during crustal fusion: Kinetic principles, geological models and implications for isotopic inheritance. Transactions of the Royal Society of Edinburgh: Earth Sciences 87, 43–56.

Watson, E. B., Harrison, T. M.,1983. Zircon saturation revisited: temperature and compositional effects in a variety of crustal magma types. Earth Planet Sci. Lett. 64, 295–304.

Watts, K.E., Leeman, W.P., Bindeman, I.N., Larson, P.B., 2010. Supereruptions of the Snake River Plain: Two-stage derivation of low-$\delta^{18}O$ rhyolites from normal-$\delta^{18}O$ crust as constrained by Archean xenoliths. Geology 38, 503–506.

Watts, K.E., Bindeman, I.N., Schmitt, A.K., 2011. Large-volume rhyolite genesis in caldera complexes of the Snake River Plain: Insights from the Kilgore Tuff of the Heise volcanic field Idaho with comparison to Yellowstone and Bruneau-Jarbidge rhyolites. J. Petrol. 52, 857–890.

Wiedenbeck, M., Allé, P., Corfu, F., Griffin, W.L., Meier, M., Oberli, F., von Quadt, A., Roddick, J.C., Spiegel, W., 1995. Three natural zircon standards for U-Th-Pb, Lu-Hf, trace element and REE analyses. Geostand. Newslett. 19, 1–23.

Williams, I. S., 1998. U-Th-Pb geochronology by ion microprobe: In: McKibben, M.A., Shanks, W.C., Ridley, W.I. (eds) Applications of Microanalytical Techniques to Understanding Mineralizing Processes. Rev. Econom. Geol. 7, 1–35.